



**HAL**  
open science

# Contribution of neutron/X-ray tomography for the drying modeling of cohesive porous media

Hani Cheikh Sleiman

► **To cite this version:**

Hani Cheikh Sleiman. Contribution of neutron/X-ray tomography for the drying modeling of cohesive porous media. Material chemistry. Université Grenoble Alpes [2020-..], 2021. English. NNT : 2021GRALI014 . tel-03548231

**HAL Id: tel-03548231**

**<https://theses.hal.science/tel-03548231>**

Submitted on 30 Jan 2022

**HAL** is a multi-disciplinary open access archive for the deposit and dissemination of scientific research documents, whether they are published or not. The documents may come from teaching and research institutions in France or abroad, or from public or private research centers.

L'archive ouverte pluridisciplinaire **HAL**, est destinée au dépôt et à la diffusion de documents scientifiques de niveau recherche, publiés ou non, émanant des établissements d'enseignement et de recherche français ou étrangers, des laboratoires publics ou privés.

## THÈSE

Pour obtenir le grade de

### DOCTEUR DE L'UNIVERSITE GRENOBLE ALPES

Spécialité : **Matériaux, Mécanique, Génie-Civil, Electrochimie**

Arrêté ministériel : 25 mai 2016

Présentée par

**Hani CHEIKH SLEIMAN**

Thèse dirigée par **Matthieu BRIFFAUT**, Maître de conférences HDR, UGA et Co-encadrée par **Stefano DAL PONT**, Professeur, UGA et **Alessandro TENGATTINI**, Maître de conférences, UGA

préparée au sein du **Laboratoire Sols, Solides, Structures et Risques (3SR)** dans l'**École Doctorale I-MEP2 – Ingénierie – Matériaux, Mécanique, Environnement, Énergétique, Procédés, Production**

## Contribution of neutron /X-ray tomography for the drying modelling of cohesive porous media

Soutenance de thèse prévue le **28/01/2021**, devant le jury composé de :

**M. Farid BENBOUDJEMA**

Professeur à l'École Normale Supérieure Paris-Saclay, Rapporteur

**Mme. Catherine DAVY**

Professeur à l'École Centrale de Lille, Rapporteur

**M. Fekri MEFTAH**

Professeur à l'INSA Rennes, Président

**M. Giuseppe SCIUME**

Maître de conférences à l'Université de Bordeaux, Examineur

**M. Bruno HUET**

Docteur Ingénieur de recherche chez LafargeHolcim R&D, Examineur

**M. Jean-Luc ADIA**

Docteur Ingénieur de recherche chez EDF R&D, Invité

**M. Matthieu BRIFFAUT**

Maître de conférences HDR à l'université Grenoble Alpes, Directeur de thèse

**M. Stefano DAL PONT**

Professeur à l'université Grenoble Alpes, Co-encadrant

**M. Alessandro TENGATTINI**

Maître de conférences à l'université Grenoble Alpes, Co-encadrant



# Abstract

The drying of cement-based materials affects directly their durability, which has a major economic, societal, and environmental impact.

The conventional experimental techniques such as gravimetric and sensor-based measurements, which are employed to study the drying-driven processes, provide only bulk-averaged or point-wise measurements which are not sufficient to characterize these processes. However, the significant advances in full-field techniques have allowed unprecedented insight into these local processes. Notably, for cement-based materials, x-ray and neutron tomography lend themselves as highly complementary tools for the study of their THM behavior. In fact, the high sensitivity to density variations of x-ray imaging gives access to the developments of fractures, in 4D (3D+time). On the other hand, neutron tomography allows the study of the evolution of the moisture field in 4D, thanks to its high hydrogen sensitivity.

This Ph.D. takes advantage of these two highly complementary techniques, which, together with advanced numerical modeling tools, allowed for a novel experimental/numerical insight to study the drying-driven physical processes in cement-based materials. In this work, two experimental campaigns were performed at the NeXT instrument located at the ILL. In the first campaign, neutron tomography was employed to characterize the moisture distribution of a set of cylindrical mortar samples which were set to dry sequentially in a TH controlled environment ( $T=20\text{ }^{\circ}\text{C}$ ,  $\text{RH}=35\%$ ) to represent different hydric states. The main phases of the mortar (aggregates, cement paste, and voids) were separated, and saturation profiles were deduced and validated against the weight loss measurements. In the second experimental campaign, more complexity was added to the experimental drying conditions by heating concrete and cement paste samples up to moderate temperature which has led to the appearance of cracks in the later sample. The analysis of the acquired simultaneous neutron/x-ray data-set (once aligned in time and across modalities) allowed for the quantification of the 4D moisture profiles which were found to predict an overall water loss at hydric equilibrium coherent with the corresponding analytical analysis. In the cement paste sample, the x-ray dataset captures the evolution of an extensive cracking network, opening, and propagation toward the core of the sample. Then, a novel analysis procedure was proposed which allowed the extraction of these fractures and the analysis of their interplay with local drying as captured through neutron imaging.

On the other hand, the numerical approach employed in this study consisted of improving the numerical model predictive capacity by assessing the implications of common simplifications on the modeling response. These common simplifications can be divided in three main categories which regard the consideration of gaseous transport modes, the TH and HM couplings, and the morphological description of the material. Quantification of these simplifications effects regarding the used model and the choice of TH coupling laws was done by comparing mass loss response surfaces in relative humidity and temperature space for multiple configurations. The results show relative error maps at early, mid, and late drying stages for every compared case. On the other hand, the simplification regarding the HM coupling was evaluated in a 2D mesoscopic simulation framework where an artificial concrete mesostructure had to be generated for cracking localization purposes. The cracking impact was then assessed both locally on the saturation fields and on the global mass loss response. Finally, a CT-FE mapping scheme was proposed which consisted of extracting the mesoscale morphology of concrete (aggregates and pores) from x-ray/neutron attenuation fields and presenting it explicitly on a FE mesh. This has permitted to perform 3D multiphase THM simulation of concrete at the mesoscale.

# Resumé

Le séchage des matériaux cimentaires affecte directement leur durabilité, ce qui a un impact économique, sociétal et environnemental majeur.

Les techniques expérimentales conventionnelles, qui sont utilisées pour étudier les processus de séchage, ne fournissent que des mesures moyennées ou ponctuelles qui ne sont pas suffisantes pour caractériser ces processus intrinsèquement hétérogènes. Cependant, les progrès significatifs dans les techniques de plein champ ont permis une observation sans précédent de ces processus locaux. Notamment, la tomographie par rayons X et neutrons se prête comme des outils très complémentaires pour l'étude du comportement THM des matériaux cimentaires. En effet, la grande sensibilité aux variations de densité de l'imagerie par rayons X donne accès aux évolutions des fractures, en 4D (3D + temps). D'autre part, la tomographie neutronique permet d'étudier l'évolution du champ d'humidité en 4D, grâce à sa haute sensibilité à l'hydrogène.

Ce travail a tiré profit de ces deux techniques très complémentaires, qui, associées à des outils de modélisation numérique avancés, ont permis une nouvelle vision expérimentale/numérique pour étudier les processus physiques induits par le séchage dans les matériaux cimentaires.

Dans ce travail, deux campagnes expérimentales ont été réalisées sur l'instrument NeXT situé à l'ILL. Dans la première campagne, la tomographie neutronique a été utilisée pour caractériser la distribution d'humidité d'un ensemble d'échantillons de mortier cylindrique qui ont été mis à sécher séquentiellement dans un environnement TH contrôlé ( $T = 20\text{ °C}$  et  $RH = 35\%$ ) pour représenter différents états hydriques. Les principales phases du mortier (granulats, pâte de ciment et vides) ont été séparées, et des profils de saturation ont été déduits et validés par rapport aux mesures de perte de poids. Dans la deuxième campagne expérimentale, plus de complexité a été ajoutée aux conditions de séchage expérimentales en chauffant des échantillons de béton et de pâte de ciment à une température modérée, ce qui a conduit à l'apparition de fissures dans l'échantillon ultérieur. L'analyse de l'ensemble de données neutrons/rayons X simultanément acquis a permis de quantifier les profils d'humidité 4D. Dans l'échantillon de pâte de ciment, les données de la tomographie rayons X ont capturé l'évolution d'un vaste réseau de fissuration ainsi que leurs ouvertures et leur propagation vers le cœur de l'échantillon. Ensuite, une nouvelle procédure d'analyse a été proposée qui a permis l'extraction de ces fractures et l'analyse de leur interaction avec le séchage local tel que capturé par imagerie neutronique.

D'autre part, l'approche numérique employée dans cette étude a consisté à évaluer les implications des simplifications courantes sur la réponse de modélisation. Ces simplifications communes peuvent être divisées en trois grandes catégories qui concernent la prise en compte des modes de transport gazeux, les couplages TH et HM et la description morphologique du matériau. La quantification de ces effets de simplification concernant le modèle utilisé et le choix des lois de couplage TH a été réalisée en comparant les surfaces de réponse de la perte de masse dans un espace d'humidité relative et de température pour plusieurs configurations. Les résultats montrent des cartes d'erreur relative aux stades de séchage précoce, intermédiaire et tardif pour chaque cas comparé. D'autre part, la simplification concernant le couplage HM a été évaluée dans un cadre de simulation mésoscopique 2D. L'impact de la fissuration a ensuite été évalué à la fois localement sur les champs de saturation et sur la réponse globale de la perte de masse. Enfin, un schéma CT-EF a été proposé qui a consisté à extraire la morphologie du béton (agrégats et pores) des images rayons X/neutrons et de la présenter explicitement sur un maillage EF. Cela a permis de réaliser des simulations THM multiphasique 3D du béton à l'échelle mésoscopique.

# Contents

0.1	Industrial context . . . . .	1
0.2	Scientific context . . . . .	1
0.3	Thesis methodology and structure . . . . .	3
<b>1</b>	<b>Litterature review</b>	<b>5</b>
1.1	Drying-related physical processes in cement-based porous media . . . . .	5
1.1.1	Chemical dependency: hydration reaction implications . . . . .	5
1.1.1.1	Thermal dependency: impact of the temperature . . . . .	7
1.1.1.2	Hydraulic dependency . . . . .	7
1.1.1.3	Mechanical dependency: impact of creep and cracks . . . . .	9
1.2	Experimental investigations into drying-related processes . . . . .	10
1.2.1	Site measurement techniques . . . . .	10
1.2.1.1	Drilling techniques . . . . .	10
1.2.1.2	Electrical techniques . . . . .	10
1.2.1.3	Thermographic Imaging . . . . .	10
1.2.2	Techniques developed for research . . . . .	11
1.2.2.1	Classical measurements techniques . . . . .	11
1.2.2.2	Full-field measurement techniques . . . . .	11
1.2.3	Neutron and x-ray imaging to characterize hydro-mechanical behavior of cement-based porous media . . . . .	14
1.2.3.1	Interaction with matter . . . . .	14
1.2.3.2	Attenuation law . . . . .	15
1.2.4	Instrumentation . . . . .	15
1.2.4.1	Neutron and x-ray sources . . . . .	16
1.2.4.1.1	Neutron . . . . .	16
1.2.4.1.2	x-ray . . . . .	16
1.2.4.2	Neutron beam collimation . . . . .	17
1.2.4.3	Detection . . . . .	17
1.2.4.4	Neutron Imaging . . . . .	17
1.2.4.4.1	Neutron Transmission Radiography . . . . .	17
1.2.4.5	Neutron computed tomography . . . . .	18
1.2.4.5.1	Radon transform . . . . .	18
1.2.4.5.2	Fourier slice theorem . . . . .	18
1.2.4.5.3	Filtered Back Projection . . . . .	20
1.2.5	Imaging artifacts . . . . .	21
1.2.6	Applications of neutron imaging for durability studies of cement-based materials . . . . .	21
1.2.6.1	Moisture transport in sound cement-based materials . . . . .	21
1.2.6.2	Moisture transport in cracked cement-based materials . . . . .	22
1.2.6.3	Moisture transport in heated concrete . . . . .	22
1.2.7	Applications of x-ray imaging to study the mechanical behavior of cement-based materials . . . . .	23
1.2.8	Why neutron and x-rays for concrete . . . . .	24
1.3	Numerical modeling of drying-related processes in cement-based materials . . . . .	26
1.3.1	Upscaling procedure from the micro-scale . . . . .	26
1.3.2	Macroscopic modeling . . . . .	27
1.3.2.1	Momentum conservation equation . . . . .	27
1.3.2.2	Constitutive equations . . . . .	27
1.3.2.3	Permeability . . . . .	29

1.3.3	Mesoscopic modeling . . . . .	31
1.3.3.1	Mesh generation . . . . .	31
1.3.3.2	Application of mesoscopic modeling in the literature . . . . .	31
1.4	Summary of the literature review . . . . .	33
<b>2</b>	<b>Influence of common simplifications on the drying of cement-based materials up to moderate temperatures</b>	<b>35</b>
2.1	Introduction . . . . .	36
2.2	Multiphase Thermo-Hydric modeling . . . . .	37
2.2.1	Derivation of mass and energy conservation equations . . . . .	37
2.2.2	Final form equations . . . . .	39
2.3	Simplified modeling . . . . .	39
2.4	Constitutive equations . . . . .	40
2.4.1	Modeling choices . . . . .	40
2.5	Multiphase model validation up to moderate temperature . . . . .	43
2.6	Different models and behavior laws consequences on drying response . . . . .	44
2.6.1	Geometry, mesh, initial conditions and Boundary conditions . . . . .	44
2.6.2	Results: mass loss response surfaces . . . . .	45
2.6.3	Discussion: relative error maps . . . . .	48
2.6.3.1	Transfer modes impact . . . . .	48
2.6.3.2	Desorption isotherms, relative permeability and permeability to liquid water evolution in function of temperature choice impact . . . . .	49
2.6.3.3	Permeability to water evolution in function of temperature impact . . . . .	50
2.7	Conclusion . . . . .	50
2.8	Appendix . . . . .	51
<b>3</b>	<b>Drying of mortar at ambient temperature studied using high resolution neutron tomography and numerical modeling</b>	<b>53</b>
3.1	Introduction . . . . .	54
3.2	Material and methods . . . . .	55
3.2.1	Specimens . . . . .	55
3.2.2	Mass loss history . . . . .	55
3.2.3	Neutron acquisition . . . . .	56
3.3	Segmentation and grey value gradients . . . . .	57
3.4	Results . . . . .	58
3.4.1	Radial gradients . . . . .	58
3.4.2	From attenuation values to saturation gradients . . . . .	59
3.4.2.1	Saturation profiles . . . . .	59
3.4.2.2	Validation to mass loss measurements . . . . .	61
3.5	Modeling of moisture transfer . . . . .	62
3.5.1	Numerical model . . . . .	62
3.5.2	Model inputs, initial and boundary conditions: . . . . .	63
3.5.3	Model calibration and back-calculation of hydraulic properties . . . . .	64
3.6	Conclusion . . . . .	66
3.7	Data availability statement . . . . .	66
<b>4</b>	<b>Simultaneous x-ray and neutron 4D tomographic study of drying-related hydro-mechanical behavior of cement-based material at moderate temperatures</b>	<b>67</b>
4.1	Introduction . . . . .	68
4.2	Material and methods . . . . .	70
4.2.1	Specimens . . . . .	70
4.2.2	Heating cell . . . . .	71
4.2.3	Thermal testing conditions . . . . .	72
4.2.4	Neutron and x-ray tomography acquisition . . . . .	73
4.3	Quantification of hydro-mechanical processes through image processing . . . . .	74
4.3.1	Single mode and multi-modal registrations . . . . .	74
4.3.2	Analysis of the hydric behavior of the concrete sample . . . . .	76
4.3.2.1	Image segmentation and granulometry analysis . . . . .	76
4.3.2.2	Evolution of mixture attenuation . . . . .	78

---

4.3.2.3	Estimation of the capillary water fraction evolution . . . . .	78
4.3.3	Cement paste drying . . . . .	80
4.3.4	Hydro-mechanics of cement paste . . . . .	81
4.3.4.1	Cracking extraction for cement paste . . . . .	81
4.3.4.2	Cracking local effect on water content . . . . .	83
4.4	Conclusion . . . . .	86
4.5	Data availability statement . . . . .	86
4.6	Appendix . . . . .	87
4.6.1	Radial gradient analysis . . . . .	87
4.6.2	Registration and volumetric strain measurement . . . . .	87
<b>5</b>	<b>Conclusions and perspectives</b>	<b>89</b>
5.1	Summary of this doctoral work . . . . .	89
5.1.1	x-ray/neutron tomography measurements of drying-driven processes in cement-based materials . . . . .	89
5.1.2	Numerical modeling of the thermo-hydro-mechanical behavior of cement-based materials. . . . .	89
5.2	Main findings . . . . .	89
5.3	Perspectives . . . . .	90
<b>A</b>	<b>2D hydro-mechanical mesoscopic modeling: effect of a strong hydro-mechanical coupling</b>	<b>92</b>
A.1	Meso-structure generation . . . . .	92
A.2	Input parameters and boundary conditions . . . . .	93
A.3	Results: Saturation, damage and crack opening fields . . . . .	94
A.4	Hydro-mechanical coupling effect on the mass loss . . . . .	97
<b>B</b>	<b>3D image-based THM mesoscopic modeling of concrete</b>	<b>99</b>

# List of Figures

1	26 years of growth in Shanghai city between 1987 and 2013. Source: <a href="https://www.theatlantic.com/photo/2013/08/26-years-of-growth-shanghai-then-and-now/100569/">https://www.theatlantic.com/photo/2013/08/26-years-of-growth-shanghai-then-and-now/100569/</a>	1
2	China used more cement between 2011 and 2013 than the U.S. in the entire 20 <sup>th</sup> century. Sources: <i>USGS, cement statistics 1900-2012</i> ; <i>USGS Mineral industry of China 1900-2013</i> . . .	2
3	Highly vulnerable structures: (a) Nuclear power plants (b) Dams. . . . .	2
1.1	(a) pores size distribution in a cement paste: a six orders of magnitude variation, adapted from [Mehta, 1986] (b) Nano-pores distribution in different types of cement-based materials: cement paste (w/c = 0.5) C05, cement paste (w/c = 0.8) C08, mortar (w/c = 0.5) M05 and mortar (w/c = 0.8) M08 characterized using mercury intrusion porosimetry (MIP), adapted from [Rougelot, 2008]. (c) Schematic representation of the C-S-H microstructure showing the C-S-H backbones in solid lines, adsorbed water in full red circles, gel water in empty green circles, adapted from [Wyrzykowski et al., 2017] . . . . .	6
1.2	The measurement of the relative humidity decrease induced by self-desiccation. Adapted from [Kim and Lee, 1999] . . . . .	7
1.3	Impact of the temperature on the drying: (a) relative mass loss curves showing the temperature effect on the drying kinetics and the total amount of water leaving the system. (b) Impact of the temperature on the desorption isotherms. Adapted from [Caré, 2008] and [Drouet et al., 2015] . . . . .	8
1.4	Evaporation speed ( $\text{kg m}^{-2} \text{h}^{-1}$ ) as a function of air temperature, relative humidity, concrete temperature and wind velocity, Adapted from [Institute] . . . . .	8
1.5	Drying shrinkage at varying RH and temperature ( $T = 20, 50$ and $80^\circ\text{C}$ ), Adapted from [Brue et al., 2017] . . . . .	9
1.6	Different mechanisms contributing to the decrease of water flow in pores/cracks. Adapted from [Desmettre, 2011] . . . . .	10
1.7	Detection of water leaking on the roof of a building. Source: <a href="https://www.pixelthermographics.co.uk/buildings/roof-leak-thermographic-survey">https://www.pixelthermographics.co.uk/buildings/roof-leak-thermographic-survey</a> . . . . .	11
1.8	Classical measurement techniques: (a) cement-based samples drying in a thermo-hydric controlled environment, (b) Relative humidity sensor (source [Granja et al., 2014]), (c) Measurement of displacement induced by the desiccation shrinkage of a $4 \times 4 \times 16$ cement-based sample. . . . .	12
1.9	3D reconstructed ECT of electrical relative permittivity $\Delta\epsilon_r$ after 12, 24, 48, 96 and 144h of water ingress in mortar samples [Voss et al., 2019] . . . . .	13
1.10	(Left) first x-ray radiograph taken by Wilhelm Conrad Rontgen of his wife's hand wearing a ring, taken on 22 <sup>nd</sup> of December 1895. (Right) First neutron radiography of a pressure gauge, fire hydrant and test tubes filled with $H_2O$ and $D_2O$ . Adapted from (Wikimedia Commons) and [Peter, 1946]. . . . .	14
1.11	Different interactions of x-rays and neutrons with atomic structures: (top left) x-rays interact with the electron shell, yielding an increasing attenuation with the atomic number as seen in the table at (top right). On the other hand, neutrons interact with the atomic nuclei (bottom right) with no specific correlation between their attenuation and the atomic number. Adapted from [Strobl et al., 2009] and [Tengattini et al., 2020c]. . . . .	15
1.12	A schematic scheme of a typical neutron imaging beamline . . . . .	16
1.13	A comprehensive summary of commonly-used analytical tomographic reconstruction methods. Drawing inspired from ASTRA Toolbox youtube channel. . . . .	19

1.14	(Top) water content line profiles of a drying concrete sample at 30 °C. (Bottom) Radiography attenuation field of the same sample at different hydric states. adapted from [de Beer et al., 2004b]. . . . .	22
1.15	Neutron images of water ingress in cracked steel-reinforced mortar showing the local effects of the vertical cracks and the presence of horizontal rebars on the local water content evolution [Zhang et al., 2010]. . . . .	23
1.16	(Left) sequence of vertical slices of sequential 3D reconstructed volumes showing the advancing drying front in 4mm HPC and 8mm HPC. (Top right) a higher resolution 3D reconstruction of the 8mm HPC sample at the end of test. (Bottom right) the quantification of the effect of the aggregate size on the drying kinetics of the two samples. adapted from [Dauti et al., 2018d]	24
1.17	The same horizontal slice of a concrete sample as seen by (top left) x-ray and (top right) neutrons (color map were inverted for presentation purposes). The sample was prepared using $D_2O$ instead of $H_2O$ to take advantage of the isotope sensitivity of neutron ( $D_2O$ being one order of magnitude less attenuating than $H_2O$ ). The different interactions of the two beams with matter demonstrate their complementarity, each by emphasizing different morphological features of the concrete. (Bottom left) spatial alignment of the two volumetric information, also called multimodal registration, enables phase separation as seen in (bottom left) where 5 phases were identified on a bi-modal joint histogram. Adapted from [Yehya et al., 2018] and [Roubin et al., 2019] . . . . .	25
1.18	Concrete as shown in 4 different scales: Structural, mesoscopic, pore and molecular scales. . .	26
1.19	Comparison between commonly used hydro-mechanical coupling laws in case of weak diffused damage configuration. . . . .	30
1.20	Permeability through macro-cracks having different crack opening accounting additionally to the effect of the cracking roughness. . . . .	31
1.21	Three different approaches in generating concrete mesostructure: (a) perfect sphere particles respecting the particle size distribution [Nguyen, 2010], (b) FE structured mesh taking into account 4 material phases (aggregates, mortar, void and ITZ) identified thanks to x-ray tomography [Huang et al., 2015], (c) Projection of a 3D segmented x-ray image on an unstructured mesh used to perform E-FEM mechanical simulations [Stamati et al., 2018]. . .	32
1.22	Different type of concrete mesoscopic simulations: (a) Crack opening field of a meso-concrete with spherical aggregates submitted to tensile (left) and compressive (right) mechanical loading, adapted from [Nguyen, 2010]; (b) Crack opening field of a meso-concrete having its mesostructure projected from a 3D x-ray image, adapted from [Huang et al., 2015]; (c) damage field resulting from a thermo-hydro-mechanical simulation of a meso-concrete with spherical aggregates, adapted from [Xotta et al., 2015]; (d) Water content fields obtained resulting from a multiphase thermo-hydro-mechanical simulation of a homogenized concrete with a single aggregate calibrated to 3D neutron tomography, adapted from [Dauti et al., 2018a] . . . . .	33
2.1	Desorption isotherm's evolution in function of temperature . . . . .	41
2.2	Drouet's permeability evolution in function of temperature ( $T_c = 35.7$ ) . . . . .	42
2.3	Geometry, mesh and thermo-hydral boundary conditions applied in the validation simulation	43
2.4	Validation of the model at moderate temperature . . . . .	44
2.5	Geometry, mesh and boundary conditions for the comparative analysis . . . . .	45
2.6	Relative mass loss response surfaces for four different cases (listed in table 1) at (a) early-drying stage, (b) mid-drying stage and (c) late-drying stage. (a) 15 days . . . . .	46
2.7	Multiphase model vs. simplified with all the hydric properties' evolutions in function of temperature relative error maps at 15, 50 and 365 days respectively . . . . .	48
2.8	Multiphase model vs. simplified with all the hydric properties' evolutions in function of temperature mass loss evolution at 30%RH and 80°C . . . . .	49
2.9	Simplified model with all the hydric properties' evolutions in function of temperature vs. Simplified model with no hydric properties evolutions relative error map at 3, 20 and 365 days respectively. . . . .	49
2.10	Simplified model with only permeability evolutions in function of temperature vs. Simplified model with no hydric properties evolution (except density and viscosity) relative error maps at 5, 50 and 365 days respectively. . . . .	50
2.11	Gas pressure, capillary pressure and saturation fields at 30% RH and 80°C external conditions after 50 days of drying . . . . .	52

2.12	Gas pressure, capillary pressure and saturation fields at 50% RH and 20°C external conditions after 50 days of drying . . . . .	52
3.1	Drying of mortar samples: (a) Sample drying in a thermo-hydric controlled environment (b) Total samples mass loss history . . . . .	56
3.2	Segmentation and labelling processing adopted in this work. To the left: rendering of a representative 3D reconstructed attenuation field. In the middle: rendering of the binary image after histogram-based segmentation. To the right: Labelled 3D volume isolating the individual grains, whose color corresponds to the assigned incremental index. . . . .	57
3.3	Analysis of the attenuation profiles: (a) radiography showing the sample in the field of view (b) Grey value gradients of all the scanned sample . . . . .	58
3.4	(a) Montage showing the partitioning of the sample in the radial direction so as to keep a similar number of pixels in each division. Evolution of grey value with respect to the radius for different saturation states and different positions in the sample: (b) Bottom (b) middle (c) Top . . . . .	59
3.5	A comparison between experimental and numerical cumulative granulometry taking into account the resolution limitation of the neutron tomography scans . . . . .	60
3.6	Neutron-based measurement of saturation gradients of mortar samples at different hydric states. The measurement accounts for the variability of the fluids gray value attenuation coefficients. . . . .	61
3.7	Comparison between the balance-measured mass loss and the one deduced from image analysis.	62
3.8	Mesh and boundary conditions . . . . .	63
3.9	Behavior laws . . . . .	64
3.10	Mass loss comparison of the: (red) balance measurements, (blue) image-based measurements and (cyan) FE estimation. The shaded area being to account for the variability of the acquired measurements. . . . .	65
3.11	Saturation gradients . . . . .	65
4.1	Vertical and horizontal slices of the 3D reconstructions of the neutron and x-ray tomographies of the concrete sample, highlighting the high complementarity of the micro-structural information obtained with these techniques. The neutron attenuation field (the average attenuation of the materials contained in a voxel $\mu_n$ ) on the left of the partially saturated concrete sample highlights aggregates and pores from the cement paste which is further differentiated in dry and wet. Nonetheless pores and aggregates have comparable attenuation in the neutron tomography whereas they have significantly different x-ray attenuations $\mu_x$ , as shown on the right. Their rigorous coupling is made possible by their multi-modal registration (detailed in section 4.3.1). . . . .	70
4.2	The designed heating setup: (a) Disassembled setup highlighting the positions of the sample wrapped with aluminum tape for moisture isolation and rockwool for heat isolation, the exhaust output and the infrared radiator (b) schematic view. . . . .	72
4.3	Measured temperature on the top surface of the tested sample . . . . .	73
4.4	Heating cell in beam-line (x-ray source yet to be moved): the cell is to be crossed by a neutron flux on a first axis and by an x-ray flux on a nearly-perpendicular second axis . . . . .	74
4.5	Evolution of neutron attenuation field $\mu_n$ and x-ray attenuation field $\mu_x$ throughout the drying experiment which was captured statistically thanks to joint histograms. . . . .	75
4.6	Schematic of the segmentation procedure used to remove the aggregates and sand grains from the moisture analysis. An “Otsu” threshold was used as operator-independent guess of the threshold value. A sensitivity analysis of any the potential error induced by this segmentation step was performed by repeating all ensuing analysis for user-defined min and max threshold values. . . . .	77
4.7	Particle size distribution procedure: (Left) Vertical slice of a labelled aggregate volume, (Right) Equivalent-sphere particle size distribution: threshold sensitivity analysis and comparison with experimental sieving measurements . . . . .	77
4.8	Gray value attenuation gradient evolution along the sample height . . . . .	78
4.9	Capillary water volume fraction evolution along the sample height . . . . .	79
4.10	Variation of the gray value gradients with respect to the initial hydric state. . . . .	81
4.11	The cracking extraction procedure . . . . .	82
4.12	Cracks initiation and propagation in time extracted from x-ray tomography: (left) 007, (middle) 012, (right) 017 . . . . .	83

---

4.13	Horizontal slices through registered tomographies in both modalities: (left) neutron, (middle) x-ray and (right) “checkerboard” . . . . .	84
4.14	3D visualisation of cracks and neutron images after multimodal registration : normalized neutron volume (left), 3D denoised x-ray cracks (middle) and combined images (right). . . . .	84
4.15	Crack dilation procedure . . . . .	85
4.16	Cracking local effect on the normalized hydric behavior over the height of the sample: $D_n$ being the dilated mask of the cracks $x$ times, $C$ being the cracks . . . . .	85
4.17	Normalized Cracking local effect on the hydric behavior . . . . .	86
4.18	Horizontal cross-section of the sample partition into equivolumetric hollow cylinders . . . . .	87
4.19	Radial gradient evolution of the concrete sample (average of 5 slices in each height region) . . . . .	87
4.20	Residual fields of the (095 – 009) x-ray tomography (a) before registration and (b) after registration . . . . .	88
A.2	FE mesh and hydro-mechanical boundary conditions [Nguyen, 2010] . . . . .	93
A.3	Saturation fields at 3, 100 and 1200 days resulting of the 2D mesoscopic simulations: without coupling (left) and with coupling (right) . . . . .	95
A.4	Damage fields at 3, 100 and 1200 days resulting of the 2D mesoscopic simulations: without coupling (left) and with coupling (right) . . . . .	96
A.5	Crack opening fields at 3, 100 and 1200 days resulting of the 2D mesoscopic simulations: without coupling (left) and with coupling (right) . . . . .	97
A.6	Assessment of the hydro-mechanical coupling effect on global mass loss in the first drying cycle. . . . .	98
B.1	CT-FE mapping scheme to perform 3D THM simulation of concrete at the mesoscale while representing the aggregates real morphology . . . . .	100

# List of Tables

2.1	Table resuming the model and behavior laws used for each subplot. . . . .	46
2.2	Table resuming the compared cases: the used model and the behaviour law choices. . . . .	48
4.1	Composition of the concrete used for sample 2 . . . . .	71
A.1	Input Parameters for the hydro-mechanical 2D mesoscopic simulations . . . . .	93

# Introduction

## 0.1 Industrial context

In his book *Making the Modern World: Materials and Dematerialization*, Vaclav Smil, a distinguished Professor Emeritus in the Faculty of Environment at the University of Manitoba in Canada, argued that the most important man-made material is concrete, both in terms of the amount we produce each year and the total mass humans have laid down so far. The production of cement is in growth and it is not expected to plateau any soon. In 1950, the same amount of steel and cement is produced; however, by 2010, steel production had grown by a factor of 8, but cement had gone up by a factor of 25. In fact, despite that some rich countries are leveling off, developing countries are catching up. For instance, figure 1 shows the significant transformation of Shanghai between 1987 and 2013, which received an additional 17 million inhabitants to its original 6 million in these 26 years. To illustrate the extent of these numbers, *Smil* evoked



Shanghai, 1987



Shanghai, 2013

Figure 1: 26 years of growth in Shanghai city between 1987 and 2013. Source: <https://www.theatlantic.com/photo/2013/08/26-years-of-growth-shanghai-then-and-now/100569/>

what he calls “the most stunning statistic” in his book that china has used more cement in three years (between 2011 and 2013) than the U.S used in the entire 20<sup>th</sup> century (see figure 2).

However, two major problems arise from this large usage of cement. The first being its high carbon footprint, where cement industry is responsible of 8% of the global CO<sub>2</sub> emission. The second major problem being is its very high economic bill. In fact, the main issue of reinforced concrete as a building material is that it deteriorates due to its exposition to aggressive environmental factors and that trillions of dollars are consequentially required for repairing operations in order to maintain and prolongate the structural serviceability. It is therefore of key importance to improve the durability of cement-based materials to prevent or moderate their economic, social and environmental repercussions.

## 0.2 Scientific context

The improvement of the cement-based material durability cannot happen without an understanding of the complex multi-physics processes responsible for the material degradation. The understanding of such mechanisms and their dependencies constitutes the cornerstone of avoiding or moderating their impact or at least predicting their extent on the structural integrity. Durability, being an abstract concept, requires some tangible indicators to characterize it. Indeed, the degradation of the cement matrix, the corrosion of steel rebars and the presence of cracks are among the most symptomatic indicators that point out a

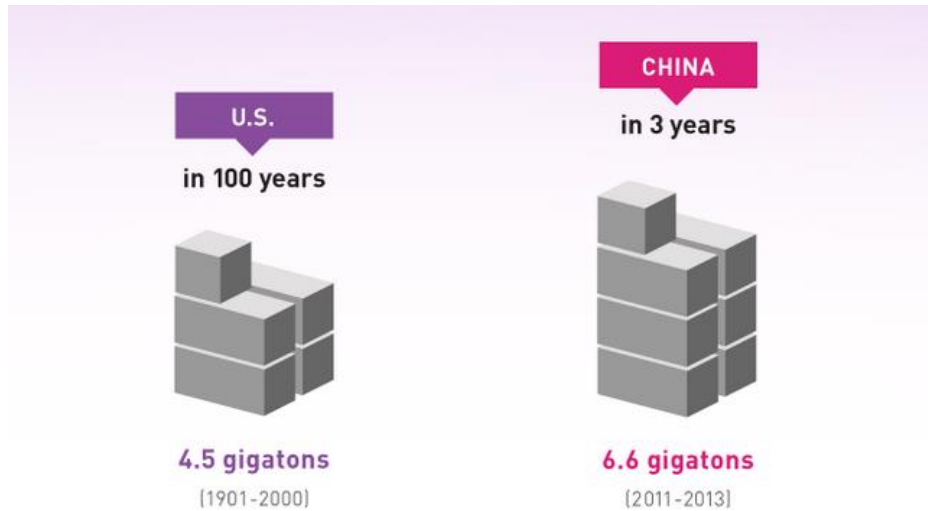


Figure 2: China used more cement between 2011 and 2013 than the U.S. in the entire 20<sup>th</sup> century.  
Sources: *USGS, cement statistics 1900-2012*; *USGS Mineral industry of China 1900-2013*.

loss in durability potential of cement-based materials. Interestingly, a key role is played by the moisture transport in the material pore network in causing the three aforementioned degrading mechanisms of the mechanical performance. In fact, the variation of water saturation affects the penetration rate of aggressive chemicals and their diffusion in the material through the interconnected porosity. In addition, the rate of corrosion in its propagation period can be described by the relative humidity in the concrete [Tuutti, 1982]. Capillary moisture transport induces also volumetric deformations in the cement matrix, *i.e.*, shrinkage in case of drying and swelling in case of wetting. These deformations get restrained by many factors, *e.g.*, the presence of impermeable aggregates and sand particles, and generate stress gradients which can lead to cracking in case they exceed the material tensile strength. It is therefore extremely important to understand the fundamental physical processes controlling the moisture transport in cement-based materials to assess their implications on their durability especially on highly vulnerable structures such as nuclear power plants and dams (see figure 3). Drying, being a side of the moisture transport coin (wetting being the other



Figure 3: Highly vulnerable structures: (a) Nuclear power plants (b) Dams.

side), has been extensively studied in the previous few decades. However, it's still being studied nowadays since a sufficient comprehension of this process is not achieved yet. Particularly, the evolution of hydric gradients between the saturated core of the sample and the exchange surface is still poorly characterized in the literature as well as the effect of the local heterogeneity (aggregates, macro-pores, cracks, *etc*) on the hydraulic properties under chemo-thermo-hydro-mechanical loading.

This manuscript presents a contribution in the direction of comprehension and characterization of these complex multi-physics multi-scale processes, taking advantage of the combination of x-ray and neutron tomography tools. Notably, x-ray, being sensitive to density variations helped to characterize the cracking propagation in the tested cement-based materials, in 4D (3D + time). On the other hand, neutron tomog-

raphy allowed the study of the evolution of the moisture field in 4D, thanks to its high hydrogen sensitivity. The combination of these two techniques has provided a unique insight in thermo-hydro-mechanical couplings, the effect of cracks on the water content field for instance. Moreover, the tomography-based full-field measurements have constituted an experimental ground truth to validate and improve the predictive capacity of the advanced numerical modeling used in this study.

### 0.3 Thesis methodology and structure

The thesis manuscript consists of a bibliography chapter, three articles and two appendices summarizing the work done for three years. It is organized as follows:

- In chapter 1, a state of the art on the PhD topic is given. This chapter is divided into three main sections. The first section deals with the drying-related physical processes in cement-based materials defining the most important chemo-thermo-hydro-mechanical dependencies of the drying process. The second section enumerates the different experimental techniques used to investigate the drying-related processes, with a strong emphasis on the neutron and x-ray tomography. The last section is dedicated to numerical modeling of the thermo-hydro-mechanical behavior of cement-based materials with attention to the different types of mesoscopic modeling approaches in the literature.
- Chapter 2 (article 1) presents the influence of common simplifications on the drying modeling of cement-based materials. It investigates the effect of neglecting the transport mechanisms related to gas phases (vapor and dry air) on the global drying response, at different environmental relative humidity and up to moderate temperature. This was done by comparing a multiphase model that describes three fluid phases and their interactions in the pore network to a monophasic model which accounts only for the liquid water permeation process. In addition, the paper assesses the implications of neglecting the effect of not accounting for the thermally induced evolution of hydraulic properties such as the evolution of desorption isotherms and the permeability to liquid water.
- Chapter 3 (article 2) introduces the first experimental campaign at Institut Laue-Langevin (ILL), where a set of mortar samples, each having a different hydric state, were scanned using neutron tomography. The hydric gradients resulting from the unidirectional moisture flow between the core and the exchange surface were evaluated thanks to a transition methodology between gray value and water saturation, which was validated to mass loss balance measurements. The experimental dataset was then used to fit a numerical model, whose use was validated in the previous chapter and which has enabled the characterization of the system hydraulic conductivity by inverse analysis.
- Since environmental drying can occur in more complex configurations, *i.e.*, at moderate temperature or in cracked material systems, *etc.*, Chapter 4 (article 3) deals with the second campaign at ILL, where the characterization of drying-driven processes of heated cement-based materials using simultaneous x-ray and neutron tomography was done. The evolution of moisture profiles at moderate temperature was evaluated as well as the effect of cracking on the local water content.
- Finally, Chapter 5 presents the conclusions and perspectives of this work.
- Appendices: Other valuable results obtained in this PhD and which were not yet published are shown in two appendices, notably, the results of numerical simulations performed at the mesoscale. In the first appendix, the effect of strong hydro-mechanical coupling, both on local and global drying kinetics and crack propagation, is shown in 2D mesoscopic simulations. In the global context of this PhD, this appendix is considered as a continuation to chapter 1, while the common simplification being the disregard of the HM coupling in the drying modeling.

On the other hand, the second appendix presents a CT-FE mapping scheme which allows to simulate the THM behavior of concrete while representing its true morphology at the mesoscale. This new development permits an objective comparison of simulation fields with the one provided by the x-ray and neutron tomography, such as the cracking and saturation fields presented in chapter 4.



# Chapter 1

## Litterature review

### 1.1 Drying-related physical processes in cement-based porous media

A cement-based material is, at the very least, composed of cement paste (cement+water) which be mixed with aggregates (sand particle, in case of mortar; sand and aggregates in case of concrete) and additives (plasticizers, fibers, *etc*). When cement powder is mixed with water, an exothermic chemical reaction, called hydration, takes place and produces the solid skeleton made out of solid gel, chemically-bound water and dehydrated cement, and a pore network. This network is spread over different scales of observations as it can be seen in figure 1.1. It can vary drastically between different types of cement-based materials both on the occupied volume and distribution of pores' radii [DeSa, 2007]. With the exception of entrapped and entrained air bubbles, one can distinguish between two types of porosity. The capillary porosity being the first type having a dimension range between 0.01 and 50  $\mu\text{m}$  and which is highly affected by the water to cement ratio (w/c) used to hydrate the cement powder. The second porosity type corresponds to that of the hydrates (products of hydration) also known as C-S-H (standing for Calcium Silicate Hydrates), which has a much smaller diameter measured in few nanometers.

In absence of aggressive agents, the porosity is filled mainly with water and dry air. However, this water can exist in different physical states:

- **Free water:** which is the water in liquid form that is free to move in the capillarity if any flow is induced.
- **Vapor:** resulting from the evaporation dynamics happening at the interface between the liquid water and the dry air in the porosity.
- **Adsorbed water:** resulting from the adhesion of the water molecules on the pore walls.

Cement-based materials, like any other porous material, are in thermodynamic imbalance (chemical, thermal, hydric and mechanical imbalance). Unless if the material is placed in laboratory-controlled conditions, this imbalance remains mainly due to the variability of the external environment conditions such as temperature and relative humidity. After casting, cement-based materials usually have a higher hygrometry than that of the environment. Water existing in the porous network tends to leave the material toward the external environment in order to establish a hydric equilibrium. This thermodynamic process is called drying, which in turn, can induce other processes affecting the durability and serviceability of the material, such as cracking. It is of great importance to understand the drying physical mechanisms in order to avoid, or at least predict, its implications on the material structural integrity.

Drying can be broadly characterized by two parameters: the kinetics of the process and the amount of water leaving the pore network. These two quantifiable parameters manifest a strong dependency on the material chemo-thermo-hygro-mechanical states and on the environmental conditions. In the following, these dependencies are categorized and detailed.

#### 1.1.1 Chemical dependency: hydration reaction implications

**The initial amount of capillary water in the system:** After casting, the hydration reaction starts between the cement powder and the water to produce hydration products: solid gel, water gel, capillary

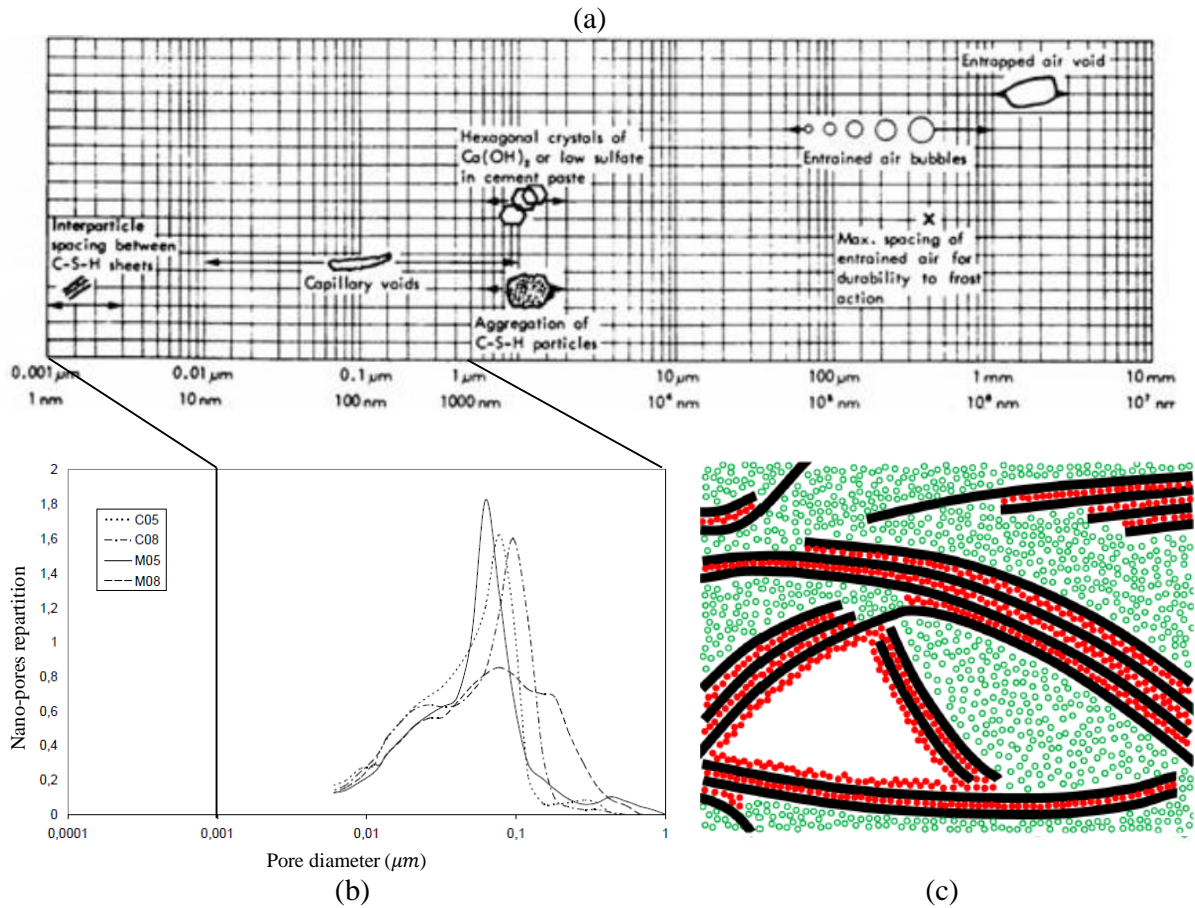


Figure 1.1: (a) pores size distribution in a cement paste: a six orders of magnitude variation, adapted from [Mehta, 1986] (b) Nano-pores distribution in different types of cement-based materials: cement paste ( $w/c = 0.5$ ) C05, cement paste ( $w/c = 0.8$ ) C08, mortar ( $w/c = 0.5$ ) M05 and mortar ( $w/c = 0.8$ ) M08 characterized using mercury intrusion porosimetry (MIP), adapted from [Rougelot, 2008]. (c) Schematic representation of the C-S-H microstructure showing the C-S-H backbones in solid lines, adsorbed water in full red circles, gel water in empty green circles, adapted from [Wyrzykowski et al., 2017]

water and some remaining unreacted cement emphasizing a maximum degree of achievable hydration below one. Being a chemical reaction, many attempts were done to calculate the amount of each hydration product by the use of stoichiometry. Such calculations estimate the volume fractions of the reaction products in function of the water content and the evolving degree of hydration [Powers, 1960][Jensen and Hansen, 2001][Jensen and Hansen, 2002]. This latter is dependant on the water to cement  $w/c$  ratio used in the mixture. This dependency has been characterized experimentally in the literature by [Mills, 1960],[Waller, 1999]. Combining the stoichiometric approach with the empirical characterization of the hydration degree, one can obtain an estimation of the initial amount of water existing in the capillarity. Such an estimation was done in [Bentz, 2006] for different types of curing conditions. In the case of a sealed sample, the volume fraction of liquid water  $\phi(w)$  reads:

$$\phi_W(t) = \frac{\rho_{cem}(w/c) - (f_{exp} + \rho_{cem}CS)\alpha}{1 + \rho_{cem}(w/c)} \quad (1.1)$$

where  $\rho_{cem}$ ,  $f_{exp}$ ,  $CS$  and  $\alpha$  are respectively the density of cement ( $3.2 \text{ g cm}^{-3}$ ), the volumetric expansion coefficient of the solid hydration products, the chemical shrinkage per gram of cement and the degree of hydration. Under saturated curing conditions for small-enough cement-based samples, the chemical shrinkage is considered to be compensated for by absorption of the external water ( $CS = 0$ ). It follows that the volume fraction of capillary water is equal to that of the pore network.

On the other hand, there exists a second approach, of experimental nature, to estimate the initial water content in the pore network. It consists of measuring the relative humidity decrease in the porosity by means of humidity sensors as seen in figure 1.2. Additional experimental characterization of the desorption isotherm

$(RH, S_l)$  is required in order to map these relative humidity measurements to water saturation states.

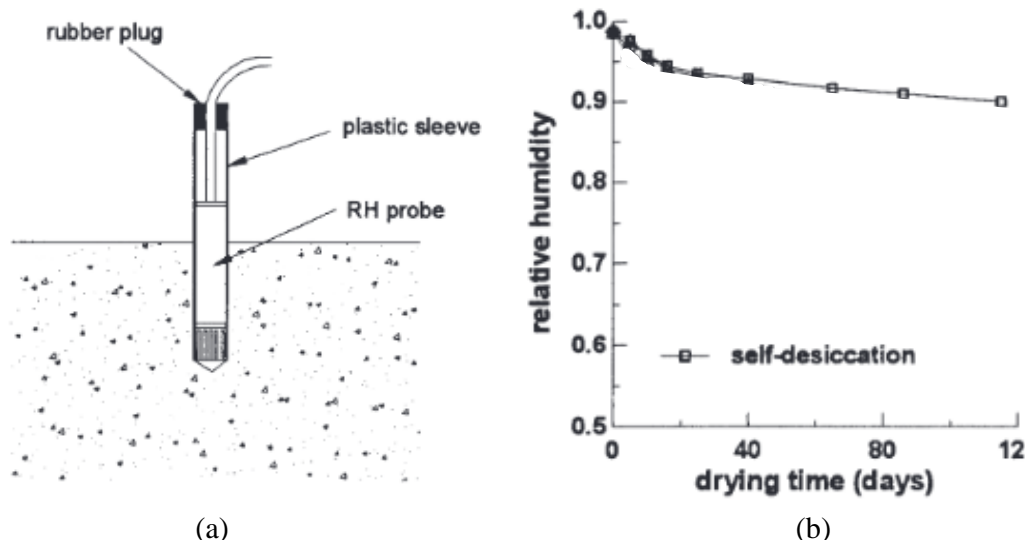


Figure 1.2: The measurement of the relative humidity decrease induced by self-desiccation. Adapted from [Kim and Lee, 1999]

#### 1.1.1.1 Thermal dependency: impact of the temperature

- **Temperature impact on the physical properties of the fluids:** The physical properties of the fluids such as density, viscosity, saturation vapor pressure, *etc.* evolve in function of temperature. This has been well characterized in the literature [ASHRAE, 2001]. For more information about their constitutive behavior, the reader is referred to read the appendix of chapter 2.
- **Thermal incompatibility between the aggregates and the cement-paste:** Aggregates and cement-paste have different thermal dilation/contraction properties [Mindeguia et al., 2013]. When subjected to sufficiently high temperatures, this thermal incompatibility causes cracking in the cement matrix [La Borderie and Menou, 2007]. In their turn, those cracks induce a faster drying process.
- **Temperature impact on the hydraulic properties:** Adsorption is an exothermic process [Brunauer, 1945],[Gregg, 1986]. According to the law of Van't Hoff and to the principle of Le Chatelier [Atkins and de Paula, 2006], these kinds of processes get hindered when temperature increases and get enhanced when this later decreases. Therefore, an increase of temperature promotes the desorption of the water molecules previously adsorbed at the pore wall [Poyet, 2009]. On the macro-scale, this thermally-induced dynamics between the adsorbed water and the free water can be characterized by characterizing the water retention curves [Drouet, 2010]. It can be seen in figure 1.3(b) how these desorption isotherm curves evolve in function of temperature. It follows that at a fixed relative humidity, the amount of water remaining in the system depends strongly on the temperature of the medium. This can also be seen on the mass loss curve which attains higher hydric equilibrium when temperature increases [Caré, 2008].

In addition, the temperature also affects the drying kinetics as can be seen on the mass loss curves in figure 1.3(a), emphasizing a non-negligible evolution of the system permeability at moderate temperature [Drouet et al., 2015].

#### 1.1.1.2 Hydraulic dependency

- **Impact of the saturation state on the hydraulic properties:** During drying, the water saturation level in the pore network decreases. This process affects the hydraulic properties such as permeability and diffusivity of the different phases. For instance, when saturation drops, the effective permeability of liquid water decreases while one of the air increases. This has been well studied and established in multiphase porous media literature by the concept of relative permeability [Mualem, 1976][Genuchten, 1980].

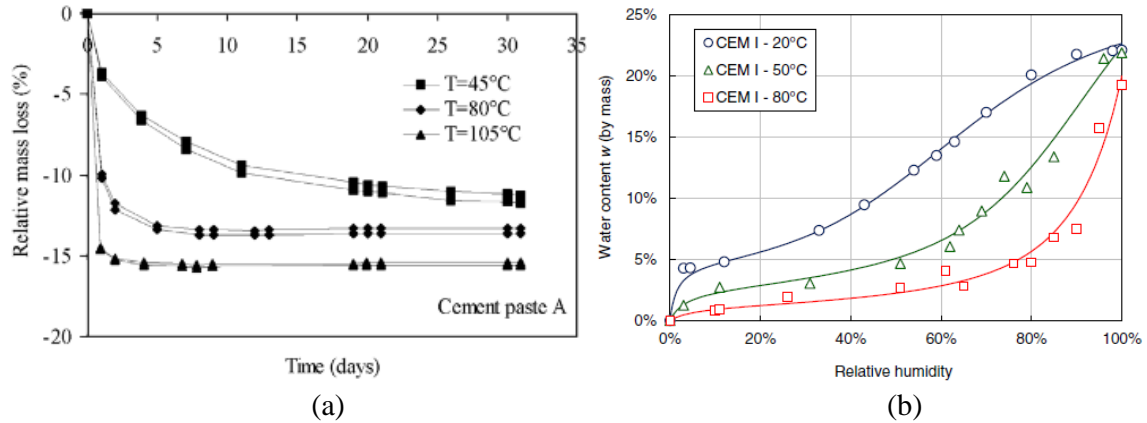


Figure 1.3: Impact of the temperature on the drying: (a) relative mass loss curves showing the temperature effect on the drying kinetics and the total amount of water leaving the system. (b) Impact of the temperature on the desorption isotherms. Adapted from [Caré, 2008] and [Drouet et al., 2015]

- Impact of the external drying environment conditions on the surfacic evaporation speed:** In addition to the evaporation that happens inside the pore network, the liquid water escaping the medium through the exchange surface evaporates when it meets the environment. This evaporation dynamics creates a transitional boundary layer between the sample and the external environment where the relative humidity is not equal to the one of the drying environment. The evaporation speed depends on many factors such as air temperature, relative humidity, concrete temperature and wind velocity as illustrated in figure 1.4 but also on the material surface condition (surface porosity, surface roughness, surface moisture) [Institute][Carette et al., 2019].

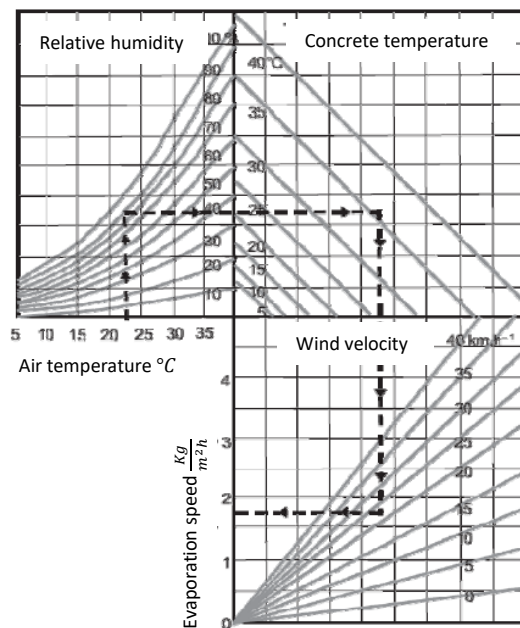


Figure 1.4: Evaporation speed ( $\text{kg m}^{-2} \text{h}^{-1}$ ) as a function of air temperature, relative humidity, concrete temperature and wind velocity, Adapted from [Institute]

- Impact of the saturation state on the material drying shrinkage:** The liquid water leaving the pore network causes capillary depression (caused by variations in capillary pressure through Kelvin-Laplace law, disjoining pressure and surface tension in the connected porosity) which in turn leads to macroscopic volume contraction. This drying shrinkage depends strongly on the amount of paste in the volume [Bissonnette et al., 1999] and can be correlated phenomenologically to the amount of free water loss through a coefficient of drying shrinkage [Granger, 1995][Hilaire, 2014]. The loss of adsorbed water due to desorption at moderate temperature also induces volume reduction as illustrated for a

concrete drying at 20, 50 and 80 °C in figure 1.5, but whose drying shrinkage coefficient constancy is not granted for all types of cement-based materials and since different types of processes may occur in the concerned nano-porosity (hydrogen de-bonding, ion-dipole interactions and Van der Waals forces) [Brue et al., 2017].

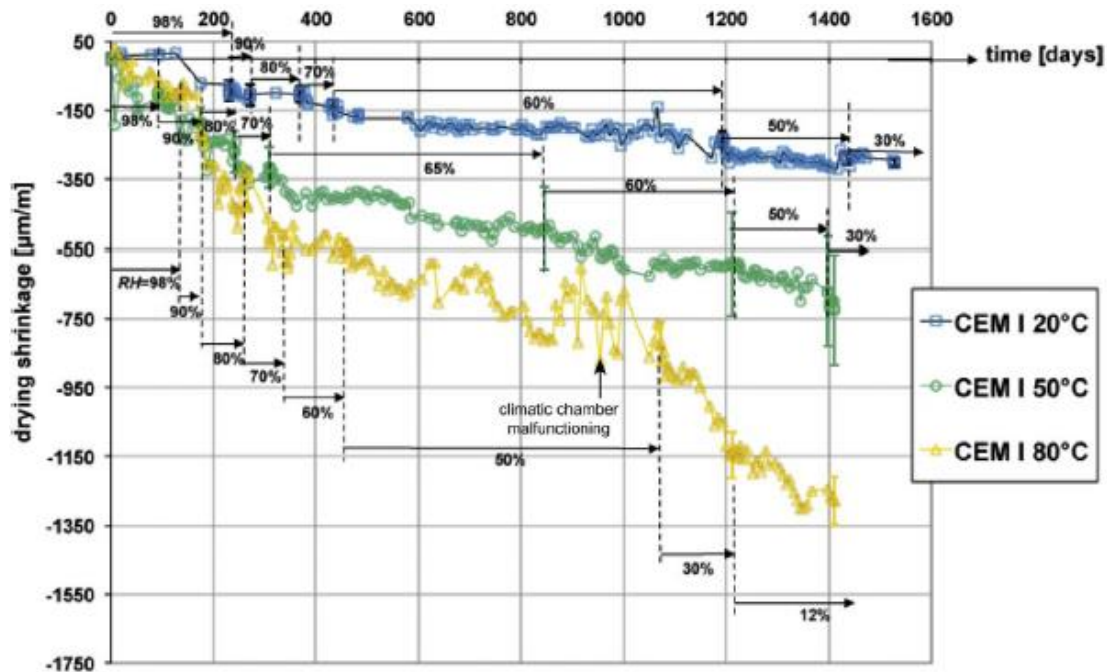


Figure 1.5: Drying shrinkage at varying RH and temperature ( $T = 20, 50$  and  $80\text{ }^{\circ}\text{C}$ ), Adapted from [Brue et al., 2017]

- **Impact of drying/wetting cycles:** Many authors in the literature reported anomalous water transport mechanisms when multiple drying/wetting cycles are considered [Tavangarrad et al., 2019][Zhang and Angst, 2020][McDonald et al., 2020]. This anomalous transport is manifested by the sorption/desorption curves hysteresis and the first sorption cycle irreversibility. Many explanations were suggested to explain this transport abnormality, all pointing toward different processes inducing micro structural variations of the pore network, such as calcite formation after the first drying cycle, flow-blockage by micro-particles, and delayed hydration solid products isolating channels of the interconnect porosity [Desmetre, 2011] (see figure 1.6).

### 1.1.1.3 Mechanical dependency: impact of creep and cracks

- **Cracking:** Cement-based materials undergo different types of shrinkages (chemical and drying) and creep strains which can be prevented by the aggregates. This strain prevention leads to stress concentration which can get higher than that the material tensile strength, leading consequently to cracking. Those cracks have a non-negligible hydraulic effect and can speed up the drying process by creating new exchange surfaces.
- **Creep:** In addition to the contribution of creep to damage [Mazzotti and Savoia, 2003], creep in its two forms (basic and desiccation creep) can have a major impact on the drying of cement-based materials. Basic creep is the deformation of a sealed cement-based sample subtracting the endogenous and instantaneous elastic deformations while drying creep is the total deformation of a drying sample subtracting the endogenous and desiccation shrinkages together with the basic creep deformation. Many mechanisms were proposed to try explaining the creep strains [Benboudjema, 2002], however, the most common explanation suggests that the adsorbed water molecules diffuse in the micro-pore neighborhood inducing a rearrangement of C-S-H layers. In fact, the micro-diffusion of adsorbed water theory seems to be the most plausible since an oven-dry sample doesn't show any creep deformation. These mechanisms should be taken into account since they can induce non-negligible variations in the drying kinetics and the total amount of water leaving the system.

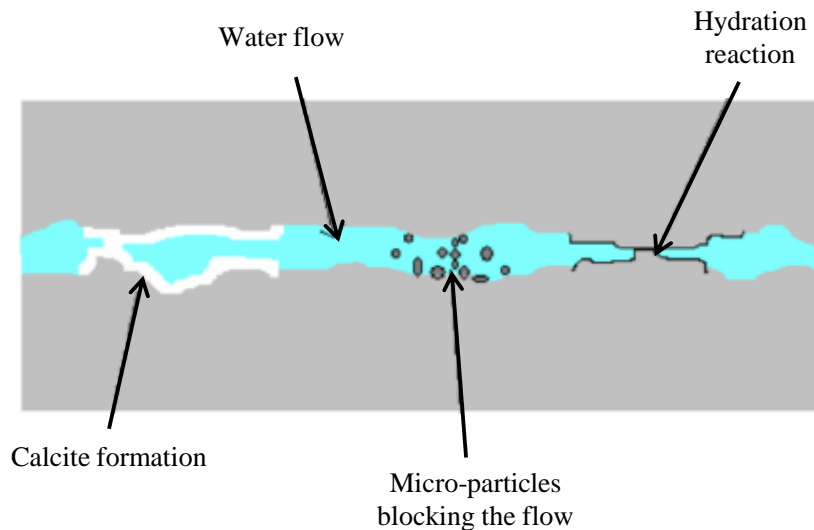


Figure 1.6: Different mechanisms contributing to the decrease of water flow in pores/cracks. Adapted from [Desmettre, 2011]

## 1.2 Experimental investigations into drying-related processes

### 1.2.1 Site measurement techniques

Surveyors of civil engineering structures are interested in estimating the moisture content in building materials to avoid consequences that can lead to structural damage and start remedial actions. For instance, a specialist in flooding repairs has to monitor the drying of a building before starting the repairing operation. Many site measurement techniques are in hands of building experts, each having advantages and drawbacks regarding accuracy level, spatio-temporal characterization and economic considerations. A description of commonly used site techniques is shown in the following.

#### 1.2.1.1 Drilling techniques

The drilling method consists of drilling holes in the material to be tested and measure its water content gravimetrically by calculating its weight loss before and after oven drying. The moisture content can be assessed differently if a calcium carbide meter is used for instance, where the reacting moisture and calcium carbide release acetylene gas. The rise of pressure in the sealed container is proportional to the moisture content. However, this technique is not only destructive but also invasive since the heat generated by drilling affects the sample drying, altering therefore the global moisture measurement.

#### 1.2.1.2 Electrical techniques

Mineral water is an excellent electricity conductor. This has lead to characterize the electrical properties of porous materials (resistance, impedance and capacitance) in function of their moisture content. The commercial devices available in the market measure one of these quantities when good electrical contact is established with the material being measured. However, the measurements acquired by this technique are material-specific since the absolute value of moisture content in a certain material requires additional careful calibrations. Furthermore, its accuracy can be affected by the concentration of ions in the porosity and the presence of iron in the material matrix. Finally, the technique allows only for surfacic measurement that can up to a few centimeters in the depth of material.

#### 1.2.1.3 Thermographic Imaging

Thermal cameras can be employed to investigate moisture and water intrusion since the hydric state of a material affects its thermal properties. From this technique a surfacic temperature field is obtained, where the variation of temperature on a supposedly homogeneous thermal state can be correlated to the presence of water concentration as shown in figure 1.7. This technique is therefore used to identify the extent of moisture and not to evaluate the moisture content.

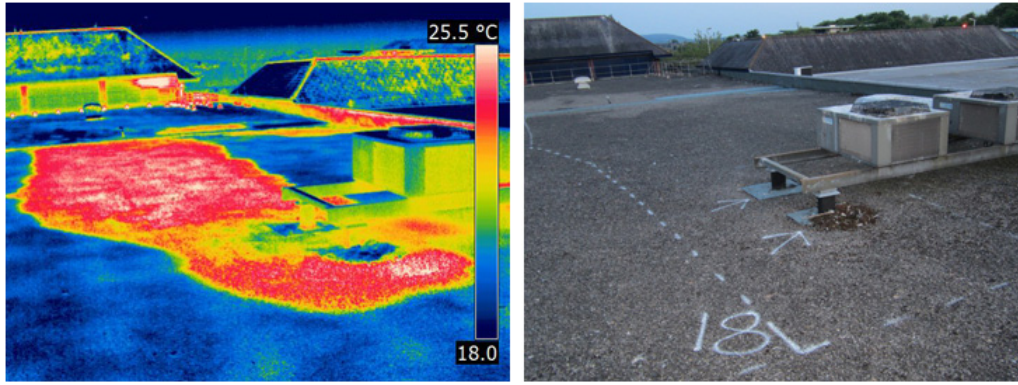


Figure 1.7: Detection of water leaking on the roof of a building. Source: <https://www.pixelthermographics.co.uk/buildings/roof-leak-thermographic-survey>

## 1.2.2 Techniques developed for research

Unlike site measurement techniques, the ones developed for research enable more accurate detection and moisture content estimation for samples submitted to drying or wetting in controlled hygro-thermal conditions.

### 1.2.2.1 Classical measurements techniques

Classical measurement techniques consist of making "point-wise" or "bulk-averaged" series of measurements in time. Regarding drying-related processes in cement-based materials, 3 types of experimental measurements have been extensively used in the literature: weight loss measurement by gravimetry, point-wise sensor-based measurements of the relative humidity and measurement of the global displacement of the sample induced by drying shrinkage. A representation of these three techniques is given in figure 1.8

- **Weight loss:** this method consists of measuring the mass of a sample submitted to drying in a thermohydric controlled environment at different moments in time. The method characterizes the kinetics and the total amount of moisture escaping from the porous medium to the outer environment.
- **Relative humidity sensors:** This method measures the relative humidity inside the cement-based material at a specific point in space. Multiple sensors are usually used to characterize the relative humidity gradients at different depth from the exchange surface in a unidirectional flow configuration [Rahimi-Aghdam et al., 2019],[Carette et al., 2019],[Ma et al., 2020]. Additional identification of the desorption isotherm is required in order to get the saturation gradients. Many types of sensor technology are used in the literature, each requiring a careful calibration and measurement procedures [Granja et al., 2014]. However, the point-wise nature of the measurement in an intrinsically heterogeneous medium such as concrete might misrepresent the hydric state of the material.
- **Drying shrinkage measurement:** This method consists of acquiring successive measurement of the change in the size of the sample using displacement transducers. When displacement variation measurements are plotted against weight variation, the slope of the near-linear curve represents the drying shrinkage coefficient. However, this measurement being averaged doesn't consider the local displacement that can localize and forms cracking.

### 1.2.2.2 Full-field measurement techniques

In the last few decades, the development of full-field measurement techniques together with the increasing computational capacity of computers allowed unprecedented access to observe local processes [Viggiani et al., 2012][Viggiani and Tengattini, 2019]. Indeed, each local measurement can be considered as an averaged response of the processes happening at a lower scale. However, these local observations permit a more sophisticated and enriched characterization of the material constitutive behavior and allow therefore for a better predictive capacity of their responses in a scale of interest. In the field of geomechanics and material engineering, a lot of techniques falling into this category have been developed, each having their advantages and limitations. Particularly, for cement-based materials, techniques such as Nuclear Magnetic

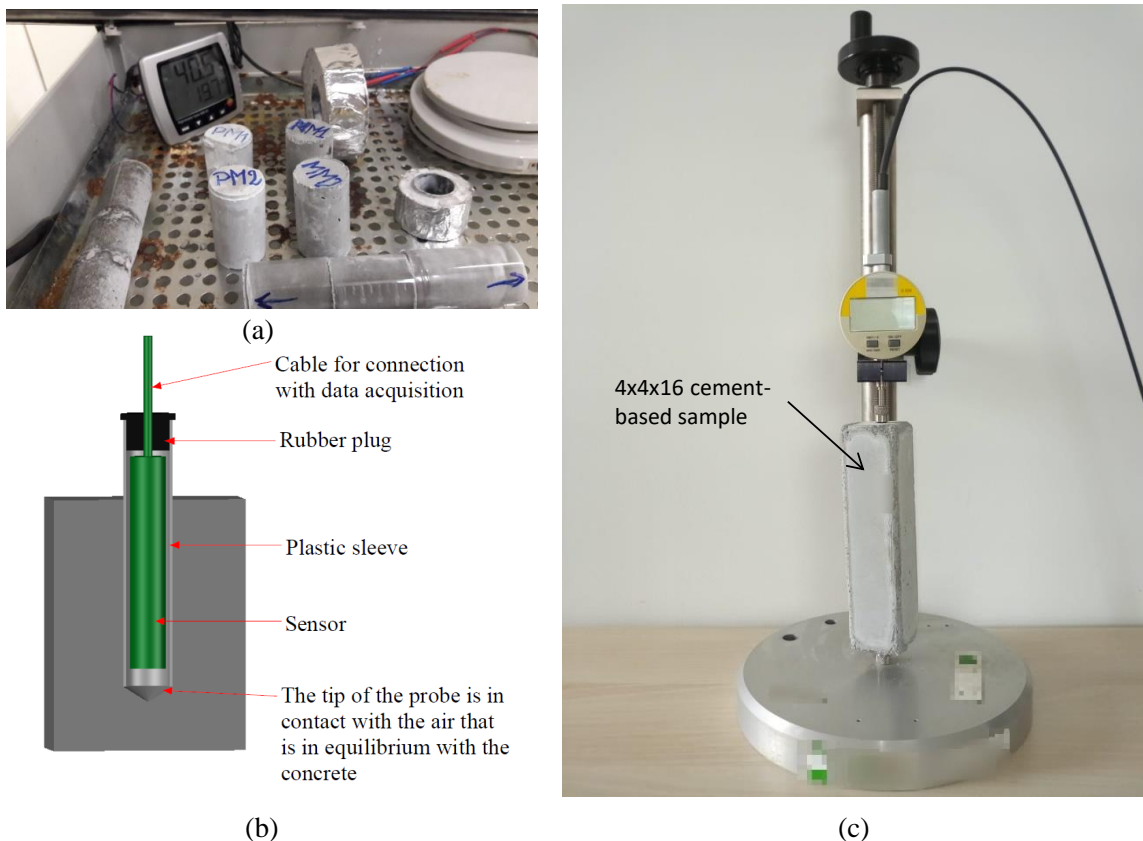


Figure 1.8: Classical measurement techniques: (a) cement-based samples drying in a thermo-hydric controlled environment, (b) Relative humidity sensor (source [Granja et al., 2014]), (c) Measurement of displacement induced by the desiccation shrinkage of a  $4 \times 4 \times 16$  cement-based sample.

Resonance (NMR), Advanced Electrical Techniques and radiation attenuation techniques (x-rays, neutron, gammadensimetry, *etc*) were used repeatedly to characterize the material hydro-mechanical behavior [Roels et al., 2004] [Phillipson et al., 2007]. In the following, a rapid glance is given for the widely used techniques in this domain followed by a particular interest in x-ray and neutron tomography, being the main experimental tools used during the PhD.

- Nuclear Magnetic Resonance spectroscopy (NMR)** NMR spectroscopy is a widely used technique in a variety of disciplines ranging from medical imaging, oil industry, material science, *etc* to investigate the atomic structure of molecules. In the context of moisture transport, a narrower branch of this technique namely  $^1\text{H}$  NMR can be used to detect the variations related to the hydrogen atom present in water. The hydrogen atoms within a sample, which is submitted to a magnetic field, get excited once exposed to radio wave pulses. They eventually relax back to their initial state releasing a signal. The measurement of this relaxation signal can be correlated to the number of hydrogen atoms in the sample which can be related subsequently to absolute water content if appropriate calibration is performed [Phillipson et al., 2007]. In addition, the relaxation signal depends on the type of molecular bonding of the water molecules. Therefore, this technique can be used to characterize the different states of water in a concrete sample since it can differentiate the chemically bonded water (due to hydration), the physically adsorbed and the free capillary water [Faure et al., 2005][Fourmentin et al., 2017]. However, the technique has some limitations related to the physico-chemical magnetic properties of the cement matrix (the presence of iron oxide for instance) affecting the water detection in small porosity [Hall et al., 1997]. For this reason, White Portland Cement (WPC) instead of Ordinary Portland Cement (OPC) should be used since it doesn't contain iron in its chemical mixture.

The imaging branch of this technique: Nuclear Magnetic Imaging (MRI) can investigate the 3D moisture content and morphological aspects of White Portland Cement [Marfisi et al., 2005]. However, multiples images have to be acquired, each using a different protocol each time, in order to optimize the phases separation.

- Advanced Electrical Techniques** The electrical properties of porous materials depend on their moisture content [Knowler, 1927]. The measurement of electrical impedance, capacitance or resistance can be used therefore in order to characterize the moisture content in those materials [Norberg, 1999][Allam et al., 2020]. The advanced variations of those techniques, such as Electrical Resistance Tomography (ERT) may be used to obtain 3D characterization of moisture gradients and chloride distribution in cement-based materials by measuring its corresponding internal 3D conductivity fields [Karhunen et al., 2010b][Karhunen et al., 2010a]. However, this technique requires good ohmic contact between the electrodes and the wet surfaces of the sample, therefore applicable only to a material having high moisture content. Recently, the work of [Voss et al., 2016] overcame this problem by using a similar electrical imaging technique: Electrical Capacitance Tomography (ECT). This technique doesn't require any ohmic contact establishment and can be used to characterize the 3D moisture content in porous material by characterizing its 3D permittivity variation  $\Delta\epsilon_r$ . This is illustrated in figure 1.9, where the temporal evolution of permittivity variation was characterized in 3D for concrete samples having different  $w/c$  ratio. The water content fields can be therefore computed when proper calibration is done (for samples having known hydric content) or by the use of appropriate mathematical models [Voss et al., 2019].

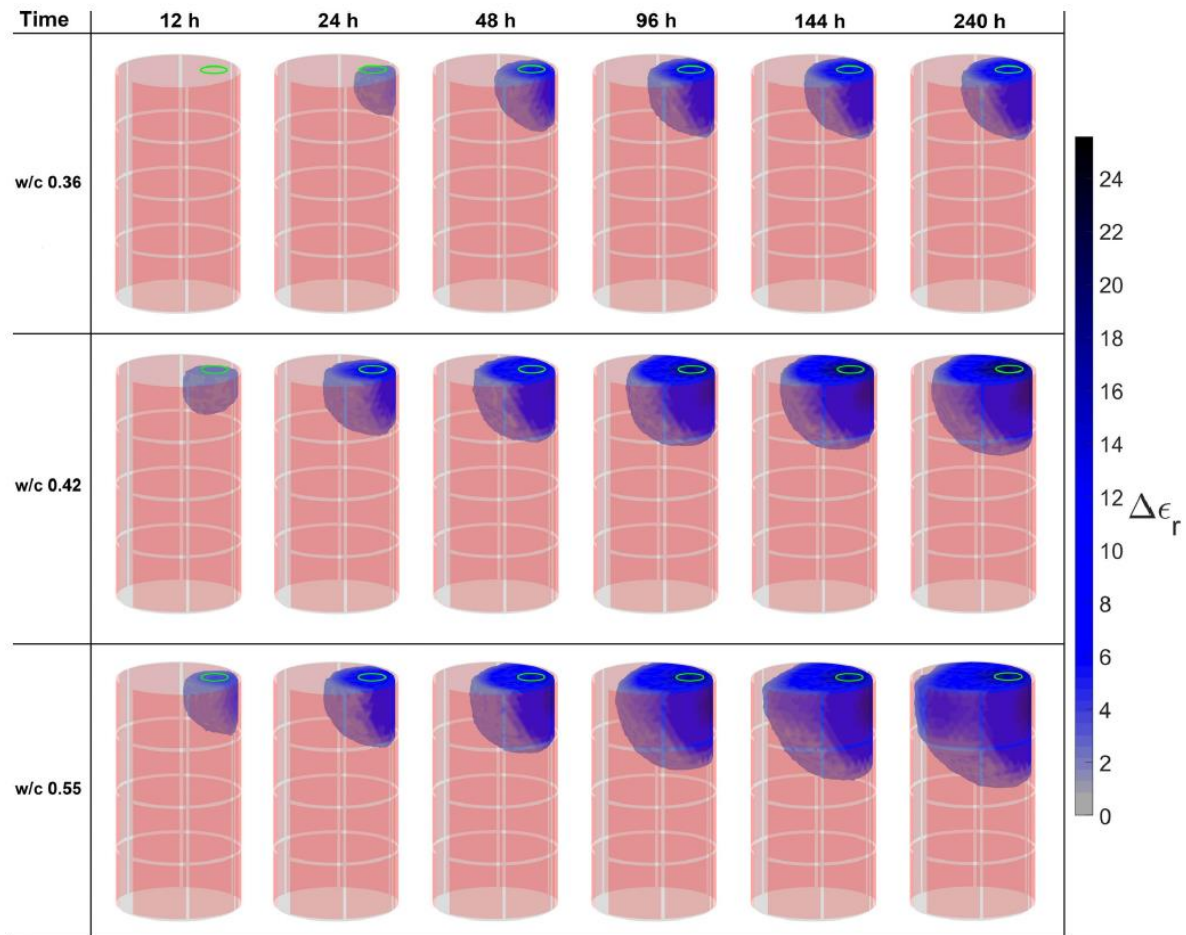


Figure 1.9: 3D reconstructed ECT of electrical relative permittivity  $\Delta\epsilon_r$  after 12, 24, 48, 96 and 144h of water ingress in mortar samples [Voss et al., 2019]

These methods have the advantage over other advanced techniques (NMR, neutron,  $\gamma$ -ray or x-ray imaging) by not being limited to small size samples and by having a relatively lower financial cost. However, despite having a high temporal resolution, their spatial resolution remains comparatively much lower due to the ill-conditioned nature of the reconstruction problem [Voss, 2020].

- Radiation or particle attenuation techniques** Several methods fall into this category of measurement techniques, perhaps the most eminent are x-rays, neutrons and gammadensimetry. A full section

will be dedicated to the two former techniques, being the main experimental tools used in this PhD. A glance of the latter, gammadensimetry, is given in here. Gammadensimetry is a non-destructive technique that can be used to evaluate the hydro-mechanical processes in cement-based materials [Nielsen, 1972]. The  $\gamma$ -rays emitted by a  $\gamma$ -source are attenuated by the sample before finally reaching the detector. The attenuation variations of the incident beam can be correlated to the hydro-mechanical processes happening in the material such as drying or carbonation [da Rocha et al., 2001][Villain and Thiery, 2006a]. However, the random nature of radioactive emissions can be in some cases a significant source of error affecting the repeatability of the measurement [Villain and Thiery, 2006b] especially for heterogeneous materials having high absorption coefficient [Nofziger, 1978][Roels et al., 2004].

### 1.2.3 Neutron and x-ray imaging to characterize hydro-mechanical behavior of cement-based porous media

In 1895, Wilhelm Conrad Röntgen discovered accidentally x-rays while trying to test whether cathode rays could pass through glass. Neutrons were discovered four decades after by James Chadwick in 1932. The latter was trying to understand the theoretical imbalance of the energy necessary to maintain the electrons in the atom. The first x-ray radiograph was taken by Röntgen for his wife left hand and found that these rays can penetrate through human tissues as seen in figure 1.10. News spread worldwide and few years after doctors started to use x-ray in the medical field. The first neutron radiograph was taken in 1935 by H. Kallmann and E. Kuhn [Peter, 1946][Perfect et al., 2014]. Several technical and technological developments were done to reach nowadays imaging potential of the two techniques, among which we cite the technical improvement of the film in the 1950s followed by the electronic imaging and the introduction of the CCD imaging devices in the 1970s and 1980s. For more information regarding the history of neutron imaging, the reader is referred to the work of [Brenizer, 2013].

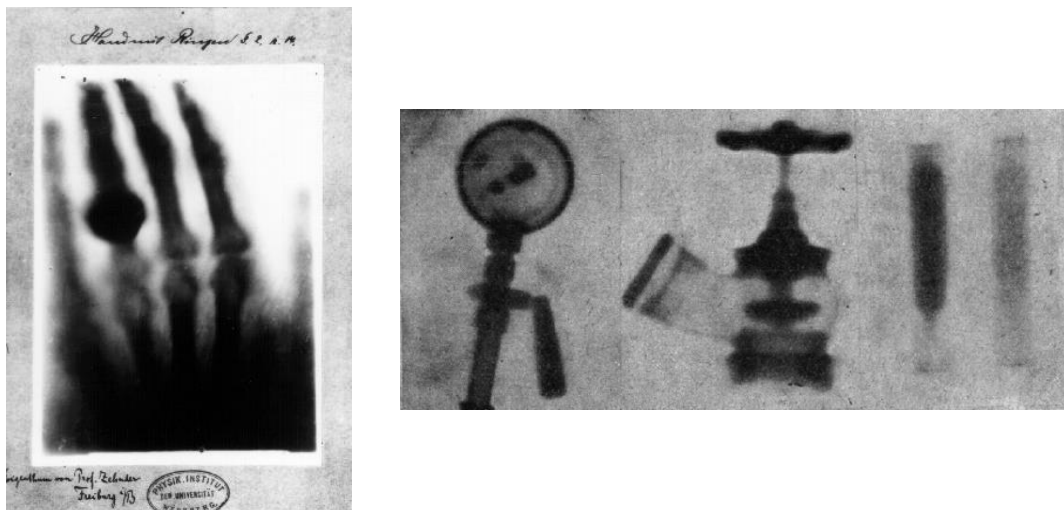


Figure 1.10: (Left) first x-ray radiograph taken by Wilhelm Conrad Röntgen of his wife's hand wearing a ring, taken on 22<sup>nd</sup> of December 1895. (Right) First neutron radiography of a pressure gauge, fire hydrant and test tubes filled with  $H_2O$  and  $D_2O$ . Adapted from (Wikimedia Commons) and [Peter, 1946].

#### 1.2.3.1 Interaction with matter

Neutrons and x-ray interact differently with the atomic structure. Neutrons interact with the nucleus of the atom unlike x-ray that interacts with the electron shell. Neutrons are therefore sensitive to different isotopes such as Hydrogen and Deuterium present respectively in  $H_2O$  and  $D_2O$  as seen in figure 1.10. In fact, the attenuation of neutrons by  $D_2O$  is around one order of magnitude lower by that of  $H_2O$  [Yehya, 2018].

x-ray, on the other hand, has an increasing attenuation with the atomic elements (which is not the case for neutrons) and therefore doesn't shown any sensitivity for isotope elements. The different interactions of these two techniques with each element of the periodic table is shown in figure 1.11.



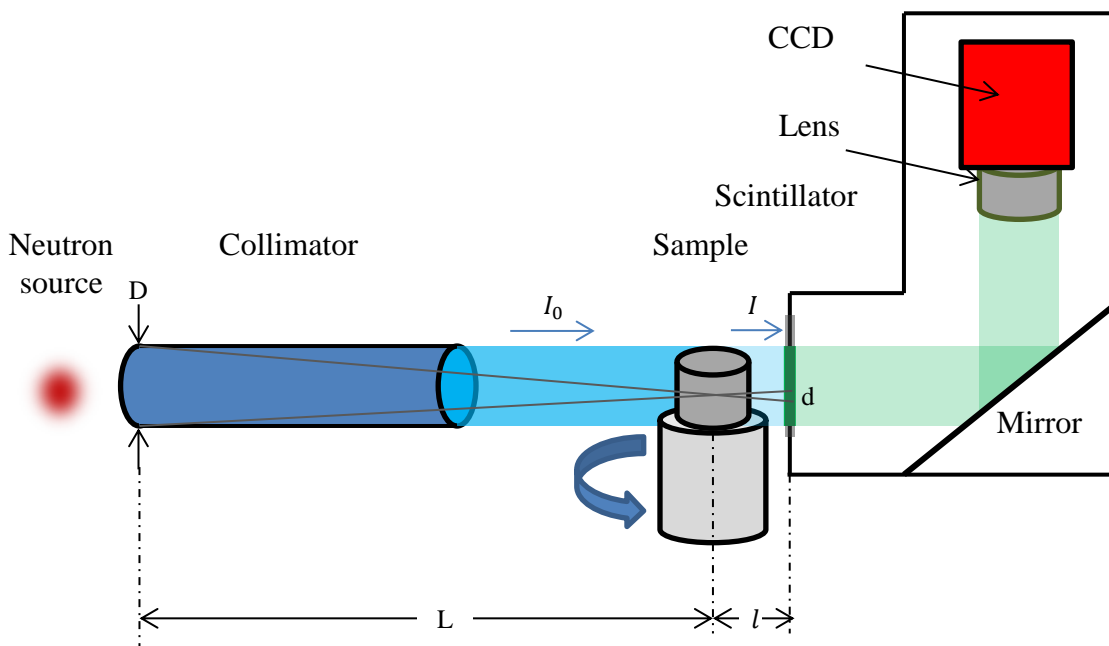


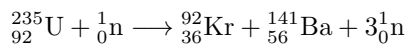
Figure 1.12: A schematic scheme of a typical neutron imaging beamline

On the other hand, x-ray imaging can be performed in laboratory (x-ray tomograph) or in large scale synchrotron. A laboratory-scale x-ray scanner requires only a source and a detector while a synchrotron facility requires much more sophisticated components.

#### 1.2.4.1 Neutron and x-ray sources

**1.2.4.1.1 Neutron** For imaging applications, a very high neutron flux is required in order to reduce the time to conduct an experiment and acquire satisfyingly high resolution radiographies. Only large devices neutron sources fulfill this requirement.

- **High-energy particle accelerators** A spallation source consists on accelerating protons to high energy levels (around 96% of light speed) and focusing them on a target material (generally, tantalum or tungsten) in order to prompt the emission of neutrons. Using this method, 20 to 30 neutrons are released per nucleus, taking away a big part of the initial protons energy. Well-known operational facilities that use spalling sources to produce neutrons are the ISIS institute in UK, Paul Scherrer Institute (PSI) in Switzerland and JPARC in Japan.
- **Nuclear fission reactors** Nuclear fission reactors are the alternative large devices that can produce a high flux of neutrons through nuclear fission chain reaction. A Uranium 235 atom is bombarded with a neutron, causing it to split generally into a Barium and a Krypton atoms in addition to three high speed neutrons.



However, the neutrons speed should be slowed down to sustain the chain reaction. Therefore, in typical nuclear power plant, a moderator should be used ( $\text{H}_2\text{O}$  or  $\text{D}_2\text{O}$  at low temperature). The resulting beam of net neutron gain is divided in energy-based sub-categories. Among these categories, only cold ( $<0.025\text{eV}$ ) and thermal (about  $0.025\text{eV}$ ) neutrons can be used in imaging domain, each having its advantage. Thermal neutrons have a higher penetration power but cold neutrons allow a better contrast. Among the operational facilities that use nuclear fission to produce neutrons we cite the NBSR-NIST in USA, NESCA in south Africa and Institut Laue-Langevin (ILL) in France, the latter having the highest neutron flux in the world [Tengattini et al., 2020b].

**1.2.4.1.2 x-ray** x-ray sources are divided in two categories:

- **x-ray tube** x-ray is emitted when high speed electrons hits a metal anode target. Only 1% in the electron beam is converted into photons. The rest 99% is transformed into heat, which is problematic

since it can melt the anode. To overcome this, the anode should be continuously rotated allowing each time a new surface to be exposed to the electron beam. The produced beam of photons is polychromatic, conical and generally have a low brilliance (in comparison to synchrotron x-ray beam). In an x-ray tube, voltage and current intensity are controlled. The former defines the mean energy of the photons emitted (the higher the voltage the higher the mean energy of the x-ray photons). The current intensity, on the other hand, controls the number of electrons bombarding the anode, therefore, the number of photons emitted.

- **Synchrotron** x-ray beam in a synchrotron is emitted when the negatively charged electron beam is deviated by a magnetic field. They are emitted in the tangential direction of the curved trajectory of electrons contained in a closed-loop hoop path. The synchrotron x-ray beam is monochromatic, parallel and has a high brilliance (photon/second, per  $mm^2$ ).

#### 1.2.4.2 Neutron beam collimation

While the x-ray beam generated by a laboratory scanner is conical, the neutron beam is quasi-parallel (less than 1 degree divergence). This divergence has an effect on the so-called geometric unsharpness  $d$ , being one of two features affecting the image resolution (the second feature being the detection unsharpness discussed in the next paragraph). This geometric unsharpness can be seen in figure 1.12 and can be determined geometrically by:

$$d = l / \left( \frac{L}{D} \right) \quad (1.5)$$

Where  $l$  is the sample to detector distance,  $D$  is the aperture diameter and  $L$  is the aperture-object distance; the ratio  $L/D$  being called the collimation ratio. The higher this ratio is, the lower the geometrical unsharpness thus the higher the resolution gets. However, this comes at the cost of a lower incident neutron flux which requires therefore a longer exposure time.

#### 1.2.4.3 Detection

Neutrons (or x-rays), after being attenuated by the sample, are detected by a scintillator which is a special chemical compound having the property of luminescence. In other words, the scintillator absorbs the energy of the incident ionizing radiation and transforms it in visible light. This visible light can then be captured by an electronic image sensor (CCD, CMOS or amorphous silicon detector) present in cameras.

Unlike the x-ray beam, the neutron beam is parallel. There is no possibility therefore to control the resolution and the field of view by simply adjusting the source to the sample distance. Instead, the field of view is adjusted by changing the position of the camera from the scintillator. This distance, together with the mounted lens and the camera pixel size determines the field of view.

#### 1.2.4.4 Neutron Imaging

**1.2.4.4.1 Neutron Transmission Radiography** A neutron radiograph is a 2D attenuation field of a material integrated over its thickness. The generalized Beer-Lambert-Bouguer law defines the attenuation response of a scanned generalized material composed of a number of species.

For applications related to water ingress or drying in porous materials, the detection of the water thickness evolution using this technique is of great importance in order to assess the hydraulic behavior of the tested material. It can be determined as follow: Considering a porous mixture having initially at  $t_{ini}$  a hydric state represented by a liquid saturation  $S_l$  between 0 and 1 and having an averaged attenuation coefficient of  $\mu_m$  and a thickness of  $\tau_m$ . The Beer-Lambert-Bouguer law reads:

$$I(t_{ini}) = I_0 e^{(-\tau_m \mu_m)} \quad (1.6)$$

During water uptake or loss, in imbibition or drying experience respectfully, the gain or loss in transmissivity of the neutron beam at time  $t$  can be implemented in the Beer-Lambert-Bouguer law by considering the addition or loss of an equivalent water layer of thickness  $\tau_w$ .

$$I(t) = I_0 e^{-(\mu_m \tau_m \pm \mu_w \tau_w)} \quad (1.7)$$

The change of water mass at a time  $t$  expressed in ( $kg\ m^{-3}$ ):

$$W(t) = \pm \frac{\rho_w V_w}{V_{tot}} = \frac{\rho_w \tau_w}{\tau_m} \quad (1.8)$$

Replacing  $\tau_w$  by its expression in equation 1.7, the following expression of moisture content is obtained:

$$W(t) = \pm \frac{\rho_w}{\mu_w \tau_m} \log \left( \frac{I(t)}{I(t_{ini})} \right) \quad (1.9)$$

#### 1.2.4.5 Neutron computed tomography

The mathematical basis for tomographic reconstruction was formulated by Radon at the beginning of the last century [Radon, 1917]. Abstractly, reconstruction is a multidimensional inverse problem where the challenge is to return an estimate of a 3D object from a finite number of 2D projections. There exist mainly two types of reconstruction methods: algebraic reconstruction technique (ART) and analytical ones.

The first category considers the reconstruction as an iterative optimization problem [Gordon et al., 1970][Vontobel et al., 2006] where the final goal is to solve a system of linear equations  $Wv = p$ , where:  $v$  represents the voxels of the generated output image arranged as a vector of dimension  $n$ ,  $p$  is a 1D projection data vector of  $m$  elements, each representing a measurement taken at a certain detector in a projection direction.  $W$  is a sparse  $m \times n$  matrix whose values represent the relative contribution of each output voxel  $v_j$  to the sinogram. The main advantage of this reconstruction technique is that it allows easily the incorporation of prior geometrical knowledge about the system  $f(x, y)$ . Accurate reconstruction can be therefore created with a lower radiation dose and consequently a lower signal-to-noise ratio. However, the main drawback of this method is the high computational cost.

Analytical methods on the other side are computationally lesser demanding, therefore they are widely more used [Kak and Slaney, 2001]. Three main concepts are required to be learned in order to satisfyingly understand the reconstruction procedure: Radon transform, Fourier slice theorem and Filtered Backprojection method. A holistic explanation of the different concepts related to tomographic reconstruction can be seen in figure 1.13. In the end, in most cases, reconstruction techniques uses simplifying assumptions in order to facilitate the algorithmic computations. For instance, the beam rays are considered to be parallel, a necessary assumption for a slice-by-slice reconstruction. Also, the beam is considered monochromatic which neglect the energy dependency on the material attenuation coefficient.

**1.2.4.5.1 Radon transform** Considering a hypothetical 2D object whose surfacic object function  $f(x, y)$  is known and a 1D rotating detector function  $p_\theta(t)$  receiving the rays coming from an angle  $\theta$  with the  $y$ -axis defined as  $L(\theta, t)$  and where  $t$  is the intersection of the ray and the detector. The detector function can be expressed as the integral of the object function  $f(x, y)$  over the ray  $ray(\theta, t)$ .

$$p_\theta(t) = \int_{ray(\theta, t)} f(x, y) dl \quad (1.10)$$

Repeating the operation for all the  $360^\circ$  projection angles, a transformation function called Radon transform that condensates all the projections continuously taken in a “sinogram” represented in the  $(t, \theta)$  space. Each row in this sinogram represents the detected ray at a certain point  $t$  in the detector for a different  $\theta$  angle in each cell. The reason behind the name sinogram comes from the fact that if Radon transform is applied for a 0D point object (or Dirac function  $\delta_D$ ), the outcome of the Radon transform results in a sine wave in the projection  $(t, \theta)$  space. Since Radon transform is a linear operator, each object function  $\mu(x, y)$  can be therefore described as a set of Dirac pulses, each giving a sine wave in the projection space.

For practical reasons related to the finitude of the detector cells and the discrete nature of the detector (or object) rotation, a discretized version of the continuous Radon transform should be used.

**1.2.4.5.2 Fourier slice theorem** This section requires a prior basic knowledge in Fourier transform mathematics which can be learnt in [Sanderson, 2018]. To represent the object function  $f(x, y)$  on the Fourier domain  $(\eta, \zeta)$ , one can take advantage of its detector functions  $p_\theta(t)$  for a set of different angles. In fact, the Fourier slice theorem states that a 1D Fourier transform  $P_\theta(\omega)$  of the detector function  $p_\theta(t)$  at an angle  $\theta$  corresponds to a line in the 2D Fourier representation  $F(\eta, \zeta)$  of the object function  $f(x, y)$  at the same angle  $\theta$ . In fact, the 2D Fourier transform of  $f(x, y)$  reads:

$$F(\eta, \zeta) = \int_{-\infty}^{\infty} \int_{-\infty}^{\infty} f(x, y) e^{-i2\pi(\eta x + \zeta y)} dx dy \quad (1.11)$$

and the 1D Fourier transform of the detector function  $p_\theta(t)$  reads:

$$P_\theta(\omega) = \int_{-\infty}^{\infty} \int_{-\infty}^{\infty} f(x, y) e^{(-i2\pi\omega(x \cos \theta + y \sin \theta))} dx dy \quad (1.12)$$

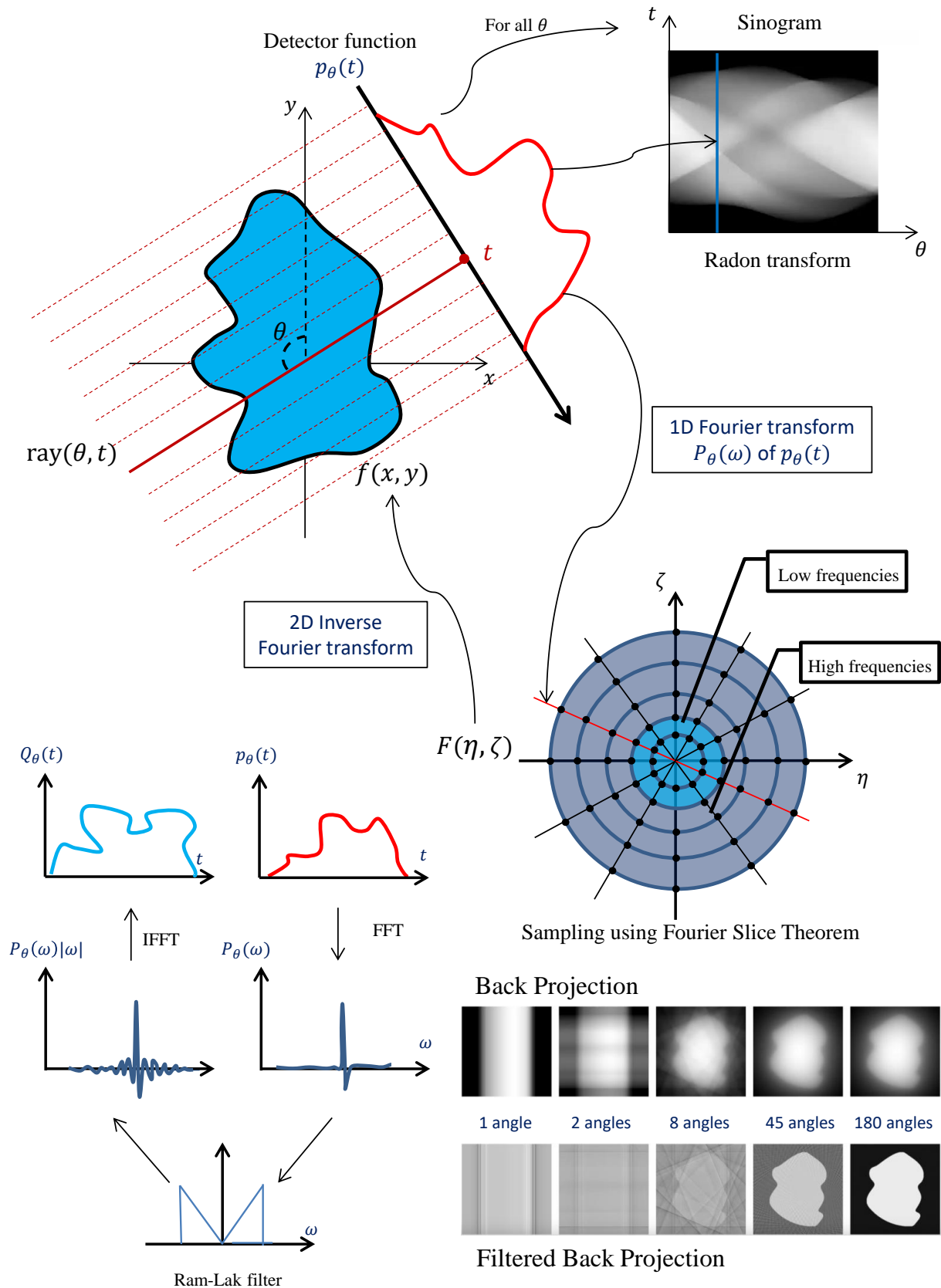


Figure 1.13: A comprehensive summary of commonly-used analytical tomographic reconstruction methods. Drawing inspired from ASTRA Toolbox youtube channel.

if we replace  $\eta$  by  $\omega \cos \theta$  and  $\zeta$  by  $\omega \sin \theta$ , we get:

$$P_\theta(\omega) = F(\omega \cos \theta, \omega \sin \theta) \quad (1.13)$$

proving therefore the Fourier Slice Theorem. The problem of the direct usage of this method is related to the sampling in the Fourier domain. The low frequencies are sampled more densely than the high frequencies. The latter is responsible for the details and the sharpness of the image. The direct application of this method leads eventually to a blurry reconstruction which requires the usage of specific filters.

**1.2.4.5.3 Filtered Back Projection** Recalling the 2D inverse Fourier transform, the object function is linked the one represented in the Fourier domain by the following expression:

$$f(x, y) = \int_{-\infty}^{\infty} \int_{-\infty}^{\infty} F(\eta, \zeta) e^{i2\pi(\eta x + \zeta y)} d\eta d\zeta \quad (1.14)$$

To convert from Cartesian to polar coordinates in the frequency domain, the following substitutions have to be made:

$$\begin{aligned} \eta &= \omega \cos \theta \\ \zeta &= \omega \sin \theta \\ d\eta d\zeta &= \omega d\omega d\theta \end{aligned} \quad (1.15)$$

The inverse Fourier transform of a the function in the polar coordinates reads:

$$f(x, y) = \int_0^{2\pi} \int_{-\infty}^{\infty} F(\omega, \theta) e^{i2\pi\omega(x \cos \theta + y \sin \theta)} \omega d\omega d\theta \quad (1.16)$$

The integral can be performed from  $0$  to  $\pi$  instead for  $2\pi$  since the radiographies get mirrored.

$$F(\omega, \theta + \pi) = F(-\omega, \theta) \quad (1.17)$$

This requires the use of the absolute value of the filter  $|\omega|$  in the integral. and let  $t$  the intersection between the beam ray and the detector be expressed in the Cartesian coordinate system:

$$t = x \cos \theta + y \sin \theta \quad (1.18)$$

the object function expression becomes:

$$f(x, y) = \int_0^{\pi} \left[ \int_{-\infty}^{\infty} F(\omega, \theta) |\omega| e^{i2\pi\omega t} d\omega \right] d\theta \quad (1.19)$$

Or, the evaluation of the 2D Fourier transform (in the frequency domain )  $(\omega, \theta)$  of the object function  $f(x, y)$  at a certain angle  $\theta$  is equal to the 1D Fourier transform  $P_{\theta}(\omega)$  of the detector function  $p_{\theta}(t)$ . The integration therefore reduces to:

$$f(x, y) = \int_0^{\pi} \left[ \int_{-\infty}^{\infty} P_{\theta}(\omega) |\omega| e^{i2\pi\omega t} d\omega \right] d\theta \quad (1.20)$$

Written differently,

$$f(x, y) = \int_0^{\pi} Q_{\theta}(t) dt \quad (1.21)$$

where  $Q_{\theta}(t)$  is the inverse Fourier transform of the Fourier transform of the detector function multiplied by the Ram-Lak filter  $|\omega|$ . Taking into account the discrete nature of the radiographic acquisition, the continuous formulation of the object reconstruction reduces to:

$$f_d(x, y) = \frac{\pi}{n} \sum_{k=1}^n Q_{\theta_i}(x \cos \theta_i + y \sin \theta_i) \quad (1.22)$$

where  $f_d(x, y)$  is the discrete representation of the object function  $f(x, y)$  and  $n$  is the total number of angular stations [Strobl et al., 2009] [Perfect et al., 2014] [Al-Hussani and Al-Hayani, 2014] [Palenstijn et al., 2013].

### 1.2.5 Imaging artifacts

Among the factors that contribute in polluting the images we cite: the detector system electronic noise, the spatio-temporal variations of the incident beam and inhomogeneity in the scintillator. Those factors can be corrected by normalizing all the acquired images by the so-called “dark” and “flat” field, *i.e.*, by the background noise of the camera and the unencumbered beam. Specifically to neutron imaging, the images can get polluted additionally by high-energy neutrons and  $\gamma$ -rays which leave white spots in the scintillator. An erosion (low-pass) filter should be therefore applied to decontaminate the images.

The second type of artifacts, namely beam hardening and scattering, are more challenging to correct, since they require a physics-based methodology. Beam hardening is a spectral effect induced by the polychromatic nature of the incident beam. In a cylindrical sample, neutrons (or x-ray photons) are absorbed more along a longer path going through the center of the sample than the ones grazing its edge. This causes a virtual higher attenuation near the sample circumferential border. In the case of cement-based materials, this artifact intensity can evolve with the evolving water content. For that, special calibration should be used, using materials having well-known hydric states, in order to correct for this evolving artifact. Scattering on the other hand, is caused by the interaction of neutrons with some atoms, as with hydrogen present in water. When a large amount of water is present in the sample or when the sample is very close to the detector (which is essential to acquire high-resolution images), scattering becomes a significant component in attenuation. Numerous approaches have been proposed to correct for this artifact [Hassanein et al., 2005; Hassanein, 2006; Hassanein et al., 2006a,b]. however, more work in this direction is still needed to characterize this process in evolving water content conditions [Tengattini et al., 2020c].

### 1.2.6 Applications of neutron imaging for durability studies of cement-based materials

A wider bibliographical study of application of neutron imaging of moisture flow in cement-based materials and more generally in porous media can be found in [Perfect et al., 2014] [Zhang et al., 2018] [Tengattini et al., 2020c]. In here, a sufficient overview is given of the application of this technique for durability studies related to the topic of this PhD. Therefore, only studies that are related to moisture flow in sound and cracked concrete, submitted or not to a temperature gradient, are shown.

#### 1.2.6.1 Moisture transport in sound cement-based materials

Many studies were led to characterize the moisture transport in sound cement-based material in terms of transport processes (drying and imbibition), quantifying hydraulic and microstructure properties such as (sorptivity, porosity, permeability, *etc*) and other hydraulic local processes.

The first study of moisture transport in cement-based material using neutron transmission radiography (NTR) was published in 1972 by [Reijonen and Pihlajavaara, 1972]. The radiographic moisture profiles were analyzed in Portland cement mortars and the measurement of the moisture decrease associated with carbonation led to determine the thickness of the carbonation layer.

Capillary suction was also investigated using NTR in [Justnes et al., 1989] where the height and the shape of the water front were visualized during imbibition test of an oven-dry mortar sample. The effect of water to cement ratio on the water ingress front speed was investigated in [de Beer et al., 2005] (from  $w/c = 0.5$  to  $w/c = 0.7$ ).

Quantitative measurements by NTR of hydraulic and micro-structure properties such as porosity and sorptivity can be found in [de Beer et al., 2005] [Brew et al., 2009] [McGlinn et al., 2010]. Recently, permeability of concrete was characterized using *in-situ* neutron tomography [Yehya, 2018; Yehya et al., 2018]. The sample cast and cured using heavy water (attenuating 10 times fewer neutrons than normal water) was submitted to a pressure gradient of normal water. The speed of penetration of the normal water front, pushing the capillary heavy water, can be correlated to the Darcy velocity which in turn defines a 3D permeability field of the sample.

Local hydraulic processes were also investigated in [Maruyama et al., 2009] and [Trtik et al., 2011] where it was observed that saturated lightweight aggregates can serve as reservoirs during the drying process to feed the surrounding drying matrix. Other local processes such as the effect of steel rebars on the permeability field was studied in [Yehya, 2018].

Finally, up to the author’s knowledge, only one study investigated in drying of cement-based materials at low temperatures: [de Beer et al., 2004b] employed NTR to characterize water gradients during the natural drying process which can be seen in figure 1.14. Drying is rarely studied since the dynamics of the process are very slow at low temperatures which requires many days of access to the beam-line.

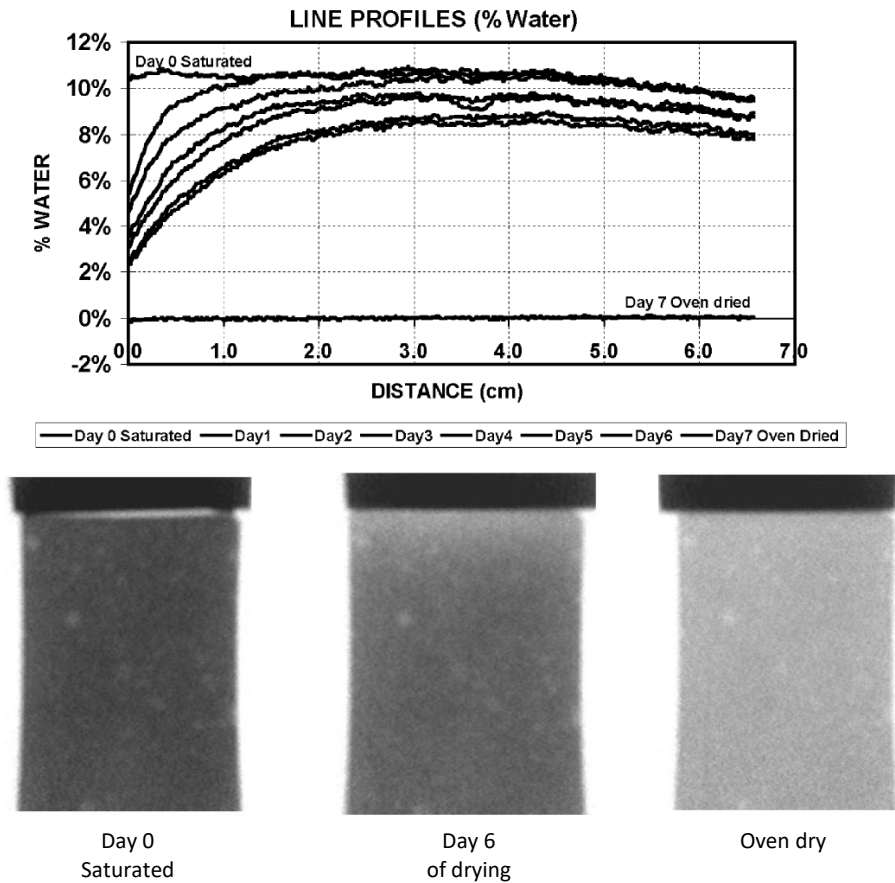


Figure 1.14: (Top) water content line profiles of a drying concrete sample at 30 °C. (Bottom) Radiography attenuation field of the same sample at different hydric states. adapted from [de Beer et al., 2004b].

### 1.2.6.2 Moisture transport in cracked cement-based materials

Cracking in cement-based materials serves as a preferential path of moisture transport as seen in figure 1.15. Neutron imaging is therefore a suitable tool to study the local effect of those cracks on the local water content evolution. The work of [Kanematsu et al., 2009] is one of the earliest to quantitatively measure the water penetration into concrete through cracks. It was found that the water ingress speed and local distribution depends strongly on the initial hygrometry of the sample. In a similar fashion, neutron radiography was also utilized to characterize different variations of cement-based material such as strain-hardening cement-based composite (SHCC) [Wittmann et al., 2010][Zhang et al., 2010b], steel-reinforced mortar [Zhang et al., 2010][Zhang et al., 2011] and textile-reinforced concrete (TRC) [Lieboldt and Mechtcherine, 2013]. Recently, neutron radiography was used *in-operando* to study the dynamics of vapor penetration in cracked concrete [Lukić et al., 2020]. The study aims to replicate a leakage situation through cracked concrete wall of a nuclear power plant.

On the other hand, the effect of cracking on the water content evolution is, up to the author knowledge, still not characterized for samples that are submitted to drying conditions. One reason could be the long time required for natural drying process which requires a long term study. In accelerated drying conditions, [Dauti, 2018] reported a qualitative observation where an initially defectuous sample has shown an accelerated drying near the crack surfaces in high temperature situation.

### 1.2.6.3 Moisture transport in heated concrete

Explosive spalling of concrete, when exposed to fire, is believed to be mostly triggered by pressure build-up due to moisture accumulation in the porosity, hence the advantage of neutrons to closely investigate this process. [Zeilinger and Huebner, 1976] visualized moisture migration when 170 °C temperature was applied to one end of a wet sample. The study aimed to mimic a type of accidental situation that can occur to the concrete containment wall in a nuclear containment building. The analysis of results permitted to calculate the vapor diffusion coefficient and the mass transfer coefficient based on acquired moisture profiles.

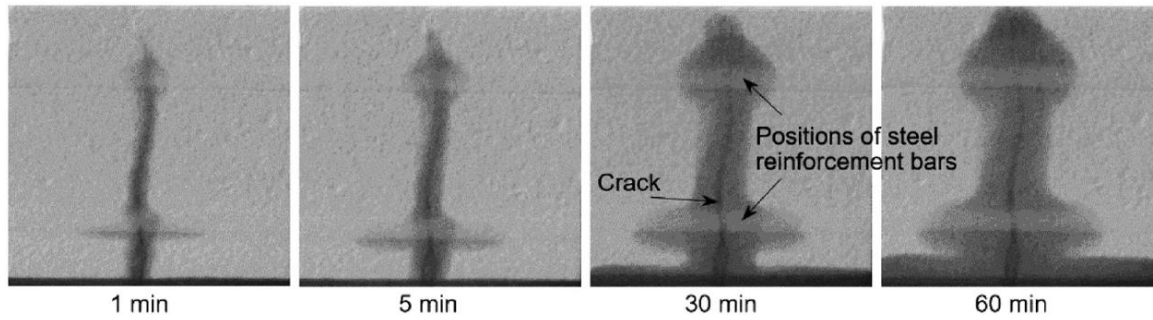


Figure 1.15: Neutron images of water ingress in cracked steel-reinforced mortar showing the local effects of the vertical cracks and the presence of horizontal rebars on the local water content evolution [Zhang et al., 2010].

Also studying the moisture flow at moderate temperature, [Kanematsu et al., 2015] investigated the water content evolution in High-Performance Concrete (HPC) during fast rate heating at the bottom surface of the sample. In addition to moisture profiles evolution, local observations were made of vapor condensation around coarse aggregates at the Interfacial Transition Zone (ITZ) and explosive spalling was observed twice after 86 s of the heating started. Similarly, [Weber et al., 2013], [Lura and Terrasi, 2014] and [Toropovs et al., 2015] applied neutron radiography to study spalling in high performance concrete. The inclusion of different additives such as Superabsorbent Polymers (SAP) and/or polypropylene (PP) fibers in the HPC mixture was investigated and their role in preventing or allowing spalling was characterized. Recently, the recent advances in high-speed neutron tomography which was made possible in satisfying resolution thanks to the Institut Laue-Langevin (ILL) highest neutron flux, [Dauti et al., 2018d] studied the behavior moisture flow and its mechanical implications in 3D using neutron tomography. Two samples having same aggregate volumetric fraction but different aggregate size distribution (a maximum of 4mm in the first sample and 8mm in the second) were heated up to 500 °C. The samples have shown different hydraulic responses despite having the same thermal profiles as seen in figure 1.16. Additionally, different variations of the sealing boundary conditions materials, hygro-thermal loading history and additives inclusions were investigated and characterized in [Tengattini et al., 2020a]. Adhesive Aluminum tapes which are commonly used for lateral sealing were found to have a negligible role in containing the moisture lateral escape at such a high temperature. Faster drying front was observed in the HPC sample for which PP fibers were added, since the melting fibers at high temperature increase the medium permeability. Finally, explosive spalling was found to occur only in the samples where the initial water content was high due to specific curing conditions and when higher heating rates were applied.

### 1.2.7 Applications of x-ray imaging to study the mechanical behavior of cement-based materials

Even though x-ray tomography was sometimes used in applications related to moisture detection in cement-based materials [Roels and Carmeliet, 2006], it is however mostly used to characterize the mechanical behavior of those materials. Particularly, this technique was widely employed to characterize the cracking initiation and propagation in multiple loading conditions. [Trtik et al., 2007] used synchrotron-based micro-tomographic analysis on a cement-based sample subject to uniaxial tension. The image analysis performed to isolate the different cement phases undermined that at small scales, dehydrated cement grains act as hard aggregates in hydrated cement matrix and therefore control the crack path. On the contrary, cracks were found to propagate through all the phases of the cement. [Meyer et al., 2009] performed in-situ micro-compression tests on foamed cementitious materials inside an x-ray scanner where deformation and fracture of a small specimen were tracked in detail. In [de Wolski et al., 2014], *in-situ* x-ray micro-tomography scans were taken of a small cylindrical specimen made out of fine-grained mortar with glass beads and which was subjected to splitting. The carried analysis tempted to characterize the micro-structure and the internal damage and to relate them to the bulk splitting strength and the fracture energy. [Yang et al., 2013] used digital volume correlation (DVC) to follow the evolution of the relative XCT scans of a concrete sample subjected to compression. Recently, [Stamati et al., 2018] [Stamati, 2020] performed tensile, compressive and triaxial tests of a micro-concrete cylindrical samples.

Other studies characterized the thermal-induced fracture network in cement paste samples exposed to high temperatures [Kim et al., 2013], however, up to the author's knowledge, no study has yet characterized

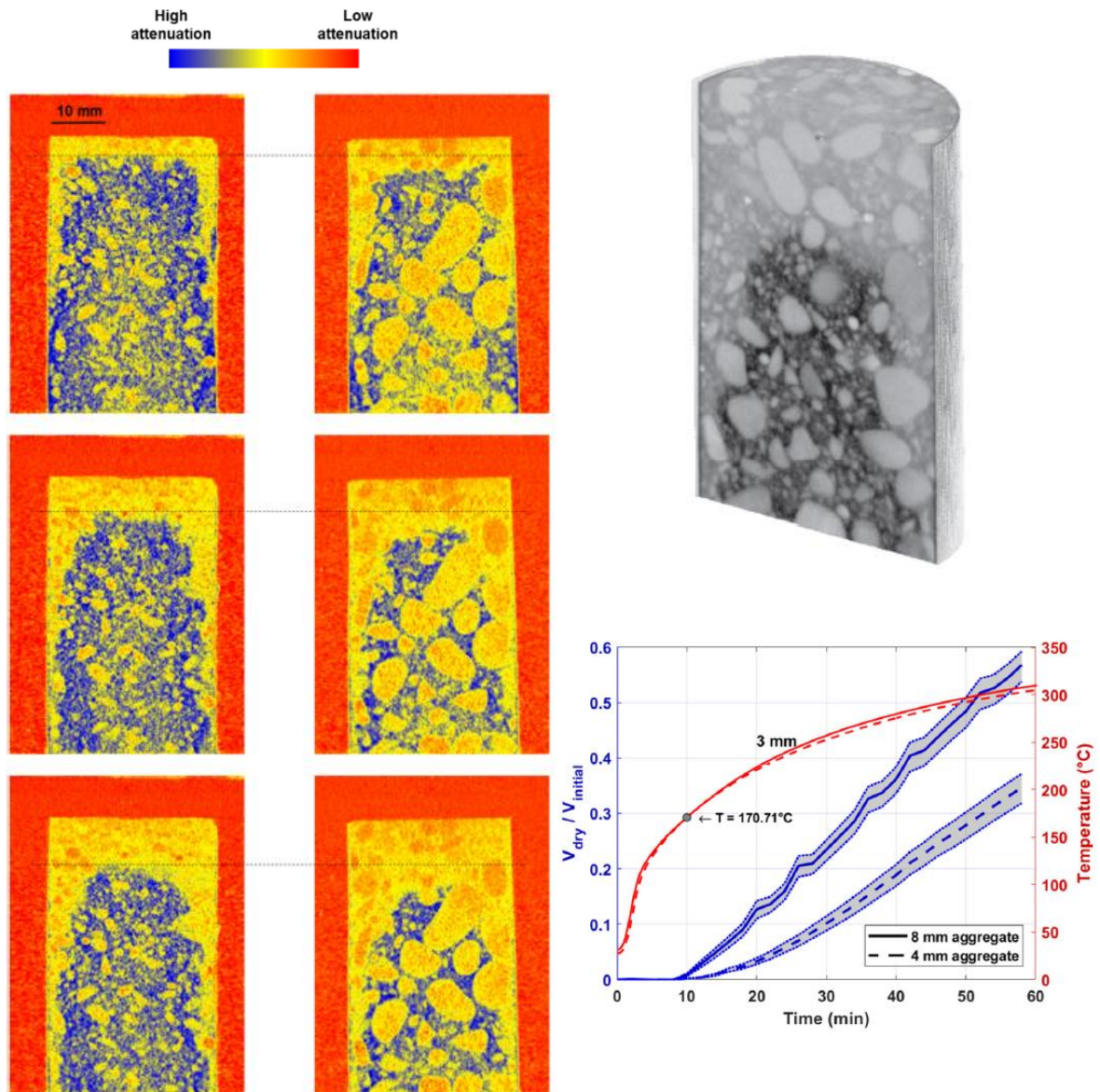


Figure 1.16: (Left) sequence of vertical slices of sequential 3D reconstructed volumes showing the advancing drying front in 4mm HPC and 8mm HPC. (Top right) a higher resolution 3D reconstruction of the 8mm HPC sample at the end of test. (Bottom right) the quantification of the effect of the aggregate size on the drying kinetics of the two samples. adapted from [Dauti et al., 2018d]

desiccation cracking induced by thermo-hydric loading and further calculate its influence on the hydraulic properties.

### 1.2.8 Why neutron and x-rays for concrete

It is clear for all what was mentioned above that x-ray and neutron are highly complementary measurement techniques that can be used to investigate a wide range of physical processes in cement-based porous media. Particularly, neutron enables the access to moisture transport processes while x-ray permits the investigation into their mechanical implication [Stavropoulou et al., 2019][Stavropoulou et al., 2020][Xu et al., 2020].

In figure 1.17, two horizontal slices of the same concrete sample at the same height can be visualized as seen by these two techniques. The neutron slice differentiates the mortar (cement paste and sand fines below the resolution) from the bigger aggregates but can hardly distinguish these latter from macro-porosity. Conversely, x-ray enables the distinction of macro-porosity and the solid-fluid phase but cannot distinguish based on intensity alone between the aggregates and the mortar phase. Each technique emphasizes therefore different phase identification and morphological description of the same material. The combined use of them

allows for a richer description of the mesoscopic structure of the material.

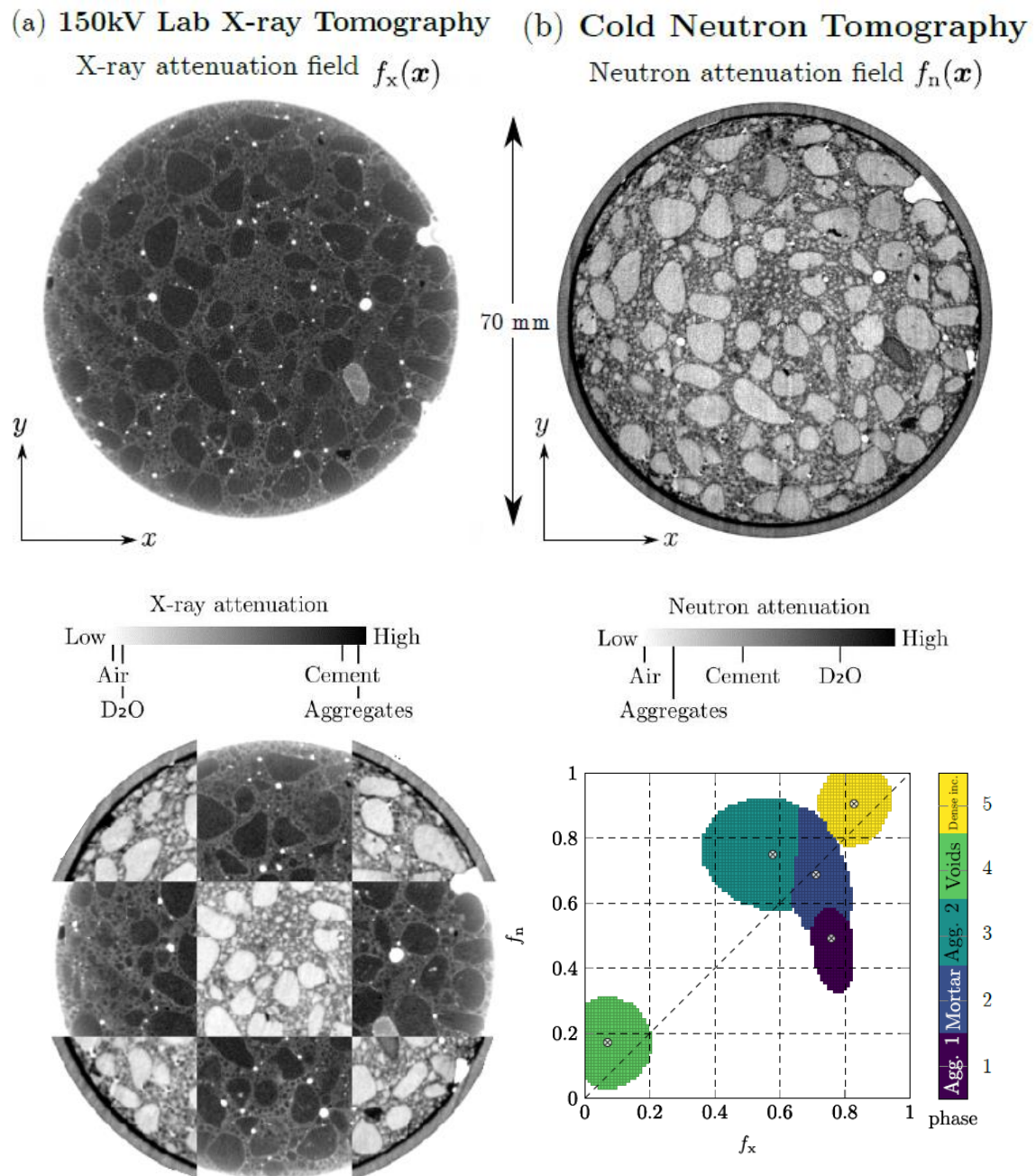


Figure 1.17: The same horizontal slice of a concrete sample as seen by (top left) x-ray and (top right) neutrons (color map were inverted for presentation purposes). The sample was prepared using  $D_2O$  instead of  $H_2O$  to take advantage of the isotope sensitivity of neutron ( $D_2O$  being one order of magnitude less attenuating than  $H_2O$ ). The different interactions of the two beams with matter demonstrate their complementarity, each by emphasizing different morphological features of the concrete. (Bottom left) spatial alignment of the two volumetric information, also called multimodal registration, enables phase separation as seen in (bottom left) where 5 phases were identified on a bi-modal joint histogram. Adapted from [Yehya et al., 2018] and [Roubin et al., 2019]

## 1.3 Numerical modeling of drying-related processes in cement-based materials

Once the experimental observations and measurements are performed, constitutive relationships of all the parameters involved in the process are constructed. Usually, these observations feed the system of energy, mass and momentum conservation equations to equate the number of equations with the number of unknowns. This system of partial differential equations, once well defined, can predict the state of the material in space and time if solved. However, it is very difficult and sometimes impossible to provide a continuous analytical solution to this system. For that, numerical approaches are developed to provide an approximation for the analytical solution in specified points in space and moments in time.

The robustness of these numerical models is strongly related to its predictive capacity. This later depends on the scale of observation. Regarding concrete, as a multiphase material involving multiphysics processes, four different scales of observations can be defined as shown in figure 1.18. It is required therefore that the numerical model developed at each scale captures the physical processes involved within, in order to fulfill its predictive potential. For instance, a mesoscale numerical model should capture the cracking morphology or the local water distribution [Huang et al., 2015]. At the nanoscale, a molecular dynamics model should capture the number of adsorbed molecule layers at the pore wall or the motion of ions in the capillary porosity for instance [Ioannidou et al., 2016].

However, all the models developed at a small scale should serve finally in enhancing the modeling at the structural scale. However, in the case of multiphase systems, all the equations to solve must be developed at the micro-scale and up-scaled at higher scales. More on that in the next section.

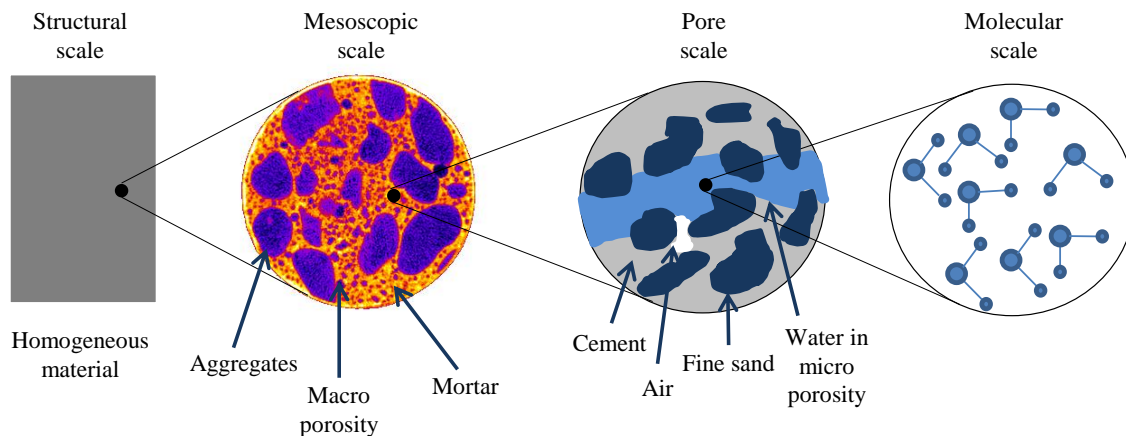


Figure 1.18: Concrete as shown in 4 different scales: Structural, mesoscopic, pore and molecular scales.

### 1.3.1 Upscaling procedure from the micro-scale

Three different upscaling approaches are possible, each relying on different assumptions and having its advantages and its inconveniences:

- The first approach writes both of the conservation equations and the constitutive equations of the multiphase system at the pore scale and average them over a REV. By that, this approach considers that elasticity-based equilibrium equation for solid grains in contact, Navier-Stokes equations and heat flow equation based on Fourier law, *etc* are valid at the micro-scale. However, pore-scale observations are hard to get, therefore, the applicability of these constitutive relations at this scale is debatable. The main advantage of this technique is that it links between the microscale coefficients and the macro scale ones. Recently, a new technique, that falls in this first category, called “Thermodynamically constrained averaging theory” also known as TCAT [Gray and Miller, 2014] was developed. Its main feature is that it writes also thermodynamics equations (*e.g.* Gibbs equation) at the pore scale and average them, yielding consistent thermodynamics between scales.

Also falling in this category are numerical upscaling methods that solves the numerical constitutive equations, such as the Cahn-Hilliard equation for realistic fluid interface behavior, at the micro-scale. Then appropriate numerical techniques are applied to upscale the behavior to the scale of interest.

- On the other hand, the second and third upscaling approaches writes only the conservation equations at the pore scale and molecular scale respectively and average them over an REV to get the equations at the macro scale [Hassanizadeh and Gray, 1979a][Hassanizadeh and Gray, 1979b]. The constitutive equations are developed at the scale of observation. Unlike the first approach, the mathematical terms generated by the upscaling approach are all physically meaningful so that they can be simplified based on physical hypotheses.

In this work, only macroscopic volume-averaged equations are reported since their derivation from the microscale is mathematically intensive and time-demanding. In addition, these developments have been done previously and can be found in [Lewis and Schrefler, 1998] and [Pesavento, 2000]. An educative series of videos concerning this topic, and more generally, the fundamentals of multiphase porous media can be found also on the web [Hassanizadeh].

### 1.3.2 Macroscopic modeling

Using FEM, there exist two categories of models to describe the behavior of cement-based materials under thermo-hydro-mechanical (THM) loading. The first category, the multiphase models, also called “complete” models, takes into account the presence of all the fluid phases in the porosity (water, vapor and dry air). It allows therefore for a sophisticated description of the physical interaction of all the phases of the material. The second category, simplified models, considers less fluid phases under some simplifying assumptions that neglect the role of a phase interaction in certain conditions. The balance equations and the constitutive laws describing the thermo-hydric behavior of the material in both model types are addressed and detailed in chapter 1. For this reason, only the mechanical constituents of the model and its implications on the thermo-hydric response are listed in this chapter.

#### 1.3.2.1 Momentum conservation equation

The mechanical behavior is determined by the volume-averaged momentum conservation equation:

$$\nabla \cdot \sigma^t + \rho \mathbf{g} = 0 \quad (1.23)$$

where  $\mathbf{g}$  is the the gravitational acceleration vector and  $\sigma^t$  is the total stress tensor. The density of the multiphase porous medium, accounting for three fluid phases in addition to the solid skeleton, is expressed as:

$$\rho = (1 - \phi)\rho_s + \phi \rho_l + \phi(1 - S_l)\rho_g \quad (1.24)$$

where  $\rho_\pi$  is the density of the  $\pi$  specie,  $\phi$  and  $S_l$  are respectively the porosity and the liquid saturation ratio.

#### 1.3.2.2 Constitutive equations

- **Effective stress principle** The effect of fluid phases pressure on the total stress is taken into account through the effective stress principle [Lewis and Schrefler, 1998]. For non-deformable solid skeleton, this principle reads:

$$\sigma' = \sigma^t + \mathbf{I}p_s \quad (1.25)$$

Where  $\sigma'$  and  $\sigma^t$  are respectively the effective and total stress tensors.  $\mathbf{I}$  is the second order unit tensor and  $p_s$  is the average pressure applied by the fluid phases on the solid phase, written as:

$$p_s = S_g p_g + S_w p_w \quad (1.26)$$

$p_g$ ,  $S_g$ ,  $p_w$  and  $S_w$  being the pressure and saturation of gas and water respectively. The generalized effective stress problem applicable to deformable solid skeleton by introducing the *Biot* coefficient  $\alpha$ . The generalized principle reads:

$$\sigma'_{\mathbf{g}} = \sigma^t + \mathbf{I}\alpha(S_g p_g + S_w p_w) \quad (1.27)$$

- **Damage model** Mazars' damage model describes the elastic-damageable concrete behavior. It is a simple robust 3D model based on damage mechanics that allows the description of the decrease of the rigidity of concrete under the effect of micro-cracks or macro-cracks generation. It relies on a scalar variable  $D$  describing the damage in an isotropic way but distinguishing despite everything between compression and traction damage. This variable is ranged between 0, sound concrete, and 1, fully damaged concrete and is driven by the equivalent strain  $\varepsilon_{eq}$  which is representative of a triaxial state

in a single variable. And since cracking is a result of a traction state, the introduced  $\varepsilon_{eq}$  defined from positive principal strains as following:

$$\varepsilon_{eq} = \sqrt{\sum_{i=1}^3 (\langle \varepsilon_i \rangle_+)^2} \quad (1.28)$$

where  $\varepsilon_i$  is the principal deformation in the direction  $i$ , and the operator  $\langle \varepsilon_i \rangle_+$  is defined in the following way:

$$\begin{aligned} \langle \varepsilon_i \rangle_+ &= \varepsilon_i \text{ if } \varepsilon_i > 0 \\ \langle \varepsilon_i \rangle_+ &= 0 \text{ if } \varepsilon_i < 0 \end{aligned} \quad (1.29)$$

The equivalent strain  $\varepsilon_{eq}$ , indicator of the tension state in the material, define the strain-based yielding surface as:

$$f = \varepsilon_{eq} - Y(D) \quad (1.30)$$

where  $Y(D)$  is the maximum between  $\varepsilon_{eq}$  and the damage threshold  $\varepsilon_{d0}$ , so that when  $f > 0$  damage occurs. The damage variable  $D$  is a combination of two modes:  $D_c$  and  $D_t$ , compressive and tensile variables respectively.

$$D = \alpha_t^\beta D_t + \alpha_c^\beta D_c \quad (1.31)$$

$\beta$  is a coefficient introduced to improve the model response to shear (usually equal to 1.06).  $\alpha_t$  and  $\alpha_c$  are two parameters calculated from the strain tensor ad which verify  $\alpha_t + \alpha_c = 1$ . For instance, in a pure tension state,  $\alpha_t = 1$  and  $\alpha_c = 0$  and vice versa in a pure compression state. The damage evolution law associated to  $D_t$  and  $D_c$  reads:

$$D_t = 1 - \frac{(1 - A_t)\varepsilon_{d0}}{\varepsilon_{eq}} - A_t e^{(-B_t(\varepsilon_{eq} - \varepsilon_{d0}))} \quad (1.32)$$

$$D_c = 1 - \frac{(1 - A_c)\varepsilon_{d0}}{\varepsilon_{eq}} - A_c e^{(-B_c(\varepsilon_{eq} - \varepsilon_{d0}))} \quad (1.33)$$

Where  $A_t$ ,  $A_c$ ,  $B_t$  and  $B_c$  are the parameters (to be identified) allowing the control of the post-peak behavior:  $A_t$  and  $A_c$  control the horizontal asymptote, while  $B_t$  and  $B_c$  control the slope respectively in tension and compression behaviors.

- **Strain partitioning** Mazars model states that the stress is given by the following:

$$\sigma = (1 - D)\mathbf{E}\varepsilon^e \quad (1.34)$$

where  $(1 - D)E$  is the rigidity of the material which undergoes a decrease when the damage  $D$  increases.  $\varepsilon^e$  is the elastic strain that is partitioned generally in terms of the total strain and other strain induced by chemo-thermo-hydro loadings and the visco-elastic nature of the material. In a simplified case, where only thermo-hydric loadings are considered, the elastic strain is decomposed as:

$$\varepsilon^e = \varepsilon - \varepsilon - \varepsilon^{th} - \varepsilon^{ds} \quad (1.35)$$

where  $\varepsilon^{th}$  and  $\varepsilon^{ds}$  are thermal and desiccation shrinkages respectively. The thermal shrinkage is considered proportional to the variation of temperature  $T - T_{ref}$  by a coefficient of proportionality  $\alpha_{th}$  also called coefficient of thermal dilation.

$$\varepsilon^{th} = \alpha_{th}(T - T_{ref})\mathbf{I} \quad (1.36)$$

The desiccation shrinkage can be modelled in the framework of porous media theory [Di Bella et al., 2016] or phenomenologically by considering its proportionality to the variation of water content. It can be expressed as:

$$\varepsilon^{ds} = \alpha_{ds}(C - C_{ref})\mathbf{I} \quad (1.37)$$

where  $\alpha_{ds}$  is the coefficient of desiccation shrinkage.

- **Regularization** To avoid mesh dependency that can lead to an incorrect response of the FE model, regularization techniques must be used. These techniques fall broadly into two approaches, a local and a non-local one. The former relies on the energy-based criterion to ensure an objective dissipation of the fracture energy through variable spatial discretization [Hillerborg, 1988]. This can be done in the case of Mazars' model by expressing the parameter  $B_t$ , controlling the post peak stress-strain curve shape, in function of the fracture energy [Sciame and Benboudjema, 2017]. In case of fine spatial discretization,  $B_t$  is usually approximated to:

$$B_t = \frac{f_t}{G_{ft}} h \quad (1.38)$$

where  $f_t$  is the tensile strength,  $G_{ft}$  is the fracture energy and  $h$  is the characteristic length. However, very recent findings showed that the hypothesis of constancy of the mode I fracture energy doesn't hold and that this quantity strongly depends on the crack-parallel normal stress [Bazant et al., 2020].

Another method of regularization can be done by the non-local approach such the one proposed in [Pijaudier-Cabot and Bazant, 1987]. In brief, it considers that the equivalent strain (or similar quantities) at any point must take into account the equivalent strain undergone by the neighborhood that falls in a zone defined by a characteristic length  $l_c$ , by the mean of an averaging weighting function  $\phi(\mathbf{x} - \mathbf{s})$ .

$$\varepsilon_{eq}(\mathbf{x}) = \frac{\int_{\omega} \phi(\mathbf{x} - \mathbf{s}) \varepsilon_{eq}(\mathbf{s}) d\mathbf{s}}{\int_{\omega} \phi(\mathbf{x} - \mathbf{s}) d\mathbf{s}} \quad (1.39)$$

The characteristic length  $l_c$  is usually taken 3 times the size of the material heterogeneity (biggest aggregate) and the weighting function is usually considered to be Gaussian.

- **Crack opening** Unlike the discrete approaches, based on fracture mechanics, that represent fractures explicitly; continuous approaches, based on damage mechanics, represent fractures by a global decrease of the stiffness of the material [Bouhjiti et al., 2018]. However, in these continuous approaches, the crack initiation must be triggered either by a weak element of the mesh or by a random distribution of the material properties using random fields [de Larrard et al., 2010]. On the other hand, regarding the crack propagation, the aforementioned regularization of the damage model ensures the objective dissipation of the fracture energy allowing therefore for a physically-based propagation. Obtaining a crack opening  $\delta$  at a certain FE of a characteristic size  $h$  relies on the knowledge of its strain field [Matallah et al., 2010]

$$\delta_{ij} = h_{EF} \varepsilon_{ij}^{uco} \quad (1.40)$$

where  $\varepsilon_{ij}^{uco}$  is the unitary crack opening strain representing the fracture strain (total strain minus the elastic one). This approach, being applicable for elasto-damageable concrete, has been extended recently to take into account the additional visco-elastic nature of the material (basic and desiccation creep) [Sciame and Benboudjema, 2017].

### 1.3.2.3 Permeability

In addition to the dependency of the permeability on the material thermal state [Drouet et al., 2015] and hydric state through the concept of relative permeability [Muallem, 1976] (more on those two effects in chapter 2), there exist a strong dependency on the material mechanical state, *i.e.*, the presence of micro and macro cracks. The total permeability of the system is a combination of two different flows: the first being through the material sound volume or which has undergone weak and diffused damage, noted Darcy permeability  $K_D$ . The second flow passing through the macro-fractures, noted  $K_F$ .

- **Permeability through sound or slightly-damaged cement-based porous medium** Many authors were interested in relating the permeability evolution in function of damage variable representative of a diffuse damage state in the material. *Bary* function is among the most used hydro-mechanical coupling laws that expresses the evolution of the permeability to damage as a power law [Gawin et al., 2002] :

$$k = k_0 \times 10^{A_D D} \quad (1.41)$$

where  $A_D$  is a fitting coefficient ranged between 1 and 4 [Dal Pont et al., 2005]. This function is used for a diffused damage situation (usually of thermal origins) in a range of validity between  $0.2 < D < 0.8$

but is commonly used over the whole domain. Another function, formulated as an isotropic exponential law, was suggested by [Picandet et al., 2001] and was found to fit well the experimental data in  $D < 0.15$  damage range. A slight variation was proposed by [Choinska et al., 2007] that used Maclaurin (Taylor) development of the exponential function around  $D = 0$  and which reads:

$$k = k_0 \times \left[ 1 + (\alpha D)^\beta + \frac{(\alpha D)^{2\beta}}{2!} + \frac{(\alpha D)^{3\beta}}{3!} \right] \quad (1.42)$$

where  $\alpha$  and  $\beta$  are fitting coefficients and depends on the type of concrete. A comparison of the different functions is shown in figure 1.19 in which ( $\alpha = 11.3$  and  $\beta = 1.64$ ) were used in [Picandet et al., 2001] function and ( $\alpha = 6.2$  and  $\beta = 1.7$ ) were used in [Choinska et al., 2007]. The function

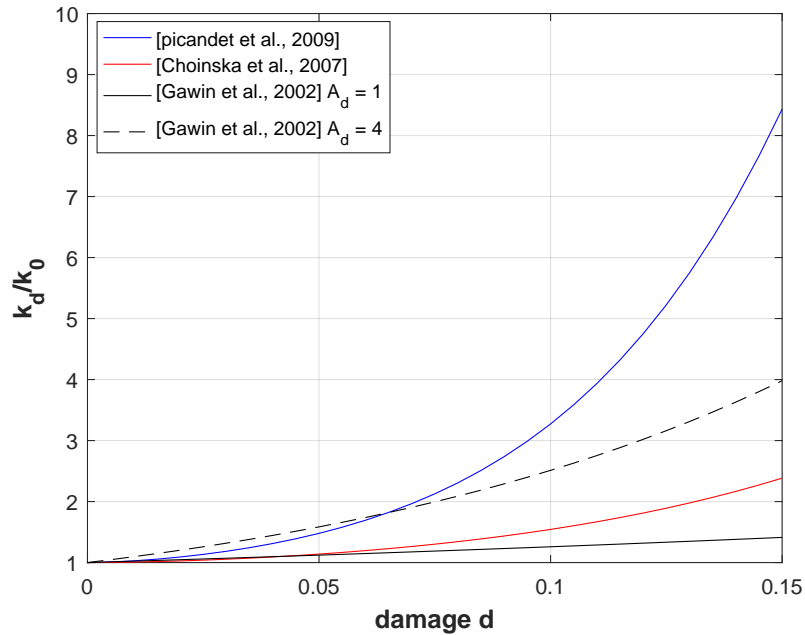


Figure 1.19: Comparison between commonly used hydro-mechanical coupling laws in case of weak diffused damage configuration.

being mathematically flexible and not physically-based formulated were found to fit a wide range of experimental data when appropriate fitting is used [El-Dandachy, 2016].

- **Permeability through macro-cracks** Once the damage level becomes significant ( $D$  close to 1), micro-cracks join together to form a macro-crack, in which the flow drastically increases. From a modeling point of view, the flow can be estimated by solving the Navier-Stokes equation in two smooth parallel plates. However, another factor representing the roughness of the crack must be added for sake of a better physical representativity. This roughness factor contribution depends on the crack opening: the smaller the crack, the bigger the impact of the roughness in resisting the flow [Rastiello et al., 2015]. The permeability through macro-crack, (also called [Poiseuille, 1840] permeability), reads:

$$k_F = \xi \frac{w_{ck}^3}{12h} \quad (1.43)$$

where  $\xi$  is the crack roughness,  $h$  is the characteristic length of the finite element and  $w_{ck}$  is the crack opening. It can be seen in figure 1.20 the permeability increase in function of the crack opening for different values of crack roughness.

Many models can be found in literature to reproduce the experimental measurements in both diffuse and localized cracking regimes, however, very few matching laws have been proposed to extrapolate the permeability value in between those two regimes [Choinska et al., 2007] [Pijaudier-Cabot et al., 2009] [El-Dandachy, 2016]. However, all the proposed laws consider a combination of the Darcy and Poiseuille permeability weighted differently by the damage variable. For instance, the matching law considered by [El-Dandachy, 2016] is expressed as:

$$K_{eq} = K_D^{(1-d)} K_F^d \quad (1.44)$$

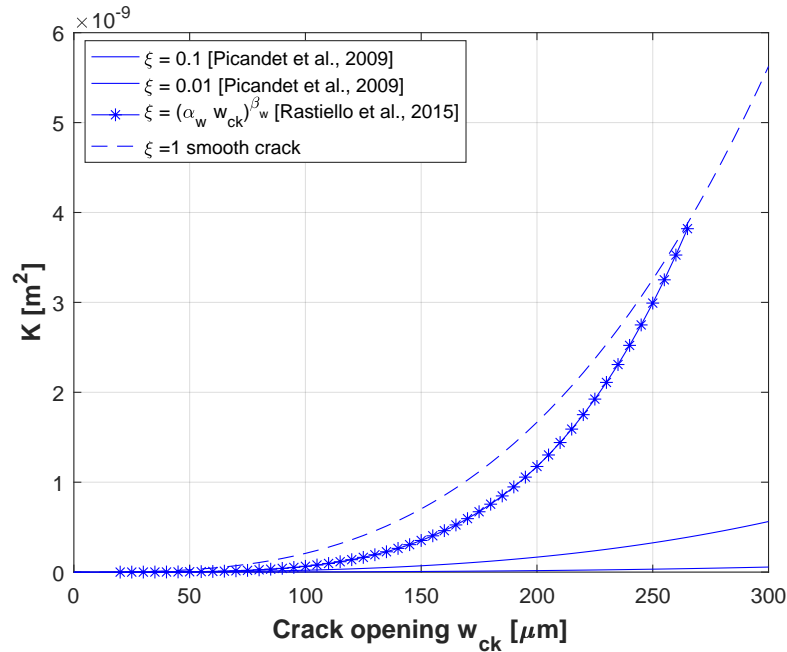


Figure 1.20: Permeability through macro-cracks having different crack opening accounting additionally to the effect of the cracking roughness.

This matching law has been validated to experimental data of a splitting test and provided a better fitting than other proposed matching law found in the literature. A generalized variation of this matching law has been proposed recently in [Bouhjiti et al., 2018] in order to take into account the unloading and the associated crack closure.

### 1.3.3 Mesoscopic modeling

Unlike macroscopic models that consider concrete as a homogeneous material, mesoscopic models take into account explicitly the mesoscopic morphological aspects. In fact, at this scale, aggregates and macro-pores are described in addition to the homogenized mortar phase made out of cement paste and sand fines. The various shapes and sizes of these heterogeneous components have a non-negligible effect on the stress field and the cracking patterns. In their turn, those cracking patterns contribute to thermo-hydric local variations such as an increase in the local permeability.

#### 1.3.3.1 Mesh generation

The generation of the meso-structure is a key component in any mesoscopic model and exists in the literature under different variations. The most famous approach consists of considering concrete as a bi-phase material accounting for the presence of aggregates idealized as perfect disks/spheres. Those disks/spheres can have random sizes and distribution within the mortar matrix [Dauti, 2018] or can be generated respecting a previously assigned particle size distribution curve [Nguyen, 2010].

The second mesh generation approach consists of projecting the phase-separated meso-structure (characterized by an imaging technique for instance) on a regular FE mesh. This method was used many times in literature where each voxel of a 3D x-ray image was mapped (after being segmented and compressed) to an element of the mesh [Huang et al., 2015][Yang et al., 2019].

The third approach consists of projecting the phase-separated meso-structure on an unstructured mesh. However, this method is only adapted for E-FEM simulations taking advantage of kinematic enhancements [Stamati et al., 2018].

The different meshing approaches and their corresponding phases separation are illustrated in figure 1.21.

#### 1.3.3.2 Application of mesoscopic modeling in the literature

Nearly all the mesoscopic models in literature take into account only the mechanical effect of the explicit consideration of aggregate inclusions. The work of Laborderie [La Borderie and Menou, 2007] compared the

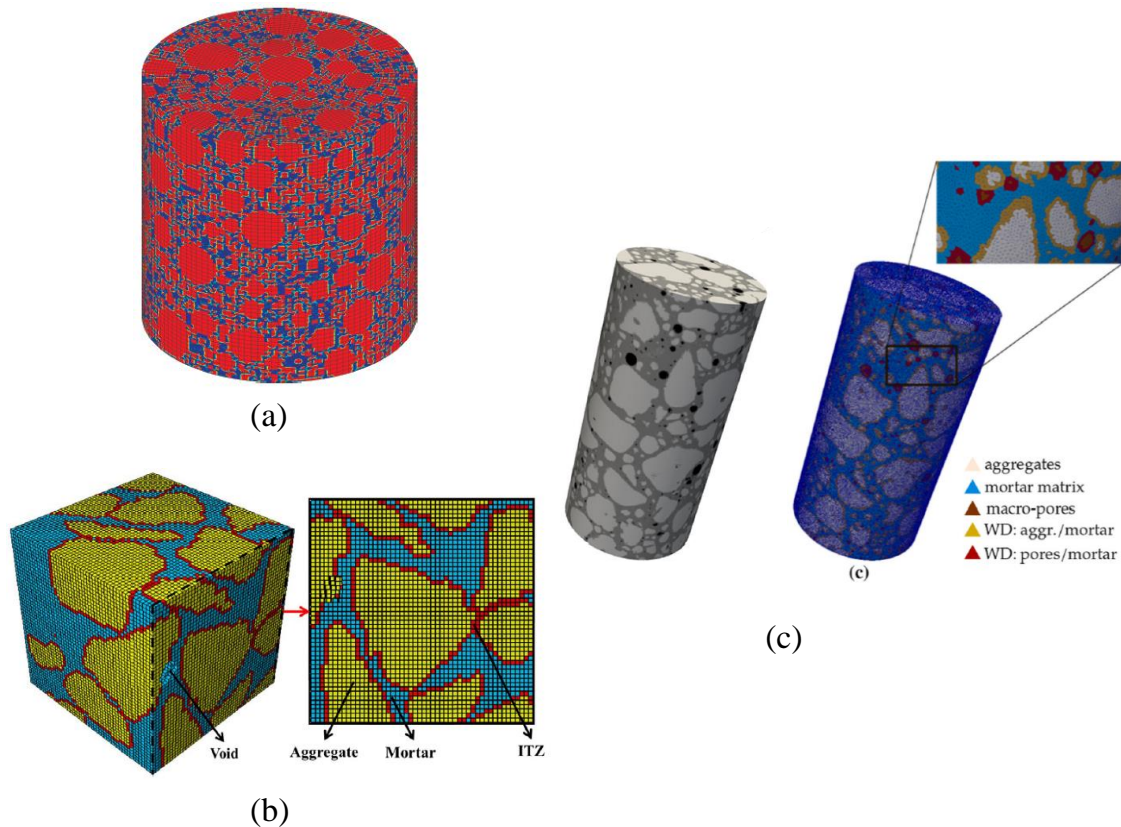


Figure 1.21: Three different approaches in generating concrete mesostructure: (a) perfect sphere particles respecting the particle size distribution [Nguyen, 2010], (b) FE structured mesh taking into account 4 material phases (aggregates, mortar, void and ITZ) identified thanks to x-ray tomography [Huang et al., 2015], (c) Projection of a 3D segmented x-ray image on an unstructured mesh used to perform E-FEM mechanical simulations [Stamati et al., 2018].

effect of real meso-structure to the equivalent idealized one in 2D. The idealization of the particle topology induced different patterns of cracking under compressive loading but was found to have a negligible effect when tensile loading was applied. [Huang et al., 2015] generated a 3D meso-concrete mesh taking into account the macro-pores, the aggregates and the ITZ, based on an XCT image. Using the concrete damage plasticity model, quantitative validation of the load-displacement curve was done and qualitative comparison of the fracturing processes was compared to the x-ray observations. Similarly, [Stamati, 2020] performed mechanical simulation of a concrete sample at the meso-scale using E-FEM model under tensile, compressive and triaxial loading. A full field comparison was performed between the strain field provided by the model and those provided by digital volume correlation (DVC).

Conversely, few works in the literature investigated the effect explicit aggregates consideration when thermal and hydraulic loadings are applied. [Xotta et al., 2015] investigated the contribution of spherical aggregates in damaging the surrounding mortar in high-temperature conditions. However, in addition to neglecting the effect of real aggregates morphology, the hydraulic model used in there considers only the liquid phase, neglecting therefore the important role of gas pressure at high temperature. Finally, [Dauti et al., 2018a] modeled a single aggregate concrete sample using a multiphase thermo-hydro-mechanical model. The behavior laws and the boundary conditions were calibrated, so that the water content field predicted by the model matched with the full-field measurements acquired by neutron tomography.

Different types of concrete mesoscopic simulations are illustrated in figure 1.22. The literature is still lacking the development of a fully-coupled multiphase THM model which takes into account the meso-structure morphological aspects.

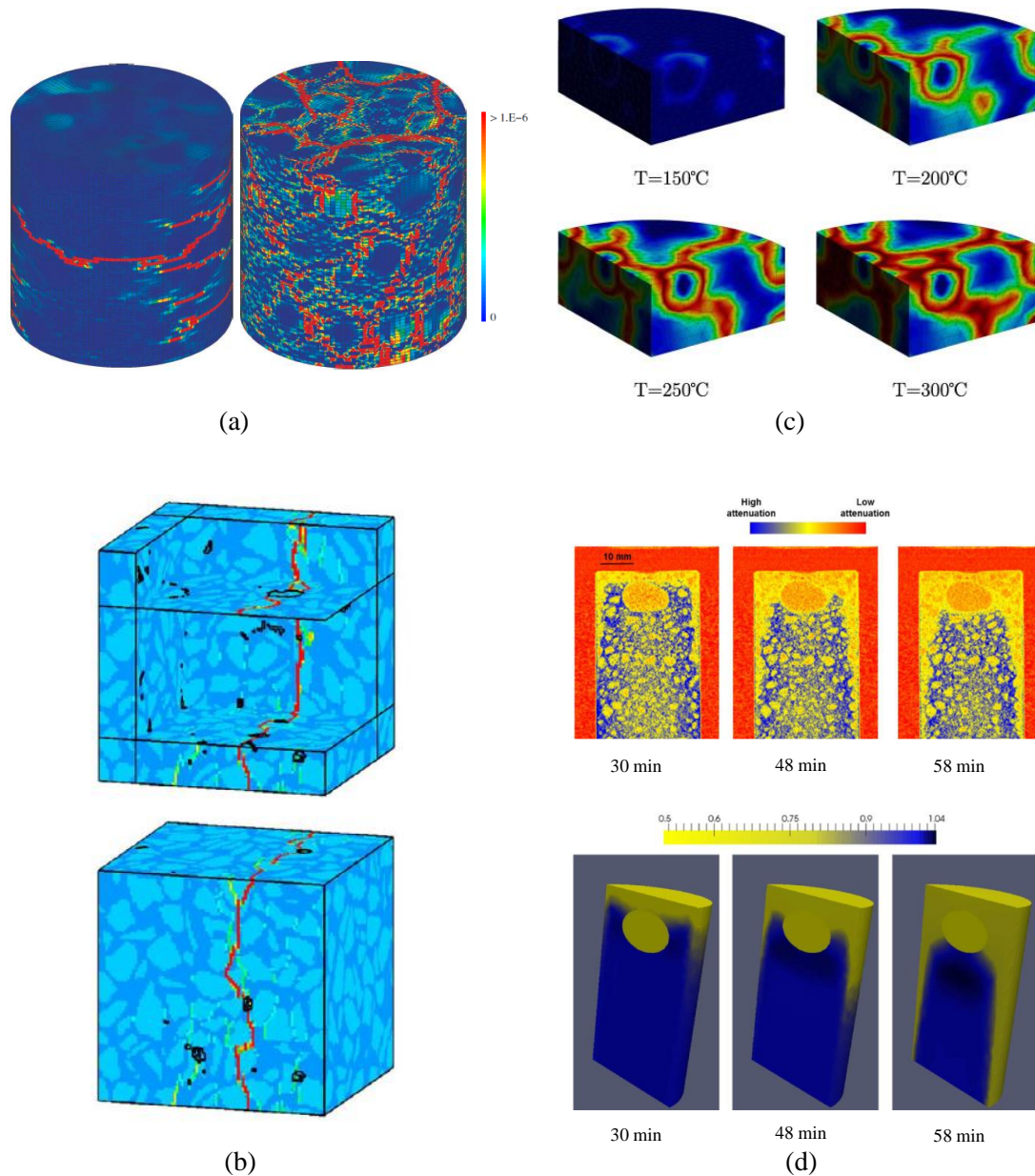


Figure 1.22: Different type of concrete mesoscopic simulations: (a) Crack opening field of a meso-concrete with spherical aggregates submitted to tensile (left) and compressive (right) mechanical loading, adapted from [Nguyen, 2010]; (b) Crack opening field of a meso-concrete having its meso-structure projected from a 3D x-ray image, adapted from [Huang et al., 2015]; (c) damage field resulting from a thermo-hydro-mechanical simulation of a meso-concrete with spherical aggregates, adapted from [Xotta et al., 2015]; (d) Water content fields obtained resulting from a multiphase thermo-hydro-mechanical simulation of a homogenized concrete with a single aggregate calibrated to 3D neutron tomography, adapted from [Dauti et al., 2018a]

## 1.4 Summary of the literature review

Drying of cement-based materials combines a multitude of coupled physical processes when submitted to thermo-hydro-mechanical loading. The classical experimental techniques employed to study these processes provides only bulk-averaged and point-wise measurements which are not sufficient to characterize the spatially variable and local processes such as the developments of hydric gradients between the core and the exposed surface of the material and the effect of cracking on the local moisture transport. However, full-field measurement techniques and particularly x-ray and neutron tomography allow for the characterization of both cracking and moisture spatio-temporal evolution in cement-based materials. The literature review done

on the use of these two techniques revealed a wide range of applications to study the moisture transport in cracked and heated cement-based materials, however, no application was yet done to study the environmental drying-driven processes. For that, two experimental campaigns were proposed in this PhD (Chapter 2 and 3) which focus on the contribution of neutron/x-ray tomography on the drying characterization of cement-based porous media.

On the other hand, the literature review done on the modeling of THM behavior of cement-based materials showed a wide range of modeling choices which simplifies the simulation framework by neglecting the gaseous transport modes, the TH and HM couplings and the true morphology of the material. The implications of these simplifications are assessed in Chapter 1 and in the appendices of this manuscript, each by setting appropriate modeling framework.

## Chapter 2

# Influence of common simplifications on the drying of cement-based materials up to moderate temperatures

### Paper context:

*The environmental drying of cement-based materials occurs in variable ranges of relative humidity and temperatures. However, to model the drying-related processes in these materials, many modeling choices were possible. In fact, the literature review on the use of numerical modeling to simulate the thermo-hydro-mechanical behavior of cement-based materials shows a discrepancy regarding the sophistication of the model physical description and the consideration of thermo-hydric dependencies. This inconsistency is illustrated by:*

- **The use of different types of TH models: complete vs. simplified:** *Since complete TH models require heavy numerical implementations and are computationally demanding, many authors have used simplified models, i.e., models which simplify the physical description of moisture transport by neglecting the presence of gaseous fluid species and their transport mechanisms. This model choice was often justified by unverified hypotheses which states that the gas pressure remains constant during drying processes.*
- **The consideration of negligence of the impact of temperature on hydraulic properties:** *Many studies in literature neglected the evolution of hydraulic properties such as permeability and desorption isotherm in function of temperature [Pesavento, 2000][Gawin et al., 2002], while other studies accounted for this dependency [de Moraes et al., 2009][Davie et al., 2018].*

*Many studies in the literature have evaluated the importance of the gaseous transport mechanisms in several cement-based materials [Mainguy et al., 2001][Thierry et al., 2007], however, no study has shown yet the impact of temperature and relative humidity on the evolution of those gaseous transport processes. Besides, no study has evaluated yet the effect of considering or neglecting the temperature impact on the hydraulic properties. The following work presents an evaluation of these common simplification impact on the drying modeling of cement-based materials up to moderate temperature. In addition, this study provides enough elements to drive the decision-making on what model to choose in different drying environments and what level of sophistication of physical description is required regarding the complex thermo-hydric behavior laws.*

### Authors:

Hani Cheikh Sleiman, Matthieu Briffaut, Stefano Dal Pont, Alessandro Tengattini and Bruno Huet.

### Paper Status:

Accepted in *International Journal of Heat and Mass Transfer*.

## Abstract

The drying of cement-based materials affects directly their durability, which has a major financial/societal impact. Notably, the variation of saturation of the porous network as well as drying shrinkage are fundamental processes since they drive together cracking and the penetration rate of aggressive chemicals. Many macroscopic models describe the moisture transport within porous media. They can be broadly divided into two main categories: multiphase macro-models which take into account the presence of three fluid phases (liquid water, vapor and dry air), and simplified models considering less phases under the main assumption of constant gas pressure during the drying process. Moreover, the choice of different behavior laws, which describe different evolutions of desorption isotherms, relative permeability, permeability to liquid water in function of temperature, has a major impact on mass loss amount and kinetics. Quantification of these simplifications effects regarding the used model and the choice of behavior laws was done by comparing mass loss response surfaces in a relative humidity and temperature space for multiple configurations. The results show relative error maps at early, mid and late drying stages for every compared case.

## 2.1 Introduction

The durability and structural serviceability of cement-based materials are directly linked to the penetration of aggressive agents into the concrete. The penetration rate is mainly governed by the saturation of the porous network and the presence of cracks. A key role is therefore played by concrete drying, which controls the saturation, which in its turn provokes shrinkage and thus potentially cracks. After casting, the concrete hygrometry is higher than the external environmental one. This non-equilibrated state induces the migration of water from the porous medium outwards. Consequently the material undergoes drying shrinkage which can be restrained, not only by the aggregates (if any), but also by the core of the element which will remain saturated for a longer time. This restraint will lead to stress generation, that will compete with the material strength and which may lead to cracking. Given the impact of this inevitable phenomenon, it is important to accurately assess the implications of the modelling assumptions regarding moisture transport phenomena within the cement-based materials.

Considered as a porous medium, a sufficient description of cement based material in a drying study is done by describing it as a material having a solid skeleton and an interconnected porosity filled with free liquid water, adsorbed water, vapor and dry air. Many progressions were done in the modeling of heat and moisture transfer in porous media. One of the earliest examples of a macroscopic model describing water transfer in porous media is the one of [Philip and Vries, 1957][Philip, 1958] who adopted Darcy's law to describe water flow in the medium, justifying this choice by means of direct experimental observations. It is observed that the permeability of the system decreases rapidly as a function of the water content. This evolution is justified through an analogy to a set of cylindrical tubes, whose permeability decreases as a function of the square of the radius. This causes the larger pores to dry before the smaller ones, creating interruptions in the interconnected porous network. In [Bazant and Najjar, 1972] the drying process is simulated by assuming that the evolution of the water content can be described through non-linear diffusion equation. The model proposed by [Benet, 1981] is instead based on the thermodynamics of irreversible processes. Herein the gaseous phase is seen as composed by dry air and water vapour. The equilibrium between liquid water and vapour is controlled by pressure, temperature and humidity, which determine a critical vapour content, described through the maximal adsorption value. [Daian, 1986] [Daian, 1987] describe the fundamental processes of water and gaseous transfers in isothermal conditions. Unlike the previous works this is not described through viscous Darcy law, whose applicability for particularly small pores is questionable. This is instead described by free molecular diffusion, accounting for Knudsen effect, which is more appropriate for elongated pores whose diameter is comparable to the mean free path of the particles. These considerations result in an expression for vapor effusion. [Moyné, 1987] is one of the first works to consider the gaseous flow under the pressure gradient caused by the discrepancy between environmental and sample conditions. In this work the description of the flow accounts for multiple gas phases in non-isothermal conditions. In the work of [Wang and Beckermann, 1993] [Wang and Cheng, 1996], the different fluid phases are averaged into one in order to reduce the number of equation to solve. In [Mainguy et al., 2001], two models are compared: The first, simplified model, is based on the hypothesis that the gas pressure remains constant within low permeable media. The second one, multiphase model, takes into account the presence of three fluid phases. It was shown that the liquid water permeation was the dominant transport mechanism at long term drying. However, an over-pressure of the gaseous phase was put in evidence and which takes several weeks to dissipate in certain configurations. It was therefore shown that, in order to capture the same mass loss kinetics by the

two models, different values of intrinsic permeability should be used. Numerical solutions of different software packages for one dimensional benchmark cases were provided in [Hagentoft et al., 2004]. Participants had to solve the same set differential equations, each one using its own method (FEM, FDM, FVM) together with slightly different meshing choice and numerical accuracy. Reasonable consensus results were found (comparable to analytical solution when provided) and the accuracy of existing HAM-software (Heat, Air and Moisture) which participated was controlled. [Gawin et al., 2006a] [Gawin et al., 2006b] proposed a fully coupled hygro-thermo-chemo-mechanical model that describes the different physical processes at the macro scale and explore their implications on the material state. [Thiery et al., 2007] introduced new laws for gas transfers regarding the diffusion coefficient of vapor in function of saturation and porosity and regarding regarding the relative permeability to gas. Then, a similar comparison to that of [Mainguy et al., 2001] was done using a multiphase model and two different types of simplified models (detailed in section 4). The comparison of the models output were discussed and the contribution of each transfer mode is quantified. In [de Moraes et al., 2009] a comparison was done of two thermo-hydro-mechanical models that differs by the fact that one relies on one conservation equation including both liquid water and vapor, while the second model relies on two conservation equations including in addition dry air. Both models were able to reproduce experimental observation of a concrete cylinder heated up to 200°C. A comparative analysis of the importance of darcyan and fickean processes in both models was then performed. [Bary et al., 2012] enhanced the multiphase model proposed in [Bary et al., 2008] by implementing a new behavior law of the water desorption isotherms as a function of temperature.

On the other hand, regarding the effect of temperature on hydric properties, Recent experimental campaigns were done in [Poyet, 2009][Drouet, 2010]. They consisted of measuring the effect of temperature on water retention isotherms at 20°C, 50°C and 80°C and for a range of different relative humidities, controlled by the used type of salt [O'Brien, 1947] [Greenspan, 1977]. The measurements were acquired once the hydric equilibrium is considered to be reached for concrete and cement paste respectively studied in the two aforementioned recent studies. In [Drouet et al., 2015] a simplified numerical model was proposed to estimate, by inverse analysis, the effect of moderate temperatures on permeability, which would be cumbersome by direct measurement in partially saturated porous media.

To summarize, macroscopic models describing water transfer in porous media can be broadly classified in two categories: simplified models, which relies on the constant gas pressure hypothesis and the multiphase models accounting for the presence of all the fluid species of interest with their individual transfer modes. Thermal effects on hydric properties should be taken into account since drying can happen at moderate temperatures regardless of the site conditions.

This paper propose a strategy to extrapolate the comparative study of simplified and multiphase models up to moderate temperatures and for a full range of possible relative humidity. It also quantifies the impact of common simplifications regarding the taking into account of the temperature effect on hydric properties. In this work, we start by outlining the governing equations of the multiphase model in Section 3. Then, in section 4, the underlying assumptions of possible modeling simplifications are presented together with the the ensuing governing equation of the used simplified model in this study. Afterwards, well established constitutive laws are detailed, and different modelling choices used by different authors are discussed in section 5. The implementations done within the multiphase model (here used as reference model) are then validated at moderate temperatures in section 6. Finally, in section 7, a comparison between the predictions of the multiphase and simplified models as well as the effect of the various constitutive laws on the global mass loss response are presented and discussed.

## 2.2 Multiphase Thermo-Hydric modeling

### 2.2.1 Derivation of mass and energy conservation equations

The multiphase model adopted in this work relies on macroscopic equations derived from Hybrid Mixture Theory [Hassanizadeh and Gray, 1979a] [Hassanizadeh and Gray, 1979b] [Hassanizadeh and Gray, 1980] which were first applied to geomechanics in [Lewis and Schrefler, 1998].

Within the framework of mass and heat transfer in partially saturated porous media, a mathematical description of the conservation of all the existing entities in the system has to be done. A conservation equation can be formulated as:

$$\frac{\partial}{\partial t} density + \nabla \cdot flux = source(orsink) \quad (2.1)$$

The rate of change of the density of a quantity, plus the flux diverging from its boundaries must be equal to the production/intake from any internal source/sink.

This general formulation can be applied to mass, and specifically to the mass of the species existing in cementitious porous media: liquid water, water vapor and dry air. The three corresponding equations are then:

$$\frac{\partial m_l}{\partial t} + \nabla \cdot (m_l v_{l-s}) = -\dot{m}_v \quad (2.2)$$

$$\frac{\partial m_v}{\partial t} + \nabla \cdot (m_v v_{g-s}) + \nabla \cdot (m_v v_{v-g}) = \dot{m}_v \quad (2.3)$$

$$\frac{\partial m_a}{\partial t} + \nabla \cdot (m_a v_{g-s}) + \nabla \cdot (m_a v_{a-g}) = 0 \quad (2.4)$$

where  $m_\pi$  is the mass of the  $\pi$  specie,  $\pi$  being  $s$ ,  $l$ ,  $v$  or  $a$  respectively, solid, liquid water, vapor or dry air.  $v_{\pi-\pi'}$  describes the relative velocity of the specie  $\pi$  with respect to the  $\pi'$  one. The mass of the different species are expressed in terms of density  $\rho_\pi$ , porosity  $\phi$  and liquid saturation rate  $S_l$ .

$$m_s = (1 - \phi)\rho_s \quad (2.5)$$

$$m_l = \rho_l S_l \phi \quad (2.6)$$

$$m_v = \rho_v (1 - S_l) \phi \quad (2.7)$$

$$m_a = \rho_a (1 - S_l) \phi \quad (2.8)$$

The relative velocity of liquid and gas species with respect to the solid skeleton is expressed using Darcy's law:

$$v_{g-s} = -K \frac{k_{rg}}{\mu_g} \nabla p_g \quad (2.9)$$

$$v_{l-s} = -K \frac{k_{rl}}{\mu_l} \nabla p_l \quad (2.10)$$

Where, for the  $\pi$  specie,  $\mu_\pi$  is the dynamic viscosity,  $\nabla p_\pi$  is the gradient of pressure,  $k_{r\pi}$  is the relative permeability.  $K$  represents the intrinsic permeability of the system.

Diffusion which describe the velocity of a certain liquid or gas specie  $\pi$  with respect to another liquid or gas specie  $\pi'$ , is described by Fick's law:

$$j_v = -\rho_g D \nabla \left( \frac{\rho_v}{\rho_g} \right) = -j_a \quad (2.11)$$

where  $j_\pi$  is the diffusion flux of a substance  $\pi$  and  $D$  is the diffusivity coefficient. Accounting for all transfer modes, the mass fluxes of the different species can be summed up in the following equations.

$$m_l v_{l-s} = -K \frac{\rho_l k_{rl}}{\mu_l} \nabla p_l \quad (2.12)$$

$$m_v v_{g-s} + m_v v_{v-g} = -K \frac{\rho_v k_{rg}}{\mu_g} \nabla p_g - D \rho_g \frac{M_v M_a}{M_g^2} \nabla \left( \frac{p_v}{p_g} \right) \quad (2.13)$$

$$m_a v_{g-s} + m_a v_{a-g} = -K \frac{\rho_a k_{rg}}{\mu_g} \nabla p_g - D \rho_g \frac{M_v M_a}{M_g^2} \nabla \left( \frac{p_a}{p_g} \right) \quad (2.14)$$

Regarding energy conservation, general macroscopic conservation equation of a multi-phase medium accounts for heat rate stored within the system, conductive and convective heat flows and finally the heat variations resulting from phase changes.

$$\rho C_p \frac{\partial T}{\partial t} + (m_l C_l v_{l-s} + m_g C_g v_{g-s}) \cdot \nabla T + \nabla \cdot (-\lambda \cdot \nabla T) = -H_{vap} \dot{m}_{vap} \quad (2.15)$$

where  $\rho C_p$  is the volumetric heat at constant pressure,  $C_\pi$  is the heat capacity of the  $\pi$  specie,  $\lambda$  is the thermal conductivity,  $H_{vap}$  is the enthalpy of vaporization, that can be considered as the amount of energy required to transform liquid water to vapor and finally,  $\dot{m}_{vap}$  is the vapor mass source.

### 2.2.2 Final form equations

Writing explicitly the mass in function of density, porosity and saturation rate, and velocities as expressed in Darcy's and Fick's law, and expressing the densities' change rate in function of the depending primary variables using chain rule, the final form conservation equation of the dry air, vapor and liquid water and energy can be written as:

Dry air:

$$(1 - S_l)\phi\left(\frac{\partial\rho_a}{\partial T}\frac{\partial T}{\partial t} + \frac{\partial\rho_a}{\partial p_c}\frac{\partial p_c}{\partial t} + \frac{\partial\rho_a}{\partial p_g}\frac{\partial p_g}{\partial t}\right) - \rho_a\phi\left(\frac{\partial S_l}{\partial T}\frac{\partial T}{\partial t} + \frac{\partial S_l}{\partial p_c}\frac{\partial p_c}{\partial t}\right) + (1 - S_l)\rho_a\frac{\partial\phi}{\partial T}\frac{\partial T}{\partial t} - \nabla \cdot \left(K\frac{\rho_a k_{rg}}{\mu_g}\nabla p_g - D\rho_g\frac{M_v M_a}{M_g^2}\nabla\left(\frac{p_a}{p_g}\right)\right) = 0 \quad (2.16)$$

Water species:

$$(S_l\rho_l - (1 - S_l)\rho_v)\frac{\partial\phi}{\partial T}\frac{\partial T}{\partial t} + S_l\phi\frac{\partial\rho_l}{\partial T}\frac{\partial T}{\partial t} + \phi(\rho_l - \rho_v)\left(\frac{\partial S_l}{\partial T}\frac{\partial T}{\partial t} + \frac{\partial S_l}{\partial p_c}\frac{\partial p_c}{\partial t}\right) + (1 - S_l)\phi\left(\frac{\partial\rho_v}{\partial T}\frac{\partial T}{\partial t} + \frac{\partial\rho_v}{\partial p_c}\frac{\partial p_c}{\partial t} + \frac{\partial\rho_v}{\partial p_g}\frac{\partial p_g}{\partial t}\right) - \nabla \cdot \left(K\frac{\rho_l k_{rl}}{\mu_l}(\nabla p_g - \nabla p_c)\right) - \nabla \cdot \left(K\frac{\rho_v k_{rg}}{\mu_g}\nabla p_g - \nabla \cdot \left(D\rho_g\frac{M_v M_a}{M_g^2}\nabla\left(\frac{p_a}{p_g}\right)\right)\right) = 0 \quad (2.17)$$

Energy:

$$\rho C_p\frac{\partial T}{\partial t} - K\left((C_l\frac{\rho_l r_l}{\mu_l}(\nabla p_g - \nabla p_c) + C_g\frac{\rho_v r_g}{\mu_g}\nabla p_g)\right) \cdot \nabla T + \nabla \cdot (-\lambda \cdot \nabla T) = -H_{vap}\dot{m}_{vap} \quad (2.18)$$

Using finite element method, the weak form of the equations (16),(17) and (18), which were derived in [Lewis and Schrefler, 1998], [Pesavento, 2000], are spatially discretized. The numerical implementation was done in a monolithic fashion during the work of both [Sciumè, 2013][Sciumè et al., 2013] for chemo-hydro-thermo-mechanical modeling of concrete at early age, and by [Dauti, 2018] for thermo-hydro-mechanical modeling of concrete at high temperature. The monolithic approach was proven to be 10-20 times faster than the initial staggered approach used by [Dal Pont et al., 2011]. The temporal discretization was done using the theta-method numerical integration scheme [Bathe and Wilson, 1972]. Finally, it is important to mention that the model in its current form captures only thermo-hydral mechanisms related to long-term behavior of cement-based materials. Therefore, no early-age mechanisms effects (related to hydration reaction), such as self-heating or self-desiccation were taken into account. In addition, no thermo-mechanical or hydro-mechanical couplings were considered.

## 2.3 Simplified modeling

There exist two types of simplified models that are widely used in literature and they can be both derived from the multiphase model described above. The first type relies on two assumptions. The gas pressure is considered to remain equal to the atmospheric pressure: In terms of magnitude, this pressure is much smaller (in absolute value) than the liquid pressure (around 96 MPa) in partially saturated concrete medium at ambient temperature. In addition, local pressure built ups are considered to dissipate quasi-instantaneously within the system. The second assumption considers the Darcyan flow of gas negligible compared to the diffusive one. Mathematically, this can be modelled as a single diffusion differential equation:

$$\left(\phi\frac{\partial S_l}{\partial t}\right) - \nabla \cdot [(D_l + D_v)\nabla S_l] = 0 \quad (2.19)$$

Where  $D_l$  is the "liquid water diffusivity" and  $D_v$  is water vapor diffusivity and they are expressed as follow:

$$D_l = \frac{K_l k_{rl}}{\mu_l} \frac{dp_c}{dS_l} \quad (2.20)$$

$K_l$ ,  $k_{rl}$  and  $\mu_l$  are respectively the intrinsic permeability, the relative permeability and the dynamic viscosity of liquid water.

$$D_v = \frac{D}{p_v} \left(\frac{\rho_v}{\rho_l}\right)^2 \frac{dp_c}{dS_l} \quad (2.21)$$

where  $D$  is the diffusivity factor,  $p_v$  is the vapor pressure,  $\rho_v$  is the vapor density and  $\rho_l$  is the liquid water density.

The second type of simplified model relies on an additional assumption which considers the liquid permeation as the dominant water transport mechanism and that phase transformation happens only at the surfaces exposed to the environmental conditions. Equation (19) simplifies into:

$$\left(\phi \frac{\partial S_l}{\partial t}\right) - \nabla \cdot [(D_l) \nabla S_l] = 0 \quad (2.22)$$

We note that the primary variable in these two models can be any of the following parameters: capillary pressure  $p_c$ , saturation rate  $S_l$ , relative humidity  $h_r$  or water content  $C$ , since the relations between these parameters are well established either by Kelvin law [ $p_c, h_r$ ], Van Genuchten law [ $S_l, p_c$ ] or by direct porous media transition [ $S_l, C$ ].

The second simplified model, which represents the liquid permeation as the dominant transport mechanism, is often written in terms of capillary pressure in the literature. The differential equation is written as follow:

$$\left(\phi \frac{\partial S_l}{\partial p_c}\right) \frac{\partial p_c}{\partial t} - \nabla \cdot \left(\frac{K k_{rl}(S_l(p_c))}{\mu_l}\right) \nabla p_c = 0 \quad (2.23)$$

By analogy to heat differential equation, one can name  $\left(\phi \frac{\partial S_l}{\partial p_c}\right)$  the hydric capacity and  $\left(\frac{K k_{rl}(S_l(p_c))}{\mu_l}\right)$  the hydraulic conductivity. This model is the one used in this comparative study. Equation (23) is discretized using the FE software Castem2017 under the heat module accounting for the non-linear hydric conductivity term which depends on capillary pressure solution. The temporal discretization is done using theta-method scheme.

## 2.4 Constitutive equations

The classical constitutive equations for gas density, vapor pressure, saturation vapor pressure, liquid water density, species viscosity and the enthalpy of vaporization are listed in the Annex.

### 2.4.1 Modeling choices

The classical [Genuchten, 1980] formulation is adopted to obtain a consistent data-set in the expression of desorption isotherms and relative permeability. The desorption isotherm family equation reads:

$$S_l(P_c) = \left[ \left( -\frac{P_c}{a} \right)^{\frac{1}{1-b}} + 1 \right]^{-\frac{1}{b}} \quad (2.24)$$

The parameters  $a$  and  $b$  are the fitting parameters. These parameters values depend on the material formulation and the temperature. Recently, the evolution of the desorption isotherms in function of temperature varying between  $20^\circ C$  and  $80^\circ C$  has been put in evidence by [Drouet et al., 2015]. Therefore, there is a need to include the effect of temperature in isotherms formulation in the case of modeling the behavior of cementitious material in non-isothermal conditions. This was recently done by [Davie et al., 2018], who took temperature effect in an indirect way by accounting for its effect on porosity, surface tension and permeability. This formulation relied on the work of [Leverett, 1941]: While trying to extrapolate capillary pressure data between rock types that differ in permeability, porosity and wetting properties, [Leverett, 1941] showed that there exist an empirical relationship between capillary pressure and water saturation. The dimensionless function that was found is called Leverett J-function and is expressed as follow:

$$J(S_l) = \frac{P_c(S_l)}{\gamma_0} \sqrt{\frac{K_0}{\phi_0}} \quad (2.25)$$

where the square root term is considered as a hydraulic characteristic length of the capillary radii.

Inspired by Leverett's work, [Davie et al., 2018] extrapolated the aforementioned function to higher temperatures, in order to get a temperature-dependant set of isotherms. The capillary pressure as a function of temperature and saturation reads:

$$P_c(S_l, T) = J(S_l) \gamma(T) \sqrt{\frac{\phi(T)}{K(T)}} \quad (2.26)$$

The final expression of saturation can be expressed as follow:

$$S_l(P_c, T) = \left[ \left( -\frac{1}{a} \cdot P_c \frac{\gamma_0}{\gamma(T)} \sqrt{\frac{\phi_0}{K_0}} \sqrt{\frac{K(T)}{\phi(T)}} \right)^{\frac{1}{1-\frac{1}{b}}} + 1 \right]^{-\frac{1}{b}} \quad (2.27)$$

Porosity of cementitious materials remains constant for moderate temperature  $\phi(T) = \phi_0$  (less than  $100^\circ C$ ) [Tenchev et al., 2001]. The temperature dependence of the surface tension  $\gamma(T)$  is well-known (e.g. IAPWS-95 formulation - The International Association for the Properties of Water and Steam). The permeability to liquid water function  $K(T)$  is suggested by [Drouet et al., 2015] (back-calculation of permeability from mass loss curves). In a more condensed way, Davie's isotherms has been derived from Van Genuchten's one with the parameter  $a = a(T)$  and  $a(T)$  is expressed as follow:

$$a(T) = a \frac{\gamma(T)}{\gamma_0} \sqrt{\frac{K_0}{\phi_0}} \sqrt{\frac{\phi(T)}{K(T)}} \quad (2.28)$$

For sake of a clearer presentation, the evolution of the isotherms in function of temperature is shown in relative humidity - liquid water saturation  $[h - S_l]$  space where  $S_l$  reads:

$$S_l(h, T) = \left[ \left( -\frac{1}{a} \cdot R_v T \rho_l(T) \ln(h) \frac{\gamma_0}{\gamma(T)} \sqrt{\frac{\phi_0}{K_0}} \sqrt{\frac{K(T)}{\phi(T)}} \right)^{\frac{1}{1-\frac{1}{b}}} + 1 \right]^{-\frac{1}{b}} \quad (2.29)$$

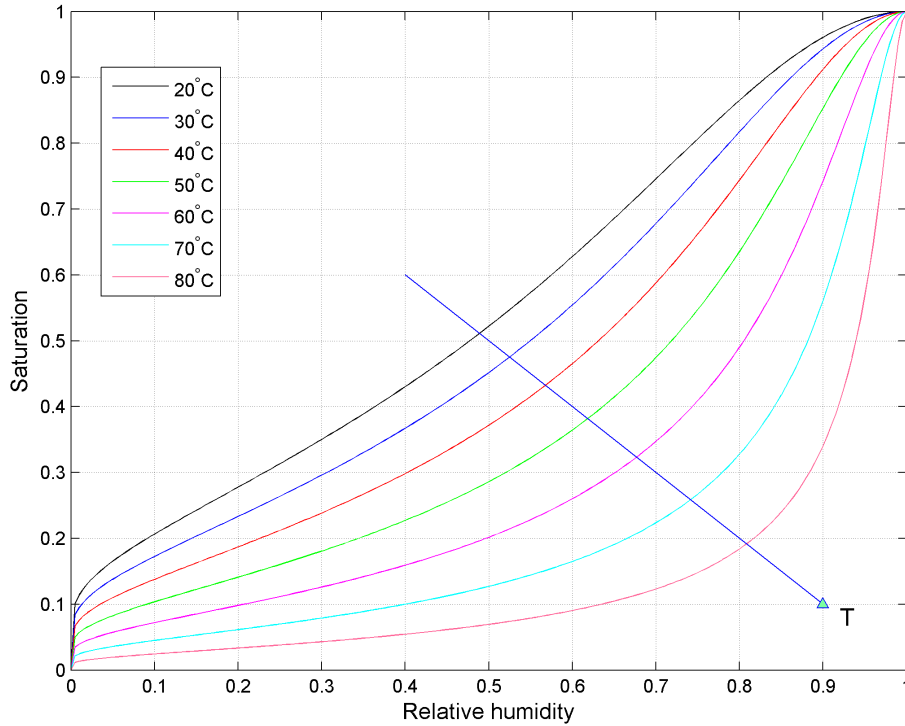


Figure 2.1: Desorption isotherm's evolution in function of temperature

As for the derivatives, the derivative of  $S_l$  in function of  $p_c$  reads:

$$\frac{\partial S_l}{\partial p_c} = \frac{\frac{1}{b}}{\left(\frac{1}{b} - 1\right)a(T)} \left(\frac{|p_c|}{a(T)}\right)^{\frac{1}{1-\frac{1}{b}}-1} \left[ 1 + \left(\frac{|p_c|}{a(T)}\right)^{\frac{1}{1-\frac{1}{b}}} \right]^{-1-\frac{1}{b}} \quad (2.30)$$

This relation is needed to be explicitly written for the simplified model where it appears in the hydric capacity term.

The evolution of the permeability liquid water in function of temperature used in this study was taken, as

mentioned, from [Drouet et al., 2015] inverse analysis since direct measurements are extremely difficult to be done for partially saturated porous media. One can put in question the use of the simplified model to fit the mass loss experimental data at moderate temperature by fitting the permeability values. However, the authors justify this choice by the fact that the fitting process was done only at 85% relative humidity external condition, meaning that the transport mechanisms related to vapor and dry air are neglected in the porous medium.

$$K_w^{int}(T) = K_0 * \left( \exp \left( \exp \left( \left( \frac{T - T_0}{T_c} \right) - 1 \right) \right) \right) \quad (2.31)$$

It is worth noting that this permeability function is not valid for higher sets of temperature (higher than 80°C) since it predicts non-physical permeability values due to its double exponential formulation.

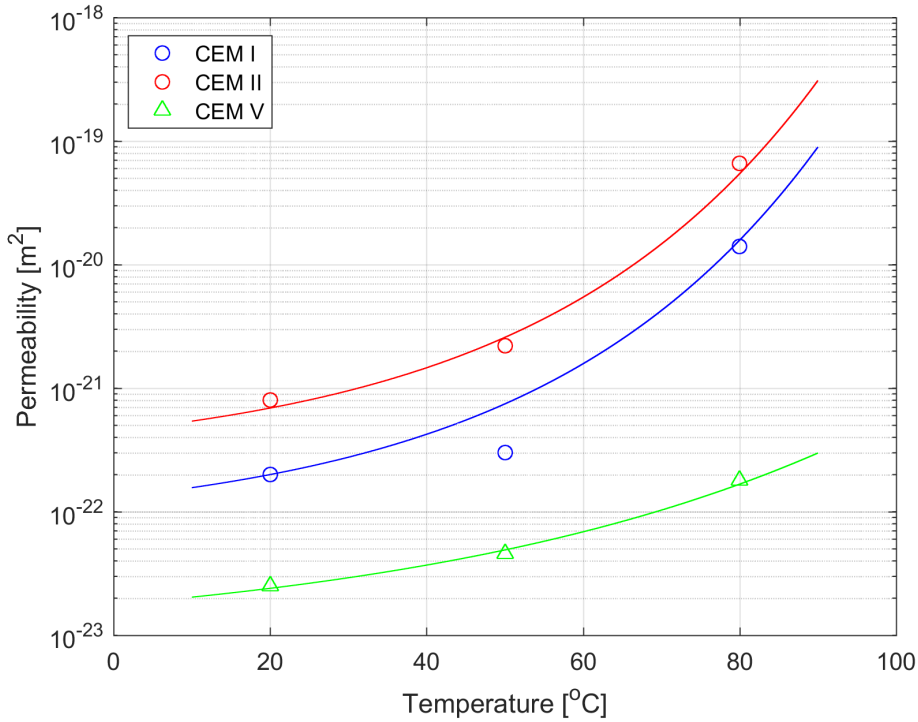


Figure 2.2: Drouet's permeability evolution in function of temperature ( $T_c = 35.7$ )

The use of a more complete model in this study may help to validate or not the choice of using the simplified model to characterize the evolution of permeability in function temperature.

The relative permeability formulation used is as well the one of [Genuchten, 1980] where it is expressed in function of  $S_l$ , thus depending on the same two fitting coefficients [a, b]. The higher the temperature is, the lower the value of  $S_l$  ( $a = a(T) \neq cte$ ) at equilibrium and the lower the relative permeability to liquid water (and the higher the relative permeability to gas). Therefore, these two parameters  $K_{rl}$  and  $K_{rg}$  are key parameters in controlling the drying kinetics.

$$K_{rg} = \sqrt{1 - S} \left( 1 - S^b \right)^{2/b} \quad (2.32)$$

$$K_{rl} = \sqrt{S} \left( 1 - \left( 1 - S^b \right)^{1/b} \right)^2 \quad (2.33)$$

As for the behavior laws that are only used for the multiphase model, [Perre and Degiovanni, 1990] proposes an evolution of vapor diffusivity into dry air in function of temperature and gas pressure.

$$D_{va}(T, p_g) = D_{v0} \left( \frac{T}{T_0} \right)^{B_v} \frac{p_{g0}}{p_g} \quad (2.34)$$

Where  $D_{v0} = 2.58 \times 10^{-5} m^2 s^{-1}$  is the diffusion coefficient at ambient condition and  $B_v = 1.667$ . The effect of liquid water saturation and the tortuosity of the porous network is taken into account in an effective diffusivity parameter  $D$  [Dauti, 2018]:

$$D = (1 - S_l)^{A_v} \phi \tau D_{va}(T, p_g) \quad (2.35)$$

where  $A_v$  is a constant having a value usually between [1 and 3], and  $\tau$  is the tortuosity factor expressed as:

$$\tau(\phi, S_l) = \phi^{1/3} (1 - S_l)^{7/3} \quad (2.36)$$

## 2.5 Multiphase model validation up to moderate temperature

The model has been validated multiple times at low temperature [Meftah et al., 2012] and at high temperature [Dal Pont et al., 2007] [Dauti et al., 2018b]. This section is dedicated to validate the newly implemented procedures meant to capture thermo-hydral aspects of cement-based materials at moderate temperature. The experimental campaign main results showed in [Drouet, 2010], consists of mass loss data set for different cement types at almost full range of relative humidity and at three different temperatures  $20^\circ C$ ,  $50^\circ C$  and  $80^\circ C$ . Comparing the experimental results to the reference multiphase TH model is of a great interest, especially since the permeability to liquid water evolution in function of temperature used function is the one back-calculated by [Drouet et al., 2015] using the simplified model. The use of the multiphase model allows to test the simplification hypothesis especially in the case when the external conditions are  $[80^\circ C, 85\%RH]$ . Samples are initially considered saturated, Dirichlet-type boundary conditions are applied on the mesh shown in Figure 3.

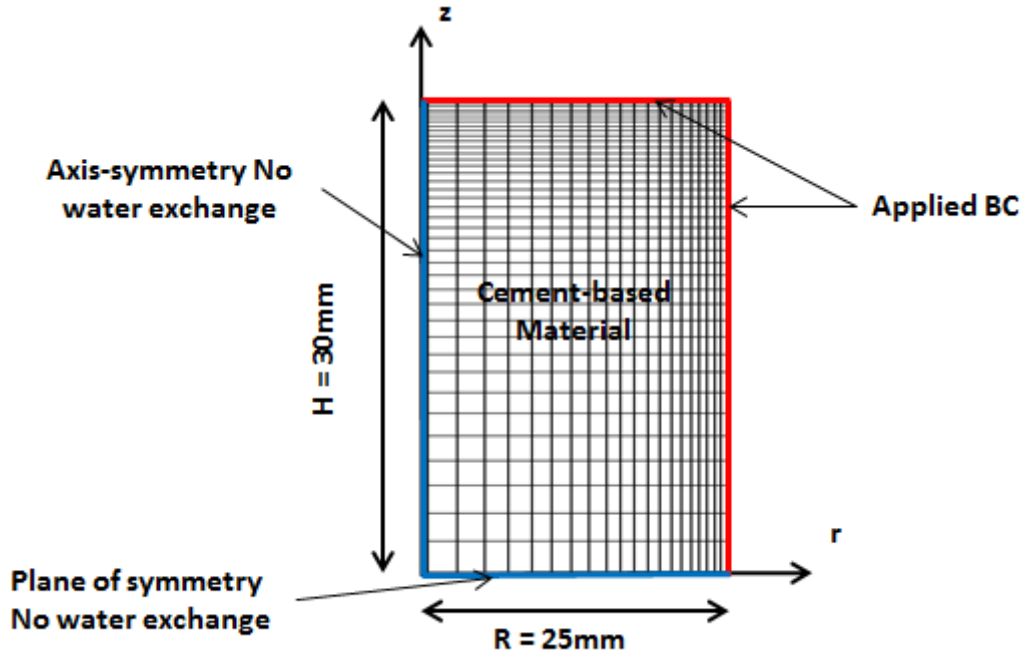


Figure 2.3: Geometry, mesh and thermo-hydral boundary conditions applied in the validation simulation

The choice of behavior laws used in this simulation are the Drouet back-calculated double exponential permeability function, and Van Genuchten type of isotherms with different couplet of fitting coefficient depending on the external relative humidity and temperature conditions. The same input parameters and behavior laws belonging to the first cement type CEM 1 of the reference study were used. Concerning the boundary conditions, constant temperature and relative humidity were applied on the top and lateral surfaces, even though the relative humidity in the drying environment was reported to be saturated for 12 days, the effects seem to be corrected for on the experimental mass loss curves.

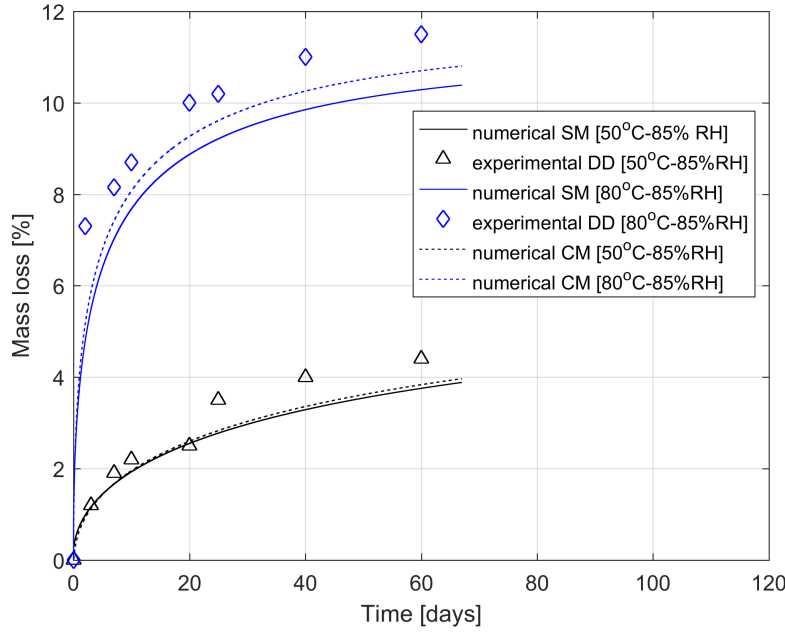


Figure 2.4: Validation of the model at moderate temperature

The numerical mass loss curve have the same trend as the experimental data. However, a slight under estimation (about 0.5%) can be seen between the two results and this can be due to two reasons. First, the samples which are put to dry at  $80^{\circ}\text{C}$  have more porosity than the averaged value given by [Drouet et al., 2015], which give the first uncertainty on the initial amount of water existing in the porous media. The second reason may be coming from the use of the permeability function back-calculated is actually slightly under-fitting the mass loss experimental data. However, the assumption made by [Drouet et al., 2015] by using the simplified model at such a high temperature ( $80^{\circ}\text{C}$ ) but at high relative humidity, is validated. The contribution of other transport mechanisms is negligible.

## 2.6 Different models and behavior laws consequences on drying response

The main strategy proposed in this numerical study consists of considering four sets of simulations covering wide-range of moderate temperatures and environmental relative humidity, in order to reply to two major needs:

1. The need to test the limit of the simplified models and its simplification hypothesizes over moderate temperature domain.
2. The need to clarify the effect of temperature on both permeability and isotherms and their influence on the drying response, since there is a tendency to underestimate this impact and to use no evolving functions for moderate temperature domain. The first reference set of simulations was done using the multiphase model while the three others were done using the monophasic model. These later three sets are different considering their used behavior laws. In the first monophasic set, all the hydric properties evolve in function of temperature (intrinsic, relative permeability and desorption isotherms) while in the other two sets some evolutions were shut down (no evolutions were considered in the second monophasic set. Intrinsic permeability was the only evolving parameter in the third monophasic set). Each set includes 84 simulations in order to cover all different combinations of temperature and relative humidity ranging respectively from  $20^{\circ}\text{C}$  to  $80^{\circ}\text{C}$  and from 30%RH to 85%RH

### 2.6.1 Geometry, mesh, initial conditions and Boundary conditions

The specimen consists of a cylinder of  $2[\text{cm}]$  diameter and  $6[\text{cm}]$  of height of the CEM 1 material type [Drouet et al., 2015]. Indeed, drying duration depends on the sample's geometry. However, the analysis can be sort of temporally "normalized" by using the expressions: early-drying stage, mid-drying stage and late-drying

stage for whatever sample geometry. However, for sake of minimizing the computational time cost, it has been modeled taking advantage of the axisymmetry and the plane symmetry existing (figure (5)). The mesh used for these simulations consists of a degraded mesh going from 1 mm to 0.2 mm in the  $+r$  direction, and from 2 mm to 0.2 mm in the height direction, as seen in the same figure. For both models, hydric boundary conditions (thermo-hydric in case of multiphase model) are applied as Dirichlet type boundaries by imposing a capillary pressure obtained by inverse analysis of the Kelvin-Laplace having both external temperature and relative humidity.

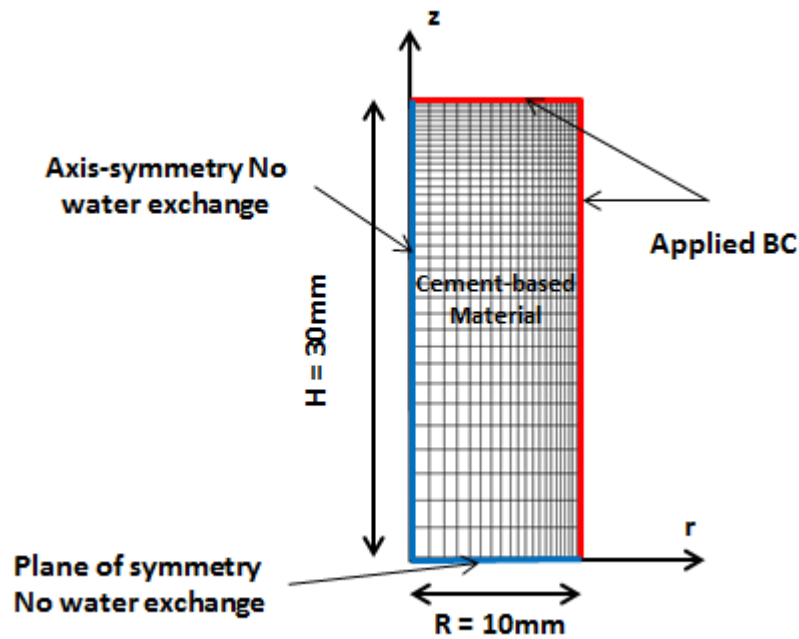


Figure 2.5: Geometry, mesh and boundary conditions for the comparative analysis

Initially, for all simulations, the sample is considered to be fully saturated. Dirichlet type boundary conditions was chosen as not to include additional exchange variables that affect the drying kinetics of the system.

## 2.6.2 Results: mass loss response surfaces

While some intermediate results are shown in the Annex (gas pressure, capillary pressure and saturation fields), the result of interest which is the mass loss surface response is shown in this paragraph. Indeed, comparing these intermediate results are of great importance. For instance, capillary pressure maps are strongly linked to drying shrinkage and therefore to the cracking probability of the material. In addition, saturation maps are strongly linked to carbonation/corrosion problems. However, due to the number of parameters involved and the non-representativity of these quantities in 2D maps, these quantities were not investigated into.

The mass loss surface response evolution in function of time is presented at 3 instants of interest: early-drying stage: 15 days (figure 6)(a), mid-drying stage: 50 days (b) and final-drying stage: 365 days (c). The 3D surfaces are shown as filled contour maps and results are condensed in subplots showing:

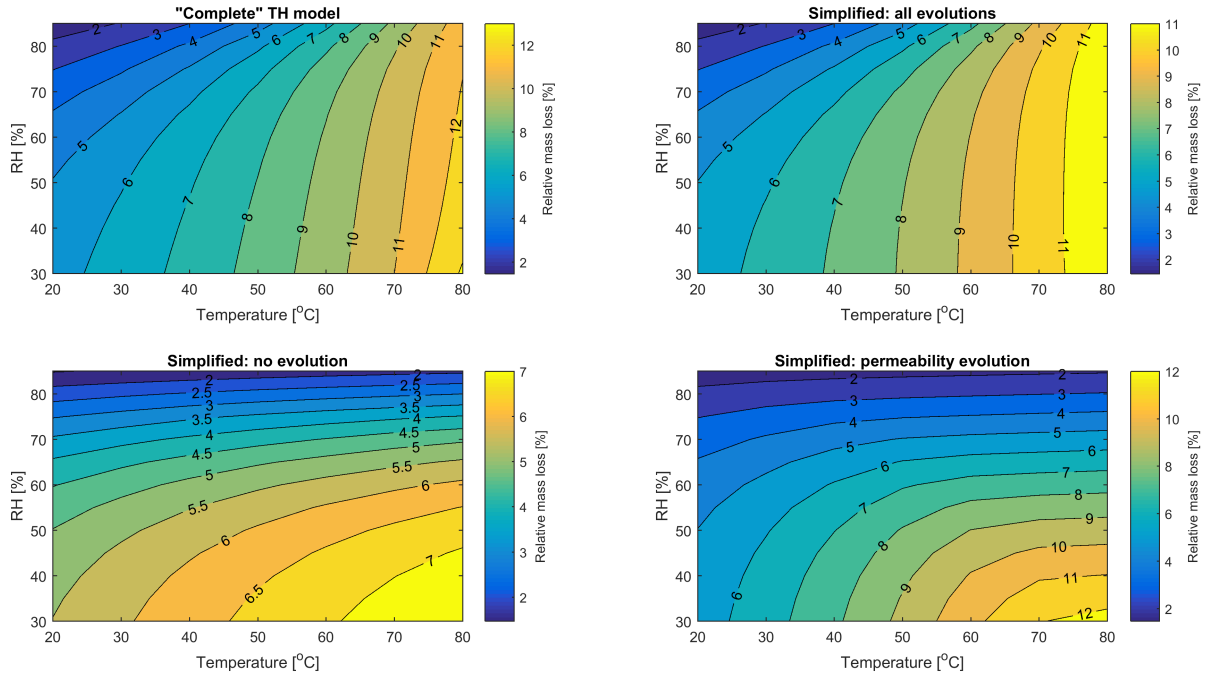


Figure 2.6: Relative mass loss response surfaces for four different cases (listed in table 1) at (a) early-drying stage, (b) mid-drying stage and (c) late-drying stage.  
(a) 15 days

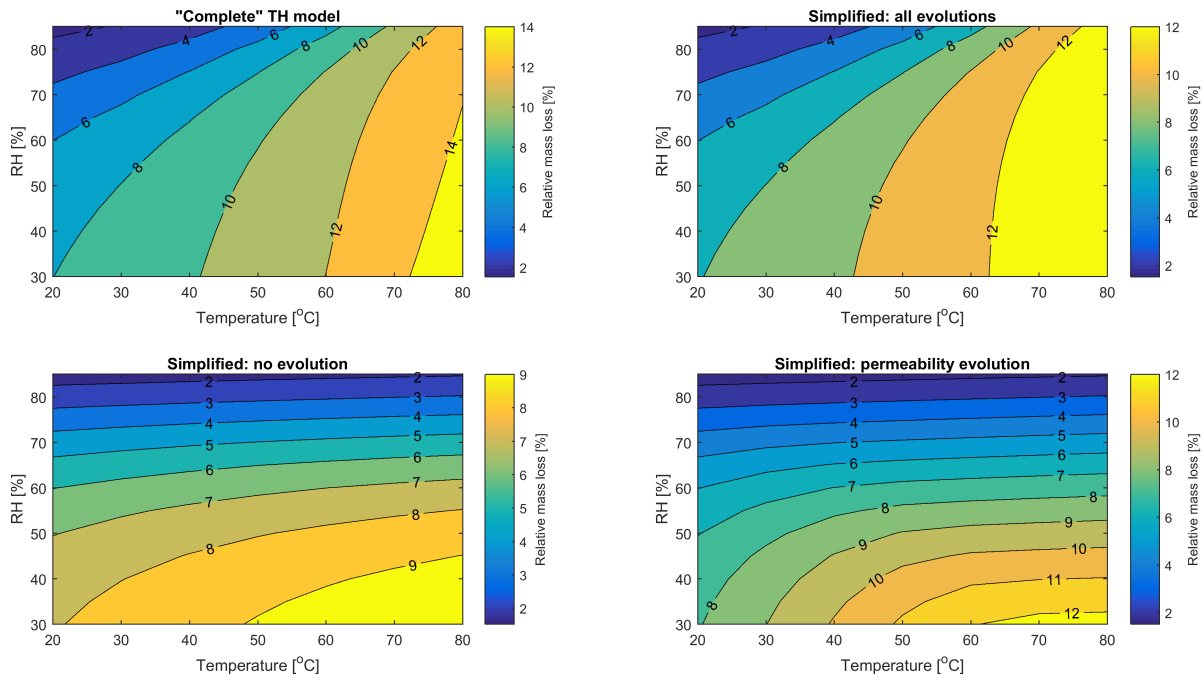
Table 1 resume the model and behavior laws used in each set of simulations resulting each a mass loss subplot.

On the top left, the response surface of the relative mass loss in  $[T, RH]$  space resulting from the set of

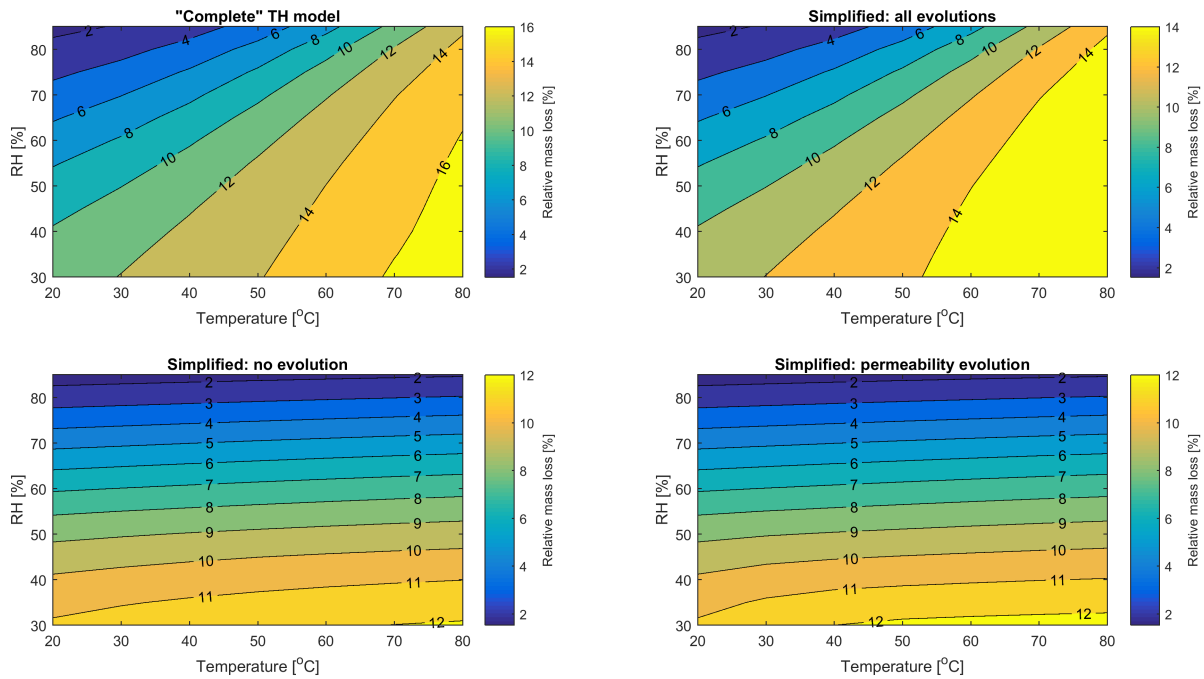
Subplot	Used model	$[K_l, S_l \ \& \ K_{rl}] = f(T)$
Top left	Multiphase	✓
Top right	Simplified	✓
Bottom left	Simplified	✗
Bottom right	Simplified	✓ (except $S_l \ \& \ K_{rl}$ )

Table 2.1: Table resuming the model and behavior laws used for each subplot.

simulations performed by the multiphase TH model is shown at 15 days. On top right, the surface response resulting from the set of simulations performed by the simplified model taking into account the evolution of isotherms, relative permeability and permeability to liquid water in function of temperature (viscosity and water density evolves in all the cases). Bottom left plot shows the surface response resulting from the set of simulations performed by the simplified model but where no evolution of isotherms, relative permeability and permeability to liquid water with respect to temperature are taken into account. Finally, on bottom left, the results show the surface response resulting from the set of simulations performed by the simplified model with permeability to liquid water evolving in function of temperature (isotherms and relative permeability don't evolve).



(b) 50 days



(c) 365 days

The multiphase TH model shows always a higher mass loss compared to the simplified model on the whole [RH-T] domain. Figure 8 shows that the hydic equilibrium is established at a 16 [%] mass loss. Using this 2D representation  $[t, \Delta m]$ , it can be shown, that even in the extreme hydic boundary conditions and after a year of drying, the simplified model doesn't reach equilibrium when all the behavior laws are evolving in function of temperature. The reason behind the non-equilibrium reaching is the very small value of relative permeability for liquid water. While simplified models with no evolutions and with permeability evolution shows similar response surfaces after 365 days, their responses at early and mid drying stages are not comparable (different kinetics).

## 2.6.3 Discussion: relative error maps

### 2.6.3.1 Transfer modes impact

It is apparent from Figures 7 to 9, that the assessment of the implications of the different models and laws described above is not straightforward. For that, relative errors subplots are drawn in order to facilitate the comparison between these 4 modeling cases. Their comparison can be done following three approaches. One possible method is to plot relative error maps which are computed as the difference of the mass loss maps, then divided by the one with the highest values. The compared cases are summarized in table 2.

	Used model		$[K_l, S_l \& K_{rl}] = f(T)$	
	Model 1	Model 2	Model 1	Model 2
Case 1	Multiphase	Simplified	✓	✓
Case 2	Simplified	Simplified	✓	✗
Case 3	Simplified	Simplified	✓(except $S_l \& K_{rl}$ )	✗

Table 2.2: Table resuming the compared cases: the used model and the behaviour law choices.

The first case concerns the comparison of the multiphase TH model and the simplified model with all the evolutions of the hydric properties in function of temperature. Mainly, what is to be quantified in this case is the influence of the rigorous description of the hydric phases in the multiphase model. As described in the equations listed in section 3, the multiphase model describes the presence of vapor and dry air, the change of phases as well as their flow and diffusion within the porous medium under pressure and relative pressure gradients. The evolution of the relative error shows the zone affected by the model use is situated between  $50^\circ\text{C}$  and  $30\%$  relative humidity and  $80^\circ\text{C}$  and  $60\%$  relative humidity. The relative error is at its highest at mid drying stage and not at early stage due to kinetics effects nor at late stage due to the capacity of the porous medium to retain water. However, to explain this, one should recall that the multiphase model is able to reach faster the hydric stability since it has additional two transfer modes for both vapor and dry air phases (Darcy's and Fick's modes), and that's not the case for the simplified model which takes much more time in order to approach the asymptotic relative mass loss value. At an early drying stage, the dominating transfer mode is Darcy's one for liquid water, and that explains why the relative error map is not maximal at the beginning. However, with lower hydric gradients, the effect of the other transfer modes starts to appear leading to a faster water evacuation. On the other hand, the time needed by the simplified model to reach the hydric equilibrium can be explained due to the effect of relative permeability which is a function of the Van Genuchten parameter  $a(T)$  in the  $S_l$  term, giving a very low value of  $k_{rl}$  and resulting thus in a higher water evacuation resistance of the porous medium. This could be clearly presented in a 2D mass loss curve in function of time (plotted for each model at a fixed temperature and relative humidity). The extreme case, the one corresponding to  $80^\circ\text{C}$  and  $30\%$  relative humidity is the one taken to better present the case.

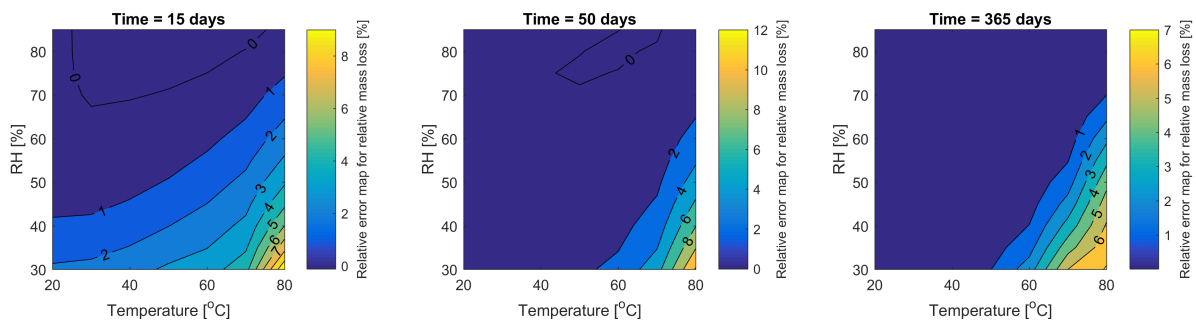


Figure 2.7: Multiphase model vs. simplified with all the hydric properties' evolutions in function of temperature relative error maps at 15, 50 and 365 days respectively

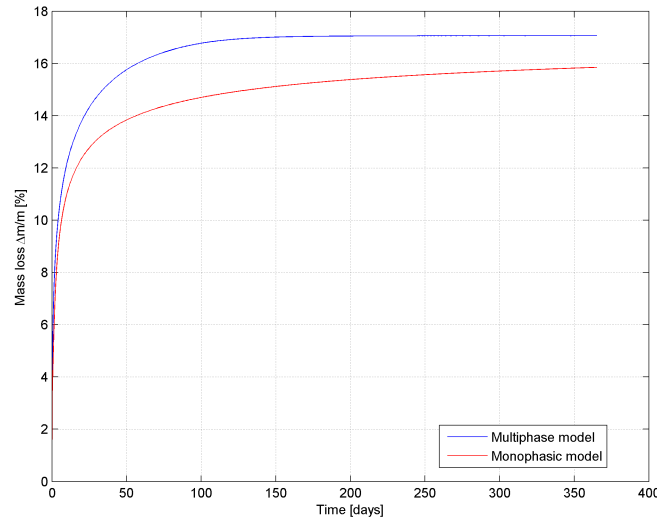


Figure 2.8: Multiphase model vs. simplified with all the hydric properties' evolutions in function of temperature mass loss evolution at 30%RH and 80°C

One should not forget to mention at the end that an important influential parameters on this comparison is the gas diffusivity coefficient that might change the time needed by the multiphase model to reach the hydric equilibrium with the external environment.

### 2.6.3.2 Desorption isotherms, relative permeability and permeability to liquid water evolution in function of temperature choice impact

The second case concerns the comparison of the simplified model with all hydric properties evolutions and the simplified model with no evolution of water retention curves and permeability in function of temperature (viscosity and liquid water density are evolving in function of temperature in both models). This comparison is of major importance since it investigates into the common simplification that considers no evolution of water retention curves when temperatures are below 100°C (see for instance [Pesavento, 2000]). In addition, in these simulations, the intrinsic permeability assigned as a model parameter is the one to water.

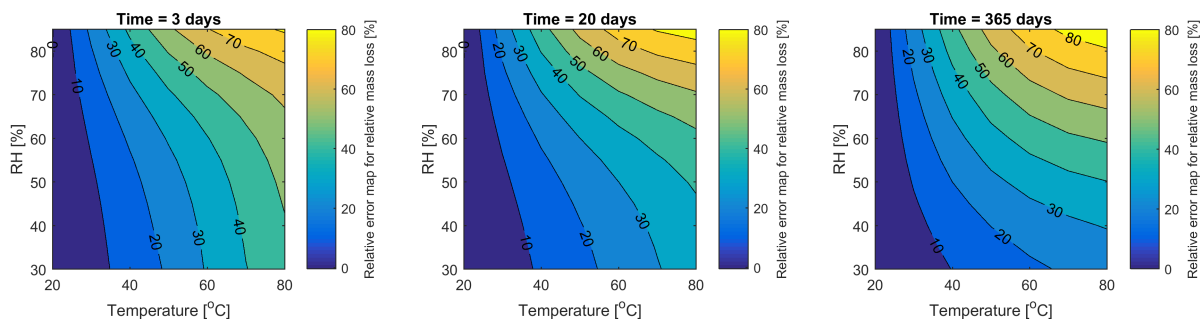


Figure 2.9: Simplified model with all the hydric properties' evolutions in function of temperature vs. Simplified model with no hydric properties evolutions relative error map at 3, 20 and 365 days respectively.

As shown in the figure 9, water retention curve evolution in function of temperature is not taken into account, and without considering the early stage, where drying kinetics are very high if the permeability evolution in function of temperature is taken into account, mass loss error results can reach 80%. The highest error is done in the high temperature - high relative humidity zone and is due mainly to the strong non linearity of the isotherms curves in the 85%-100% relative humidity range as seen in figure 1. This is mainly due to the difference of drying kinetics between the two models (Permeability evolving or not in function of temperature). The lower the relative humidity and the temperature are, the higher is the time that will be taken by the sample to approach hydric equilibrium with its environment.

### 2.6.3.3 Permeability to water evolution in function of temperature impact

In order to quantify the effect of constant permeability assumption in range of moderate temperatures, two sets of simulations were considered (case 3 in table 2). The same model was used in both sets (simplified model) as well as for behavior laws, except for the permeability where in one set it is considered to be constant whereas in the other it is evolving in function of temperature.

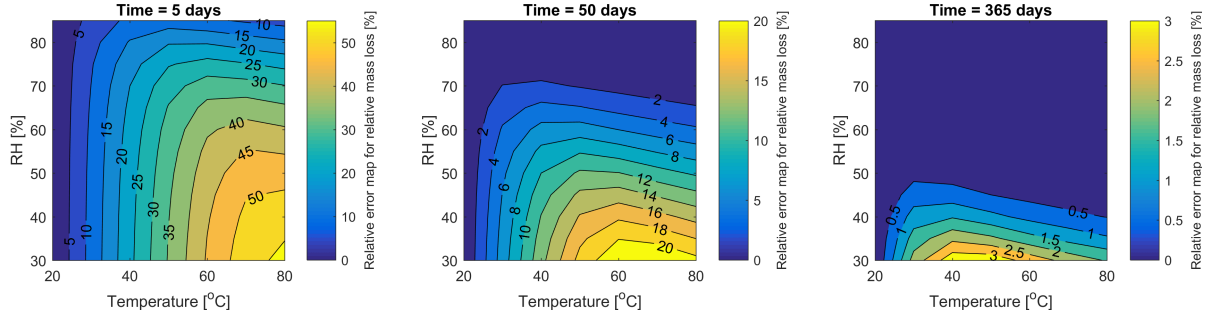


Figure 2.10: Simplified model with only permeability evolutions in function of temperature vs. Simplified model with no hydic properties evolution (except density and viscosity) relative error maps at 5, 50 and 365 days respectively.

Three relative error maps at three different times of interest are presented in Figure 10. As expected, the drying kinetics, which are at their fastest at the early stages of drying are not caught when permeability doesn't evolve with temperature, leading to higher errors. This error reduces with time, since for both set of simulations, the same desorption isotherm curve is used. It follows that all mass loss curves will tend to approach the same asymptotic value that depends only on the imposed external relative humidity. The isoles are inclined (for a constant relative humidity) so that at higher temperatures they reach hydic equilibrium faster. This could be explained by the fact that for the simplified model with no evolution of the permeability, the kinetics depends only on water density and viscosity. The higher the temperature is, the lower the values of density and viscosity are; and the lower these values are, the faster the hydic equilibrium is reached.

## 2.7 Conclusion

The influence of common simplifications on the modelling of drying of cement-based materials up to moderate temperatures was studied in this article. These simplifications can be divided into 2 main categories: 1- model simplification, when the flows of the three fluid phases of interest are not all described by the governing equations. 2- modeling choices simplifications, when the impact of temperature on the evolution of some hydic properties (mainly water retention curves, relative permeability and permeability to liquid water) are/aren't all taken into consideration. Four different set of simulations were performed using the two different models and/or different behavior laws over a [30%-85%]RH - [20°C-80°C] range where environmental drying of cement-based materials could occur. The comparison between the multiphase model and the simplified model, having both all the hydic properties evolving as a function of temperature, shows that the relative error between the two mass loss response surfaces could reach 12% at mid-drying stage. This is due to the contribution of the additional transfer modes present in the multiphase model which help it reach the hydic equilibrium faster, and the high resistance to liquid water evacuation from the porous medium imposed by the low values of relative permeability to liquid water in the simplified model. The second comparison was performed between simplified models considering in one case the evolution of all hydic properties as a function of temperature and in the other case water density and viscosity evolutions only. The relative error maps of the two mass loss response surfaces show errors that can reach up to 80% in high temperature and high relative humidity zone. This is mainly due to the different kinetics issued from different relative permeabilities and permeability to water values, as well as from desorption isotherms curves evolutions allowing more water evacuation. Finally, in order to decouple the effects of the isotherms and the intrinsic permeability, two sets of simulations were considered using the simplified model. In the first set no evolutions of hydic properties, except density and viscosity, are considered. In addition to this, the second set considers the evolution of the permeability to water. The error maps show a local maximum of 50% at 5 days, and the errors decrease with time in the whole [RH-T] space down to 3% after one year of drying.

Finally, the quantification of the effect of common simplifications on thermo-hydral simulations for a type of cement-paste was performed. The study defined a methodology to extend the comparison between models and assessing the impact of the simplification of behavior laws up to moderate temperatures for a range of relative humidities. The results shown are only valid for the configuration chosen (Geometry, material type, behavior laws, initial parameters, initial saturation..), therefore, the study of a different material type will surely lead to different error maps.

## 2.8 Appendix

The gases in the porous medium are treated as ideal gases, so that the following formula applies

$$\rho_{\pi} = p_{\pi} \frac{M_{\pi}}{RT} \quad (2.37)$$

where  $\pi$  is the gas specie (dry air or vapor),  $M_{\pi}$  is the molar mass of the  $\pi$  specie and  $R$  is the universal gas constant. Using Dalton's law, the total gas pressure is equal to the sum of the pressure of the separate species.

$$p_g = p_a + p_v \quad (2.38)$$

As to calculate the vapor pressure, Kelvin's law equation is considered. The relative humidity can be written as the ratio between the vapor pressure and the saturated vapor pressure, and the vapor pressure reads:

$$p_v = p_{vs}(T) \exp\left(\frac{M_v}{\rho_l RT} (p_g - p_c - p_{vs}(T))\right) \quad (2.39)$$

where the liquid density is a function of temperature, and which can be described as done by [Furbish, 1997].

$$\rho_l = \sum_{n=0}^5 b_n T^n + (p_{l-1} - p_{l-2}) \sum_{n=0}^5 a_n T^n \quad (2.40)$$

The saturation vapor pressure is expressed in function of temperature following the Hyland-Wexler relationship [ASHRAE, 2001].

$$p_{vs}(T) = \exp[C_1/T + C_2 + C_3 T + C_4 T^2 + C_5 T^3 + C_6 \ln(T)] \quad (2.41)$$

In the same reference, the fluids viscosity that are temperature dependent are expressed, as for vapor and dry air:

$$\mu_v = \mu_{v0} + \alpha_v (T - T_0) \quad (2.42)$$

$$\mu_a = \mu_{a0} + \alpha_a (T - T_0) + \beta_a (T - T_0)^2 \quad (2.43)$$

where  $\mu_{v0} = 8.85 \times 10^{-6} Pa.s$ ,  $\alpha_v = 3.53 \times 10^{-8} Pa.s.K^{-1}$ ,  $\mu_{a0} = 17.17 \times 10^{-6} Pa.s$ ,  $\alpha_a = 4.73 \times 10^{-8} Pa.s.K^{-1}$  and  $\beta_a = 2.22 \times 10^{-11} Pa.s.K^{-1}$ . As for the total gas viscosity, it depends on the pressure ratio of its component:

$$\mu_g = \mu_v + (\mu_a - \mu_v) \left(\frac{p_a}{p_g}\right)^{0.608} \quad (2.44)$$

The liquid water viscosity, which is also temperature dependent, is approximated by [Thomas and Sansom, 1995]

$$\mu_l = 0.6612.(T - 229)^{-1.562} \quad (2.45)$$

Concerning the thermal properties, especially the property of interest: the enthalpy of vaporization, which is a measure of the amount of energy required to transform liquid water into gas, is expressed by means of Watson formula [Reid et al., 1987]

$$\Delta H_{vap} = 2.672.10^5 (T_{crit} - T)^{0.38} \quad (2.46)$$

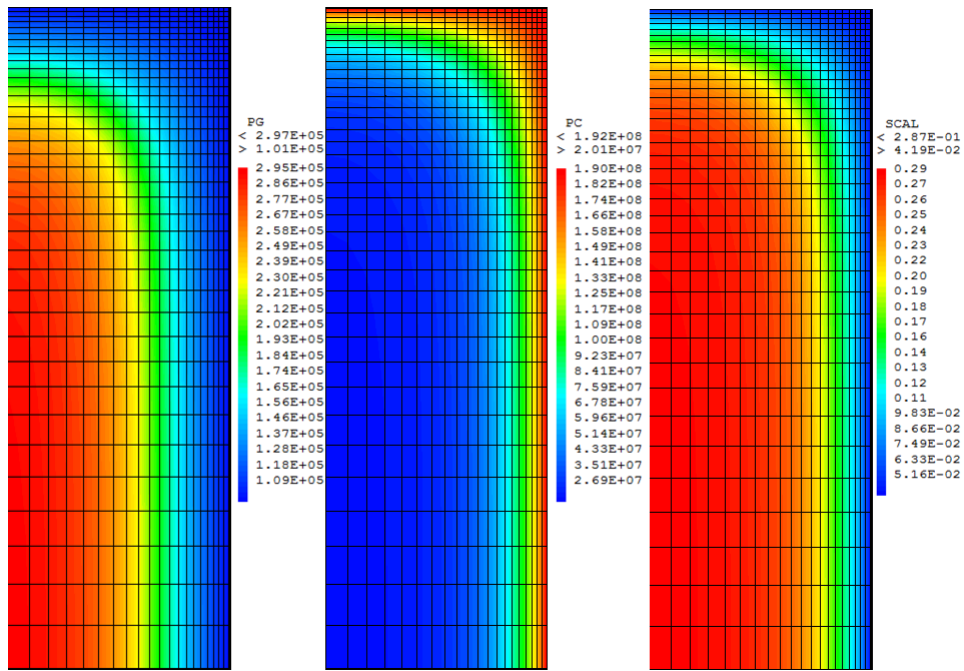


Figure 2.11: Gas pressure, capillary pressure and saturation fields at 30% RH and  $80^{\circ}C$  external conditions after 50 days of drying

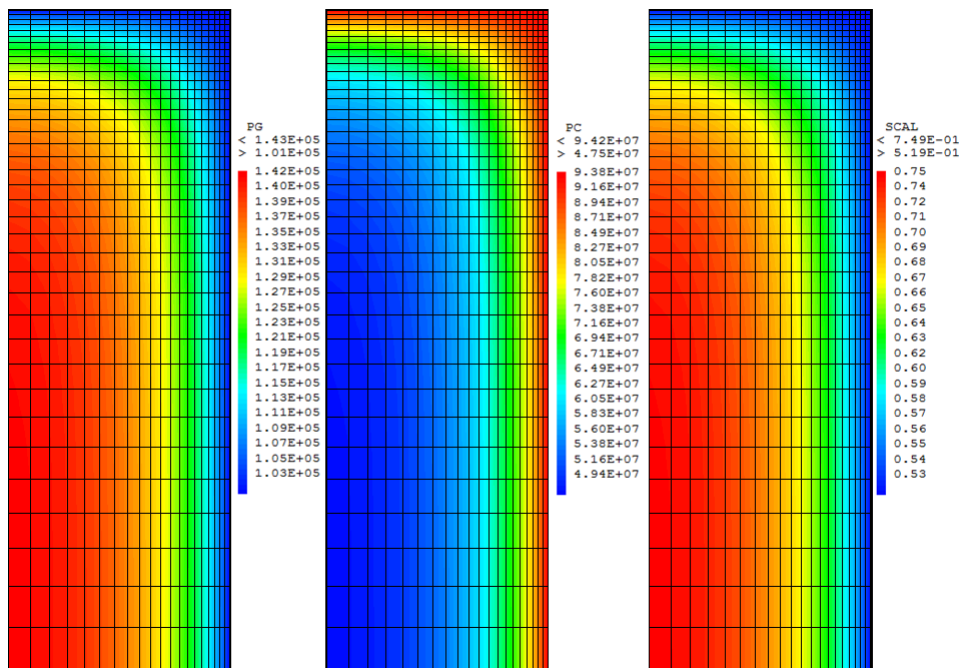


Figure 2.12: Gas pressure, capillary pressure and saturation fields at 50% RH and  $20^{\circ}C$  external conditions after 50 days of drying

## Chapter 3

# Drying of mortar at ambient temperature studied using high resolution neutron tomography and numerical modeling

### Paper context:

*The classical approaches used to characterize drying in cement-based materials suffer from several limitations. On one hand, the gravimetric technique which consists of acquiring successive measurements of the mass loss of a drying sample describes only the temporal evolution of the drying processes. On the other hand, the sensor-based point-wise measurement of relative humidity doesn't necessarily characterize the 3D moisture transport processes in an intrinsically heterogeneous porous medium. Having this lack of spatial characterization of hydric gradients, numerical models, as the ones used in chapter 1, cannot be calibrated properly and fails therefore to evaluate reliably the spatial hydric states and the hydraulic properties of the medium. The following chapter provides a reliable method to measure the 4D (3D + time) evolution of hydric states and characterize the hydraulic properties by using a combined experimental/numerical approach. This approach takes advantage of neutron tomography to provide the spatial measurements required to accurately calibrate a commonly used FE model.*

### Authors:

Hani Cheikh Sleiman, Alessandro Tengattini, Matthieu Briffaut, Bruno Huet, Stefano Dal Pont

### Paper Status:

Ready for submission in *Construction and Building Materials*

## Abstract

The drying of cement-based materials affects their thermal, hydraulic and mechanical properties and contributes to the loss of their durability potential. The conventional techniques employed to study the moisture transfer such as gravimetry weight loss and point wise invasive sensor-based measurements cannot characterize fully and accurately this 4D spatio-temporal process. Conversely, neutron tomography, among the other full-field non invasive measurement techniques, lends itself as an ideal tool to study the moisture transport process due to the high attenuation of neutron by hydrogen.

In this study, a set of cylindrical mortar samples were placed sequentially to dry in a thermo-hydric controlled environment ( $T=20\text{ }^{\circ}\text{C}$ ,  $\text{RH}=35\%$ ) in order to represent different hydric states. The samples were sealed in their lateral direction in order to force a unidirectional moisture flow. A set of neutron tomographies were then acquired for the different samples, which, once analyzed using appropriate image processing methods, lead to gray value attenuation profiles over the samples' height. A multiphase partitioning of the remaining mortar in solid (after removing the big aggregates captured by the resolution), air and moisture is then proposed in order to evaluate the saturation profiles at different drying periods. The validation of the proposed procedure is then done by comparing the neutron-based weight loss measurements against the ones measured by the balance.

Finally, both of the experimental mass loss and hydric gradients are used to calibrate a finite element FE simplified hydric numerical model in order to measure indirectly the permeability of the porous medium and the hydric convective exchange coefficient of the controlled environment.

## 3.1 Introduction

The drying of cement-based materials has inevitable and significant effects on their durability potential. After casting, cement-based materials generally have a higher hygrometry than the surrounding environment. The water located in the porous network tends then to migrate toward the external environment in order to establish the hydric equilibrium. Consequently, the material undergoes drying shrinkage, which can be restrained, not only by the presence of aggregates, but also by the core of the sample that remains saturated for a longer time. The ensuing deformations restrain lead to stress generation that can cause cracking. Additionally, the variation of relative humidity in the interconnected porosity affects the material hydraulic properties (such as hydraulic conductivity and diffusivity [Mualem, 1976][Perre and Degiovanni, 1990]), chemical properties (such as hydration degree [Sciumè et al., 2013] and the kinetics of degrading chemical reactions [Pan et al., 2012]), thermal properties (such as thermal conductivity [Baggio et al., 1993]), mechanical properties (such as creep [Bazant and Chern, 1985]), fire resistance [Dauti et al., 2018d][Tengattini et al., 2020a], *etc.* It follows that characterising the hydric state and its evolution is pivotal for understanding its vital implications on the structural integrity of cement-based materials.

Several methods has been used to characterize the cement based material hydric state and properties. They can be broadly divided into three main categories: bulk-averaged or point-wise methods, full-field measurement techniques and indirect numerical modeling methods. Within the first group, the measure of the evolution of mass loss in time of a sample subject to drying is perhaps the most used method [Baroghel-Bouny, 1994][Baroghel-Bouny et al., 1999]. Despite its widespread adoption, perhaps related to the ease of its implementation, this measurement is a macroscopic average of the highly heterogeneous response of the materials and cannot provide insight about the spatial distribution water content. To overcome this limitation, many authors have employed point-wise sensor-based measurements techniques to assess relative humidity in a particular point in space [Kim and Lee, 1999][Ma et al., 2020]. However, these point-wise approaches have variable accuracy depending on their proximity to different species (porosity, aggregates) in a multiphase porous medium. Furthermore, they require the identification of the sorption/desorption isotherms of the material to relate the relative humidity to saturation [Carette et al., 2019]. Moreover, this measurement doesn't necessarily provide sufficient description of the intrinsically three-dimensional water content field.

In the last few decades, the development of full-field measurement techniques have allowed unprecedented insight into local processes [Viggiani et al., 2012]. In regards to moisture transfer in porous media, many of those techniques have been employed; such as Nuclear Magnetic Resonance NMR [Faure et al., 2005] [Fourmentin et al., 2017][McDonald et al., 2020], Radiation attenuation techniques (such as Gammadensimetry [Villain and Thiery, 2006b]) Electrical techniques (Electrical Capacitance Tomography ECT [Voss, 2020]) Electromagnetic Non-Destructive Evaluation ENDE techniques [Loubser Du Plooy et al., 2015].

A particularly effective tool is Neutron Imaging, which lend itself as a very powerful non-destructive and

non-invasive technique to study the moisture distribution in porous materials due to the high attenuation of neutrons by hydrogen [Perfect et al., 2014][Zhang et al., 2018][?]. The 2D/3D attenuation fields resulting from the radiography/tomography can be correlated to water content when proper calibration is performed [Stavropoulou et al., 2020][Cheikh Sleiman et al., 2020b].

Beside the intrinsic interest of understanding the evolving moisture profiles, the spatial distribution of moisture content is essential to rigorously calibrate thermo-hydric numerical models [Rahimi-Aghdam et al., 2019] [Cheikh Sleiman et al., 2020a]. This calibration can, in turn, be used to characterize indirectly the material hydraulic properties which are anomalously characterized experimentally, such as permeability. In fact, the gas permeability can be 3 orders of magnitude higher than water permeability both because of pre-drying induced cracking and of pore-wall physically adsorbed water removal. On the other hand, the water permeability can only be measured in saturated conditions, thus in a configuration where drying cracks effect on the drying kinetics are not taken into account. For these reasons, it is generally agreed that indirect numerical method is more reliable than the aforementioned experimental ones in measuring the intrinsic permeability. However, due to the high number of model parameters and the mathematical flexibility of the constitutive laws, many solutions can be found, specifically when experimental data-sets related to local water content distribution in the material are not measured [Carette et al., 2019].

In this contribution, we propose an approach that sufficiently characterize the hydric state and properties of a cement-based porous medium while emphasizing the major contribution of 3D neutron tomographic data sets. In section 3.2 the experimental campaign is described pointing out the composition of the mortar samples, their mass loss history and the neutron tomography settings. Then, a number of image processing methods and an elaborated methodology based on multiphase porous media considerations are shown in section 4.3.2.1 and 4.3. This has permitted the characterisation of saturation gradients at different instances in time. The resulting hydric gradients were then validated to mass loss history provided by gravimetric experimental data sets in section 3.4.2.2 and were then used as a sufficient data set to be fitted by a common numerical model in section 3.5. Once calibrated, the model allowed an indirect measurement of the intrinsic permeability and the coefficient of hydric exchange.

## 3.2 Material and methods

### 3.2.1 Specimens

The experimental campaign presented here involves 14 samples, all made out of EN standard mortar. The water to cement ratio  $w/c$  is equal to 0.5 and the sand (standard sand CEN EN 196-1) to cement ratio  $s/c$  is equal to 3. These cylindrical samples were cored out from a bigger bloc, which was casted and kept 2 days in its mold in sealed conditions and then was placed in a bath of water to cure. A diamond coring bit of 12 mm inner diameter was then used to core out the samples. While one side of the samples was smooth from the mold effect, the other side had to be further cut and smoothed using a rotating blade system equipped with a water jet to avoid local thermal gradients. The final cylindrical samples had a height of 40 mm and were kept in water to avoid potential water exchanges with the environment that can be induced by the imperfectness of sealing conditions. However, due to time constraints, only 11 out of 16 samples were chosen to be scanned based on their different drying periods.

### 3.2.2 Mass loss history

In order to induce different hydric states in the same material, the samples were placed sequentially in a drying environment. Each sample was first weighted and then rolled in three layers of adhesive aluminum tape on the longer side to avoid lateral moisture leakage, in order to induce a unidimensional moisture flow. The mass of aluminum tape was also measured for each sample to correct the measured mass loss. The samples were then put sequentially to dry in a thermo-hydric controlled environment, with no ventilation, at 20 °C and 35 % relative humidity controlled with  $MgCl_2 \cdot 6H_2O$  saturated solution. The samples mass loss was characterised then in time as shown in figure 3.1.

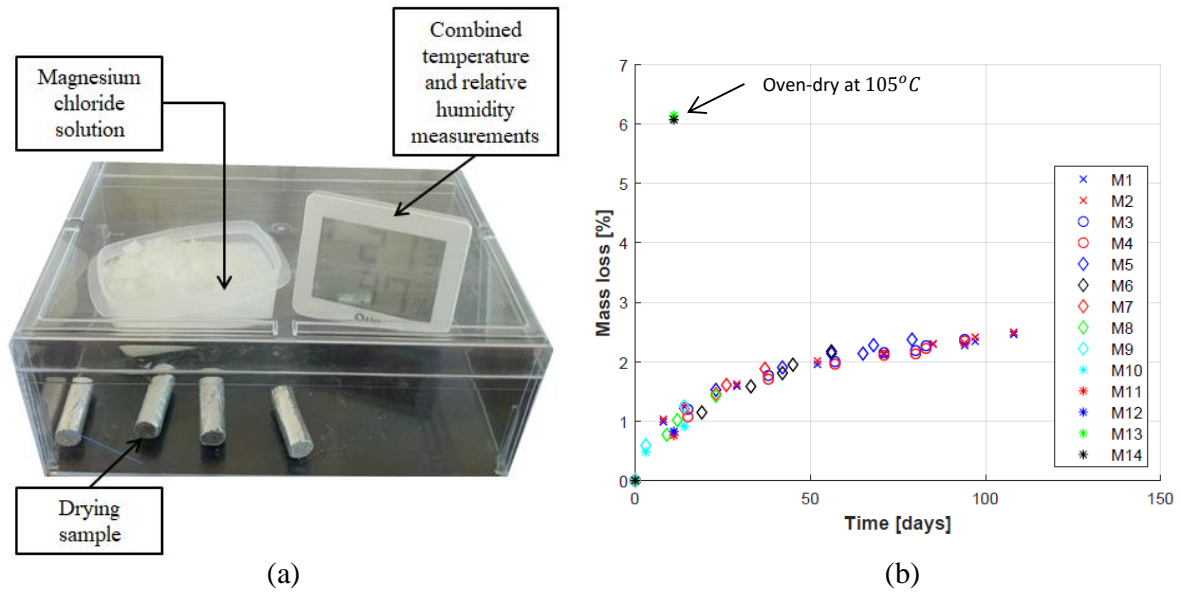


Figure 3.1: Drying of mortar samples: (a) Sample drying in a thermo-hydric controlled environment (b) Total samples mass loss history

In addition, two mortar samples were put to dry in an oven set to 105 °C to obtain a reference hydric state which is key for the quantification analysis as will be shown in the next section. Given the small size of the samples, the high temperature of the environment in which they were placed, and the duration of drying of 11 days, the mass loss of these two samples is here considered to correspond to hydric equilibrium.

### 3.2.3 Neutron acquisition

The neutron tomographies were acquired at the NeXT-Grenoble beamline (detailed in [Tengattini et al., 2020b]), which takes advantage of the world-leading cold neutron flux, and located at the Institut Laue-Langevin (ILL) in Grenoble, France.

Before transporting the samples to the beamline, each sample was weighted and sealed to prevent any water exchange with the environment. Their weight was re-measured before and after each scan to ensure that no (or negligible) drying occurred during tomographic acquisition, which was found to be the case. An identical set of neutron acquisition parameters was selected for all the tested specimens. In absence of rapid dynamic processes occurring in the samples, these parameters were optimised to maximise spatial resolution. In this case, 1088 projections were acquired in 2 hours and 54 minutes over a 360° rotation, each radiography being the average of three radiographies, each 3.2 with seconds exposure. To achieve this, an infinity corrected optical setup was employed, coupling a 50 mm Canon Lens with a 122 mm Heliflex lens, as detailed in [Tengattini et al., 2020c]. This setup yields a 16 μm pixel size. Given the small pixel size, a 20 μm thick  $Gd_2O_2S : Tb^6LiF$  scintillator was employed, A 30 mm pinhole  $D$  (corresponding to a neutron flux of  $3 \times 10^8$  ncm<sup>2</sup>s at the sample, placed 10 meters away) was selected to achieve a true resolution of about 30 μm. Each neutron radiography was the average of 3 individual projections each with a 3.2 s exposure, resulting in a sigma to noise  $SNR = 14$ .

Each set of radiographies was reconstructed into the corresponding 3D volume by means of the Feldkamp (FDK) back projection algorithm, as implemented in the commercial software X-act (from RX-Solutions). An example of a 3D neutron attenuation field of the mortar sample is reported in figure 3.2.

### 3.3 Segmentation and grey value gradients

Moisture transport happens essentially in the interconnected porosity of the cement given the comparatively low permeability of aggregates and sand particles. Therefore, in order to isolate the contribution of this phase, it is beneficial to identify and remove these particles from the neutron tomographies. Their identification (a process named segmentation in image processing) can in this case be achieved thanks to the lower neutron attenuation (*i.e.*, the gray value of the voxels comprising them) of aggregates with respect to that of the cement paste. An histogram-based segmentation of the grains can then be achieved based on whether a voxel has a value above or below a suitably chosen threshold. In this work, to ensure repeatability and avoid user dependency, this threshold was determined based on an algorithm named “*IJ\_IsoData*” [?] available in *ImageJ* software [Schindelin et al., 2012]. This method allows the identification of the aggregates from the surrounding mortar (cement paste and sand fines below the imaging resolution) as illustrated in figure 3.2. Once the particles are isolated it is straightforward to “remove” them from the subsequent elaborations.

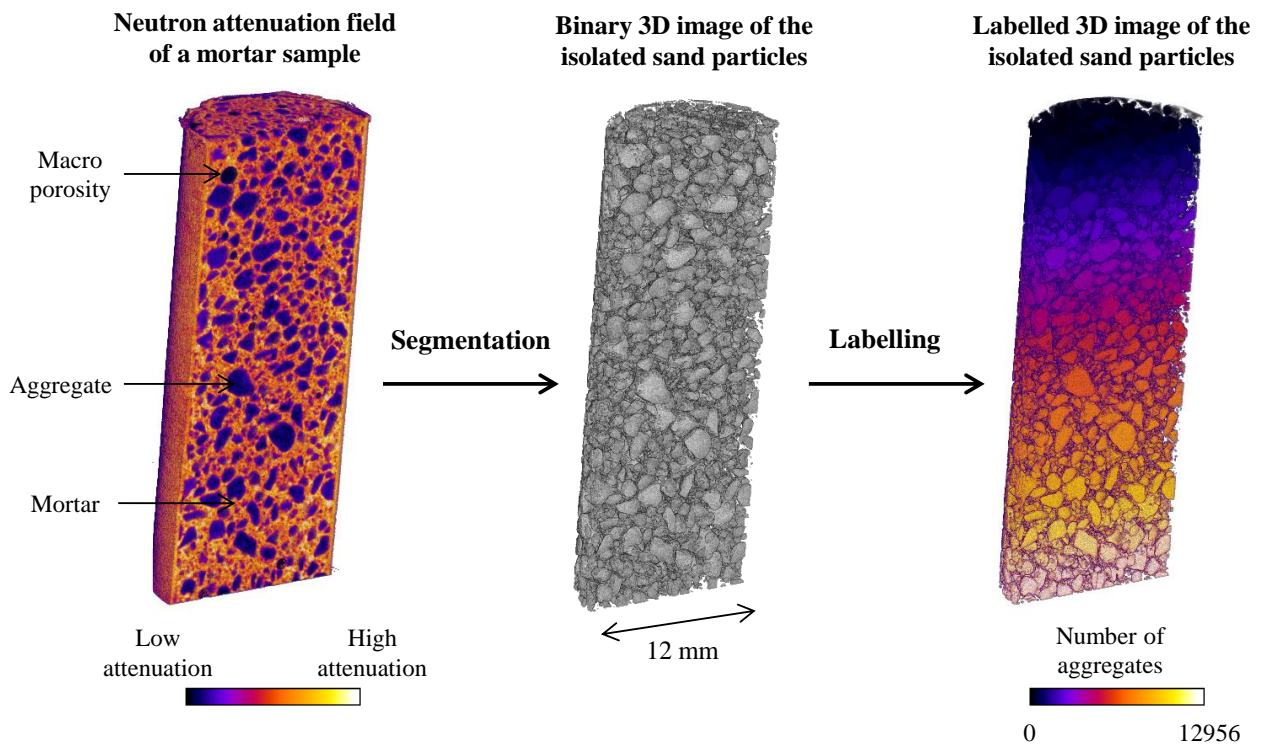


Figure 3.2: Segmentation and labelling processing adopted in this work. To the left: rendering of a representative 3D reconstructed attenuation field. In the middle: rendering of the binary image after histogram-based segmentation. To the right: Labelled 3D volume isolating the individual grains, whose color corresponds to the assigned incremental index.

A first indication of the evolution of the moisture content due to drying is reported in figure 3.3, which shows the average grayvalue over the half-height of each sample (the half being completely within the field of view, given that the sample was larger than the field of view under for the chosen resolution). Each point in the plot corresponds to the average grey value mortar voxels in a 10 pixels-thick disk, along the height of the sample. The variation of gray value attenuation shown in figure 3.3 can be correlated to the variation of the hydric state along the height and drying stage as shown in the next section.

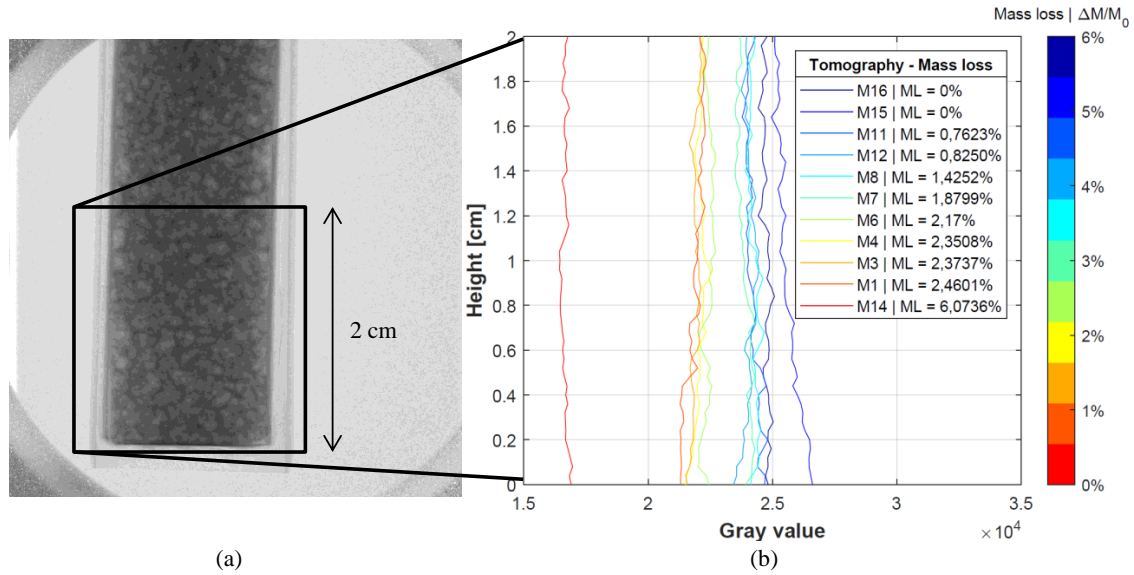


Figure 3.3: Analysis of the attenuation profiles: (a) radiography showing the sample in the field of view (b) Grey value gradients of all the scanned sample

From figure 3.3 it can be observed that the reference samples with no mass loss (M15 and M16) show a slightly different initial water distribution. While in sample M15 the gray value attenuation profile suggests a uniform moisture content along its height, sample M16 shows an apparent moisture concentration near the top surface. This might be related to local variations in water content in between the mortar blocs from which the cylindrical samples were cored. Samples M15, M7 and M8 were in fact extracted from a different bloc different than the other samples. For this reason, in the upcoming analyses, the gray value of each sample is normalised to the corresponding reference sample cored from the same block. This measurement shows again the importance of the full-field nature of the proposed approach over the local, point-wise ones which could have led in this case to misleading conclusions.

## 3.4 Results

### 3.4.1 Radial gradients

As aforementioned the experimental campaign was conceived to impose a uni-directional drying front by sealing the lateral surface with multiple layers of aluminium tape. The three-dimensional nature of tomography allows the verification of this assumption through the study of the variation in attenuation values along the radial direction. To have a sufficient number of voxels for statistical representativity, the average over concentric (hollow) 20 slices-thick rings was compared. Additionally, to account for any heterogeneity in aggregate content (which were removed from these statistics as detailed above), a counter of voxels in each mortar tubal sub-volume was set to account for any statistical variability related to the total count of voxels.

This operation was repeated at three different heights representing the top, middle and bottom of the sample, as reported in figure 3.4 b, c and d, respectively. In each of these subfigures this operation is repeated for three representative samples at three distinct drying stages. figure 3.4 shows virtually no radial gradient between the core and the external surface of the sample, in all conditions and along the height. In addition, this measurement confirms previous observations in [Toulemonde and Le Maou, 1996][Boucher, 2016], where adhesive aluminum was found to be effective at low temperature for periods shorter than 6 months. The samples were therefore considered to be perfectly sealed, justifying the hypothesis of unidirectional drying adopted in the following sections, which will only focus on vertical gradients averaged over the sample width.

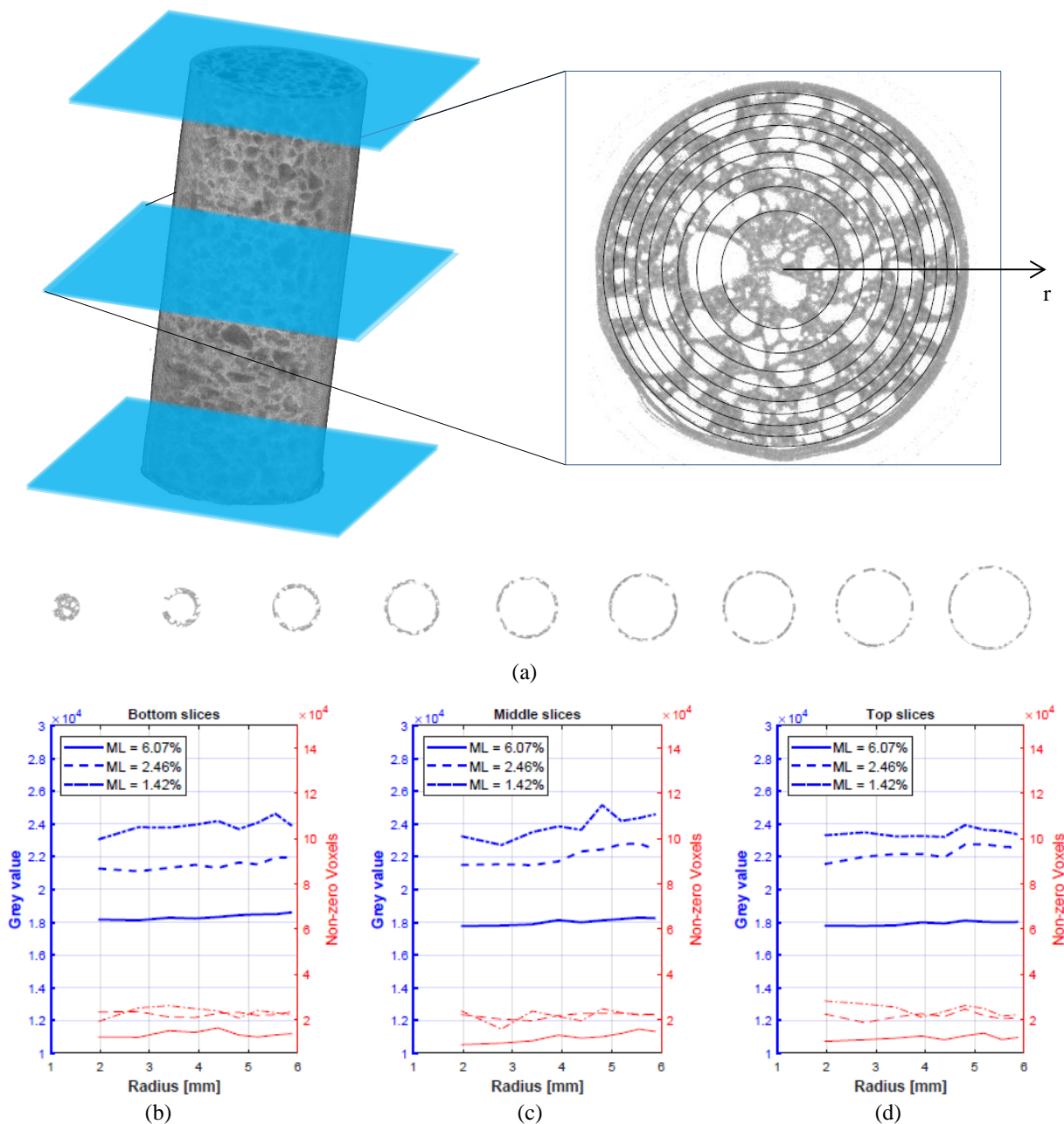


Figure 3.4: (a) Montage showing the partitioning of the sample in the radial direction so as to keep a similar number of pixels in each division. Evolution of grey value with respect to the radius for different saturation states and different positions in the sample: (b) Bottom (b) middle (c) Top

### 3.4.2 From attenuation values to saturation gradients

#### 3.4.2.1 Saturation profiles

Once the aggregates are removed as detailed in section 4.3.2.1), the remaining material is a partially saturated mortar (cement paste and sand fines below the imaging resolution). This can be further subdivided in three species: dry mortar “*dm*” (mixture of solid gel, unhydrated cement, chemically-bonded water and sand fines), capillary water “*cw*” and air “*a*”.

The gray value (measured attenuation) of the mortar considered as a multiphase mixture “*mix*”, can be therefore expressed as the sum of these individual components:

$$\mu_{mix} = W_{cw}\mu_{cw} + W_a\mu_a + W_{dm}\mu_{dm} \quad (3.1)$$

Where  $W_i$  and  $\mu_i$  are respectively the volumetric fraction and the gray value of the specie  $i$ .

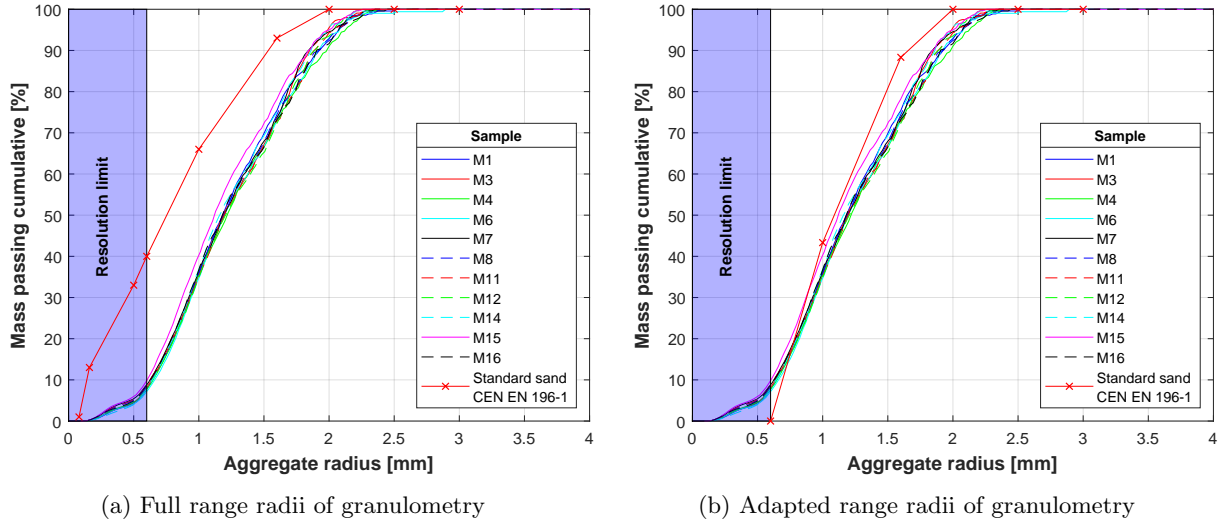


Figure 3.5: A comparison between experimental and numerical cumulative granulometry taking into account the resolution limitation of the neutron tomography scans

Assuming no variation of mass related to the dry mortar specie (negligible effect of hydration or dehydration reactions) and neglecting the volumetric variation effect on attenuation (*e.g.*, drying shrinkage), the variation of the compound attenuation between two saturation states can be expressed as:

$$\Delta\mu_{mix} = \Delta W_{cw}\mu_{cw} + \Delta W_a\mu_a \quad (3.2)$$

Where the variation of the volumetric fraction of air is equal to the reduction of water ( $\Delta W_a = -\Delta W_{cw}$ ) since the moisture leaving the porosity is replaced by air. The variation of capillary water volume fraction writes:

$$\Delta W_{cw} = \frac{\Delta\mu_{mix}}{\mu_{cw} - \mu_a} \quad (3.3)$$

The gray value of air  $\mu_a$  can be directly measured from the tomographies and was found to average 7900 (gray value) with a standard deviation  $\sigma_a$  of 1000. On the other hand, the gray value of water  $\mu_w$  was measured in multiple water-filled macro porosity in the reference samples. It averaged 50500 with a standard deviation of 2000. It should be noted, nonetheless, that this value can slightly vary depending on the hydric state of the material, because of the scattering contribution to the attenuation. The attenuation law of water can in fact diverge from the Beer-Lambert law, as generally the case for highly scattering elements in high concentration. For the specific energy spectrum of the used NeXT beamline, this discrepancy from the Beer Lambert was measured, for example, in [Stavropoulou et al., 2019]. A possible approach to correct for this spurious fluctuation is then to account for a correction based on the observed correlation between equivalent water thickness “ $x$ ” and water attenuation contribution, as measured on a reference, water-filled wedge sample. For thicknesses between 0 mm and 4 mm this can be fit with a second order polynomial  $\mu_w(x) = ax^2 + bx + c$ , where for this beamline  $a = -0.0052$ ,  $b = -0.0023$  and  $c = 0.3107$ . Assuming that this correction, measured in radiography, is also valid in tomography, the water gray value varies then non-linearly between 50500 and 57000 in between the reference, wet state and and ultimate, oven dry state.

The estimation of a saturation profile from capillary water volumetric fraction can be expressed as:

$$S_l = S_l^i - \Delta S_l = S_l^i - \frac{\Delta W_{cw}}{\hat{\phi}_m} \quad (3.4)$$

Where  $S_l$  is the saturation of liquid water,  $S_l^i$  is the reference initial saturation (correcting for self-desiccation effect) and  $\hat{\phi}_m$  is the averaged porosity of the mortar phase having only its sand fines (less than 600  $\mu\text{m}$ ) after removing the bigger particles using segmentation. In order to calculate this averaged parameter, the quantification of the aggregate fines that were not captured by the neutron scans resolution is a key point. For this reason, a granulometric analysis was done by applying the “watershed” morphological operation [Beare and Lehmann, 2006] on the segmented image that enabled the separation of individual grains as illustrated in figure 3.2. The volume of each grain is then measured and converted into a radius of a volume-equivalent

sphere. This conversion allows for a particle size distribution characterization as seen in figure 4.7, where the cumulative volume passing is plotted against the experimental sieving measurements. The comparison shows the expected mismatch between the two measurements. The volumetric fraction of fines  $\xi_f$  not captured by the neutron resolution is estimated to be 40%. It follows that the averaged porosity of the mortar after segmentation (cement and sand fines) can be estimated as:

$$\hat{\phi}_m = \phi_{cp} - \xi_f(\phi_{cp} - \phi_m) \quad (3.5)$$

where  $\phi_m$  is the mortar porosity equal to 16% and  $\phi_{cp}$  is the cement paste porosity estimated to 37% as referred by [Rougelot, 2008].

Finally, the only parameter that requires identification is the initial saturation. Although the initial hydric states show variation in the gray value plots in figure 3.3, an averaged initial saturation of 78% was taken as a reference value for all the samples. The variation of this parameter shifts the  $l$  profiles to lower or higher absolute hydric states but does not affect the overall water removal between the initial reference and current level of saturation. This parameter was chosen as the maximum value that shifts the saturation profile of the oven-dry sample to less than 10% of saturation. The value of 10% is believed to be a reasonable value when compared to similar cementitious materials as the ones mentioned in [Poyet, 2009].

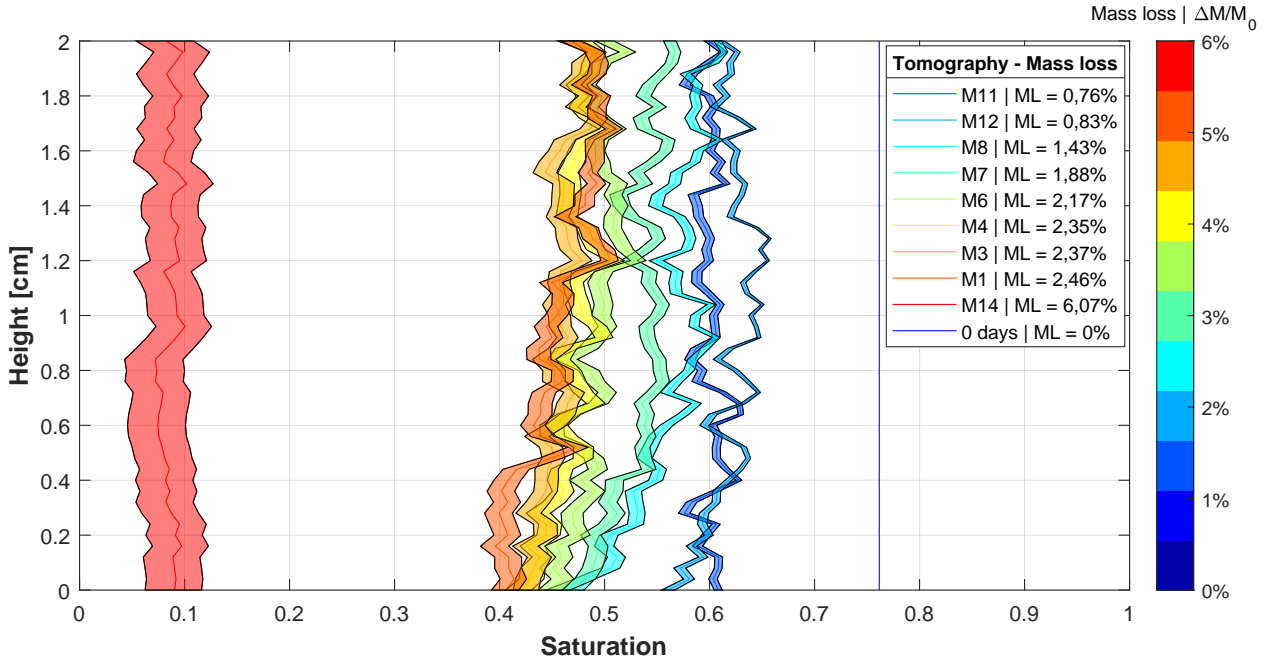


Figure 3.6: Neutron-based measurement of saturation gradients of mortar samples at different hydric states. The measurement accounts for the variability of the fluids gray value attenuation coefficients.

The saturation profiles show an overall gradient between the exchange surface and the core of the sample of almost 10% mainly due to the absence of ventilation in the drying controlled environment. In addition, each profile shows local gradients pointing out a variability in the distribution of water in the porosity.

### 3.4.2.2 Validation to mass loss measurements

The robustness of the grayvalue-saturation transition is verified using direct comparison between mass loss using two different measurements. The first one, being the reference measurement, is provided by the balance weighting while the second one relies on integrating the tomography-based saturation profiles over the height of each sample. It can be calculated using both the saturation profile  $S_l^t$  corresponding to a drying-period  $t$  and the reference initial saturation profile  $S_l^0$ , leading to the following relationship

$$\Delta M_t = \frac{(S_l^0 - S_l^t) \cdot \rho_l \cdot \hat{\phi}_m}{\rho_m^{sat}} \quad (3.6)$$

Where  $\rho_l$  is the water density,  $\hat{\phi}_m$  is the averaged porosity of the mortar having only its sand fines (less than 600  $\mu\text{m}$ ) after removing the bigger particles using segmentation and  $\rho_m^{sat}$  is the density of mortar accounting

for the full granulometry.

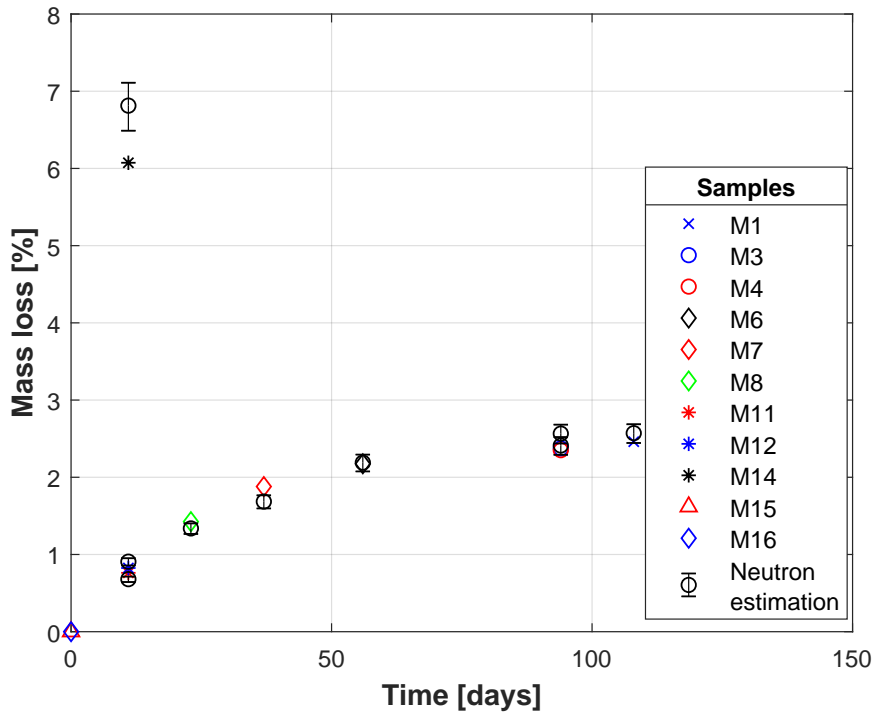


Figure 3.7: Comparison between the balance-measured mass loss and the one deduced from image analysis.

The so deduced mass loss for all the scanned samples, compared to the balance measurements is reported in figure 3.7. The error bars for the imaging-based approach, show the effect of the aforementioned variability in the coefficient of attenuation of water and air. Despite the specificity in the composition of each sample, which can induce hydric variability as well as all the assumption previously stated, the gravimetry-based and tomography-based measurements are in good agreement.

### 3.5 Modeling of moisture transfer

To further understand the processes at play, numerical models are of course crucial to complement the information not accessible through imaging. When implemented within finite element simulations reproducing the experimental conditions it is in fact possible to validate not only the overall drying but also the spatio-temporal gradients made available by the presented experimental campaign.

Different numerical models exist to model the moisture transport in unsaturated porous media. They can be broadly divided into two main categories: complete and simplified models. While the former establishes a rigorous description of all the species of interest (liquid water, vapor and dry air) [Dal Pont et al., 2007][Dauti et al., 2018c], the later propose a set of assumptions that simplifies the physical description of the involved processes. This simplification is valid when the gas pressure in the interconnected porosity remains equal to the atmospheric pressure, which means that all local pressure built ups dissipate quasi-instantaneously and when the liquid permeation is the dominant water transport mechanism. In this work, regarding the drying conditions which where set in the controlled environment (drying temperature of 20 °C and relative humidity of 35%), and regarding the material in study (mortar having a water to cement ratio of 0.5), we assume that the use of a simplified model is valid [Thiery et al., 2007] [Cheikh Sleiman et al., 2020a].

#### 3.5.1 Numerical model

The simplified model derives from the mass conservation equation of the liquid water in the porous system.

$$\frac{\partial m_l}{\partial t} + \nabla \cdot (m_l v_{l-s}) = 0 \quad (3.7)$$

where  $m_l$  is the mass of liquid water and  $v_{l-s}$  is the velocity of the liquid water with respect to the solid skeleton of the material. The mass of water is expressed in terms of density  $\rho_l$ , porosity  $\phi$  and liquid saturation rate  $S_l$ .

$$m_l = \rho_l S_l \phi \quad (3.8)$$

whereas its velocity with respect to the solid skeleton is expressed using Darcy's law.

$$v_{l-s} = -K \frac{k_{rl}}{\mu_l} \nabla p_l \quad (3.9)$$

Where  $K$ ,  $k_{rl}$  and  $\mu_l$  are respectively the intrinsic permeability of the system, the relative permeability and the dynamic viscosity of liquid water. Considering water as an incompressible fluid ( $\rho_l = \text{cte}$ ), and assuming the existence of a differentiable function between saturation and capillary pressure, the conservation equation reads:

$$\left[ \frac{\partial S_l}{\partial p_c} \right] \frac{\partial p_c}{\partial t} - \nabla \cdot \left[ \left( \frac{k_{rl}(S_l)K}{\mu_l} \nabla p_c \right) \right] = 0 \quad (3.10)$$

The equation (11) requires the definition or description of four properties: porosity  $\phi$ , a differentiable function of saturation with respect to capillary pressure  $S_l(p_c)$ , intrinsic permeability  $K$  and relative permeability  $k_{rl}$ . Assuming that the hydration reaction of cement ended before the samples were submitted to drying, the micro-structural properties, in particular porosity and intrinsic permeability are constant parameters. The water retention curve (desorption isotherm) can be described by the Van Genuchten family of equations [Genuchten, 1980] that reads:

$$S_l(p_c) = \left[ \left( -\frac{p_c}{a} \right)^{\frac{1}{1-b}} + 1 \right]^{-\frac{1}{b}} \quad (3.11)$$

The parameters  $a$  and  $b$  are fitting parameters. The Mualem [Mualem, 1976] model is used in the expression of relative permeability to liquid water. The relative permeability in function of water saturation reads:

$$K_{rl} = \sqrt{S_l} (1 - (1 - S_l^b)^{1/b})^2 \quad (3.12)$$

By analogy to heat differential equation, one can name  $(\phi \frac{\partial S_l}{\partial p_c})$  the hydraulic capacity and  $(\frac{K k_{rl}}{\mu_l})$  the hydraulic conductivity. Equation (11) is therefore discretized using the finite software Cast3m under the heat module accounting for the non-linear hydric conductivity term which depends on capillary pressure solution. The temporal discretization is done using theta-method scheme.

### 3.5.2 Model inputs, initial and boundary conditions:

A quarter of the sample was described in axisymmetric condition. A total number of 182 eight-nodes elements was used for meshing the 2D surface, which was refined near the imposed boundary condition to ensure better convergence and higher results accuracy as shown in figure 3.8.

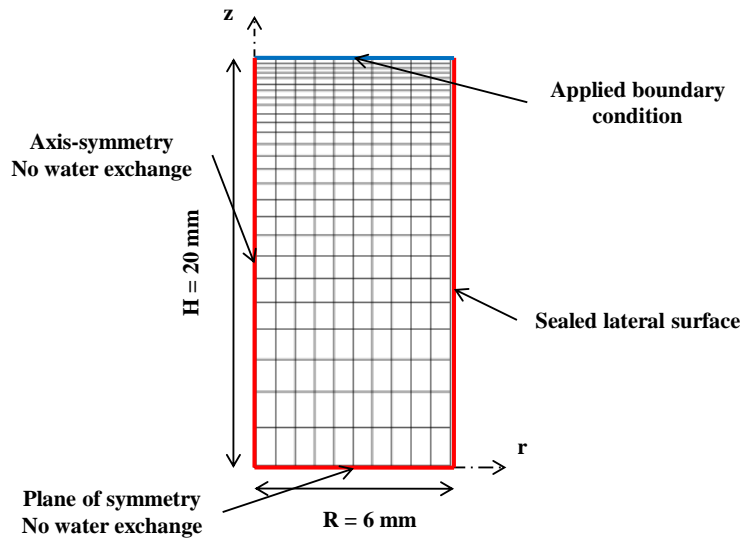


Figure 3.8: Mesh and boundary conditions

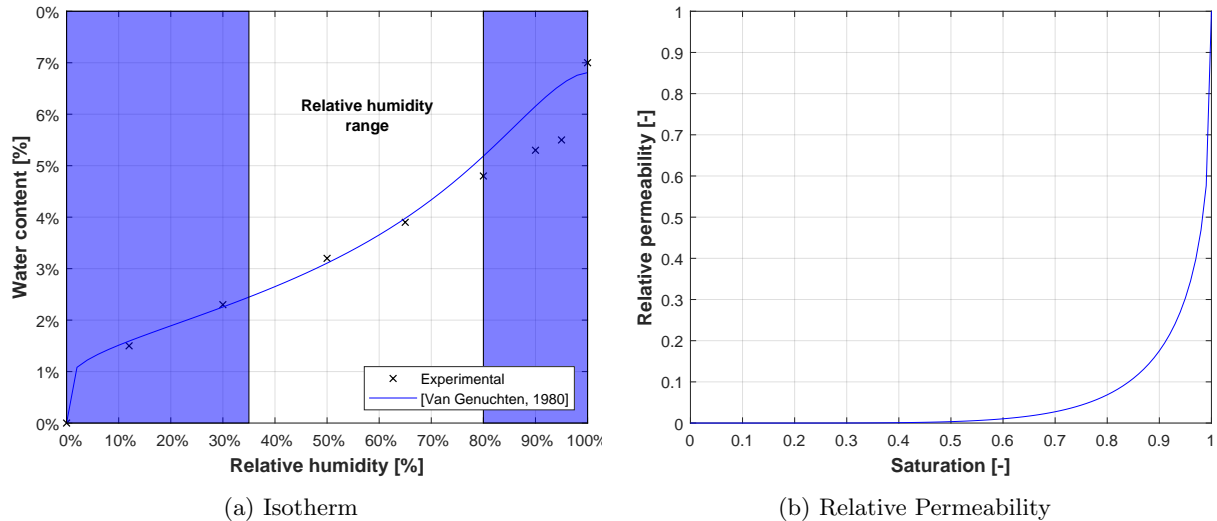


Figure 3.9: Behavior laws

Two types of boundary conditions can be considered in addressing the drying modelling of porous systems. The first, Dirichlet boundary condition, consists on imposing the relative humidity (or its equivalent, depending on the differential equation primary variable) of the controlled chamber directly at the air-concrete interface. However, this usually overestimate the interface exchanges and neglect the presence of a so-called boundary-layer whose moisture content depends gradually on the distance to the material surface. This boundary-layer depends on the chamber temperature, the ventilation wind-speed and on the material surface conditions. From modelling perspective, it could be modelled using Neumann type boundary conditions that can be generally expressed as:

$$\vec{J}_{bc} = h_{bc} \cdot (p_c^s - p_c^e) \cdot \vec{n} \quad (3.13)$$

Where  $p_c^s$  and  $p_c^e$  are respectively the equivalent surfacic and external capillary pressure,  $\vec{J}_{bc}$  is the water flux and  $h_{bc}$  is the convective exchange coefficient. This latter parameter has a wide variety (up to 4 orders of magnitude) depending on the material and the experimental campaign conditions [Özbolt et al., 2016] [Zhang et al., 2015]. However, due to the experimental conditions in this campaign, notably the presence of no ventilation, it is expected to get a low value of this convective exchange parameters.

As mentioned in section 3.5.1, the model requires the definition of 4 properties, namely porosity  $\phi$ , a differentiable function of saturation with respect to capillary pressure  $S_l(p_c)$ , intrinsic permeability and relative permeability. With the exception of the intrinsic permeability (more precisely, permeability to water), all these properties were characterized experimentally in [Rougelot, 2008], which will help feeding the inputs and the fitting procedure of the numerical model. The initial relative humidity value is taken equal to 80% which corresponds to an initial saturation state of 78%. The correspondence of relative humidity/saturation is based on the desorption isotherm reported in the aforementioned reference.

### 3.5.3 Model calibration and back-calculation of hydraulic properties

After setting the initial parameters of the model, the fitting constants, *i.e.*  $a$  and  $b$  in equation (12), need to be assigned in the family curves of  $S_l(p_c)$  and  $K_{rl}(S_l)$  in order to fit at best the experimental data. The desorption isotherms are characterized in the work of [Rougelot, 2008]. However, up to the authors knowledge, no direct experimental characterization of the relative permeability of the studied material is reported in the literature. The parameter  $b$ , identified in the van Genuchten law, was therefore used in the Mualem function in order to obtain a consistent data-set.

Once the isotherms are fitted and the relative humidity function is defined consequently, two remaining parameters are still missing for assignment: the intrinsic permeability  $K$  and coefficient of hydric convection  $h_{bc}$ . On the other hand, two experimental data-sets are remaining: the mass loss history and the saturation gradients. The two parameters are to be found based on the fact that the permeability  $K$  affects mainly the mass loss history and the convection coefficient  $h_{bc}$  affects the surfacic saturation value.

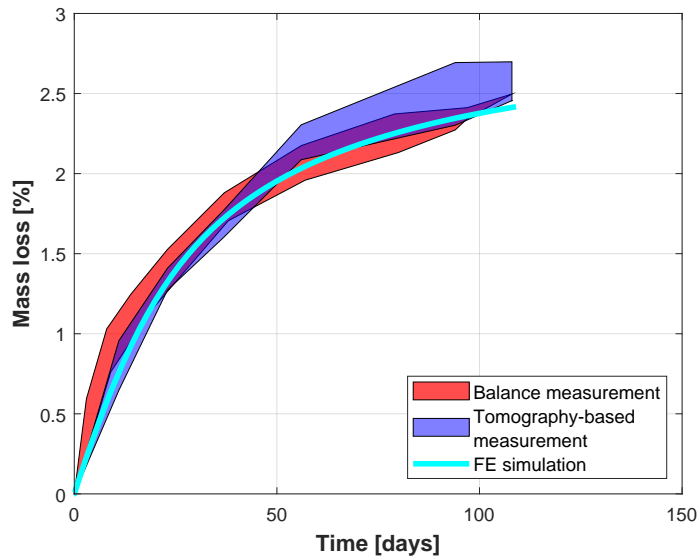


Figure 3.10: Mass loss comparison of the: (red) balance measurements, (blue) image-based measurements and (cyan) FE estimation. The shaded area being to account for the variability of the acquired measurements.

When those two parameters are well assigned, satisfying fitting of mass loss experimental data and saturation gradients can be obtained as in figure 3.10 and figure 3.11.

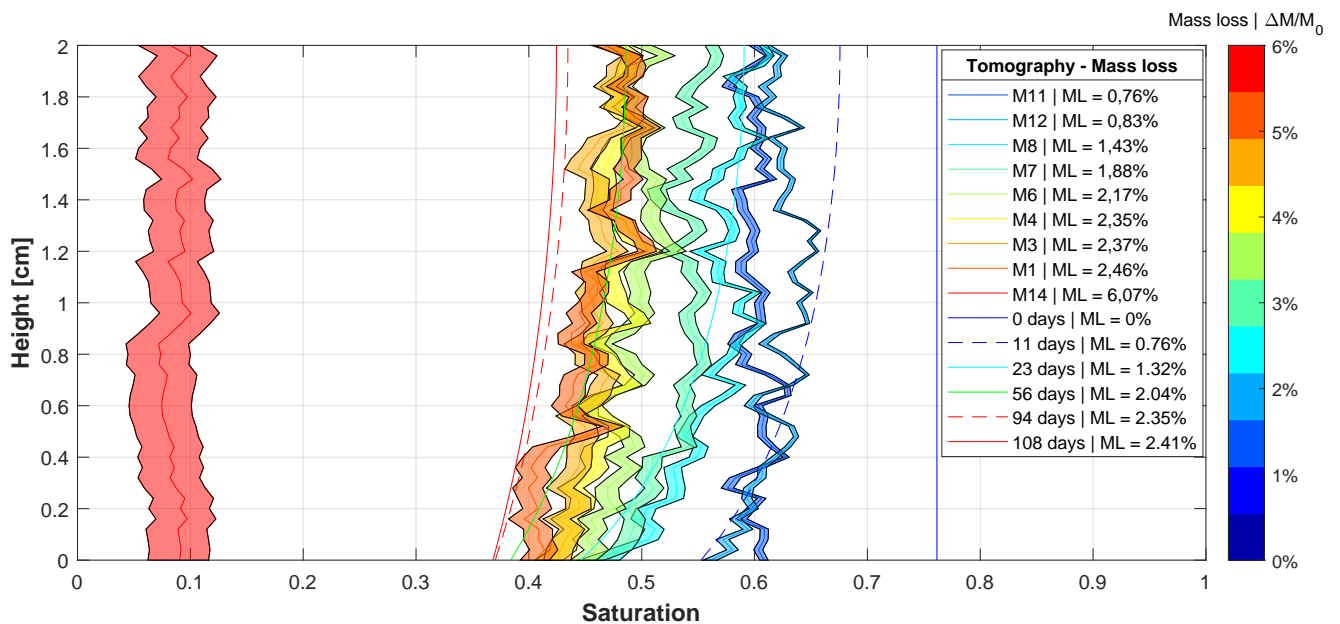


Figure 3.11: Saturation gradients

From the back analysis,  $K$  and  $h_{bc}$  are found to be equal to  $10^{-20}$  and 0.4 respectively. The value of  $h_{bc}$  was found two order of magnitude lower than other reported studies [Soleilhet et al., 2020]. This is mainly due to absence of ventilation in the hydrically controlled chamber. On the other hand, the value of  $K$  is slightly higher than the common estimation of this parameter. This can be related to the choice of the numerical model which takes only the permeation of liquid water into account without considering the diffusion of vapor in the system. The low value of coefficient of hydric exchange reduced the kinetics of the process which gave therefore more time to the slow diffusion of vapor to takes place in the porosity. The high value of the back-calculated parameter “ $K$ ” is therefore due to the summation of two distinct water transport processes: liquid water permeation and vapor diffusion.

## 3.6 Conclusion

In this paper, an experimental-numerical approach was proposed to fully characterize the hydric state and properties of cement-based porous media. The originality of this work lies in the application of neutron tomography for the first time for the drying of cement-based material at low temperature.

A set of laterally-sealed cylindrical samples were put to dry sequentially in a thermo-hydric controlled chamber having their weight loss characterized in time. A set of neutron tomography were then acquired for those samples and resulted in a set of attenuation profiles. Using an elaborated multiphase partitioning, the different species contribution to the total attenuation of the mixture was calculated. This has led for the estimation of the volumetric fraction of water that was lost at a certain drying period with respect to a reference non-drying sample. An additional transition from volumetric fraction to saturation of liquid water was established by estimating the initial saturation and the porosity of the material.

The saturation profiles were plotted versus the height of the sample and showed a 10% gradient between the exchange surface and the core of the sample. The overall water loss of each sample calculated from the image-based saturation profiles were compared to acquired balance measurements and were found in a good agreement.

After characterizing the spatio-temporal hydric state of the material, *i.e.* mass loss history and saturation gradients, a simplified hydric finite element model was used to satisfyingly reproduce the experimental results. This commonly used model simplifies the physical description of the processes involved in the drying by considering only the permeation of liquid water. The fitting of the experimental data sets has led to the indirect back calculation of hydraulic properties such as intrinsic permeability and coefficient of hydric convection.

## 3.7 Data availability statement

The raw neutron tomography data-sets of the mortar samples are available at:

<http://doi.ill.fr/.../ILL-DATA.UGA-98> - the analyzed experiment are in folders 01\_M1, 02\_M7, 03\_M11, 05\_M14, 06\_M15, 07\_M6, 08\_M16, 09\_M8, 10\_M4 and 12\_M3.

## Chapter 4

# Simultaneous x-ray and neutron 4D tomographic study of drying-related hydro-mechanical behavior of cement-based material at moderate temperatures

### Paper context:

*It has long been thought that controlled laboratory drying conditions, i.e., at  $T = 20^{\circ}\text{C}$ , is representative of environmental drying ( $T < 60^{\circ}\text{C}$ ). However, recent studies have shown a non-negligible impact of temperature on the evolution of hydraulic properties, namely the permeability to liquid water and the first desorption isotherms [Poyet, 2009][Drouet et al., 2015]. Additionally, at such moderate temperatures, cracks are likely to develop due to the differential thermo-hydral strains between the aggregates and the paste. These cracks can have a significant impact on the local drying kinetics in the damaged materials. This chapter addresses these two issues by characterizing both the evolution of moisture gradients and the hydraulic impact of cracks in heated cement-based materials. This was done by taking advantage of the high complementarity between neutron and x-ray tomography, to track the moisture transport and follow the cracking initiation and propagation respectively.*

*This chapter presents therefore a more complex and realistic study of drying than the one presented in chapter 2 since it includes the additional thermal and mechanical effects, i.e., the effect of temperature on hydraulic properties and the effect of cracks on the local drying. The experimental findings constitutes a sufficient dataset to calibrate and improve the predictive capacity of the THM numerical models, in terms of thermo-hydric coupling as shown previously in chapter 1 and in terms of hydro-mechanical coupling as will be shown in the shortcoming annex 1.*

### Authors:

Hani Cheikh Sleiman, Alessandro Tengattini, Matthieu Briffaut, Bruno Huet, Stefano Dal Pont

### Paper status:

Submitted to *Cement and Concrete Research*

## Abstract

The drying of cement-based materials is intimately related to their durability, which has significant economic, social and environmental repercussions. The evolution of the saturation of the pore network and the associated drying shrinkage are in fact leading causes of cracking and of the ensuing penetration of aggressive chemicals.

This process is highly heterogeneous, due to the thermo-hydric spatial gradients developing in the material from the exposed surfaces to its core and because of local effects, driven by the intrinsically heterogeneous micro-structure (*e.g.*, by the distribution of pores and aggregates). It follows that macroscopic, sample-scale measurements cannot fully disclose the complexity of the underlying processes. In the last few decades, significant advances in full-field techniques have allowed an unprecedented insight into these local processes. For cement-based materials, x-ray and neutron tomography lend themselves as ideal, and highly complementary, tools for the study of their thermo-hydro-mechanical behavior. Notably, the high sensitivity to density variations of x-ray imaging gives access to the developments of fractures, in 4D (3D + time). On the other hand, neutron tomography allows the study of the evolution of the moisture field in 4D, thanks to its high hydrogen sensitivity. The combination of these two techniques provides a unique insight in thermo-hydro-mechanical couplings, *e.g.*, the effect of cracks on the water content field.

This contribution presents novel 5D datasets (3D tomographies along time, plus truly simultaneous x-ray and Neutron rapid acquisitions) *in-operando* of a cement paste and of a concrete sample heated at moderate temperatures (up to 140 °C).

The analysis of this 5D data-set (once aligned in time and across modalities) allows for example a quantification of the 4D moisture profiles which were found to predict an overall water loss at hydric equilibrium coherent with the corresponding analytical analysis. In the cement paste sample, the x-ray dataset captures the evolution of an extensive cracking network, opening and propagation toward the core of the sample. A novel analysis procedure is here proposed which allows the extraction of these fractures and the analysis of their interplay with local drying as captured through neutron imaging. This for example reveals the depth of penetration of drying in the vicinity of the fractures along time, which is essential for the assessment and calibration of hydro-mechanical coupled models.

## 4.1 Introduction

The durability and structural serviceability of cement-based materials are major concerns in civil engineering due to their significant economic, social and environmental implications [Smil, 2014]. Drying plays a central role in this, given that the changes in saturation of the pore network, together with the associated drying shrinkage are leading processes in the cracking of concrete [El Tabbal et al., 2020]. This is also pivotal in controlling the potential penetration of aggressive chemicals [Tuutti, 1982].

Historically, the vast majority of laboratory studies on the drying of cement based materials have been performed at ambient temperatures (20 °C), which is generally assumed to be either directly representative of the engineering applications or sufficient for direct extrapolation to moderate temperature regimes. Nonetheless, in recent studies [Poyet, 2009; Drouet et al., 2015], temperature was found to have a major effect, not only on the drying kinetics, but also on the amount of free water leaving the porous network. This process is highly heterogeneous, given that significant thermo-hydric spatial gradients develop in between the material exposed surfaces and its core. Additionally, the spatial distribution of pores and aggregates, as well as the opening of cracks, can severely alter these overall gradients. Consequently, macroscopic-scale measurements (*e.g.*, global mass loss) or pointwise sensor-based relative humidity measurements cannot fully capture these highly heterogeneous governing processes. In the last few decades, significant advances in full-field techniques have allowed an unprecedented insight in these local processes [Viggiani et al., 2012; Viggiani and Tengattini, 2019] such as electrical capacitance tomography [Voss, 2020], magnetic resonance [McDonald et al., 2020; Faure et al., 2005; Pel and Huinink, 2009], gammadensimetry [Villain and Thiery, 2006b,a], *etc.* Particularly, x-ray tomography has long been used to study cementitious materials, because of its sensitivity to density variations. It has for example been widely employed to characterize the cracking initiation and propagation in multiple loading conditions such as uniaxial tension [Trtik et al., 2007; Stamati et al., 2018], compression [Meyer et al., 2009; Yang et al., 2013], splitting [de Wolski et al., 2014] and triaxial loading [Stamati, 2020]. Neutron imaging is comparatively less known in this domain but it lends itself as an ideal tool to study the varying moisture profiles thanks to its high sensitivity to hydrogen and its compounds [Perfect et al., 2014; Zhang et al., 2018; Tengattini et al., 2020c]. This technique has been for example widely used to characterize hydraulic processes such as natural drying [de Beer et al., 2004b; Maruyama et al., 2009; Trtik et al., 2011],

front tracking in two-fluid flow [Jailin et al., 2018; Yehya et al., 2018; Kanematsu et al., 2009], water uptake into cracked concrete [Wittmann et al., 2010; Zhang et al., 2010,b, 2011, 2016; Schroeff et al., 2015], moisture migration in heated concrete [Zeilinger and Huebner, 1976; Dauti et al., 2018d; Tengattini et al., 2020a], *etc.*

This extensive application of x-ray and neutron tomography for the study of cementitious materials has nonetheless generally focused on only one of these two highly complementary techniques. Their combined use is comparatively more recent, and follows the development of facilities allowing their combined use. One such facility is the NeXT-Grenoble instrument at the Institute Laue-Langevin in France [Tengattini et al., 2020b]. When these two techniques are combined together, a unique insight is gained into thermo-hydro-mechanical THM couplings, such as, for example the effect of cracks on water content field [Stavropoulou et al., 2019, 2020]. The complementary of these two techniques is particularly evident in the specific case of cementitious materials as shown in figure 4.1, which highlights how only their combined use allows the detection of the key phases (aggregates, pores and cement paste) and of the processes studied here (drying).

The aim of this contribution is in fact to observe and quantify the complex interplay between drying of cementitious materials and damage, in 4D (3D+time). This experimental quantification is, in turn, essential for the calibration, validation and improvement of state-of-the-art numerical models [Dal Pont et al., 2007; Cheikh Sleiman et al., 2020a], for example in order to identify parameters related to THM coupling [Bouhjiti et al., 2018]. Specifically, this paper focuses on the measurement of moisture migration and crack propagation in cement paste and concrete exposed to moderate temperatures. These heating tests are performed using a bespoke heating cell (introduced in section 4.2.2) while acquiring *in-situ simultaneous* x-ray and Neutron tomographies at the NeXT-Grenoble instrument. This imaging facility enjoys the highest cold neutron flux in the world for imaging purposes, of particular importance given the required spatio-temporal resolution.

To study these micro-scale processes and take full advantage of the multi-modality of the acquisitions, it is essential to register (align) subsequent tomographies along time as well as across acquisition modalities, as detailed in section 4.3.1. A number of image analyses methods, dedicated to the study of moisture migration and the quantification of the local effect of fractures on it are also introduced here (sections 4.3.2 and section 4.3.4.2). The results captured the hydric state evolution of the heated samples with the help of a proposed transition between neutron attenuation and water content. In addition, the x-ray cracking extraction coupled with the neutron attenuation field has given a unprecedented estimation of cracking local effect on drying.

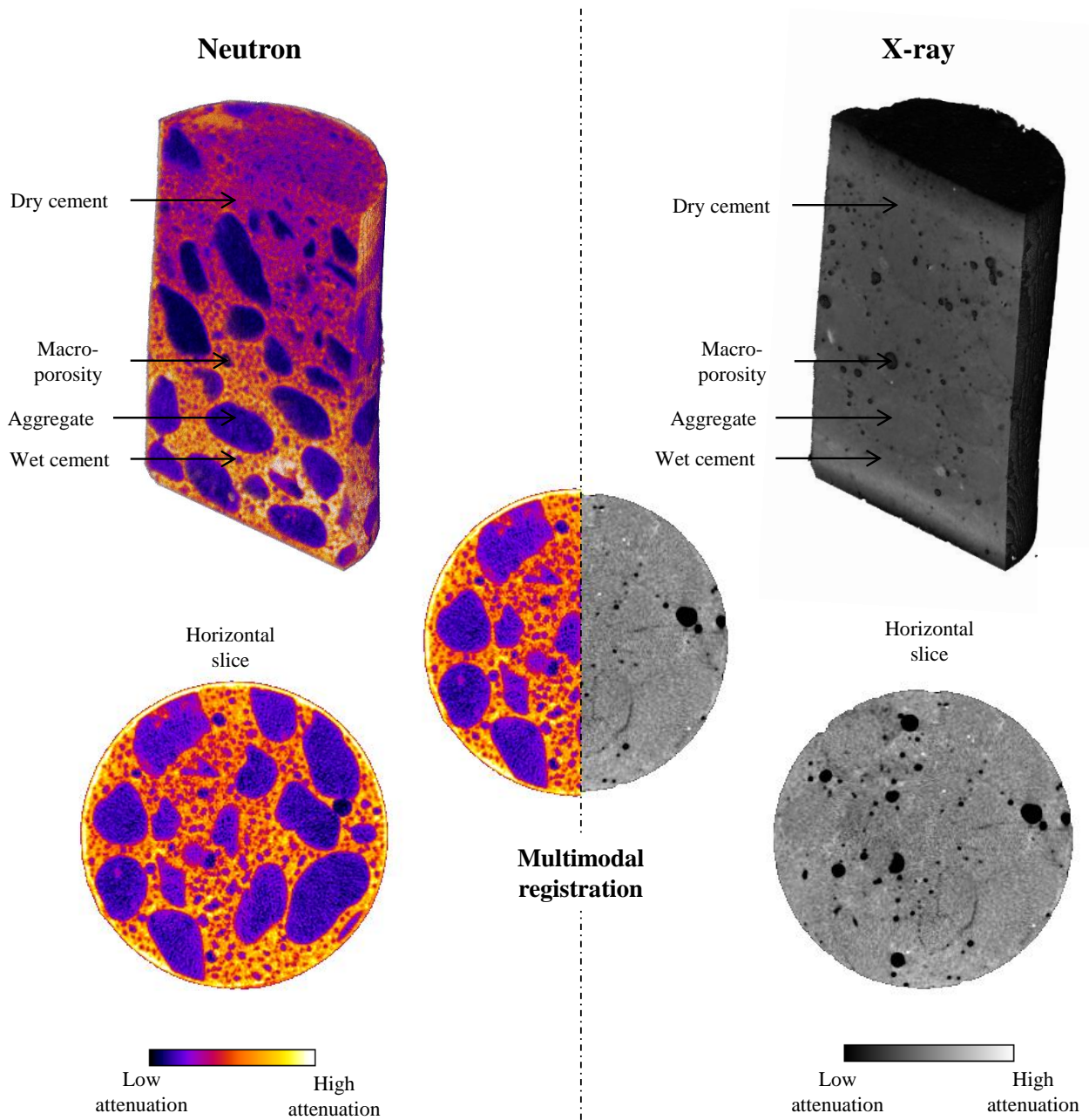


Figure 4.1: Vertical and horizontal slices of the 3D reconstructions of the neutron and x-ray tomographies of the concrete sample, highlighting the high complementary of the micro-structural information obtained with these techniques. The neutron attenuation field (the average attenuation of the materials contained in a voxel  $\mu_n$ ) on the left of the partially saturated concrete sample highlights aggregates and pores from the cement paste which is further differentiated in dry and wet. Nonetheless pores and aggregates have comparable attenuation in the neutron tomography whereas they have significantly different x-ray attenuations  $\mu_x$ , as shown on the right. Their rigorous coupling is made possible by their multi-modal registration (detailed in section 4.3.1).

## 4.2 Material and methods

### 4.2.1 Specimens

Two experimental campaigns were performed on two samples, a cement paste one and a concrete one. The water to cement ratio of the former is 0.5 ( $w/c = 0.5$ ). The material was cast within a commercial plastic mold imposing a cylindrical shape of 6 cm in height and 3.5 cm in diameter. The cement sample was cast

using heavy water  $D_2O$ , a form of water that contains a larger than normal (99.8 %, in this case) amount of the hydrogen isotope deuterium ( $^2H$  or  $D$ ), rather than the more common hydrogen-1 isotope. Heavy water is nearly one order of magnitude less neutron-attenuating than normal water. This is made necessary by the high interaction between neutrons and hydrogen, which would be sufficient to attenuate virtually all the neutrons in these samples [Stavropoulou et al., 2019], inducing an unacceptable signal-to-noise ratio in the tomographies. Given that a change in the sample geometry (and notably a reduction of the radius) would negatively affect the representativity of the sample, heavy water is employed here in lieu of normal water. Heavy water is virtually identical to “light” or ordinary water in terms of its physico-chemical properties:  $D_2O$  is 11% denser and 20% more viscous than  $H_2O$ , the other properties such as boiling temperature, fusion temperature, surface tension, *etc* being even closer together for the two isotopes [Chaplin, 2017]. The effect of the use of  $D_2O$  on the cement hydration reaction is reported for example in [Christensen et al., 1986; King et al., 1988], which show that the induction period and the time to the maximum evolution of  $C_3S/D_2O$  heat evolution [W/K] are delayed when compared to those of  $C_3S/H_2O$ . However, the final value of the integrated heat output is remarkably similar. In addition, the mechanical compression stress/strain curves reported in [Yehya, 2018] of two concrete mixed respectively with  $H_2O$  and  $D_2O$  are virtually identical. Based on these observations, for the purposes of this paper, it is assumed that the conclusions drawn for heavy water-cast samples are applicable to the equivalent cement cast with ordinary water.

The sample was cast with a type K thermocouple implanted within the paste upon casting around the middle height for measuring the temperature. The exact location of the welding point of the thermocouple has been accurately determined *a-posteriori* from the tomographies and found to be 35 mm from the top. Another thermocouple was added at the sample top surface to better assess the effect of the air gap between the radiator and the sample on the heating process. After casting, the sample was left in its mold for a month, after which was placed in a bath of heavy water maintained at 20 °C.

The composition of the second, concrete sample, is detailed Table 4.1. The cylindrical specimen was cored out from a well-vibrated larger bloc using a diamond coring bit with an inner diameter of 27 mm, and has a height of 45 mm. Unlike the cement paste sample, the concrete specimen was cast, cured and saturated using normal water. In this case, in fact, the relatively high volume fractions of sand and aggregates (which are less neutron-attenuating than the hydrated paste) allow a sufficient signal-to-noise ratio for representative sample sizes without the need for the adoption of heavy water.

Just before testing, the sample was wrapped in three layers of self-adhesive aluminium tape (aluminium being particularly neutron transparent), to minimise moisture escape from the lateral surfaces during the test, to induce a unidirectional moisture flow. The aluminium tape used in the test (3M<sup>TM</sup> High Temperature Aluminum Foil Tape 433) has a working temperature up to 316 °C. The sample was also equipped with a type K thermocouple at mid-height (attached to the lateral surface) and a second thermocouple was placed at the top of the sample to measure its surface temperature.

Concrete composition	Quantities [ $Kg/m^3$ ]
Water	174
Cement (CEM I B 52.5)	348
Sand (1.8 mm)	826
Gravel (0.5/8 mm)	991

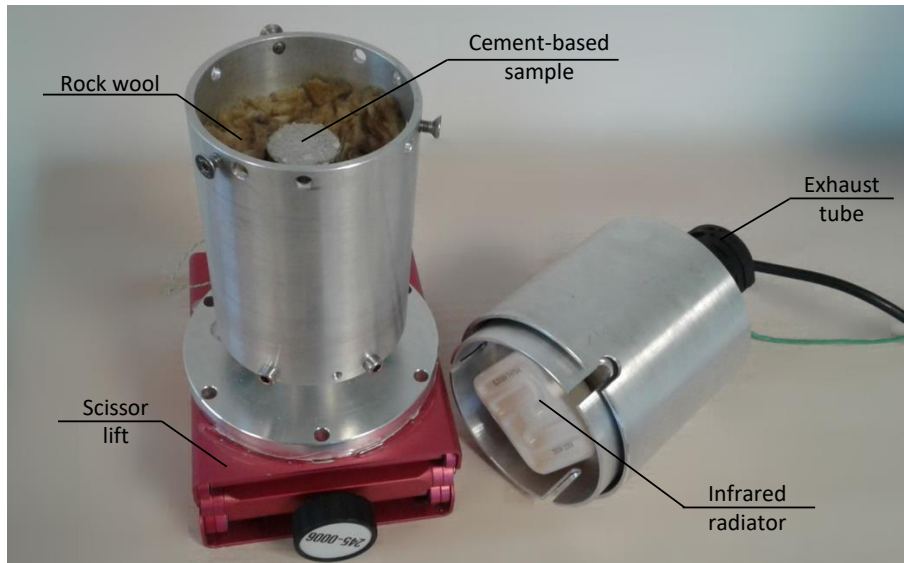
Table 4.1: Composition of the concrete used for sample 2

## 4.2.2 Heating cell

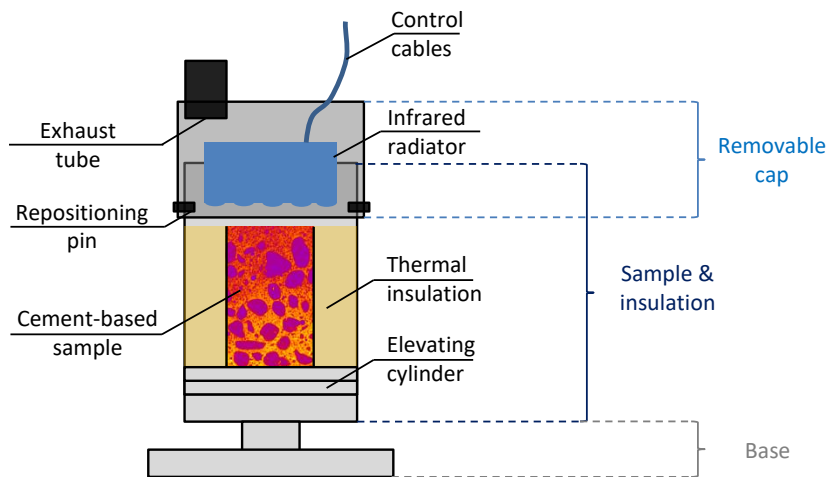
A novel heating cell, based on the prototype presented in [Dauti et al., 2018d] was developed in this work. The improved design allows the reduction of minimum distance from the sample to the detector which influences the ultimate resolution (as detailed in a next section).

The designed cell has a principal functionality of heating the samples on their top surface, from which the moisture is extracted. The materials and design were chosen to be as transparent as possible to both neutrons and x-ray, while also fulfilling other needs related to safety requirements. It is for example equipped with an exhaust tube connected to a vacuum system in order to evacuate gases and airborne dust that could become slightly radioactive when exposed to a neutron beam. The cell components are assembled in two principal parts (figure 4.2). The part on the left of the figure is the base of the cell, supporting a cylindrical tube of 80 mm inner diameter and 110 mm height. This tube contains the sample, which is surrounded by rock wool (acting as lateral heat insulator). The top part of the cell contains the heating source, which is in

this case a ceramic infrared radiator (Elstein) with a square surface of 36 cm<sup>2</sup> and a power of 250 W. The temperature of the radiator is servo-controlled thanks to a built-in thermocouple connected to regulator. The radiator is fixed to the cap-like aluminum piece containing all the electrical elements and on which the exhaust evacuation system is fixed.



(a)



(b)

Figure 4.2: The designed heating setup: (a) Disassembled setup highlighting the positions of the sample wrapped with aluminum tape for moisture isolation and rockwool for heat isolation, the exhaust output and the infrared radiator (b) schematic view.

### 4.2.3 Thermal testing conditions

In both experimental campaigns, the temperature of the radiator was servo-controlled. Given the air gap of few millimeters between radiator and sample, there is a slight discrepancy between the imposed temperature and the one at the top of the sample, which was measured thanks to the thermo-couple installed on its top surface. The heating temperature and duration were estimated based on preliminary numerical and experimental analyses and were adapted during the tests based on the observed results. In addition, the heating rate and duration and the maximum temperature were imposed carefully to not induce disturbances to the chemically-bonded water quantity in the material.

For the concrete sample, the temperature history in figure 4.3 (a) marks the time of the simultaneous N/X

tomographies analyzed here (in red annotation for the data used for the upcoming multi-modal registration analysis in section 4.3.1 and in blue annotation for the upcoming hydric gradient analysis in section 4.3.2). Analogously, in the temperature history in figure 4.3 (b) the the simultaneous neutron and x-ray tomographies are marked in blue, and the red annotations mark the tomographies where the hydro-mechanical analysis were performed.

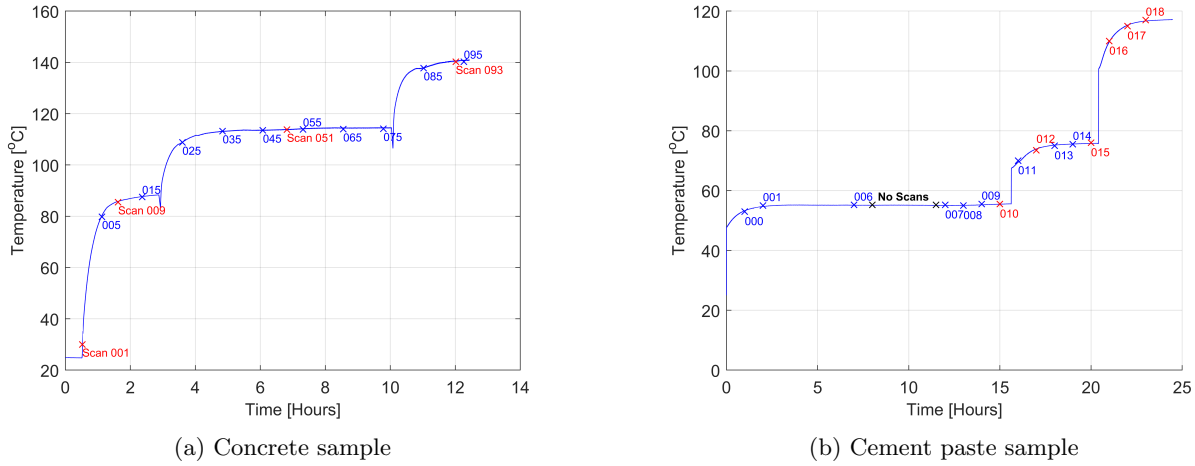


Figure 4.3: Measured temperature on the top surface of the tested sample

#### 4.2.4 Neutron and x-ray tomography acquisition

The x-ray and neutron tomographies were acquired at the NeXT-Grenoble beamline (detailed in [Tengattini et al., 2020b]).

Two slightly different sets of parameters were employed in the two campaigns on concrete and cement, respectively, each optimised for the expected speed of the processes. In the former, the temperature at the top of the sample was imposed to be relatively high (around 90 °C) at the beginning of the test suggesting a fast process. The parameters were therefore optimised to achieve simultaneous acquisitions every 7 minutes. Specifically, 900 projections were acquired over a 360° rotation (necessary for the conic x-ray geometry). For the neutron, a field of view of 60 mm was selected to cover the entire sample, by adopting a 100 mm Zeiss Macro lens, f./2.0, mounted on a Hamamtsu ORCA 4v2 camera (2048x2048 pixels). To accelerate the acquisition, each pixel was binned 4 times, yielding a 116 µm pixel size. Each neutron radiography was average over two acquisitions each with a 0.2s exposure, giving a relatively high Signal to Noise Ratio SNR=30. Given the maximum resolution attainable with the selected voxel size, a 100 µm thick LiF:ZnS scintillator was chosen. Analogously, a pinhole diameter  $D$  of 23 mm was selected (corresponding to a neutron flux of  $1.5 \times 10^8$  ncm<sup>2</sup>s), which, given its distance to the detector  $L$  of 10 m and a sample/detector distance  $l=50$  mm yields a neutron penumbra  $d = D/L * l = 115$  µm, well compatible with pixel size and scintillator thickness. These factors should yield a resolution just above 100 µm, coherent with the expected characteristic heterogeneity size. For the x-ray, the generator was set at 130 V and 230 µA, which allowed the acquisitions of 9 frames per second, each of which was then averaged over 4 projections, acquired fully simultaneously to the neutron tomographies.

The second experimental campaign, on cement paste, was set at a lower temperature, suggesting a slower process, and allowing for a higher spatial resolution to be achieved. In this case, 1200 projections were acquired over 30 minutes for a 360° rotation fully simultaneously. To achieve this, a 50 mm f./1.2 Canon Lens was adopted, yielding a pixel size of 50 µm, with no binning. Given this smaller pixel size, a thinner, 50 µm thick LiF:ZnS scintillator was selected. Additionally, a SI15 pinhole  $D$  (corresponding to a neutron flux of  $7.5 \times 10^7$  ncm<sup>2</sup>s) was selected to achieve a maximum attainable resolution of about 75 µm. Each neutron radiography was the average of 3 individual projections each with a 0.5s exposure, resulting in a SNR=47. The x-ray source was maintained at 130 V and 230 µA, and the flat panel was set still at its maximum speed of 9 frames per second, but to maintain the 30 minutes of the simultaneous tomography, each radiography was the average of 13 individual acquisitions. Between each 30 minute set of tomographies a 30 minute pause was added, to minimise unnecessary sample and environment neutron activation. It should be noted that this was chosen over a smaller pinhole/longer exposure to ensure that the sample status did not change excessively during a given tomography, which would have caused motion blurring artefacts.

These sets of radiographies were reconstructed into the corresponding 3D volumes by means of the Feldkamp (FDK) back projection algorithm, as implemented in the commercial software X-act (from RX-Solutions). Besides the aforementioned medianing of the radiographies, some small correction for beam hardening was also applied during the reconstruction step. Thanks to the calibration of the instrument the volumes are pre-aligned in the two modalities although a post-reconstruction sub-pixel alignment was also performed as detailed in the next section. An example of the 3D neutron and x-ray attenuation fields are reported in figure 4.1 for the concrete sample.

Supplementary videos showing water content evolution and the cracking propagation can be found in the online version of this article and at [https://www.youtube.com/watch?v=D5\\_\\_70ieEd4](https://www.youtube.com/watch?v=D5__70ieEd4) and <https://www.youtube.com/watch?v=kgqPe-tXmA4>.

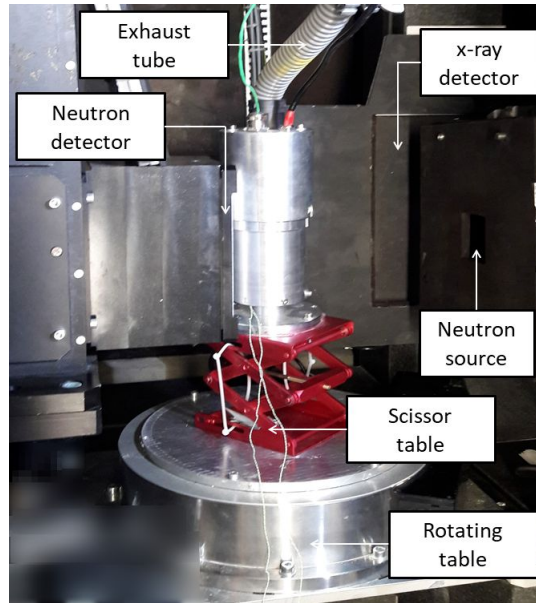


Figure 4.4: Heating cell in beam-line (x-ray source yet to be moved): the cell is to be crossed by a neutron flux on a first axis and by an x-ray flux on a nearly-perpendicular second axis

## 4.3 Quantification of hydro-mechanical processes through image processing

### 4.3.1 Single mode and multi-modal registrations

In the two experimental campaigns, two sets of “5D” tomographies (3D+time+x-ray/neutron) have been acquired. While pixels of an individual tomography are naturally “aligned”, having a coherent coordinate system, the same voxel can come to represent slightly different areas of the sample even within the same modality along time. For example, thermal expansion and system vibrations can slightly affect the position of the sample along time. Additionally, while the acquisition system is calibrated to measure and compensate for the relative position of the object between modalities, a misalignment of few tens of microns is to be expected, for example because of the relative displacement between the detectors induced by thermal expansion. It follows that to have each voxel represent the same sub-volume of the sample across time and to have a 1:1 sub-pixel correspondence between modalities, it is essential to align (register) all these 3D volumes. A cumulative misalignment would in fact be detrimental to some of the analyses presented below, which rely on the comparison between a given state and its previous configuration and across modalities to quantify the local processes.

The alignment along time relies on a well established approach, a global Digital Volume Correlation of the sample. Specifically, the intensity-based incremental Lukas & Kanade [Lucas and Kanade, 1981] approach was adopted, taking advantage of its implementation within the SPAM open source image processing suite [Andò et al., 2017; Stamati et al., 2020].

To perform the multi-modal registration, a more recent development is instead adopted. Introduced in [Tudisco et al., 2017] and implemented within the aforementioned image analysis suite SPAM in [Roubin et al., 2019], this method generalises the Lukas & Kanade same-modality registration framework for fields

obtained with multiple modes of acquisition. In brief, this method determines the linear transformation operator between the two modalities that minimises a functional similar to the single-modality one, except for the conversion of the gray value from one modality to the other, so as to have a coherent evaluation thanks to a joint histogram.

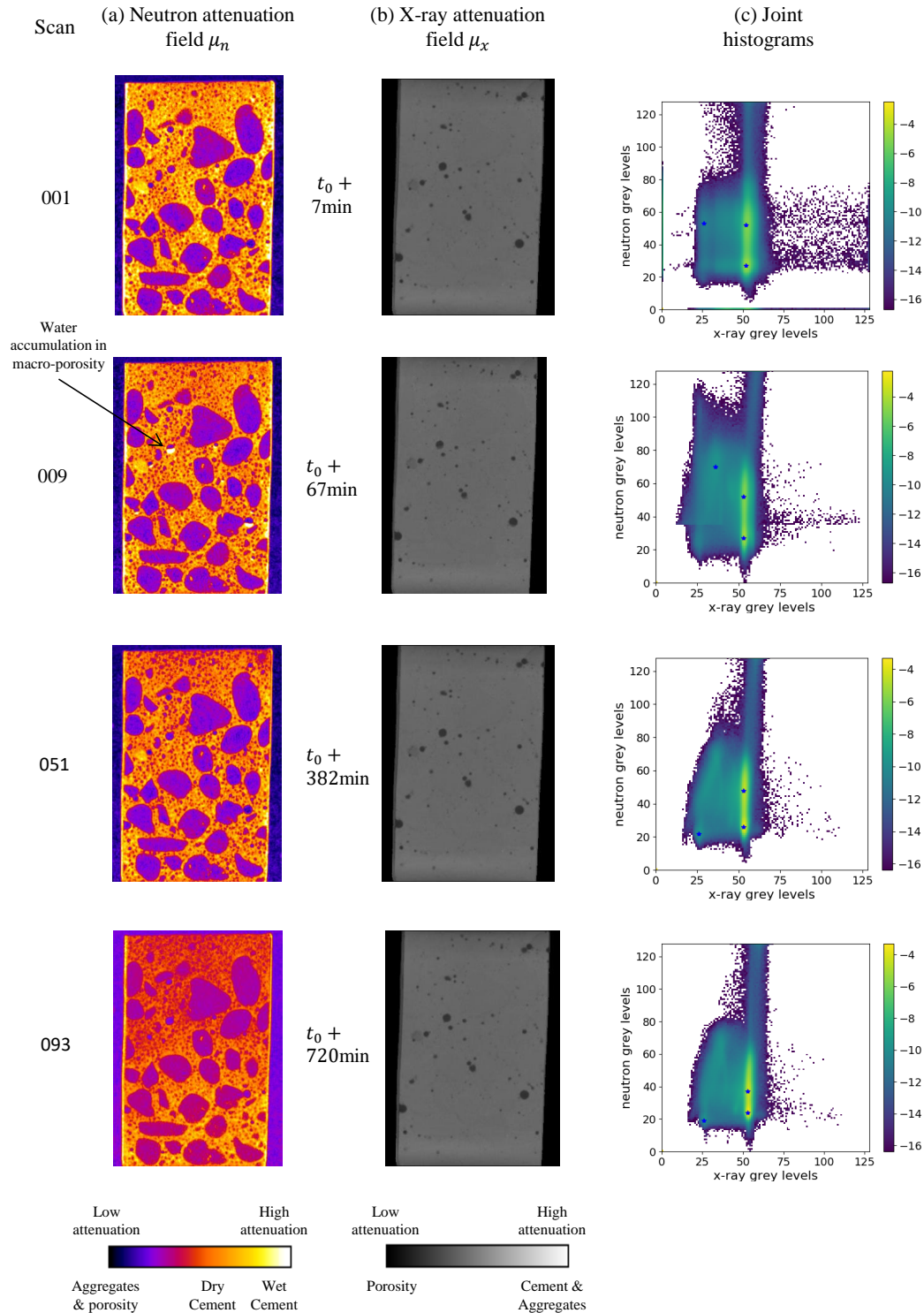


Figure 4.5: Evolution of neutron attenuation field  $\mu_n$  and x-ray attenuation field  $\mu_x$  throughout the drying experiment which was captured statistically thanks to joint histograms.

All neutron tomographies were registered to a reference neutron acquisition. This acquisition was also used as a reference alignment for the x-ray tomography acquired at the same time, adopting the multi-modal registration, to which all subsequent x-ray tomographies were also aligned, to build a geometrically coherent

5D dataset.

This is exemplified in figure 4.5, where the attenuation fields of the registered N/X tomographies are reported for four representative drying stages. The neutron tomographies (to the left of the figure) highlight how, in its initial state 001, water is visibly filling some of the relatively small macro-pores, while other macro-pores show no pore-filling. Tomography 009, acquired one hour after the beginning of heating, shows water accumulation in different macro-pores, zones of temporary lower pressure. As the drying progresses, the attenuation of neutron decreases, starting from the top of the sample, *i.e.*, closer to the radiating ceramic, where the internal relative humidity is lower. The x-ray acquisitions (in the middle of the figure) do not highlight this drying process, due to the lower attenuation of x-ray by water. The main purpose of the complementary x-ray acquisitions was in this case the study of the development of fractures, if any. As investigated more in detail in Appendix B, no cracking was observed at the used resolution for the concrete sample (unlike in the cement paste sample analysed next).

These observations are further supported by the joint histograms to the right of figure 4.5, where the colorbar shows the frequency of occurrence of any given pair of gray values (specifically, of x-ray on the x-axis and of neutron on the y-axis). In this representation, three main peaks can be identified, one corresponding to cement paste (initially with coordinates around [52, 52]), one to aggregates ([52, 27]) and one, the most scattered, to pores ([26, 53]).

This scattering is related to its modest fraction in the volume and to the dynamics of the pore-filling water which is captured throughout the joint histogram. Initially, in tomography 001, liquid water was accumulated in small macro-pores whereas the comparatively larger macro-pores were empty. As the heating starts, the pore-filling slightly increases in the macro-pores and reaches a maximum in tomography 009. This shift in the porosity corresponds to a variation of the average peak to ([38,72]) in the joint histogram, *i.e.*, higher attenuation in both modalities. The water accumulation decreases again as the sample temperature continues to increase, shifting again the porosity peak to ([26,21]), a reference value for empty pores.

Additionally, as also intuitive from the gray value images, aggregates and pores are indistinguishable in the x-ray images while quite distinct in the neutron one. As drying progresses these two peaks move closer together because of the reduction in attenuation in the neutron images.

### 4.3.2 Analysis of the hydic behavior of the concrete sample

This section explores the temporal evolution of the vertical gradients of neutron attenuation induced by drying, followed by the estimation of the corresponding water content. These experimental values are then compared to their estimations based on analytical analysis.

#### 4.3.2.1 Image segmentation and granulometry analysis

Moisture transport in concrete happens essentially in the cement paste porosity and in the macro-porosity, given that aggregates and sand grains are comparatively impermeable. In order to characterize fluid transport, the aggregates and the sand particles should not be considered in the analysis. The aggregates, larger and easily detectable in the images, were therefore isolated and removed from all ensuing analyses. This operation is relatively straightforward giving their distinct attenuation value in the neutron tomographies, much lower than that of the wet cement paste, which can be used to identify them (a process named segmentation). The choice of a threshold gray value isolating the aggregates can be *a-priori* user dependent but a number of strategies were here adopted to characterize the sensitivity of this measurement. Firstly, Otsu's method [Otsu, 1979] was adopted to choose a repeatable and user-independent value. Additionally, the sensitivity of all reported analyses to this choice was assessed by repeating all operations for two "extreme" minimum and maximum threshold values, as shown in figure 4.6, and comparing the resulting fluctuations in the measures to the general trends of the process.

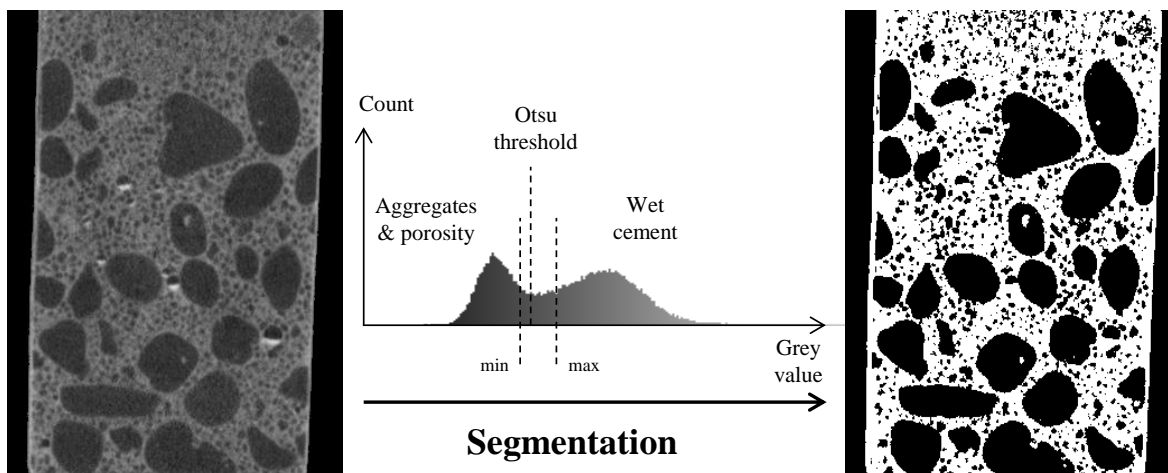


Figure 4.6: Schematic of the segmentation procedure used to remove the aggregates and sand grains from the moisture analysis. An “Otsu” threshold was used as operator-independent guess of the threshold value. A sensitivity analysis of any the potential error induced by this segmentation step was performed by repeating all ensuing analysis for user-defined min and max threshold values.

To better assess the quality of this segmentation as well as to better understand the minimum grain size removed with this technique, a granulometric analysis was also performed. This consists in separating the segmented image into the individual grains (applying a morphological operation named “watershed” [Beare and Lehmann, 2006]) and measuring the grain volume which can then be converted into the diameter of a volume-equivalent sphere. The probability density function of these grain sizes is compared in figure 4.7 against experimental sieving measurements provided in [Vu, 2007] for a range of gray value thresholds. The numerical and adapted experimental results are essentially coherent, and the slight mismatch can be explained by multiple factors. Firstly, aggregates are assumed to be perfect equivalent spheres in the image analysis, which ignores the complex morphology of the grains. In addition, this scattering could be linked to experimental mixture variability between the two experimental campaigns (this one and the one of [Vu, 2007]). It is worth mentioning all fines having an average diameter lower than 800  $\mu\text{m}$  (corresponding to 6 to 7 pixels) were not captured by segmentation due to resolution limitations. This information is key for the upcoming analytical analysis.

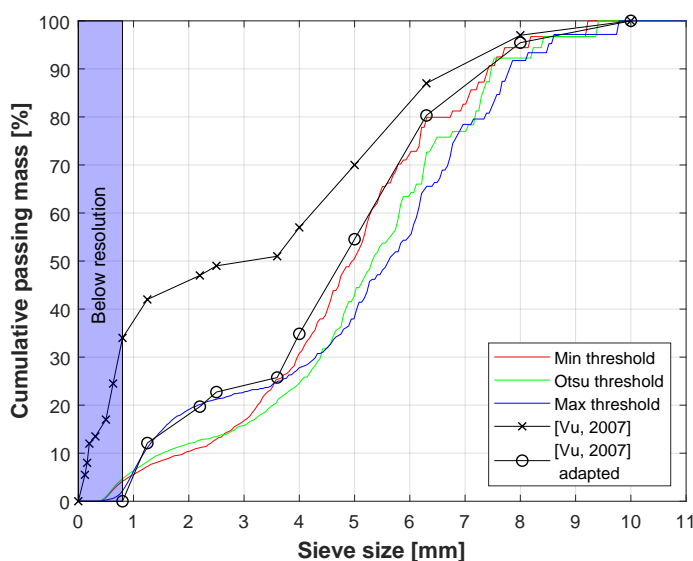


Figure 4.7: Particle size distribution procedure: (Left) Vertical slice of a labelled aggregate volume, (Right) Equivalent-sphere particle size distribution: threshold sensitivity analysis and comparison with experimental sieving measurements

#### 4.3.2.2 Evolution of mixture attenuation

After registering all the neutron volumes and segmenting the reference neutron image, the average gray level attenuation of the remaining mortar along the height of the sample is calculated for each each volume. In this operation, the gray value the “mortar” voxels (*i.e.*, all the ones not removed by the procedure detailed in the previous section) of each horizontal slice were computed for all the tomographies along the process. Additionally, only the 80% inner part of the sample was taken into consideration this analysis in order to omit any effect of the beam hardening artifact (originating from to the polychromaticity of the neutron beam and scattering) and lateral drying (due to the imperfectness of aluminum lateral sealing), as detailed in appendix A. At the beginning of the test, the gray value profiles indicate a mostly homogeneous water distribution along the sample, with local fluctuations below 5% (likely caused by variations in the initial saturation along the height of the sample). As the temperature in the sample increases, the drying process starts affecting predominantly the top of the sample. As the test progresses further, more of the sample undergoes water loss, and the gray value gradient is nearly linear along most of sample height. Eventually, the top 1.5 cm of the sample reaches an asymptotic value corresponding presumably to the hydric equilibrium for the applied boundary conditions.

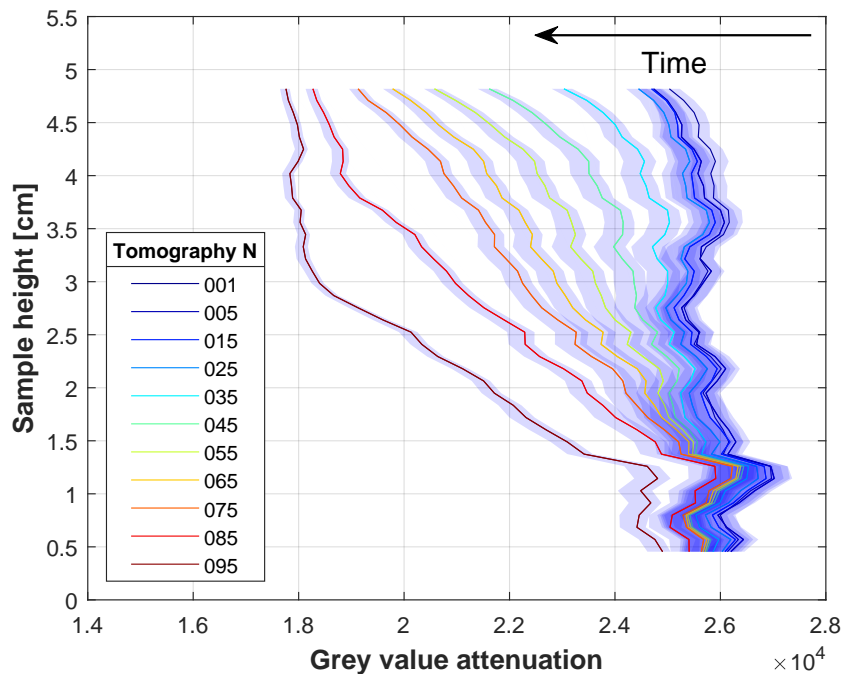


Figure 4.8: Gray value attenuation gradient evolution along the sample height

#### 4.3.2.3 Estimation of the capillary water fraction evolution

In the previous section, we analysed the evolving gray value profiles. While this is proportional to water content, the formulation and validation of behavioural laws require to estimate the corresponding variation of water content. To do so, it is important to understand how water loss is related to the attenuation of the mixture. Once the aggregates have been removed as detailed above, the attenuation of the remaining mortar voxels is the combination of the attenuation of three “species”:

- air, in the micro-porosity,
- capillary water ( $cw$ ), both free and adsorbed water in the micro-porosity,
- dry *hydrated* mortar ( $dhm$ ), comprising solid gel, unhydrated cement and chemically-bonded water

Specifically, for voxels representing mortar, the attenuation coefficient is the summation of the individual contributions of the species composing it, weighted by their volumetric fraction, which can be expressed as:

$$\mu_m = W_{cw}\mu_{cw} + W_a\mu_a + W_{dhm}\mu_{dhm}, \quad (4.1)$$

Where  $\mu_i$  and  $W_i$  are respectively the attenuation coefficient and the volumetric fraction of the specie  $i$ . To then transition from these attenuation values to an estimate of water content number of hypotheses are made here:

- The fine sand grains that remains in the material after the segmentation step detailed in section 4.3.2.1, having a diameter smaller than 800  $\mu\text{m}$ , are assumed to be homogeneously distributed in the whole volume.
- The tomographic attenuation coefficient of the water remain constant throughout the experiment. Its gray value value is here directly assessed from the images by locating and measuring water-filled macro pores at the beginning of the test. This operation is repeated in 40 separate areas, yielding an average  $\mu_w=51000$  with a standard deviation  $\sigma_w=2000$ .<sup>1</sup>
- The volumetric strain of the sample is does not induce significant variation in density (which can otherwise be treated as in [Stavropoulou et al., 2020] for instance). This assumption is supported by the lack of fractures when analyzing the residual of the x-ray fields across the test as well as by a digital volume correlation analysis, which suggests less than 0.28% volumetric strain (see appendix B).
- No chemical reaction during the test. Dehydration of the hydrated cement leading to the loss of chemically-bonded water can be neglected due the short-heating duration and the maximum temperature reached within the sample. This assumption is supported by the experimental observations of [Wang et al., 2019] where water loss due to dehydration at very low heating rates ( $<1 \text{ K min}^{-1}$ ) and for the very low equilibrium temperature was relatively low.
- Validity of the Beer-Lambert neutron attenuation law. Scattering can cause a slight deviation from this law in the presence of high water content and small sample/detector distance (e.g., [Stavropoulou et al., 2019; Kardjilov et al., 2005]), neither of which was the case in this test. This implies that a linear proportionality can be assumed in first approximation between the reconstructed attenuation (gray) value and the water content.

Following these assumptions, the variation of the measured compound attenuation can be expressed as:

$$\Delta\mu_{cp} = \Delta W_{cw}\mu_{cw} + \Delta W_a\mu_a \quad (4.2)$$

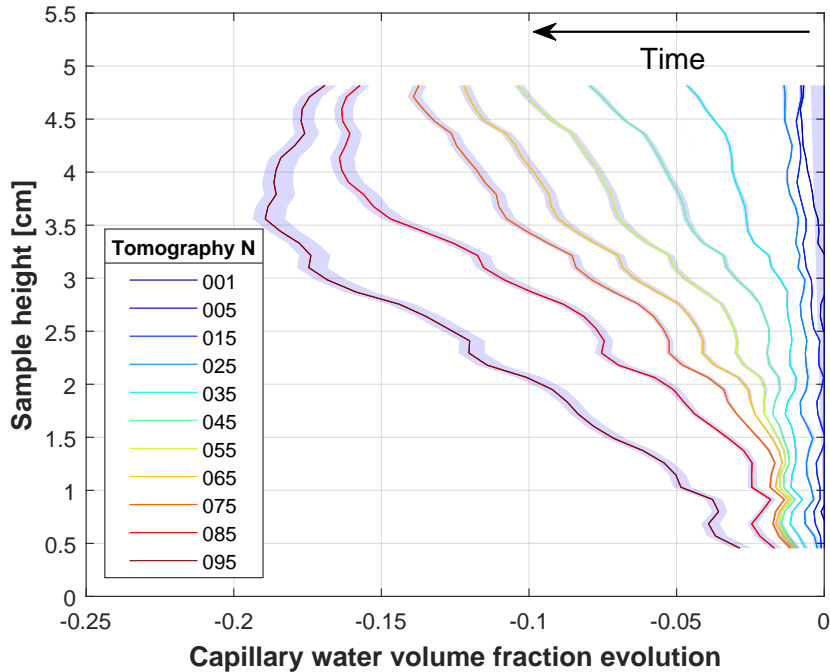


Figure 4.9: Capillary water volume fraction evolution along the sample height

<sup>1</sup>This is to be compared to the one of air which averages  $\mu_a=8700$  and has a standard deviation  $\sigma_a=500$ .

where  $\Delta\mu_{cp}$  can be measured by studying the evolution across time of a mortar voxel, and  $\mu_{cw}$ ,  $\mu_a$  can be directly measured as detailed above. Assuming that  $\Delta W_a = -\Delta W_{cw}$  it is possible to deduce  $\Delta W_{cw}$ , as reported in figure 4.9.

A further step can be made to deduce the actual water content (rather than its evolution) and thus the saturation of concrete starting from the knowledge of the initial or final saturation states. However, the initial state couldn't be assumed to be fully saturated despite the high water/cement ratio and the curing conditions, since, it was possible to observe how some of the larger pores were not saturated at the beginning of the test, thanks to the full-field measures reported (figure 4.5). On the other hand, figure 4.8 shows how, at the end of the test the topmost 1.5 cm of the sample approach an asymptotic value, which could be symptomatic of local hydric equilibrium. However, the latter cannot be precisely assigned to a saturation state. While these initial and final water content couldn't be conclusively assigned, the analysis of the absolute water content was therefore not reported here.

It can nonetheless be observed that the variation of the water content shown in figure 4.9 reaches indicatively a 20% volume fraction difference between the initial saturation state and the equilibrium one. This water volumetric fraction loss was compared to the porosity fraction in the averaged mortar phase remaining after segmentation procedure. We assume that this porosity fraction  $\hat{\phi}_m$  can be estimated by linear interpolation of two extreme porosities, the first being the one of cement paste ( $w/c=0.5$ ),  $\phi_{cp}$ , and the second being the one of the full concrete mixture,  $\phi_c$ .  $\hat{\phi}_m$  was estimated by the following equation:

$$\hat{\phi}_m = \phi_{cp} - \xi_f(\phi_{cp} - \phi_c) \quad (4.3)$$

Where  $\xi_f$  is the percentage of the sand grains that were not captured by the neutrons resolution ( $<800 \mu\text{m}$ ). Only 33% of the total sand and aggregates had a diameter below this value as seen in figure 4.7. The numerical values of  $\phi_{cp}$ ,  $\phi_c$  were reported respectively in [Rougelot, 2008] and [Vu, 2007]. All of this yield an averaged mortar porosity value of 27% which is in close agreement with the water volumetric fraction loss while keeping a margin for the non assigned initial and final saturation.

### 4.3.3 Cement paste drying

A second test was performed on cement paste at lower temperatures, inducing a slower moisture migration which in turn allowed for higher spatial resolutions, as detailed in sections 4.2.4. A similar analysis can also be performed on this sample, as reported in figure 4.10, where the gradients of gray value attenuation over the height of the sample (normalised to their initial state) show the progressive drying from the top of the sample. Analogously to the concrete sample, the gray values have been averaged over 75% of the inner volume to exclude any beam hardening and lateral drying effects.

It can be observed how, in this test, no hydric equilibrium is reached even after 24 hours of testing. Unlike the concrete test, though, it was not possible to directly convert the reported evolution of the attenuation into accurate estimates of water content evolution, given the absence of clear water-filled pores to be used as reference for water attenuation. The reported gray value evolution profiles are nonetheless proportional to the evolution of water content, which can provide an interesting insight into the coupled hydro-mechanic processes, as detailed in the next section.

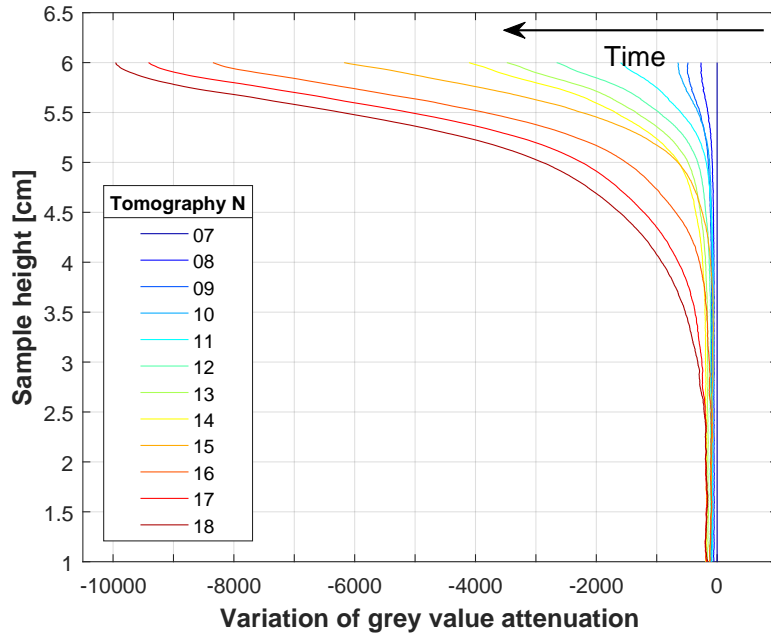


Figure 4.10: Variation of the gray value gradients with respect to the initial hydric state.

#### 4.3.4 Hydro-mechanics of cement paste

The loss of water in the porous network induces a drying shrinkage, which adds to the chemical shrinkage due to early-age behavior hydration. Unlike in the concrete sample analysed above, this leads to the cracking of the cement paste. These cracks play an important hydraulic role, given that they locally significantly increase the permeability, thus accelerating the drying process in their vicinity.

##### 4.3.4.1 Cracking extraction for cement paste

To quantify the development of fractures, the 4D x-ray dataset was studied. The influence of water loss on x-ray is modest (hence the combined use of neutrons) while their higher resolution and density sensitivity make them the ideal probe for crack detection. The fractures are in this case very thin (mostly less than  $200\ \mu\text{m}$ , equivalent to 3 pixel width), consequently, merely applying a segmentation threshold near the air value is not sufficient to isolate them. To extract the fracture network, from each (aligned) volume was therefore subtracted the initial state of the sample. This volume of residual values isolates then the key processes detected by the x-ray: on the one hand the thin but sharp variations in gray value caused by the opening fractures and, on the other, the modest, but diffused density loss caused by the water evaporation. Given the different properties of the two features, it is possible to isolate the latter effect by filtering the residual field with a 3D Gaussian kernel with a relatively large radius of 30 voxels. Subtracting then this filtered volume from the original residual field it is possible to remove the (modest but pervasive) water loss variations while leaving virtually untouched the sharper cracks which have been “smoothed” and thus mostly removed in the Gaussian filtered image. To further isolate the larger fractures and remove the less pervasive ones and any residual noise a “despeckle” filter can also be used. The full procedure is illustrated in (figure 4.11).

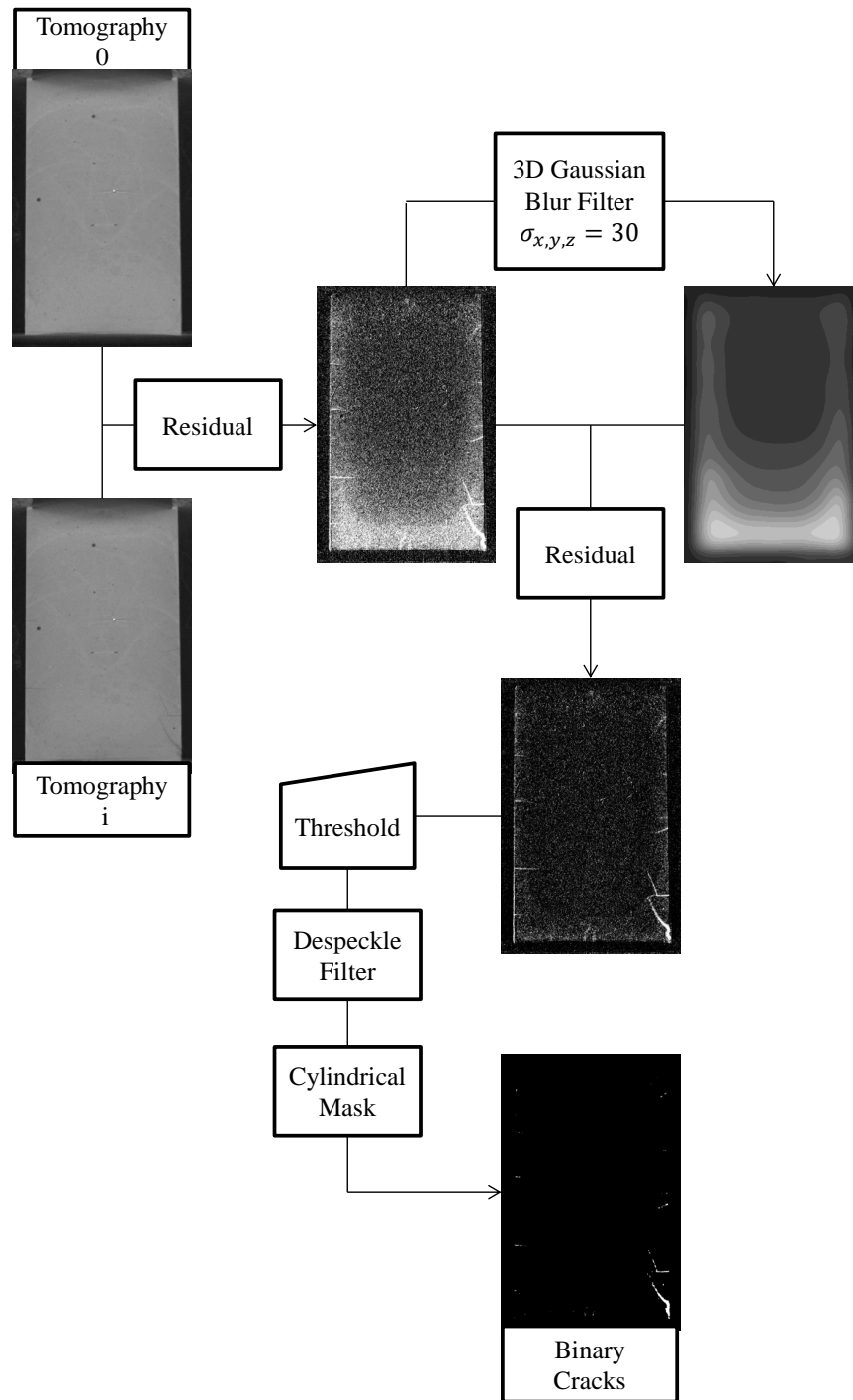


Figure 4.11: The cracking extraction procedure

The crack initiation and its propagation along the test are highlighted in figure 4.12. The cracks initially appear on the outer surface, and predominantly in the warmer top section of the sample, after indicatively 12 hours of heating, while the top surface is heated at  $55^{\circ}\text{C}$ .

This process is induced by the lateral drying, leading to a non-homogeneous saturation state between the core and the surface of the sample, generating high differential strains between these two zones, and thus cracking. This fracture network becomes progressively more pervasive and interconnected along the test, while expanding both in terms of penetration depth and fracture width.

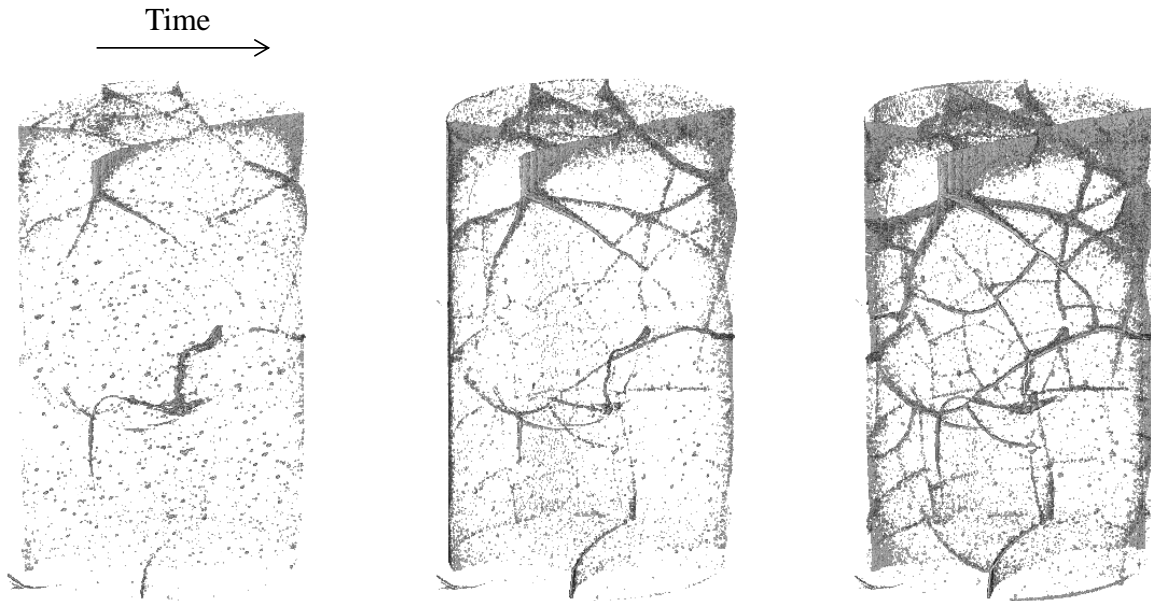


Figure 4.12: Cracks initiation and propagation in time extracted from x-ray tomography: (left) 007, (middle) 012, (right) 017

#### 4.3.4.2 Cracking local effect on water content

Once the fracture network has been isolated it is possible to assess its effect on drying thanks to the complementary neutron dataset. In order to do this, the aforementioned 5D volume registration is pivotal to ensure that each voxel represents the same volume in space across time and modalities. Horizontal slices of the sample acquired as well as a “checkerboard” in figure 4.13 visually confirm their correct alignment.

Once these volumes are aligned, and the fracture network is identified, it is relatively straightforward to study the effect of the cracks on water content by studying the evolving gray value in the neutron dataset in the vicinity of the cracks. Given the complex interplay between water content, thermal gradient, developing fracture opening and distance from the cracks, multiple aspects can be studied. Here we focus on two in particular: the effect along the thermal and the hydric gradients (thus along the sample height) and effect of the distance from the fracture.

From a technical standpoint, it is possible to identify the areas neighbouring a fracture by dilating the binary image of the cracks, for example using a cubic morphological structuring element (*i.e.*, adding, for each voxel, a cube of a known size - 4 pixels, 520  $\mu\text{m}$  in this case- centred on that voxel). The distance from the fracture is then merely the number of dilation required to reach a given voxel. The voxels neighbouring a crack were here identified as “C” (the crack itself) and then progressively as “D1”, “D2”, ..., “Dn”, as shown in figure 4.15. The position in space of the voxel is of course always known, meaning that it is possible to quantify the effect that the fracture opening has on the neutron gray value (and thus water content) as a function of the position along the sample height, and repeat this operation for different distances from the fracture. This is for example reported in figure 4.16 for four representative time steps. In this case each point in the curves represents the gray value normalised by their initial, reference value and averaged for all fractures across the entire diameter of the sample. In the first two time steps, the crack propagation only reaches the first centimeter. The curves of the different dilated volumes are mostly overlapping, indicating a very modest influence of the cracks. This area remains substantially unaffected also in the following steps simply because it approaches its hydrostatic equilibrium. Later in the test, nonetheless, the effect of fractures is far more marked in the middle and bottom of the sample, where the water content is relatively high and the drying process is slow due to the comparatively low temperature. This figure suggests that the drying process is significantly accelerated in the vicinity of the cracks and progressively reduces as we move away from the fracture.

To further study the extent of this effect, it is possible to explore the evolution of the gray value as a function of the distance from the fracture in different areas of the samples and as a function of time, as shown in figure 4.17. The cracks are confirmed to play a negligible role in the top part of the sample, but in the middle and bottom it is possible to observe that, once drying starts it starts predominantly near fracture and progressively propagates outwards as the overall drying progresses. This analysis also suggest that the

effect of the fracture can go as far as 4 mm away from it (this well above the resolution of the neutron images).

These measures are also qualitatively confirmed in figure 4.14, where it is apparent that there is a wide zone neighbouring the cracks (as detected by the x-ray images) where the local drying is accelerated (as highlighted by the reduced attenuation in the neutron volumes).

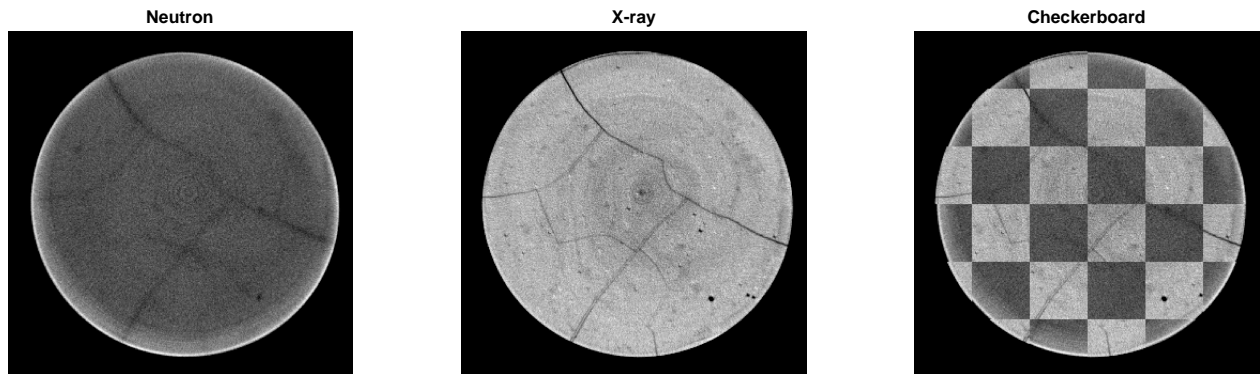


Figure 4.13: Horizontal slices through registered tomographies in both modalities: (left) neutron, (middle) x-ray and (right) “checkerboard”.

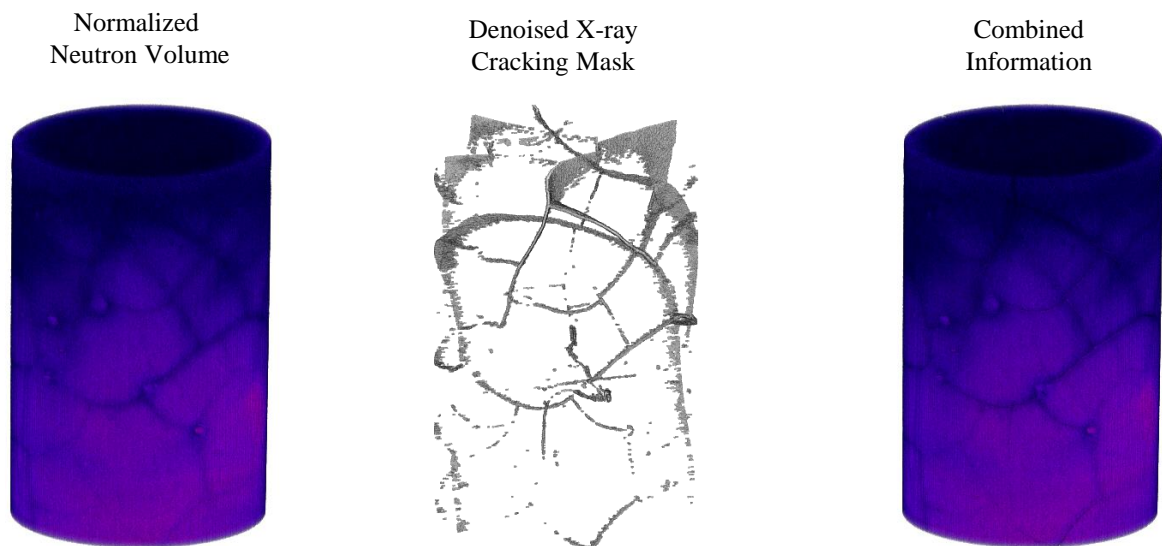


Figure 4.14: 3D visualisation of cracks and neutron images after multimodal registration : normalized neutron volume (left), 3D denoised x-ray cracks (middle) and combined images (right).

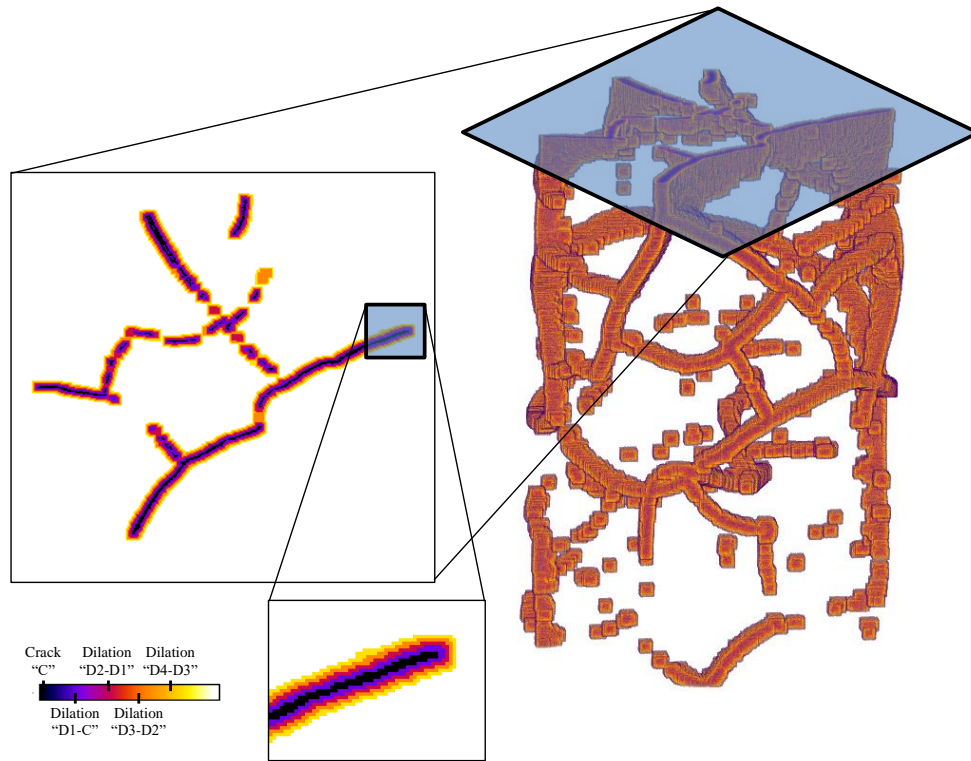


Figure 4.15: Crack dilation procedure

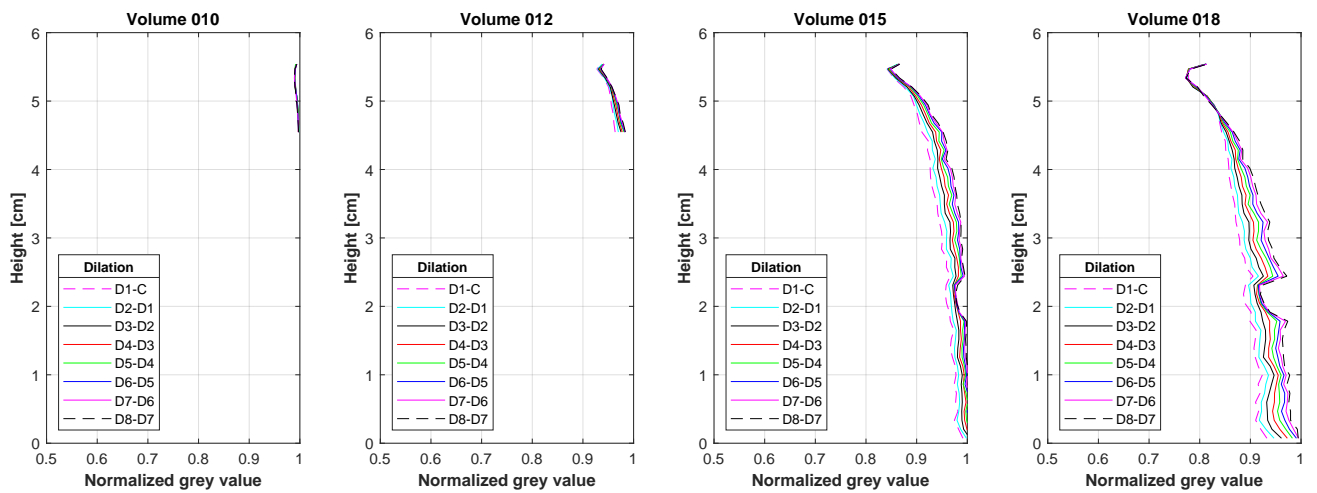


Figure 4.16: Cracking local effect on the normalized hydric behavior over the height of the sample: Dn being the dilated mask of the cracks x times, C being the cracks

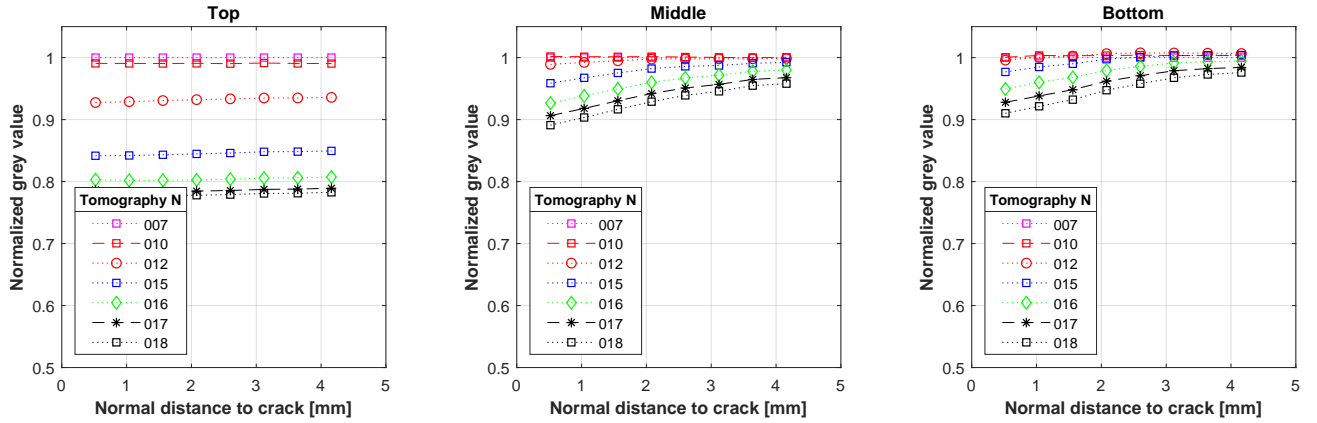


Figure 4.17: Normalized Cracking local effect on the hydric behavior

## 4.4 Conclusion

This paper studied the drying behavior of cement-based materials as revealed by a 5D dataset combining simultaneous *in-situ* neutron and x-ray tomography of samples heated up to moderate temperatures. In this case neutron tomography was employed to study the dynamics of moisture removal, while the x-ray tomography complemented this information by providing insight on the mechanical processes, and notably on crack initiation and propagation.

The evolving moisture content profiles were quantified for a concrete sample heated up to 140°. By the end of the test, the top 1.5 cm showed an asymptotic neutron attenuation profile which can be interpreted as a sign of hydric equilibrium. A transition was proposed to move from the measured attenuation fields to water content fields. The analysis has shown that the hydric equilibrium was reached when 20% volumetric fraction of capillary water was lost, a result coherent with the corresponding analytical analysis. The unique insight provided by spatio-temporal evolution of these moisture content curves across the test is expected to be pivotal for the calibration, validation and improvement of existing thermo-hydric numerical models.

In the cement paste sample, an extensive 3D cracking process was observed and its initiation and propagation were quantified thanks to the 4D x-ray dataset. A multi-modal registration was then employed to align the x-ray and neutron volumes in a coherent coordinate system. This unique spatio-temporal 5D data set allowed an unprecedented quantification of the local effect that cracking has on the drying process. It was observed for example that the crack-induced local drying was particularly pronounced in the slower drying areas (zones of lower temperature), with effects going as far as 4 mm from the crack tips. This information is also of great importance for the improvement and validation of the currently suggested hydro-mechanical coupled models that include the cracking/damage effect on the hydric behavior.

## 4.5 Data availability statement

The raw data-sets of the cement and concrete samples heated up to moderate temperature are respectively available at:

<http://doi.ill.fr/.../ILL-DATA.UGA-48> - the analyzed experiment is in folders 01-pate-MT and 02-pate-MT-morning.

<http://doi.ill.fr/.../ILL-DATA.UGA-60> - the analyzed experiment is in folder 05-B2-200deg-XN.

## 4.6 Appendix

### 4.6.1 Radial gradient analysis

In order to isolate and remove the zone in which beam hardening artifacts and lateral moisture leakage are more prominent, a radial gradient analysis is proposed here to identify and isolate this effect. After removing the aggregates, The sample is divided into 10 hollow cylinders comprising a virtually identical number of voxels. A horizontal cross-section of the different cylinders considered is shown in figure 4.18. It should be noted that the “holes” correspond to the removed aggregates.



Figure 4.18: Horizontal cross-section of the sample partition into equivolumetric hollow cylinders

The gray value is the averaged along the z-axis for each hollow cylinder. Three sub-regions of interest, including 5 slices each, are then studied at different heights. the gray values are then averaged in these sub-regions and plotted for different hollow-cylinders, *i.e.*, different radius. Finally, the gradients are plotted for different tomographies in time.

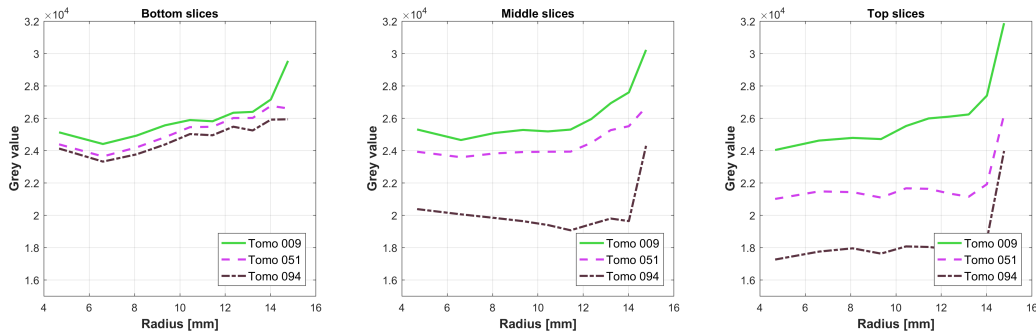


Figure 4.19: Radial gradient evolution of the concrete sample (average of 5 slices in each height region)

The the area most affected by beam hardening and lateral drying can be studied by comparing the gray value for each of these concentric cylinders along the test as reported in figure 4.19. These plots show that the areas most affected by beam hardening and lateral moisture escape are localized mostly in the last two regions. In this work therefore, analyses only considered the inner 80% core of the sample.

### 4.6.2 Registration and volumetric strain measurement

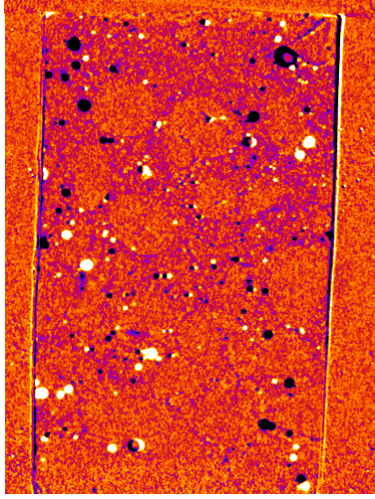
figure 4.20 shows the difference between the initial and final x-ray acquisitions (here named residual fields) before alignment, highlighting the importance of registration of the volumes. The effect of this registration is highlighted in figure 4.20b, which also shows the absence of fractures at the adopted resolution.

The transformation gradient tensor  $\mathbf{F}$  writes:

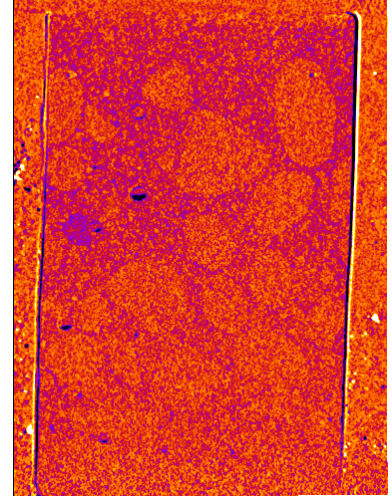
$$\mathbf{F} = \mathbf{I} + \nabla \mathbf{u} = \begin{bmatrix} F_{zz} & F_{zy} & F_{zx} & t_z \\ F_{zy} & F_{yy} & F_{yx} & t_y \\ F_{xz} & F_{xy} & F_{xx} & t_x \\ 0 & 0 & 0 & 1 \end{bmatrix} \quad (4.4)$$

Which in the case of registration of the 095 and 009 x-ray volumes writes:

$$\mathbf{F}|_{010x-009x} = \begin{bmatrix} 0.9999457 & -0.0000348 & -0.000178 & 0.0365946 \\ 0.0000231 & 1.0001880 & -0.0004087 & 0.1184489 \\ 0.0000894 & 0.0003372 & 0.9999132 & 0.3565245 \\ 0 & 0 & 0 & 1 \end{bmatrix} \quad (4.5)$$



(a) Before registration



(b) After registration

Figure 4.20: Residual fields of the (095 – 009) x-ray tomography (a) before registration and (b) after registration

$$F|_{095x-009x} = \begin{bmatrix} 0.9984237 & 0.0007269 & -0.0014159 & 1.2549339 \\ 0.0013792 & 1.0045731 & -0.0044966 & 0.6468804 \\ -0.0011933 & 0.0032826 & 0.9998339 & 0.4457981 \\ 0 & 0 & 0 & 1 \end{bmatrix} \quad (4.6)$$

where  $\mathbf{I}$  is the identity matrix and  $\nabla u$  is the gradient of the displacement vector. In the small strain framework, the strain tensor writes:

$$\epsilon = \frac{1}{2}(F + F^T) - I \quad (4.7)$$

The volumetric strain is defined as:

$$\epsilon_{vol} = tr(\epsilon) \quad (4.8)$$

which in the case of the 095 and 009 volumes is equal to  $\epsilon_{vol}|_{095x-009x} = 0.283\%$  and in case of 010 and 009 volumes is equal to  $\epsilon_{vol}|_{010x-009x} = 0.004\%$ .

# Chapter 5

## Conclusions and perspectives

### 5.1 Summary of this doctoral work

The objective of this doctoral work was to contribute to the understanding of the complex multiphysics processes occurring during drying in cement-based materials. This was done by adopting an experimental/numerical approach, *i.e.*, the use of combined neutron/x-ray tomography on one side complemented with the use of advanced THM numerical models. A brief description of this work mainlines is given below:

#### 5.1.1 x-ray/neutron tomography measurements of drying-driven processes in cement-based materials

Two experimental campaigns were performed at the Institut Laue-Langevin (ILL) to study the complex mechanisms of drying. The main objective of the first campaign was to measure the saturation gradients developing between the core of the sample and the exchange surface of cement-based materials. For that, a series of mortar samples were set to dry sequentially in a thermo-hydrally controlled environment to have different hydric states. The neutron tomography scans showed the gray value gradients developing in the samples, which was transformed to saturation gradients by means of a multiphase analytical approach. The main objectives of the second campaign were to characterize the moisture transport in heated cement-based materials and to quantify the effect of cracking on the local water content. For that, simultaneous x-ray/neutron tomography of two samples, a cement paste sample and a concrete one, were acquired. The evolution of the saturation profiles was evaluated between the core and the exchange surface of the heated concrete sample. On the other hand, the evolution of the cracking network and its local effect on the drying kinetics were quantified.

#### 5.1.2 Numerical modeling of the thermo-hydro-mechanical behavior of cement-based materials.

A comparative numerical study was done to estimate the effect of common simplifications on the drying modeling of cement-based materials up to moderate temperatures. The common simplifications which were considered are the effect of neglecting transport mechanisms related to particular fluid species in the porous network, and the effect of neglecting the hydraulic properties' thermal dependency, *i.e.*, the evolution of desorption isotherms and permeability in function of temperature. The study was performed in a relative humidity-temperature (RH-T) space ranging between 30% and 85% RH and 20 °C and 80 °C. The results showed error maps to a reference case at early, mid and late drying stages.

### 5.2 Main findings

The main finding which resulted from the experimental/numerical work performed in this thesis are summed below:

- **Saturation gradients developed in mortar samples submitted to environmental drying were measured thanks to neutron tomography:** A series of mortar samples, representing different hydric states, were scanned using neutron tomography. The saturation profiles were deduced from gray

value gradients thanks to a proposed multiphase analytical approach. This approach was validated by comparing the integrated saturation profiles to balance-based mass loss measurements.

- **Saturation gradients of heated concrete (up to moderate temperature) were measured thanks to neutron tomography:** The *in-situ* series of neutron tomography revealed the dynamics of water transport in a heated concrete both by measuring the moisture profiles evolution and by observing the local mechanisms of pore filling. The saturation profile measurements constitute an original dataset to validate numerical models in the poorly studied domain of “concrete behavior at moderate temperature”.
- **Quantification of the cracking local effect on the water content by means of simultaneous x-ray/neutron tomography:** The *in-situ* x-ray and neutron tomography revealed a dual characterization of the cracking local mechanisms. On one hand, x-ray captured the initiation and propagation of the cracks in a heated cement paste sample. On the other hand, neutrons detected the moisture migration induced by the heating gradient. The combination of the two datasets allowed the quantification of the cracking local effect on the local drying kinetics. Gradients of water were measured in the normal direction to the crack surfaces showed an extent of 4mm.
- **The permeation remains the dominant transport process at moderate temperatures for cement paste:** The comparison shown between the multiphase model (which describes all the fluid species in the pore network) and a simplified model (which describe only liquid water permeation) reveals that the error between the two models response is less than 10%, when behavior laws accounting for the temperature effect on the hydraulic properties are used. That was mainly due to the double exponential function evolution of permeability with respect to temperature.
- **Neglecting the evolution of hydraulic properties, such as permeability and desorption isotherms, with respect to temperature, induces high error values in the model response:** Many works in the literature neglected the impact of temperature on hydraulic properties for temperatures lower than 100 °C. The simulations have shown that this negligence can induce errors on the lost water amount up to 80% at different drying stages.

## 5.3 Perspectives

The work done during this PhD period partially explored the promising potential of the approach combining neutron/x-ray tomography and advanced numerical modeling in studying the THM behavior of concrete. A list of perspectives and on-going projects are mentioned in this section.

### Experiments

- **Correcting for beam-hardening:** The evolving moisture content in *in-situ* drying samples requires a dynamic correction approach for the beam-hardening artifact (depending on the integrated water thickness) occurring in neutron images. A possible correction could be based on scanning different samples whose water content is well-known. The samples could be placed in desiccators at different thermo-hydrally controlled environments until reaching hydric equilibrium. A neutron scan for each of these samples should be then acquired. A correction function of the beam hardening could be suggested to flatten the hydric gradients in the radial direction.
- **Improving further the heating setup:** coupling the heating setup used in the neutron facility with a balance to measure the evolution of mass loss occurring during the drying test. These gravimetric measurements will serve to validate the analytical multiphase approach that has served to estimate the water content fields based on gray value images of heated cement-based samples.
- **Reducing the uncertainties in neutron imaging moisture detection:** The analytical approach proposed in article 2 and 3 which proposed a transition between gray value and water content require further improvement, particularly in assessing its parameters. The scanning of reference samples having well-known hydric states could be highly advantageous in defining reference values. Additionally, scanning a conical sample of pure water could provide a better reference value of  $\mu_w$  and its dependency on the water thickness. Finally, the assessment of the “non-loss of chemically bound water” hypothesis could be checked by acquiring MRI scans (using portable MRI scanners) of the initial and the final hydric states of the sample.

- **Testing of different hydro-mechanical variations of cement-based composites:** Different thermo-hydro-mechanical boundary conditions and material compositions could have been tried to characterize their effects on the drying process. These include, but are not limited to, samples with different mechanical loading to understand the creep effect on moisture micro-diffusion mechanisms; the effect of water to cement ratio on the drying kinetics and the final amount of water leaving the sample; the different ventilation intensity on the hydric gradient shapes; *etc.*
- **Multiple drying/wetting cycles effect:** The effect of multiple drying/wetting cycles need to be studied to characterize the saturation state variations at sequential hydric equilibrium. In particular, the effect of cracks which has appeared during the first drying cycle (due to drying shrinkage) requires to be characterized for later drying cycles. The role of the cracks can be also investigated in multiple other scenarii including complex THM loading, *e.g.*, vapor condensation in cracked cement-based materials under pressure gradient.

## Numerical modeling

- **Extending the study of “common simplifications effect on the drying modeling of cement-based material” to different types of cement composites, higher ranges of temperatures and multiple drying/wetting cycles:** The common simplifications in thermo-hydric modeling, *i.e.*, the use of a non-complete physical description of the fluid phase in the pore network and the non-consideration of the thermally-induced evolution of hydraulic properties (desorption isotherms, permeability), could be extended to study different materials other than the cement paste studied in chapter 2. Indeed, the contribution of the different transport processes (permeation and diffusion) to drying and their thermal-dependencies of their hydraulic properties depends on the material studied. Therefore, the study of additional cement-based materials such as mortar, ordinary concrete (OC), high-performance concrete (HPC) having different (w/c) ratio is required to complete the previous study.

In addition, the effect of multiple drying/wetting cycles on those evolutions, particularly the evolution of desorption isotherms and permeability in the second cycle should be also considered.

Lastly, the extension of the temperature domain to moderate temperature higher than 80 °C can be also possible but require to take into account the modeling of additional processes such as dehydration (loss of chemically bound water) and thermally-induced damage.

Those extensions could help optimize the choice of model and behavior laws in different ranges of temperature and relative humidity.

- **Evaluate the effect of cracks on the drying kinetics:** This work has been partially done and is presented in the first appendix. 2D hydro-mechanical mesoscopic simulations were performed on an idealized concrete morphology which represents the aggregates as perfect disks. The drying shrinkage induced by the loss of water was restrained by the presence of aggregate which has induced cracking. A hydro-mechanical coupling law was implemented to account for the effect of cracks on the drying kinetics. The consequential local effects were presented on saturation, damage and crack opening field and compared to the case in which no strong coupling was considered. Additionally, the global effect of those cracks was also evaluated by comparing the global mass loss in between the two cases.

The effect of those cracks is still to be evaluated in multiple drying/wetting cycles. Their hydraulic effect is expected to be increasingly more important with the number of cycles until reaching a constant crack opening.

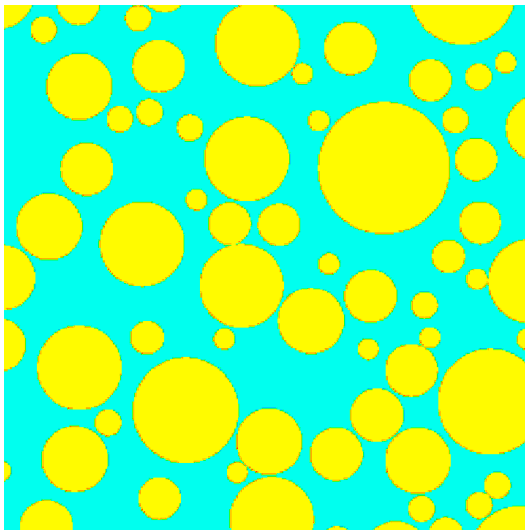
- **Accounting for the visco-elastic nature of the material:** It is necessary to account for the creep behavior in the numerical model to better simulate the mechanical behavior of the material. In fact, the modeling of drying shrinkage only is not sufficient to estimate the stresses and strains induced during drying, but other mechanisms related to stress relaxation induced by creep should be considered.
- **Simulating the concrete THM behavior at the mesoscale while considering the real morphology of the aggregates:** To capture the mesoscale morphology impact on the different processes, it is required to develop a CT-FE mapping scheme to project the material morphology on the FE mesh. This operation was performed during this PhD and is illustrated in Appendix 2. Ongoing work includes simulating the 3D multiphase THM behavior of concrete at the mesoscale of the samples tested at ILL (chapter 4). The comparison of the model response with the x-ray/neutron original measurement dataset is expected to improve the predictive capacity of the model.

## Appendix A

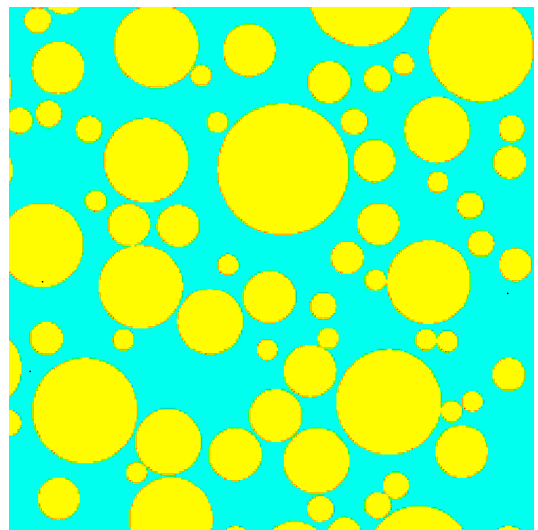
# 2D hydro-mechanical mesoscopic modeling: effect of a strong hydro-mechanical coupling

This section can be considered as a continuation of the first chapter “**Influence of common simplifications on the drying of cement-based materials up to moderate temperatures**”, since one of the major simplifications used in the drying modeling is the disregard of the two-way hydro-mechanical coupling, *i.e.*, the effect of cracks on both the local and global drying kinetics. An artificial mesoscopic concrete morphology was generated to enable the localization of cracks following the approach used in [Nguyen, 2010]. A simplified hydraulic model was used to simulate the water content evolution [Cheikh Sleiman et al., 2020a] while Mazars damage model [Mazars, 1984] was used to simulate the damage evolution due to this water loss, where the resulting crack opening are computed following [Matallah et al., 2010] approach. Finally, the continuous damage-permeability approach of [El-Dandachy, 2016] was implemented to model the hydro-mechanical coupling.

### A.1 Meso-structure generation



(a) Artificial meso-morphology with boundary effect



(b) Artificial meso-morphology with no boundary effect

## A.2 Input parameters and boundary conditions

Hydric input parameters [Cheikh Sleiman et al., 2020a]				
Parameter	Description	Value	Unit	Reference
$h_{conv}$	Coefficient of hydric exchange	20	-	-
$\mu_l$	Water viscosity	$10^{-3}$	Pa.s	-
$\rho_l$	Water density	1000	$\text{kg m}^{-3}$	-
$K_l^0$	Permeability in sound concrete	$2 \times 10^{-21}$	$\text{m}^2$	[Baroghel-Bouny, 1994]
$\phi$	Porosity	0.16	-	[Rougelot, 2008]
$\rho_s$	Solid matrix density	2200	$\text{kg m}^{-3}$	-
$a_{vg}$	Van Genuchten parameter	0.47	-	-
$b_{vg}$	Van Genuchten parameter	30	MPa	-
$RH_{ini}$	Initial internal relative humidity	0.99	-	-
Mechanical input parameters [Mazars, 1984]				
$E_{mor}$	Mortar Young modulus	30	GPa	-
$E_{agg}$	Aggregates Young modulus	60	GPa	[Stamati, 2020]
$\nu$	Poisson ratio	0.2	-	-
$f_t^{mor}$	Tensile strenght	$3.2 \times 10^6$	[Pa]	-
$kt_0^{mor}$	Damage threshold	$\frac{f_t^{mor}}{E_{mor}}$	-	-
$\alpha_{dess}$	Drying shrinkage coefficient	$6 \times 10^{-6}$	-	[Bouhjiti, 2018]
$B_t$	Mazars model parameter	10000	-	-
Hydro-mechanical coupling [El-Dandachy, 2016]				
$\alpha_{pic}$	Diffuse damage parameter	11.3	-	[Picandet et al., 2009]
$\beta_{pic}$	Diffuse damage parameter	1.64	-	[Picandet et al., 2009]

Table A.1: Input Parameters for the hydro-mechanical 2D mesoscopic simulations

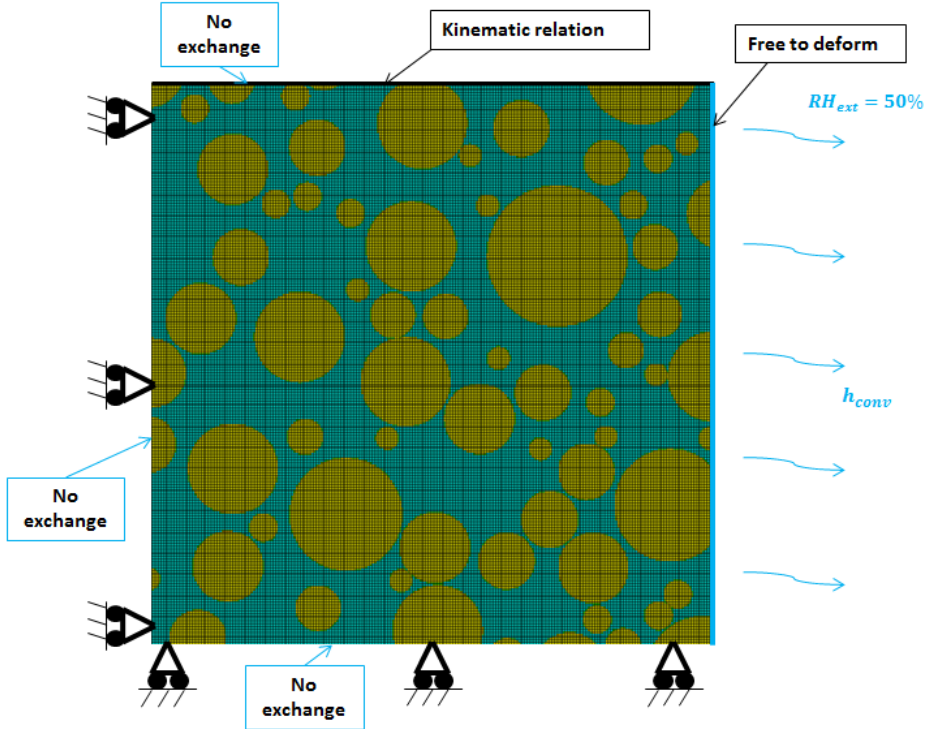


Figure A.2: FE mesh and hydro-mechanical boundary conditions [Nguyen, 2010]

Among the two types of artificial morphology of the  $10 \times 10$  concrete block, only the first one, which considers the aggregates boundary effect, is studied in this section. The input parameters for the hydro-mechanical simulations are presented in table A.1. Indeed, the damage threshold of mortar  $kt_0^{mor}$  and the drying shrinkage coefficient  $\alpha_{dess}$  are among the most influential parameters that might have a tremendous effect on the hydro-mechanical response. A sensitivity analysis is therefore required to evaluate the input parameters effect that might change from a cement-based material to another. As for the boundary conditions, a hydric convective flux is set on one side of the block while being mechanically constrained in the other three sides.

The following subsection shows a comparison between two simulations, the first being performed without hydro-mechanical coupling while the second account for it. The comparison is done both on the local measurements of water saturation, damage and crack opening and propagation evolution at early, mid and late drying stages. Finally, the global effect of the cracks on the drying kinetics is shown in figure A.6.

At the end, many other developments are still required in order to be conclusive about the obtained results. At first, a more sophisticated mechanical model that accounts for creep is needed in order to simulate the stress relaxation that might have an impact on the cracking propagation. In addition, other variations such as different material parameters, different meso-structure generation, multiple drying-wetting cycles, material real morphology consideration, *etc* can be tried as well.

### A.3 Results: Saturation, damage and crack opening fields

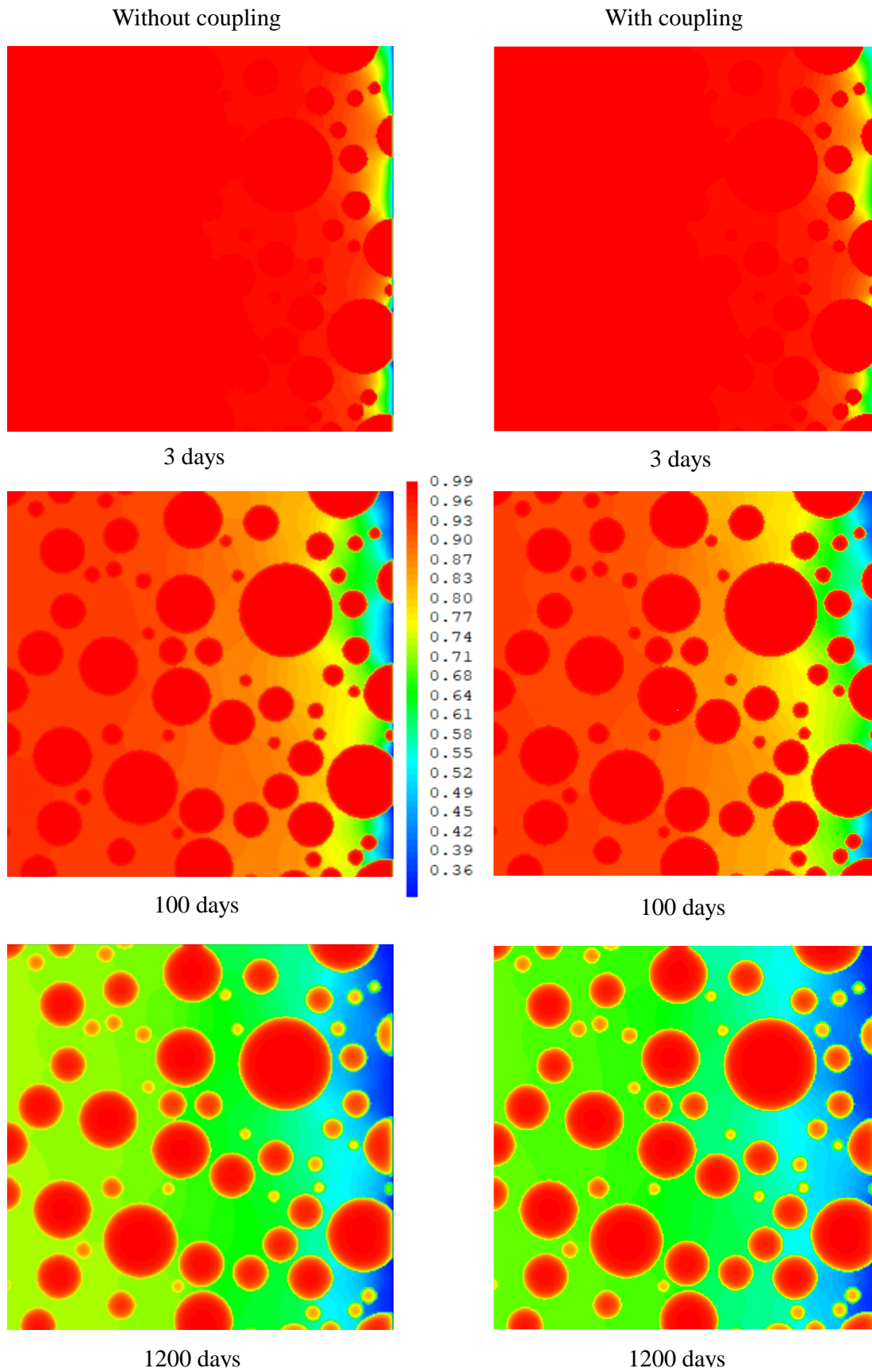


Figure A.3: Saturation fields at 3, 100 and 1200 days resulting of the 2D mesoscopic simulations: without coupling (left) and with coupling (right)

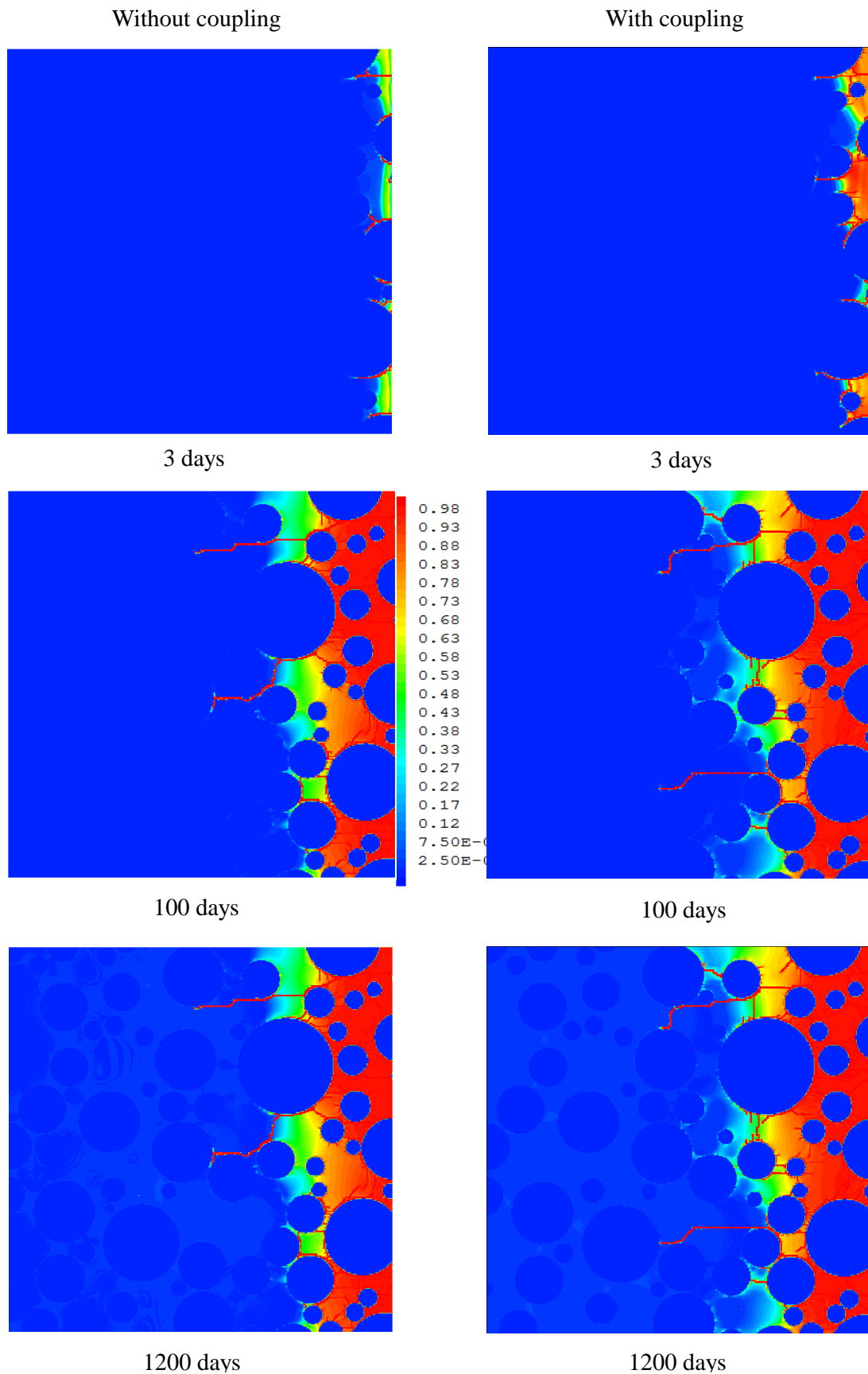


Figure A.4: Damage fields at 3, 100 and 1200 days resulting of the 2D mesoscopic simulations: without coupling (left) and with coupling (right)

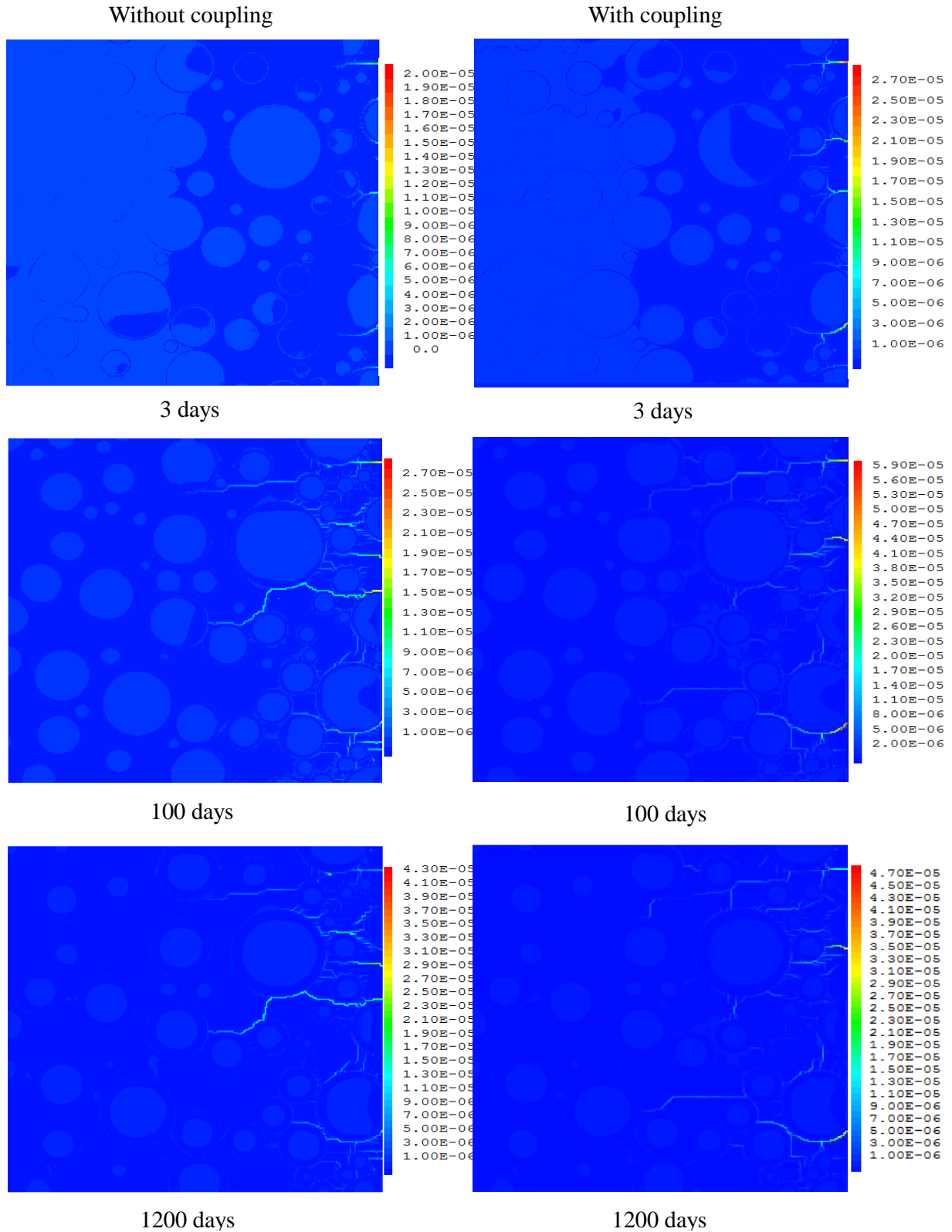


Figure A.5: Crack opening fields at 3, 100 and 1200 days resulting of the 2D mesoscopic simulations: without coupling (left) and with coupling (right)

#### A.4 Hydro-mechanical coupling effect on the mass loss

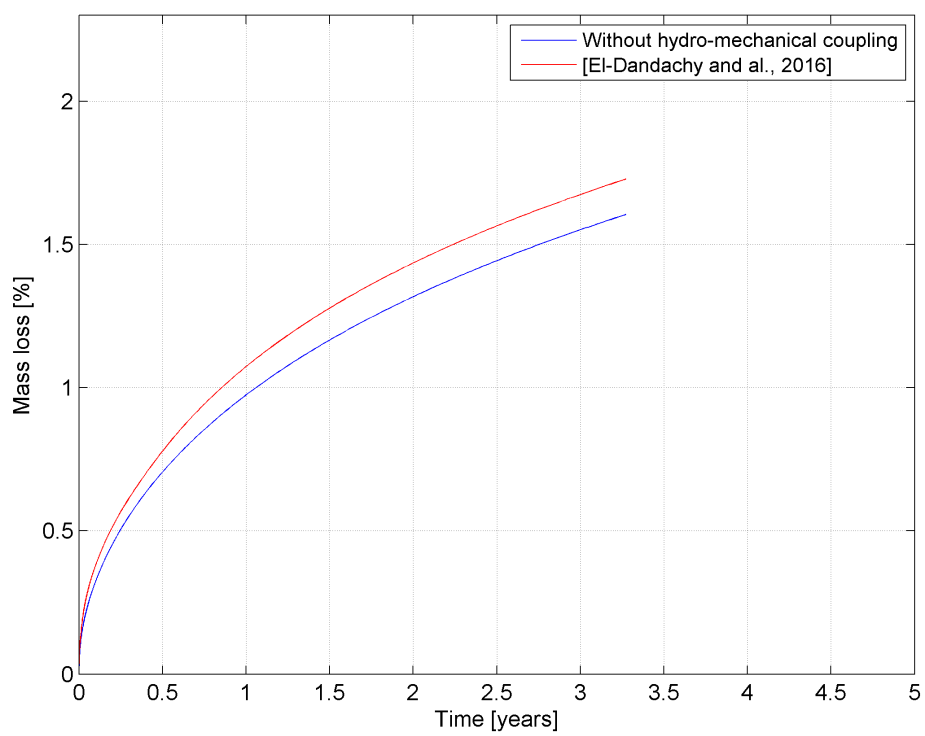


Figure A.6: Assessment of the hydro-mechanical coupling effect on global mass loss in the first drying cycle.

## Appendix B

# 3D image-based THM mesoscopic modeling of concrete

This section presents a CT-FE mapping scheme developed in the framework of this PhD, which was used to perform 3D THM simulation of concrete at the meso-scale. The procedure consists on extracting the mesoscale morphology of concrete (aggregates and pores) from x-ray/neutron attenuation fields and presenting it explicitly on a Finite Element mesh. This permits to simulate the mechanical local effects that might be generated by the heterogeneity (stress concentration, cracks, *etc*) as well as their implications on the thermo-hydric processes. The procedure also enables a quantitative full-field comparison between the neutron/x-ray fields and the numerical ones. In this section, for sake of simplicity, the aggregates are the only meso-specie that is considered from a neutron volume of a HPC (we neglect the presence of macro-porosity). The full procedure is illustrated in figure B.1, it consists on:

- Step 1: segmentation of the initial 3D neutron attenuation field to isolate the aggregates.
- Step 2: separation and labeling of the aggregates by means of a watershed algorithm.
- Step 3: (optional) manipulation of the meso-structure by removing the aggregates and sand particles having a diameter below a certain threshold.
- Step 4: scaling-down the image to reduce the numerical model's computational time cost since each voxel in the image represents a finite element in the mesh.
- Step 5: projecting the morphology on the finite element mesh using a developed procedure in Cast3m FE software.
- Step 6: Assigning the input parameters, models and boundary conditions of the two different materials to simulate the THM problem.
- Step 7: Post-processing the results which requires additional scripts development in order to extract the nodal quantities which belong to the mesh of the mortar specie or to some local region in the material for instance.

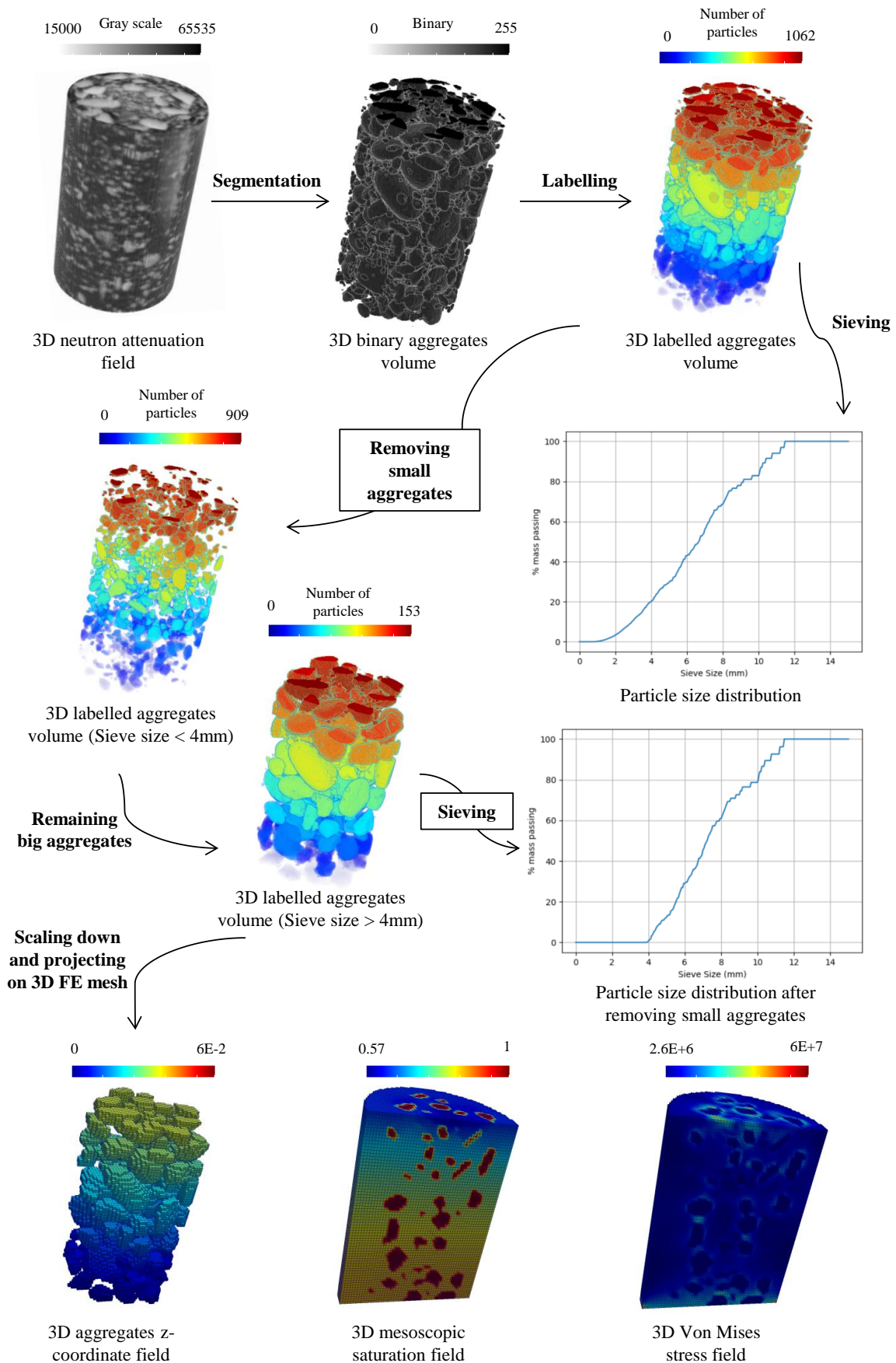


Figure B.1: CT-FE mapping scheme to perform 3D THM simulation of concrete at the mesoscale while representing the aggregates real morphology

# Bibliography

- M. Al-Hussani and M. Al-Hayani. The use of filtered back projection algorithm for reconstruction of tomographic image. *College of Engineering Journal*, pages 151–156, 01 2014.
- H. Allam, F. Duplan, J.P. Clerc, S. A., and Y. Burtschell. About electrical resistivity variation during drying and improvement of the sensing behavior of carbon fiber-reinforced smart concrete. *Construction and Building Materials*, 264:120699, 2020. ISSN 0950-0618. doi: <https://doi.org/10.1016/j.conbuildmat.2020.120699>. URL <http://www.sciencedirect.com/science/article/pii/S0950061820327045>.
- E. Andò, R. Cailletaud, R. Roubin, O. Stamati, and the SPAM contributors. The software for the practical analysis of materials. <https://ttk.gricad-pages.univ-grenoble-alpes.fr/spam/>, 2017.
- ASHRAE. *Handbook: fundamentals (International Metric System)*. 2001.
- P. Atkins and J. de Paula. Physical chemistry. *Oxford University Press*, 21:1097p, 2006.
- P. Baggio, C. Bonacina, and M. Strada. Trasporto di calore e massa nel calcestruzzo cellulare. *La Termodinamica*, page 53–60, 1993.
- V. Baroghel-Bouny. *Caractérisation microstructurale et hydrique des pâtes de ciment et des bétons ordinaires et à très hautes performances*. PhD thesis, Ecole Nationale des Ponts et Chaussées., 1994.
- V. Baroghel-Bouny, M. Mainguy, T. Lassabatere, and O. Coussy. Characterization and identification of equilibrium and transfer moisture properties for ordinary and high-performance cementitious materials. *Cement and Concrete Research*, 1999.
- B. Bary, G. Ranc, S. Durand, and O. Carpentier. A coupled thermo-hydro-mechanical-damage model for concrete subjected to moderate temperatures. *International Journal of Heat and Mass Transfer*, 2008.
- B. Bary, M.V.G. de Morais, S. Poyet, and S. Durand. Simulations of thermo-hydro-mechanical behaviour of an annular reinforced concrete structure heated up to 200°C. *Engineering Structures*, 2012.
- K. J. Bathe and E. L. Wilson. Stability and accuracy analysis of direct integration methods. *Earthquake Engineering Structural Dynamics*, pages 283–291, 1972.
- Z. Bazant, H. Nguyen, M. Pathirage, M. Rezaei, M. Issa, and G. Cusatis. New perspective of quasibrittle fracture mechanics inspired by novel test with crack-parallel compression. <https://www.youtube.com/watch?v=UyTeopPModA>, 2020. [Online; accessed 2-Jne-2020].
- Z.P. Bazant and J.C. Chern. Concrete creep at variable humidity: constitutive law and mechanism. *Materials and structures*, 18:1–20, 1985.
- Z.P. Bazant and L.N. Najjar. Non-linear water diffusion in non-saturated concrete. *Matériaux et Construction*, 1972.
- R. Beare and G. Lehmann. The watershed transform in itk-discussion and new developments., 2006.
- F. Benboudjema. *Modélisation des déformations différées du béton sous sollicitations biaxiales. Application aux enceintes de confinement de bâtiments réacteurs des centrales nucléaires*. PhD thesis, ENS Cachan, 2002.
- J.C. Benet. *Contribution à l'étude thermodynamique des milieux poreux non saturés avec changement de phase*. PhD thesis, Université des sciences et techniques du Languedoc., 1981.

- D. P. Bentz. Influence of water-to-cement ratio on hydration kinetics: Simple models based on spatial considerations. *Cement and Concrete Research*, 36(2):238 – 244, 2006. doi: <https://doi.org/10.1016/j.cemconres.2005.04.014>.
- B. Bissonnette, P. Pierre, and M. Pigeon. Influence of key parameters on drying shrinkage of cementitious materials. *Cement and Concrete Research*, 29(10):1655 – 1662, 1999. doi: [https://doi.org/10.1016/S0008-8846\(99\)00156-8](https://doi.org/10.1016/S0008-8846(99)00156-8).
- M. Boucher. *Analyse du transfert spatio-temporel des déformations entre le coeur d'un ouvrage épais et son parement : application aux enceintes de confinement*. PhD thesis, Univ. Grenoble Alpes. France., 2016.
- D. Bouhjiti. PhD thesis, Communauté Université Grenoble Alpes., 2018.
- DEM Bouhjiti, M. Ezzedine El Dandachy, F. Dufour, S. Dal Pont, M. Briffaut, J. Baroth, and B. Masson. New continuous strain-based description of concrete's damage-permeability coupling. *International Journal for Numerical and Analytical Methods in Geomechanics*, pages 1671–1697, 2018.
- J.S. Brenizer. A review of significant advances in neutron imaging from conception to the present. *Phys. Procedia*, 2013.
- D.R.M. Brew, F.C. de Beer, M.J. Radebe, R. Nshimirimana, P.J. McGlenn, L.P. Aldridge, and T.E. Payne. Water transport through cement-based barriers —a preliminary study using neutron radiography and tomography. *Nuclear Instruments and Methods in Physics Research*, pages 163–166, 2009.
- F.N.G. Brue, C. Davy, N. Burlion, F. Skoczylas, and X. Bourbon. Five year drying of high performance concretes: Effect of temperature and cement-type on shrinkage. *Cement and Concrete Research*, 99:70–85, 09 2017. doi: [10.1016/j.cemconres.2017.04.017](https://doi.org/10.1016/j.cemconres.2017.04.017).
- S. Brunauer. The adsorption of gases and vapors. *Physical Adsorption, vol. I, Princeton University Press*, 1945.
- J. Carette, F. Soleilhet, F. Benboudjema, R. Bennacer, A. Darquennes, K. Abahri, and G. Nahas. Identifying the mechanisms of concrete drying: An experimental-numerical approach. *Construction and Building Materials*, 230, 09 2019. doi: [10.1016/j.conbuildmat.2019.117001](https://doi.org/10.1016/j.conbuildmat.2019.117001).
- S. Caré. Effect of temperature on porosity and on chloride diffusion in cement pastes. *Construction and Building Materials*, 22(7):1560 – 1573, 2008. doi: <https://doi.org/10.1016/j.conbuildmat.2007.03.018>.
- M. Chaplin. Water properties (including isotopologues). [http://www1.lsbu.ac.uk/water/water\\_properties.html](http://www1.lsbu.ac.uk/water/water_properties.html), 2017.
- H. Cheikh Sleiman, M. Briffaut, S. Dal Pont, A. Tengattini, and B. Huet. Influence of common simplifications on the drying of cement-based materials up to moderate temperatures. *International Journal Of Heat And Mass Transfer*, page 119254, 2020a.
- H. Cheikh Sleiman, A. Tengattini, M. Briffaut, B. Huet, and S. Dal Pont. Simultaneous x-ray and neutron 4d tomographic study of drying-related hydro-mechanical behavior of cement-based material at moderate temperatures. *Cement and Concrete Research*, 2020b.
- M. Choinska, F. Dufour, and G. Pijaudier-Cabot. Matching permeability law from diffuse damage to discontinuous crack opening. *FRAMCOS6*, 2007.
- A. Christensen, Helmer Fjellvåg, M. Lehmann, R. Zingales, Inger Vikholm, Fabio Urso, Johann Weidlein, and Ralph Zingaro. The effect of additives on the reaction of portland and alumina cement components with water. time resolved powder neutron diffraction investigations. *Acta Chemica Scandinavica - ACTA CHEM SCAND*, 40a:126–141, 01 1986. doi: [10.3891/acta.chem.scand.40a-0126](https://doi.org/10.3891/acta.chem.scand.40a-0126).
- M.C da Rocha, L.M da Silva, C.R Appoloni, O Portezan Filho, F Lopes, F.L Melquades, E.A dos Santos, A.O dos Santos, A.C Moreira, W.E Pötter, E de Almeida, C.Q Tannous, R Kuramoto, F.H.de M Cavalcante, P.F Barbieri, A.F Caleffi, B.T Carbonari, and G Carbonari. Moisture profile measurements of concrete samples in vertical water flow by gamma ray transmission method. *Radiation Physics and Chemistry*, 61(3):567 – 569, 2001. ISSN 0969-806X. doi: [https://doi.org/10.1016/S0969-806X\(01\)00334-6](https://doi.org/10.1016/S0969-806X(01)00334-6). URL <http://www.sciencedirect.com/science/article/pii/S0969806X01003346>. 8th International Symposium on Radiation Physics - ISRP8.

- J.F. Daian. *Processus de condensation et de transfert d'eau dans un matériaux meso et macroporeux. Etude expérimentale du mortier et de ciment*. PhD thesis, Institut National Polytechnique de Grenoble, 1986.
- J.F. Daian. Diffusion de vapeur d'eau en milieu poreux. influence d'une phase capillaire dispersée. *Proc. des Journées de physique. Theme l'eau dans les matériaux*, pages 71–76, 1987.
- S. Dal Pont, B.A. Schrefler, and A. Ehrlacher. Intrinsic permeability evolution in high temperature concrete: an experimental and numerical analysis. *Transp. Porous Media*, 2005.
- S. Dal Pont, S. Durand, and B.A. Schrefler. A multiphase thermo-hydro-mechanical model for concrete at high temperatures—finite element implementation and validation under loca load. *Nuclear Engineering and Design*, 2007.
- S. Dal Pont, F. Meftah, and B.A. Schrefler. Modeling of concrete under severe conditions as a multiphase material. *Nuclear engineering and design*, pages 562–572, 2011.
- D. Dauti. *A combined experimental and numerical approach to spalling of high-performance concrete due to fire*. PhD thesis, Communauté Université Grenoble Alpes., 2018.
- D. Dauti, S. Dal Pont, M. Briffaut, and B. Weber. Modeling of 3d moisture distribution in heated concrete: From continuum towards mesoscopic approach. *International Journal of Heat and Mass Transfer*, 2018a.
- D. Dauti, S. Dal Pont, B. Weber, M. Briffaut, N. Toporovs, M. Wyrzykowski, and G. Sciume. Modeling of 3d moisture distribution in heated concrete: From continuum towards mesoscopic approach. *International Journal for Numerical and Analytical Methods in Geomechanics*, 2018b.
- D. Dauti, S. Dal Pont, B. Weber, M. Briffaut, N. Toporovs, M. Wyrzykowski, and G. Sciume. Modeling of 3d moisture distribution in heated concrete: From continuum towards mesoscopic approach. *International Journal for Numerical and Analytical Methods in Geomechanics*, 2018c.
- D. Dauti, A. Tengattini, S. Dal Pont, N. Toropovs, M. Briffaut, and B. Weber. Analysis of moisture migration in concrete at high temperature through in-situ neutron tomography. *Cement and Concrete Research*, 111: 41–55, 2018d.
- C. T. Davie, C.J. Pearce, K. Kukla, and N. Bicanic. Modelling of transport processes in concrete exposed to elevated temperatures - an alternative formulation for sorption isotherms. *Cement and Concrete Research*, 2018.
- F. de Beer, W.J. Strydom, and E.J. Griesel. The drying process of concrete: a neutron radiography study. *Applied Radiation and Isotopes*, 61:617–623, 2004b.
- F. de Beer, J.J. le Roux, and E.P. Kearsley. Testing the durability of concrete with neutron radiography. *Nuclear Instruments and Methods in Physics Research*, pages 226–231, 2005.
- T. de Larrard, J.B. Colliat, F. Benboudjema, J.M. Torrenti, and G. Nahas. Effect of the young modulus variability on the mechanical behaviour of a nuclear containment vessel. *Nuclear Engineering and Design*, 240(12):4051 – 4060, 2010. doi: <https://doi.org/10.1016/j.nucengdes.2010.09.031>.
- M.V.G. de Moraes, B. Bary, G. Ranc, S. Dal Pont, and S. Durand. Comparative analysis of coupled thermo-hydro-mechanical models for concrete exposed to moderate temperatures. *Numerical Heat Transfer*, 2009.
- S.C. de Wolski, J.E. Bolander, and E.N. Landis. An in-situ x-ray microtomography study of split cylinder fracture in cement-based materials. *Exp Mech*, 54:1227–1235, 2014. doi: 10.1007/s11340-014-9875-1.
- C. DeSa. *Etude hydro-mécanique et thermo-mécanique du béton Influence des gradients et des incompatibilités de déformation*. PhD thesis, ENS Cachan, 2007.
- C. Desmettre. *Contribution à l'étude de la perméabilité du béton armé sous sollicitations statiques et cycliques*. PhD thesis, Université de Montreal, 2011.
- C. Di Bella, M. Wyrzykowski, and P. Lura. Evaluation of the ultimate drying shrinkage of cement-based mortars with poroelastic models. *Materials and Structures*, 50, 2016. doi: 10.1617/s11527-016-0870-0.
- E. Drouet. *Impact de la température sur la carbonatation des matériaux cimentaires : prise en compte des transferts hydriques*. PhD thesis, Ecole normale supérieure de Cachan, 2010.

- E. Drouet, S. Poyet, and J.M. Torrenti. Temperature influence on water transport in hardened cement pastes. *Cement and Concrete Research*, 2015.
- M. Ezzedine El-Dandachy. *Caractérisation et modélisation de la perméabilité des bétons endommagés : Applications aux structures en béton armé*. PhD thesis, Communauté Université Grenoble Alpes, 2016.
- G. El Tabbal, P. Dangla, M. Vandamme, M. Bottoni, and S. Granet. Modelling the drying shrinkage of porous materials by considering both capillary and adsorption effects. *Journal of the Mechanics and Physics of Solids*, 142:104016, 05 2020. doi: 10.1016/j.jmps.2020.104016.
- P. Faure, S. Caré, C. Po, and S. Rodts. An MRI-SPI and NMR relaxation study of drying-hydration coupling effect on microstructure of cement-based materials at early age. *Magnetic resonance imaging*, 23:311–4, 03 2005. doi: 10.1016/j.mri.2004.11.034.
- M. Fourmentin, P. Faure, S. Rodts, U. Peter, D. Lesueur, D. Daviller, and P. Coussot. Nmr observation of water transfer between a cement paste and a porous medium. *Cement and Concrete Research*, 95:56 – 64, 2017. ISSN 0008-8846. doi: <https://doi.org/10.1016/j.cemconres.2017.02.027>.
- D. Furbish. Fluid physics in geology: An introduction to fluid motions on earth’s surface and within its crust. *OUP USA*, 1997.
- D. Gawin, F. Pesavento, and B.A. Schrefler. Simulation of damage-permeability coupling in hygro-thermomechanical analysis of concrete at high temperature. *Communications of Numerical Methods in Engineering*, 2002.
- D. Gawin, F. Pesavento, and B.A. Schrefler. Hygro-thermo-chemo-mechanical modelling of concrete at early ages and beyond. part i: Hydration and hygro-thermal phenomena. *Int. J. Numer. Meth. Engng.*, 67: 299–331, 2006a.
- D. Gawin, F. Pesavento, and B.A. Schrefler. Hygro-thermo-chemo-mechanical modelling of concrete at early ages and beyond. part ii: Shrinkage and creep of concrete. *Int. J. Numer. Meth. Engng.*, 67:332–363, 2006b.
- M.T. Van Genuchten. A closed-form equation for predicting the hydraulic conductivity of unsaturated soils. *Soil Science Society of America Journal*, 1980.
- R. Gordon, R. Bender, and G. T. Herman. Algebraic reconstruction techniques (art) for three-dimensional electron microscopy and x-ray photography. *Journal of Theoretical Biology*, 29(3):471 – 481, 1970. ISSN 0022-5193. doi: [https://doi.org/10.1016/0022-5193\(70\)90109-8](https://doi.org/10.1016/0022-5193(70)90109-8). URL <http://www.sciencedirect.com/science/article/pii/0022519370901098>.
- L. Granger. *Comportement différé du béton dans les enceintes de centrales nucléaires*. PhD thesis, Ecole Nationale des Ponts et Chaussées., 1995.
- J.L. Granja, M. Azenha, C. de Sousa, R. Faria, and J. Barros. Hygrometric assessment of internal relative humidity in concrete: Practical application issues. *Journal of Advanced Concrete Technology*, 12:250 – 265, 2014.
- W. Gray and C. Miller. *Introduction to the Thermodynamically Constrained Averaging Theory for Porous Medium Systems*. 01 2014. doi: 10.1007/978-3-319-04010-3.
- L. Greenspan. Humidity fixed points of binary saturated aqueous solutions. *Journal of Research of the National Bureau of Standards-A. Physics and Chemistry*, pages 89–96, 1977.
- S.J. Gregg. Sixty years in the physical adsorption of gases. *Colloids and Surfaces*, 21:109 – 124, 1986.
- C-E Hagentoft, A.S. Kalagasidis, and B. Adl-Zarrabi. Assessment method of numerical prediction models for combined heat, air and moisture transfer in building components: Benchmarks for one-dimensional cases. *Journal of Thermal Envelope and Building Science*, 2004.
- L. D. Hall, M.H. G. Amin, E. Dougherty, M. Sanda, J. Votrubova, K. S. Richards, R. J. Chorley, and M. Cislerova. Mr properties of water in saturated soils and resulting loss of mri signal in water content detection at 2 tesla. *Geoderma*, 80(3):431 – 448, 1997. ISSN 0016-7061. doi: [https://doi.org/10.1016/S0016-7061\(97\)00065-7](https://doi.org/10.1016/S0016-7061(97)00065-7). NMR in Soil Science.

- R. Hassanein, E. Lehmann, and P. Vontobel. Methods of scattering corrections for quantitative neutron radiography. *Nuclear Instruments and Methods in Physics Research*, pages 353–360, 2005.
- R. Hassanein, H.O. Meyer, A. Carminati, M. Estermann, E. Lehmann, and P. Vontobel. Investigation of water imbibition in porous stone by thermal neutron radiography. *Journal of physics D: Applied physics*, pages 4284–4291, 2006a.
- R. Hassanein, F. de Beer, N. Kardjilov, and E. Lehmann. Scattering correction algorithm for neutron radiography and tomography tested at facilities with different beam characteristics. *Physica*, pages 1194–1196, 2006b.
- R.K. Hassanein. *Correction methods for the quantitative evaluation of thermal neutron tomography*. PhD thesis, Swiss Federal Institute of Technology, 2006.
- M. Hassanizadeh. Fundamentals of multiphase flow in porous media. <https://www.youtube.com/watch?v=bYI2MsiPv1E&list=PLFqI4Y7hNzjm3fZfrnr9fHHYoHACS2vzM>.
- M. Hassanizadeh and W. Gray. General conservation equations for multi-phase systems: 1. averaging procedure. *Advances in Water Resources*, 1979a.
- M. Hassanizadeh and W. Gray. General conservation equations for multi-phase systems: 2. mass, momenta, energy, and entropy equations. *Advances in Water Resources*, 1979b.
- M. Hassanizadeh and W. Gray. General conservation equations for multi-phase systems: 3. constitutive theory for porous media flow. *Advances in Water Resources*, 1980.
- A. Hilaire. *Etude des déformations différées des bétons en compression et en traction, du jeune au long terme: application aux enceintes de confinement*. PhD thesis, Ecole normale supérieure de Cachan, 2014.
- A. Hillerborg. Application of fracture mechanics to concrete : summary of a series of lectures 1988. 1988.
- Y. Huang, Z. Yang, W. Ren, G. Liu, and C. Zhang. 3d meso-scale fracture modelling and validation of concrete based on in-situ x-ray computed tomography images using damage plasticity model. *International Journal of Solids and Structures*, 67-68:340–352, 2015.
- American Concrete Institute.
- K. Ioannidou, M. Kanduc, L. Li, D. Frenkel, J. Dobnikar, and E. Del Gado. The crucial effect of early-stage gelation on the mechanical properties of cement hydrates. *Nature Communications*, 2016.
- C. Jailin, M. Etxegarai, E. Tudisco, S. Hall, and S. Roux. Fast tracking of fluid invasion using time-resolved neutron tomography. *Transport in Porous Media*, 124:1–19, 05 2018. doi: 10.1007/s11242-018-1055-9.
- O. M. Jensen and P. F. Hansen. Water-entrained cement-based materials: I. principles and theoretical background. *Cement and Concrete Research*, 31:647–654, 2001.
- O. M. Jensen and P. F. Hansen. Water-entrained cement-based materials: II. experimental observations. *Cement and Concrete Research*, 32:973–978, 2002.
- H. Justnes, K. Bryhn-Ingebrigtsen, and G.O. Rosvold. Neutron radiography: an excellent method of measuring water penetration and moisture content in concrete. 1989.
- A.C. Kak and M. Slaney. Principles of computerized tomographic imaging. *Society of Industrial and Applied Mathematics*, pages Philadelphia, (327 pp.), 2001.
- M. Kanematsu, I. Maruyama, T. Noguchi, H. Iikura, and N. Tsuchiya. Quantification of water penetration into concrete through cracks by neutron radiography. *Nuclear Instruments and Methods in Physics Research*, pages 154–158, 2009.
- M. Kanematsu, S. Bae, T. Koyama, R. Inose, N. Tsuchiya, M. Tamura, Y. Nishio, T. Noguchi, D. Ito, and Y. Saitou. Evaluation of the moisture movement in high-performance concrete subjected to heating. Technical report, The Research Reactor Institute, Kyoto University, 07 2015.
- N Kardjilov, F De Beer, R Hassanein, E Lehmann, and P Vontobel. Scattering corrections in neutron radiography using point scattered functions. *Nuclear Instruments and Methods in Physics Research Section A: Accelerators, Spectrometers, Detectors and Associated Equipment*, 542(1-3):336–341, 2005.

- A. Karhunen, K. Seppänen, A. Lehtikoinen, P. Monteiro, and J. Kaipio. Electrical resistance tomography imaging of concrete. *Cement and Concrete Research*, 40:137–145, 01 2010a. doi: 10.1016/j.cemconres.2009.08.023.
- K. Karhunen, A. Seppänen, A. Lehtikoinen, J. Blunt, J. Kaipio, and P. Monteiro. Electrical resistance tomography for assessment of cracks in concrete. *ACI Materials Journal*, 107:523–531, 09 2010b.
- J.-K. Kim and C.-S. Lee. Moisture diffusion of concrete considering self-desiccation at early ages. *Cement and Concrete Research*, 29(12):1921 – 1927, 1999. doi: [https://doi.org/10.1016/S0008-8846\(99\)00192-1](https://doi.org/10.1016/S0008-8846(99)00192-1).
- K. Y. Kim, T. S. Yun, and K. P. Park. Evaluation of pore structures and cracking in cement paste exposed to elevated temperatures by x-ray computed tomography. *Cement and Concrete Research*, 50:34 – 40, 2013. doi: <https://doi.org/10.1016/j.cemconres.2013.03.020>.
- T.C. King, C.M. Dobson, and S.A. Rodger. Hydration of tricalcium silicate with d<sub>2</sub>o. *Journal of Materials Science Letters*, 7:861–863, 1988. doi: 10.1007/BF00723787.
- A. E. Knowler. On the measurement of the electrical resistance of porous materials. *Proceedings of the Physical Society*, 40(1):37–40, 1927. doi: 10.1088/0959-5309/40/1/307. URL <https://doi.org/10.1088/0959-5309/40/1/307>.
- C. La Borderie, C. Lawrence and A. Menou. Approche mésoscopique du comportement du béton. *Revue Européenne de Génie Civils*, 11:407–421, 2007.
- M.C. Leverett. Capillary behavior of porous solid. *Transactions of the American Institute of Mining and Metallurgical Engineers*, pages 152–169, 1941.
- R. Lewis and B. Schrefler. *The Finite Element Method in the Static and Dynamic Deformation and Consolidation of Porous Media*. John Wiley, 1998.
- M. Lieboldt and V. Mechtcherine. Capillary transport of water through textile-reinforced concrete applied in repairing and/or strengthening cracked rc structures. *Cement and Concrete Research*, 52: 53 – 62, 2013. ISSN 0008-8846. doi: <https://doi.org/10.1016/j.cemconres.2013.05.012>. URL <http://www.sciencedirect.com/science/article/pii/S0008884613001269>.
- R. Loubser Du Plooy, G. Villain, S. Palma Lopes, A. Ihamouten, and X. Derobert. Electromagnetic non-destructive evaluation techniques for the monitoring of water and chloride ingress into concrete: a comparative study. *Materials and Structures*, 48:369–386, 2015.
- B. D. Lucas and T. Kanade. An iterative image registration technique with an application to stereo vision. *IJCAI'81: Proceedings of the 7th international joint conference on Artificial intelligence*, 2:674–679, 1981.
- B. Lukić, A. Tengattini, F. Dufour, and M. Briffaut. Visualising water vapour condensation in cracked concrete with dynamic neutron radiography. 09 2020.
- P. Lura and G.P. Terrasi. Reduction of fire spalling in high-performance concrete by means of super absorbent polymers and polypropylene fibers: Small scale fire tests of carbon fiber reinforced plastic-prestressed self-compacting concrete. *Cement and Concrete Composites*, 49:36 – 42, 2014. ISSN 0958-9465. doi: <https://doi.org/10.1016/j.cemconcomp.2014.02.001>. URL <http://www.sciencedirect.com/science/article/pii/S0958946514000304>.
- X. Ma, J. Carette, F. Benboudjema, and R. Bennacer. Optimization of experiment methodology based on identification of parameters in concrete drying. *Construction and Building Materials*, 256:119421, 2020. ISSN 0950-0618. doi: <https://doi.org/10.1016/j.conbuildmat.2020.119421>.
- M. Mainguy, O. Coussy, and R. Eymard. Modélisation des transferts hydriques isothermes en milieux poreux. application au séchage des matériaux à base de ciment. *Etudes et recherches des laboratoires des ponts et chaussées*, 2001.
- E. Marfisi, C. Burgoyne, M. Amin, and L. Hall. The use of mri to observe the structure of concrete. *Magazine of Concrete Research - MAG CONCR RES*, 57:101–109, 01 2005. doi: 10.1680/macr.57.2.101.58705.
- I. Maruyama, M. Kanematsu, T. Noguchi, H. Iikura, A. Teramoto, and H. Hayano. Evaluation of water transfer from saturated lightweight aggregate to cement paste matrix by neutron radiography. *Nuclear Instruments and Methods in Physics Research*, pages 159–162, 2009.

- M. Matallah, C. La Borderie, and O. Manuel. A practical method to estimate crack openings in concrete structures. *International Journal for Numerical and Analytical Methods in Geomechanics*, 34:1615–1633, 2010.
- J. Mazars. *Application de la mécanique de l'endommagement au comportement non linéaire et à la rupture du béton de structure*. PhD thesis, Université Paris 6, 1984.
- C. Mazzotti and M. Savoia. Nonlinear creep damage model for concrete under uniaxial compression. *Journal of Engineering Mechanics*, 129(9):1065–1075, 2003. doi: 10.1061/(ASCE)0733-9399(2003)129:9(1065).
- P. McDonald, O. Istok, M. Janota, A. Gajewicz-Jaromin, and D. Faux. Sorption, anomalous water transport and dynamic porosity in cement paste: a spatially localised 1H NMR relaxation study and a proposed mechanism. *Cement and Concrete Research*, March 2020. URL <http://epubs.surrey.ac.uk/854077/>.
- P.J. McGlenn, F.C. de Beer, L.P. Aldridge, M.J. Radebe, R. Nshimirimana, D. Brew, T.E. Payne, and K. Olufson. Appraisal of a cementitious material for waste disposal: neutron imaging studies of pore structure and sorptivity. *Cement and Concrete Research*, pages 1320–1326, 2010.
- F. Meftah, S. Dal Pont, and B.H. Schrefler. A three-dimensional staggered finite element approach for random parametric modeling of thermo-hygral coupled phenomena in porous media. *International Journal for Numerical and Analytical Methods in Geomechanics*, 2012.
- P. K. Mehta. *Concrete Structure properties and materials*. Englewood Cliff, New Jersey, Prentice-Hall, 1986.
- D. Meyer, H.K. Man, and J.G.M. van Mier. Fracture of foamed cementitious materials: A combined experimental and numerical study. *IUTAM Symposium on Mechanical Properties of Cellular Materials*, 12, 2009.
- R.H. Mills. Factors influencing cessation of hydration in water cured cement pastes. *Special Report No. 90, Proceedings of the Symposium on the Structure of Portland Cement Paste and Concrete, Highway Research Board, Washington DC, USA*, 1960.
- J.-C. Mindeguia, I. Hager, P. Pimienta, H. Carré, and C. La Borderie. Parametrical study of transient thermal strain of ordinary and high performance concrete. *Cement and Concrete Research*, 48:40 – 52, 2013. doi: <https://doi.org/10.1016/j.cemconres.2013.02.004>.
- C. Moyne. *Transferts couples chaleur-masse lors du séchage: prise en compte du mouvement de la phase gazeuse*. PhD thesis, Institut National Polytechnique de Lorraine, 1987.
- Y. Mualem. A new model predicting the hydraulic conductivity of unsaturated porous media. *Water Resources Research*, pages 513–522, 1976.
- T.D. Nguyen. *Apport de la modélisation mésoscopique dans la prédiction des écoulements dans les ouvrages en béton fissuré en conditions d'accident grave*. PhD thesis, L'Université de Pau et des Pays de l'Adour, 2010.
- A.F. Nielsen. Gamma-ray-attenuation used for measuring the moisture content and homogeneity of porous concrete. *Building Science*, 7(4):257 – 263, 1972. doi: [https://doi.org/10.1016/0007-3628\(72\)90007-2](https://doi.org/10.1016/0007-3628(72)90007-2).
- D. L. Nofziger. Errors in gamma-ray measurements of water content and bulk density in nonuniform soils. *Soil Science Society of America Journal*, 42(6):845–850, 1978. doi: 10.2136/sssaj1978.03615995004200060001x. URL <https://access.onlinelibrary.wiley.com/doi/abs/10.2136/sssaj1978.03615995004200060001x>.
- P. Norberg. Electrical measurement of moisture content in porous building materials. 1999.
- F.E.M. O'Brien. The control of humidity by saturated salt solutions. *Journal of Scientific Instruments*, pages 73–76, 1947.
- N. Otsu. A threshold selection method from gray-level histograms. *IEEE Transactions on Systems, Man, and Cybernetics*, 9:62–66, 1979.
- J. Ožbolt, F. Oršanić, and G. Balabanić. Modeling influence of hysteretic moisture behavior on distribution of chlorides in concrete. *Cement and Concrete Composites*, 67:73 – 84, 2016. ISSN 0958-9465. doi: <https://doi.org/10.1016/j.cemconcomp.2016.01.004>. URL <http://www.sciencedirect.com/science/article/pii/S0958946516300038>.

- W.J. Palenstijn, K. Batenburg, and J. Sijbers. The astra tomography toolbox. *Proc. 13th Int. Conf. Comput. Math. Meth. Sci. Eng. (CMMSE)*, pages 1–7, 01 2013.
- J. Pan, Y. Feng, J. Wang, Q. Sun, C. Zhang, and D.R.J. Owen. Modeling of alkali-silica reaction in concrete: A review. *Frontiers of Structural and Civil Engineering*, 6, 03 2012. doi: 10.1007/s11709-012-0141-2.
- L. Pel and H. Huinink. NMR imaging of moisture and ion transport in building materials. *Journal of Solid State Electrochemistry - J SOLID STATE ELECTROCHEM*, 02 2009. doi: 10.1002/9783527626052.ch28.
- E. Perfect, C.-L. Cheng, H.Z. Bilheux M. Kang, J.M. Lamanna, M.J. Gragg, and D.M. Wright. Neutron imaging of hydrogen-rich fluids in geomaterials and engineered porous media: A review. *Earth-Science Reviews*, 2014.
- P. Perre and A. Degiovanni. Simulation par volumes finis des transferts couplés en milieux poreux anisotropes: Séchage du bois à basse et à haute température. *International Journal of Heat and Mass Transfert*, pages 2463–2478, 1990.
- F. Pesavento. *Non-linear modelling of concrete as multiphase porous material in high temperature conditions*. PhD thesis, Università degli Studi di Bologna., 2000.
- O. Peter. Neutronen-durchleuchtung z. *Naturforsch.*, 1946.
- J.R. Philip. Physics of water movement in porous solids. *Special Report N.40*, 1958.
- J.R. Philip and D.A. De Vries. Moisture movement in porous materials under temperature gradients. *Transactions, American Geophysical Union*, 1957.
- M.C. Phillipson, P. Baker, M. Davies, Z. Ye, A. McNaughtan, G.H. Galbraith, and R.C. McLean. Moisture measurement in building materials: An overview of current methods and new approaches. *Building Services Engineering Research and Technology*, 28, 11 2007. doi: 10.1177/0143624407084184.
- V. Picandet, A. Khelidj, and G. Bastian. Effect of axial compressive damage on gas permeability of ordinary and high-performance concrete. *Cement and Concrete Research*, 2001.
- V. Picandet, K. Abdelhafid, and H. Bellegou. Crack effects on gas and water permeability of concretes. *Cement and Concrete Research*, 39:537–547, 06 2009. doi: 10.1016/j.cemconres.2009.03.009.
- G. Pijaudier-Cabot and Z. Bazant. Nonlocal damage theory. *Journal of Engineering Mechanics-asce - J ENG MECH-ASCE*, 113, 10 1987. doi: 10.1061/(ASCE)0733-9399(1987)113:10(1512).
- G. Pijaudier-Cabot, F. Dufour, and M. Choinska. Permeability due to the increase of damage in concrete: From diffuse to localized damage distributions. *Journal of Engineering Mechanics-asce - J ENG MECH-ASCE*, 135, 09 2009. doi: 10.1061/(ASCE)EM.1943-7889.0000016.
- J. L. M. Poiseuille. *Recherches expérimentales sur le mouvement des liquides de nature différente dans les tubes de très petits diamètres*. Annales de chimie et physique, Tome XXI. Edition Masson, 1840.
- T. C. Powers. Physical properties of cement paste. *Proceedings of the Fourth International Symposium on the Chemistry of Cement, Washington, DC*, 1:577–613, 1960.
- S. Poyet. Experimental investigation of the effect of temperature on the isotherm of concrete. *Cement and Concrete Research*, 2009.
- J. Radon. *Berichte saechsische akademie der wissenschaften (leipzig)*. 1917.
- S. Rahimi-Aghdam, M. Rasoolinejad, and Z. Bazant. Moisture diffusion in unsaturated self-desiccating concrete with humidity-dependent permeability and nonlinear sorption isotherm. *Journal of Engineering Mechanics*, 145, 03 2019. doi: 10.1061/(ASCE)EM.1943-7889.0001591.
- G. Rastiello, J. Tailhan, P. Rossi, and S. Dal Pont. Macroscopic probabilistic cracking approach for the numerical modelling of fluid leakage in concrete. *Annals of Solid and Structural Mechanics*, 7:1–16, 03 2015. doi: 10.1007/s12356-015-0038-6.
- R. Reid, J. Prausnitz, and B. Poling. *The properties of gases and liquids*. 1987.

- H. Reijonen and S. Pihlajavaara. On the determination by neutron radiography of the thickness of the carbonated layer of concrete based upon changes in water content. *Cement and Concrete Research*, 1972.
- S. Roels and J. Carmeliet. Analysis of moisture flow in porous materials using microfocus x-ray radiography. *International Journal of Heat and Mass Transfer*, 49(25):4762 – 4772, 2006. URL <http://www.sciencedirect.com/science/article/pii/S0017931006003863>.
- S. Roels, O. Adan, H. Brocken, J. Carmeliet, R. Černý, C. Hall, H. Hens, M. Kumaran, Z. Pavlik, L. Pel, and R. Plagge. A comparison of different techniques to quantify moisture content profiles in porous building materials. *Journal of Thermal Envelope and Building Science*, 27, 04 2004. doi: 10.1177/1097196304042117.
- E. Roubin, E. Ando, and S. Roux. The colours of concrete as seen by x-rays and neutrons. *Cement and Concrete Composites*, 2019.
- T. Rougelot. *Etude multi-échelles des couplages hydriques, mécaniques et chimiques dans les matériaux cimentaires*. PhD thesis, Université des Sciences et Technologies de Lille, 2008.
- G. Sanderson. 2018. URL [www.3blue1brown.com](http://www.3blue1brown.com).
- J. Schindelin, I. Arganda-Carreras, and E. Frise. Fiji: an open-source platform for biological-image analysis. 9:676–682, 2012.
- Christof Schroeffl, Viktor Mechtcherine, Anders Kaestner, Peter Vontobel, Jan Hovind, and Eberhard Lehmann. Transport of water through strain-hardening cement-based composite (shcc) applied on top of cracked reinforced concrete slabs with and without hydrophobization of cracks - investigation by neutron radiography. *Construction and Building Materials*, 76, 02 2015. doi: 10.1016/j.conbuildmat.2014.11.062.
- G. Sciumè and F. Benboudjema. A viscoelastic unitary crack-opening strain tensor for crack width assessment in fractured concrete structures. *Mechanics of Time-Dependent Materials*, 21, 2017. doi: 10.1007/s11043-016-9327-7.
- G. Sciumè, F. Benboudjema, C. De Sa, Y. Berthaud, and B.A. Schrefler. A multiphysics model for concrete at early age applied to repairs problems. *Engineering Structures*, 57:374–387, 2013.
- G. Sciumè. *Thermo-hygro-chemo-mechanical model of concrete at early ages and its extension to tumor growth numerical analysis*. PhD thesis, Ecole Normale Supérieure de Cachan., 2013.
- V. Smil. *Making the Modern World: Materials and Dematerialization*. Wiley, 2014.
- F. Soleilhet, F. Benboudjema, X. Jourdain, and F. Gatuingt. Role of pore pressure on cracking and mechanical performance of concrete subjected to drying. *Cement and Concrete Composites*, page 103727, 08 2020. doi: 10.1016/j.cemconcomp.2020.103727.
- O. Stamati. *Effet des hétérogénéités sur le comportement mécanique du béton à l'échelle mésoscopique : apports de la micro-tomographie à rayons-x in-situ combinée à une modélisation E-FEM*. PhD thesis, 2020.
- O. Stamati, E. Roubin, E. Andò, and Y. Malecot. Tensile failure of micro-concrete: from mechanical tests to fe meso-model with the help of x-ray tomography. *Meccanica*, 11 2018. doi: 10.1007/s11012-018-0917-0.
- O. Stamati, E. Andò, E. Roubin, R. Cailletaud, M. Wiebicke, G. Pinzon, R. C. Hurley, R. Caulk, C. Couture, A. O. Laborin, D. Caillerie, T. Matsushima, O. Okubadejo, R. Rorato, P. Bésuelle, F. Bertoni, T. Arnaud, Y. Sun, A. Tengattini, J.B. Colliat, M. Saadatfar, F. E. Garcia, C. Papazoglou, I. Vego, S. Brisard, J. Dijkstra, and G. Birmpilis. spam: Software for practical analysis of materials. *JOSS the Journal of Open Source Software*, 2020.
- E. Stavropoulou, E. Andò, A. Tengattini, M. Briffaut, F. Dufour, D. Atkins, and G. Armand. Liquid water uptake in unconfined callovo oxfordian clay-rock studied with neutron and x-ray imaging. *Acta Geotechnica*, 14:19–33, 2019.
- E. Stavropoulou, E. Ando, E. Roubin, N. Lenoir, A. Tengattini, M. Briffaut, and P. Besuelle. Dynamics of water absorption in callovo-oxfordian clayrock revealed with multimodal x-ray and neutron tomography. *Frontiers*, 2020.

- M. Strobl, I. Manke, N. Kardjilov, A. Hilger, M. Dawson, and J. Banhart. Topical review: Advances in neutron radiography and tomography. *Journal of Physics D-applied Physics - J PHYS-D-APPL PHYS*, 42, 12 2009. doi: 10.1088/0022-3727/42/24/243001.
- A. H. Tavangarrad, S. Hassanizadeh, R. Rosati, L. Digirolamo, and M. Van Genuchten. Capillary pressure-saturation curves of thin hydrophilic fibrous layers: effects of overburden pressure, number of layers, and multiple imbibition-drainage cycles. *Textile Research Journal*, 04 2019. doi: 10.1177/0040517519844209.
- R.T. Tenchev, L.Y. Li, and J.A. Purkiss. Finite element analysis of coupled heat and moisture transfer in concrete subjected to fire. *Numerical Heat Transfer*, 2001.
- A. Tengattini, S. Dal Pont, H. Cheikh Sleiman, F. Kisuka, and M. Briffaut. Quantification of evolving moisture profiles in concrete samples subjected to temperature gradient by means of rapid neutron tomography: influence of boundary conditions, hygro-thermal loading history and spalling mitigation additives. *Strain*, 2020a.
- A. Tengattini, N. Lenoir, E. Andò, B. Giroud, D. Atkins, J. Beaucour, and G. Viggiani. Next-grenoble, the neutron and x-ray tomograph in grenoble. *Nuclear Instruments and Methods in Physics Research Section A: Accelerators, Spectrometers, Detectors and Associated Equipment*, page 163939, 2020b.
- A. Tengattini, N. Lenoir, E. Andò, and G. Viggiani. Neutron imaging for geomechanics: A review. *Geomechanics for Energy and the Environment*, page 100206, 2020c. doi: <https://doi.org/10.1016/j.gete.2020.100206>.
- M. Thiery, V. Baroghel-Bouny, N. Bourneton, G. Villain, and C. Stéfani. Modélisation du séchage des bétons - analyse des différents modes de transfert hydrique. *Revue Européenne de Génie Civil*, pages 541–577, 2007.
- H.R. Thomas and M. Sansom. Fully coupled analysis of heat, moisture and air transfer in unsaturated soil. *Journal of Engineering Mechanics*, 1995.
- N. Toropovs, F. Lo Monte, M. Wyrzykowski, B. Weber, G. Sahmenko, P. Vontobel, R. Felicetti, and P. Lura. Real-time measurements of temperature, pressure and moisture profiles in high-performance concrete exposed to high temperatures during neutron radiography imaging. *Cement and Concrete Research*, 68: 166 – 173, 2015. ISSN 0008-8846. doi: <https://doi.org/10.1016/j.cemconres.2014.11.003>. URL <http://www.sciencedirect.com/science/article/pii/S0008884614002233>.
- F. Toulemonde and F. Le Maou. Protection des éprouvettes de béton vis-à-vis de la dessiccation. le point sur quelques techniques de laboratoire. *Bulletin de Liaison des Laboratoires des Ponts et Chaussées*, 203: 105–119, 1996.
- P. Trtik, P. Stähli, E. Landis, M. Stampanoni, and J.G.M. van Mier. Microtensile testing and 3d imaging of hydrated portland cement. *Proceedings 6th International Conference on Fracture Mechanics of Concrete and Concrete Structures (FraMCoS-VI)*, pages 1277–1282, 2007.
- P. Trtik, B. Münch, W. Weiss, A. Kaestner, I. Jerjen, L. Josic, E. Lehmann, and P. Lura. Release of internal curing water from lightweight aggregates in cement paste investigated by neutron and x-ray tomography. *Nuclear Instruments and Methods in Physics Research*, pages 244–249, 2011.
- E. Tudisco, C. Jailin, A. Mendoza, A. Tengattini, E. Ando', and S.A. Hall. An extension of digital volume correlation for multimodality image registration. *Measurement Science and Technology*, 28, 2017.
- K. Tuutti. *Corrosion of steel in concrete*. PhD thesis, Swedish Cement and Concrete Research Institute, Stockholm, 1982.
- G. Viggiani and A. Tengattini. Recent developments in laboratory testing of geomaterials with emphasis on imaging. 2019.
- G. Viggiani, S. A. Hall, and E. Romero. Advanced experimental techniques in geomechanics. *Alert Doctoral School*, 2012.
- G. Villain and M. Thiery. Uncertainty of gammadensimetry measurements on concrete specimens. *Bulletin des Laboratoires des Ponts et Chaussees*, pages 69–82, 01 2006a.

- Géraldine Villain and M. Thiery. Gammadensimetry: A method to determine drying and carbonation profiles in concrete. *Ndt E International - NDT E INT*, 39:328–337, 06 2006b. doi: 10.1016/j.ndteint.2005.10.002.
- P. Vontobel, E.H. Lehmann, R. Hassanein, and G. Frei. Neutron tomography: method and applications. *Physica*, pages 475–480, 2006.
- A. Voss, M. Pour-Ghaz, M. Vauhkonen, and A. Seppänen. Electrical capacitance tomography to monitor unsaturated moisture ingress in cement-based materials. *Cement and Concrete Research*, 89, 11 2016. doi: 10.1016/j.cemconres.2016.07.011.
- A. Voss, P. Hosseini, M. Pour-Ghaz, M. Vauhkonen, and A. Seppänen. Three-dimensional electrical capacitance tomography – a tool for characterizing moisture transport properties of cement-based materials. *Materials and Design*, page 107967, 06 2019. doi: 10.1016/j.matdes.2019.107967.
- Antti Voss. *Imaging moisture flows in cement-based materials using electrical capacitance tomography*. PhD thesis, 02 2020.
- X. H. Vu. *Caractérisation expérimentale du béton sous fort confinement : influences du degré de saturation et du rapport eau/ciment*. PhD thesis, Université Joseph Fourier, 2007.
- V. Waller. *Relations entre la composition des betons, exothermie en cours de prise et resistance en compression*. PhD thesis, Ecole Nationale des Ponts et Chaussees, 1999.
- C.Y. Wang and C. Beckermann. A two-phase mixture model of liquid-gas flow and heat transfer in capillary porous media - i formulation. *International Journal of Heat Mass Transfer*, 1993.
- C.Y. Wang and P. Cheng. A multiphase mixture model for multiphase, multicomponent transport in capillary porous media - i. model development. *International Journal of Heat Mass Transfer*, 1996.
- J. Wang, L. Lacarrière, and A. Sellier. Multicomponent modelling of cement paste dehydration under different heating rates. *Materials and Structures*, 2019.
- B. Weber, M. Wyrzykowski, M. Griffa, S. Carl, E.H. Lehmann, and P. Lura. Neutron radiography of heated high-performance mortar. *Workshop Concrete Spalling Due to Fire Exposure*, pages 186 – 193, 2013.
- F.H. Wittmann, P. Zhang, T.J. Zhao, E. Lehmann, and P. Vontobel. Neutron radiography, a powerful method for investigating water penetration into concrete. *The 50-year Teaching and Research Anniversary of Prof. SunWei on Advances in Civil Engineering Materials.*, pages 61–70, 2010.
- M. Wyrzykowski, P. J. McDonald, K. L. Scrivener, and P. Lura. Water redistribution within the microstructure of cementitious materials due to temperature changes studied with 1h nmr. *The Journal of Physical Chemistry C*, 121(50):27950–27962, 2017. doi: 10.1021/acs.jpcc.7b08141.
- G. Xotta, G. Mazzucco, V.A. Salomoni, C.E. Majorana, and K.J. Willam. Composite behavior of concrete materials under high temperatures. *International Journal of Solids and Structures*, 64-65:86 – 99, 2015. doi: <https://doi.org/10.1016/j.ijsolstr.2015.03.016>.
- K. Xu, A. Tremsin, J. Li, D. Ushizima, C. Davy, A. Bouterf, Y. Su, M. Marroccoli, A. Mauro, M. Osanna, A. Telesca, and P. Monteiro. Microstructure and water absorption of ancient concrete from pompeii: An integrated synchrotron microtomography and neutron radiography characterization. *Journal of Applied Physics*, 2020.
- Z. Yang, W. Ren, M. Mostafavi, S. Mcdonald, and T. Marrow. Characterisation of 3d fracture evolution in concrete using in-situ x-ray computed tomography testing and digital volume correlation. pages 236–242, 01 2013.
- Z.J. Yang, B.B. Li, and J.Y. Wu. X-ray computed tomography images based phase-field modeling of mesoscopic failure in concrete. *Engineering Fracture Mechanics*, 208:151 – 170, 2019. ISSN 0013-7944. doi: <https://doi.org/10.1016/j.engfracmech.2019.01.005>. URL <http://www.sciencedirect.com/science/article/pii/S0013794418313122>.
- M. Yehya. *Propriétés de transfert dans le béton par imagerie neutronique*. PhD thesis, 2018.
- M. Yehya, E. Andò, F. Dufour, and A. Tengattini. Fluid-flow measurements in low permeability media with high pressure gradients using neutron imaging: Application to concrete. *Nuclear Instruments and Methods in Physics Research*, 890:35–42, 2018.

- A. Zeilinger and R. Huebner. Moisture transport in a concrete of the snr 300 investigated by neutron transmission. *Kerntechnik Z. Ing. aller Fachrichtungen* 18, pages 119–125, 1976.
- Jun Zhang, Jiahe Wang, and Yudong Han. Simulation of moisture field of concrete with pre-soaked lightweight aggregate addition. *Construction and Building Materials*, 96:599 – 614, 2015. ISSN 0950-0618. doi: <https://doi.org/10.1016/j.conbuildmat.2015.08.058>. URL <http://www.sciencedirect.com/science/article/pii/S0950061815302609>.
- P. Zhang, F.H. Wittmann, T. Zhao, and E.H. Lehmann. Neutron imaging of water penetration into cracked steel reinforced concrete. *Physica B: Condensed Matter*, 405(7):1866 – 1871, 2010. ISSN 0921-4526. doi: <https://doi.org/10.1016/j.physb.2010.01.065>. URL <http://www.sciencedirect.com/science/article/pii/S0921452610000852>.
- P. Zhang, F.H. Wittmann, E. Lehmann, L. Tian, and P. Vontobel. Observation and quantification of water penetration into strain hardening cement-based composites (shcc) with multiple cracks by means of neutron radiography. *Nuclear Instruments and Methods in Physics Research*, pages 414–420, 2010b.
- P. Zhang, F.H. Wittmann, T.J. Zhao, E. Lehmann, L. Tian, and P. Vontobel. Neutron radiography, a powerful method to determine time-dependent moisture distributions in concrete. *Nuclear Engineering Design*, pages 4758–4766, 2011.
- P. Zhang, P. Wang, D. Hou, Z. Liu, M. Haist, and T. Zhao. Application of neutron radiography in observing and quantifying the time-dependent moisture distributions in multi-cracked cement-based composites. *Cement and Concrete Composites*, 78, 12 2016. doi: 10.1016/j.cemconcomp.2016.12.006.
- P. Zhang, F. H. Wittmann, P. Lura, H. S. Muller, S. Han, and T. Zhao. Application of neutron imaging to investigate fundamental aspects of durability of cement-based materials: A review. *Cement and Concrete Research*, 108:152–166, 2018.
- Z. Zhang and U. Angst. Modeling anomalous moisture transport in cement-based materials with kinetic permeability. 21:837, 01 2020.